Discontinuity mappings in piecewise-smooth dynamical systems

Rohit Chawla

Student number: 19202868

The thesis is submitted to University College Dublin in fulfillment of the required degree of Doctor of Philosophy

UCD School of Mechanical and Materials Engineering

Head of School: Assoc. Prof. Vincent Hargaden
Primary supervisor: Assoc. Prof. Vikram Pakrashi

Doctoral study panel members:
Prof. Alojz Ivankovic
Assoc. Prof. Vikram Pakrashi
Asst. Prof. Kevin Nolan

University College Dublin
Dublin, Ireland
December 21, 2023

Dedicated to my parents - Rajesh & Sneha Chawla
My fiancée - Seevani Bali
My aunt - Rita Roy
My mentor - Dr. Saugata Bhattacharyya

Abstract

In various engineering applications, mechanical systems consist of several moving parts that can frequently impact each other. Due to wear and tear, such collisions may result from limited clearance between mechanical components or loosened joints. These impacts cause undesirable chaotic vibrations, often resulting in mechanical damage like fatigue, crack propagation, fracture, etc. Nonlinear dynamical systems phenomenologically model such physical systems. The state variables, modeling such systems, evolve in the phase space and are interrupted by sudden changes almost instantaneously. The time scale over which such transitions occur is generally much smaller than the time period of oscillations observed for the respective physical system. Such transitions in the phase space occur when state variables interact with a hyper-surface, which models events like impacts and collisions in the physical system. This hyper-surface, also known as a discontinuity boundary, separates the phase space into distinct regions where the state variables evolve smoothly, *i.e.* their evolution is governed by functions with well-defined higher order time derivatives. Therefore, the evolution of such systems is modeled by smooth functions except at the discontinuity boundary, thus making them piecewise-smooth. Piecewise-smooth dynamical systems are often used to model a diverse range of physical systems undergoing rapid changes in biology, electrical engineering, ecology, finance, population dynamics, etc. Numerical investigation of piecewise-smooth systems shows that they exhibit a wide variety of rich dynamical behavior collectively known as discontinuity-induced bifurcations, including routes to chaotic attractors, not observed in systems governed by smooth functions of its arguments. Such unstable responses and chaotic vibrations are undesirable in most engineering applications. This necessitates to develop a unified theory for investigations of a large class of piecewise-smooth dynamical systems. Although a well-developed bifurcation theory for smooth dynamical systems exists, they are not directly applicable to piecewise-smooth systems.

In the current literature on piecewise-smooth dynamical systems, the existing methodologies rely on the eigenvalue analysis of Poincaré maps and Monodromy matrices by constructing a discontinuity mapping. Discontinuity mappings are pivotal in the analysis of non-smooth systems since their implementation accounts for the abrupt changes to the state variables evolving in phase space, after which conventional methods like stability analysis using Floquet multipliers and Lyapunov exponents can be directly applied in their investigation. However, existing methods to calculate discontinuity mappings rely on local linearization approaches. These only consider the first few terms in the Taylor expansions of vector fields that govern how the state variables evolve in time. Such approximations can lead to incorrect estimation of impact occurrences and discontinuity mappings for non-smooth systems

with sensitive dependence on initial conditions. A deeper investigation of discontinuity mappings, presented in this thesis, obtained using conventional first-order approaches reveals that the linearized methods can predict incorrect mappings of the state variables during interaction or impact with the discontinuity barrier. These incorrect mappings necessitate the inclusion of higher-order correction terms to the widely accepted first-order discontinuity mappings, also known as saltation matrices. Furthermore, the current literature primarily focuses on discontinuity mappings of perturbations for certain limiting cases like grazing incidence.

This thesis attempts to illustrate the limitation and problem arising during the implementation of a first-order discontinuity mapping for piecewise-smooth dynamical systems of hybrid (non-smooth systems comprising ordinary differential equation and discrete maps) and Filippov type (non-smooth systems governed by multiple vector fields). The thesis derives a higher-order discontinuity mapping for hybrid and Filippov systems which resolves the issues encountered during a first-order approximation. The proposed higher-order discontinuity mappings imply that not all state variables in the local neighborhood of an impacting state should undergo a mapping near the discontinuity barrier. This contradicts the predictions of the first-order saltation matrices, which allow discrete mappings for all values of perturbations in the local neighborhood of an impacting state. Compared to the exact numerical solution, the higher-order discontinuity mapping provides accurate estimates regarding the behavior of state variables near the discontinuity boundary, which the first-order saltation matrix fails to capture.

Next, the thesis presents a numerical methodology to calculate higher-order saltation matrices from the derived higher-order transverse discontinuity mapping for hybrid and Filippov systems. The proposed approaches can be incorporated to accommodate higher-order correction terms up to any order. The thesis discusses methods to estimate Floquet multipliers and Lyapunov exponents for hybrid and Filippov systems, aided by the derived higher-order discontinuity mappings and saltation matrices. The results are verified with numerically obtained bifurcation diagrams of several representative non-smooth dynamical systems like impact oscillators undergoing instantaneous transitions in their state variables.

Further, the thesis numerically investigates the dynamical responses of a phenomenological model representing the simplest case of a non-smooth hybrid fluid-structure interaction system interacting with a rigid barrier. The instantaneous changes in the system's dynamics show a rich underlying mathematical structure in its responses. A comparison between the proposed higher-order discontinuity mappings with the first-order approaches for the representative non-smooth fluid-structure interaction system reveals that the higher-order correction terms provide better estimates of mapping as validated by the exact numerical solution. Next, numerical methods to evaluate Floquet multipliers and Lyapunov exponents are im-

plemented, which can accurately predict when bifurcations occur as validated by the corresponding bifurcation diagrams obtained independently.

The thesis concludes with an attempt to experimentally verify the occurrence of discontinuity-induced bifurcations typical to piecewise-smooth dynamical systems. An electronic circuit is implemented comprising two LCR circuits with a switching mechanism. This experimental setup is equivalent to a piecewise-smooth Filippov system. The experimental results verify topological changes in the system's dynamics, typical of non-smooth dynamical systems. The phase portraits recorded experimentally corroborate with the analytical and numerical predictions obtained independently using the proposed higher-order transverse discontinuity mapping.

Declaration

I hereby certify that the submitted work is my own work, was completed while registered as a candidate for the degree stated on the Title Page, and I have not obtained a degree elsewhere on the basis of the research presented in this submitted work.

Rohit Chawla
December 21, 2023

Acknowledgments

I sincerely thank my supervisor, Dr. Vikram Pakrashi, whose immense support, insightful feedback, and continuous guidance have been pivotal in completing this thesis. I am also deeply indebted to my collaborator and friend, Dr. Aasifa Rounak, for her invaluable advice, enthusiastic encouragement, and passion for the subject, which enriched my research experience. I thank my collaborators, Dr. Chandan Bose and Dr. Soumyajit Seth, for their valuable feedback and guidance. I thank the research studies panel members Prof. Alojz Ivankovic and Dr. Kevin Nolan for their insightful suggestions and critical feedback.

I have been blessed with admirable mentors, Dr. Saugata Bhattacharyya, Dr. Vikram Pakrashi, and Prof. Jayanta K. Bhattacharjee, who have significantly shaped my academic career. Their continuous advice and mental support have helped me grow not only in research but in my personal life as well.

On a more personal note, I would like to express my deepest appreciation to my partner, Seevani Bali, who has constantly supported me, especially when I was most vulnerable. Her continuous support, love, and care were crucial during my academic journey.

I sincerely thank all my friends in room 218A, UCD, especially Meiy, Ankush, and Ramon, for making me feel at home despite being away from India. I want to thank my childhood friend Soumyabrata Paul, with whom I have shared beautiful memories since high school. Their existence has significantly made my research career more relaxed and cheerful.

I am forever grateful to my parents, Rajesh and Sneha Chawla, for their continuous love, support, and care, for which I became the person I am today. I also sincerely thank my family, especially my aunt Rita Roy, for all the guidance and love during my undergraduate and graduate days.

I sincerely acknowledge the support from the School of Mechanical and Materials Engineering, University College Dublin (UCD), and the financial support from Interreg SIRMA Project, SEAI Remote Wind RDD/613 and HEA Covid Support Fund, UCD.

Contents

List of Figures

Articles and conferences

Articles

1. **Chawla, R.**, Rounak, A., Pakrashi, V., 2023. Stability analysis of hybrid systems with higher-order transverse discontinuity mapping. *Under review in Physical Review E*

2. **Chawla, R.**, Rounak, A., Bose, C., Pakrashi, V., 2023. Wake-induced response dynamics of a vibro-impacting system. *Under review in Nonlinear Dynamics*

3. **Chawla, R.**, Rounak, A., Pakrashi, V., 2023. Higher-order transverse discontinuity mapping for hybrid dynamical systems. *Accepted for publication in Advances of nonlinear dynamics (Conference Proceedings) and has been awarded first prize for Ali H. Nayfeh Best Paper Award at 3^{rd} International Nonlinear Dynamics Conference (NODYCON 2023), Rome, Italy.*

4. **Chawla, R.**, Seth, S. Rounak, A., Pakrashi, V., 2023. Higher-order transverse discontinuity mapping for Filippov systems. *Under preparation*

Conferences

1. **Chawla, R.**, Rounak, A., Bose, C., Pakrashi, V., 2022. Effect of impact on the dynamics of a fluid-elastic system - European solid mechanics conference (ESMC), Galway, Ireland, 2022.

2. **Chawla, R.**, Rounak, A., Bose, C., Pakrashi, V., 2022. Dynamics of a fluid-elastic system with impact - Poster presentation at Conference on wave mechanics and vibrations (WMVC), Lisbon, Portugal, 2022. *Won the best poster award in WMVC, 2022*

3. **Chawla, R.**, Rounak, A., Bose, C., Pakrashi, V., 2022. Effect of impact on the dynamics of a fluid-elastic system - Recent advances in Nonlinear Mechanics (RANM), Hanzhou, China, 2022.

4. **Chawla, R.**, Rounak, A., Bose, C., Pakrashi, V., 2022. Higher-order transverse discontinuity mapping in hybrid systems - Computational methods in engineering science (CMES), Zamosc, Poland, 2022.

5. **Chawla, R.**, Rounak, A., Pakrashi, V., 2023. Higher-order transverse discontinuity mapping of a fluid-elastic system - 3^{rd} International Nonlinear Dynamics Conference (NODYCON 2023), Rome, Italy, 2023.

Nomenclature

Acronyms

BCB Border collision bifurcation

DIB Discontinuity-induced bifurcation

DNS Direct numerical simulation

FSI Fluid-structure interaction

FSM Fundamental solution matrix

ODE Ordinary differential equation

PDM Poincaré-section discontinuity mapping

PWC Piecewise-continuous

PWS Piecewise-smooth

SDOF Single degree of freedom

STM State transition matrix

SZDM Stochastic zero-time discontinuity mapping

TDM Transverse discontinuity mapping

VIV Vortex induced vibration

ZDM Zero-time discontinuity mapping

Electronics

γ Ratio of capacitances C_1 and C_2

A Amplitude of input voltage

A_0 Dimensionless amplitude of input voltage

C_1 Capacitance of capacitor for the loop C_1-L-R_1

C_2 Capacitance of capacitors for the loop C_1-L-R_1-C_2-R_2

L Inductance of inductor

q Charge flowing in LCR circuit

q_0 Reference charge stored in C_1 at which switching occurs

q_d Dimensionless charge flowing in LCR circuit

R_1 Resistances of first LCR loop

R_2 Resistance of second LCR loop

R_{d_1} Dimensionless resistance of first LCR loop

R_{d_2} Dimensionless resistance of second LCR loop

V_0 Reference voltage across C_1

V_{in} Input voltage

Number sets

$\cap$ Intersection of two sets

$\cup$ Unions of two sets

$\in$ A member of a set

$\mathbb{C}$ Complex numbers

$\mathbb{R}$ Real numbers

$\notin$ Not a member of the set

Symbols

β Ratio of stiffness k_2 and k_1

δ Flight-time estimate of perturbed trajectory to reach $\Sigma_{i,j}$

δ_1^{ξ} First-order flight time estimate of damped impact oscillator

δ_2^{ξ} Higher-order flight time estimate of damped impact oscillator

δ_+ Positive root of higher-order flight time estimate

δ_- Negative root of higher-order flight time estimate

δ_1 First-order flight time of perturbed trajectory to reach $\Sigma_{i,j}$

λ_i i^{th} Lyapunov exponent

$\mathbb{I}_{n\times n}$ Identity matrix of size n

$\mathbf{A}$ Jacobian matrix of the velocity field $\mathbf{F}(\mathbf{x})$

$\mathbf{F}(\mathbf{x})$ Velocity field as a function of state $\mathbf{x}$

$\mathbf{F}_i(\mathbf{x})$ Velocity field as a function of state $\mathbf{x}$ in the i^{th} sub-space

$\mathbf{J}$ Similarity transformation matrix to diagonalize $\mathbf{P}$

$\mathbf{n}$ Normal vector to constant surface $H(\mathbf{x})$ or $\nabla H(\mathbf{x})$

$\mathbf{P}$ Matrix comprising eigenvectors of monodromy matrix $\mathbf{\Phi}$

$\mathbf{R}(\mathbf{x})$ A reset map of the state $\mathbf{x}$

$\mathbf{S}_1$ First-order saltation matrix

$\mathbf{S}_2$ Higher-order saltation matrix

$\mathbf{u}_i$ i^{th} eigenvector of Jacobian matrix $\mathbf{A}$

$\mathbf{x}$ Arbitrary state vector $\mathbf{x} \in \mathbb{R}^n$ of size n

$\mathbf{x}_i$ State at the instant of impact

$\mathbf{Y}$ Fundamental solution matrix

$\mathbf{y}$ Perturbation vector to the state $\mathbf{x}$

$\mathbf{y}_+$ Perturbation state after application of TDM

$\mathbf{y}_-$ Perturbation state at the instant of impact with $\Sigma_{i,j}$

$\mathbf{Y}_1$ Fundamental solution matrix to evaluate state-transition matrix

$\mathbf{Y}_2$ Fundamental solution matrix to evaluate higher-order saltation matrix

$\mathbf{Y}_{+,impact}$ Fundamental solution matrix after application of TDM

$\mathbf{Y}_{-,impact}$ Fundamental solution matrix at the instant of impact with $\Sigma_{i,j}$

∇ Gradient with respect to state $\mathbf{x}$

ω Angular requency of external periodic force

ω_{d_1} Dimensionless frequency of soft-impact oscillator

$\otimes$ Tensor product of two vector fields

Φ Monodromy matrix

Φ_i State transition matrix evolving in the sub-space S_i

$\phi_t(\mathbf{x}_0)$ Flow of state in time t initiated from $\mathbf{x}_0$

ρ_i i^{th} Floquet multiplier

σ Displacement at the instant of impact with $\Sigma_{i,j}$

$\Sigma_{i,j}$ Discontinuity boundary/switching manifold separating subspaces S_i and S_j

$\tilde{\mathbf{x}}$ A new perturbed state to primary state $\mathbf{x}$

ξ Damping coefficient of oscillator

ξ_1 Damping of soft-impact oscillator

ξ_2 Damping of pre-compressed deformable barrier

ξ_{d_1} Dimensionless damping ratio of soft-impact oscillator

ξ_{d_2} Dimensionless damping ratio of pre-compressed deformable barrier

f Amplitude of external periodic force

f_0 Dimensionless amplitude of external periodic force

f_i i^{th} component of vector field $\mathbf{F}(\mathbf{x})$

G Quadractic function of higher-order flight time estimate

$H(\mathbf{x})$ A scalar function of state $\mathbf{x}$ which defines $\Sigma_{i,j}$

I Imaginary number

k Stiffness of oscillator

k_1 Stiffness of soft-impact oscillator

k_2 Stiffness of pre-compressed deformable barrier

L_1 Relaxed position of soft-impact oscillator from fixed end

L_2 Distance of pre-compressed barrier from fixed end

m Mass of oscillator

r Coefficient of restitution

S_i i^{th} sub-space of the phase space

T Time period of external periodic force

t_+ Time instant after impact

t_- Time instant just before impact with $\Sigma_{i,j}$

t_i Instant of impact of state $\mathbf{x}$ with $\Sigma_{i,j}$

v Velocity at the instant of impact with $\Sigma_{i,j}$

x Displacement of harmonic oscillator

x_d Dimensionless displacement of soft-impact oscillator

y_i i^{th} component of the perturbation $\mathbf{y}$

$\mathrm{He}(f_{i,j})$ Hessian matrix of i^{th} component of j^{th} vector field $\mathbf{F}_j$

Pn Period n orbit with time period nT

Fluid structure interaction system

ϵ Nonlinearity parameter of Van der Pol oscillator

ϵ_r Radius of circle in phase space to measure correlation dimension

γ Stall parameter

μ Reduced structure mass

ν Correlation dimension

Ω_f Vortex-shedding frequency

ρ Density of fluid medium

τ Dimentional time measuring cylinder displacement

$C(\epsilon_r)$ Average of $N(\epsilon_r)$

C_L Lift coefficient

C_m Added mass coefficient

C_{Lo} Reference lift coefficient

D Diameter of cylinder

h Stiffness of cylinder

M Coupling factor

m_f Fluid-added mass

m_s Mass of cylinder

$N(\epsilon_r)$ Number of points to measure correlation dimension

r_f Fluid-added damping

r_s Damping of structure oscillator

S_t Strouhal number

U Fluid flow velocity

U_r Reduced fluid flow velocity

X Lift force on cylinder

Y Cylinder displacement

y Non-dimensional cylinder displacement

Chapter 1

Introduction

1.1 Non-smooth systems arise everywhere

A wide range of engineering applications are subjected to sudden changes in the environment during their operation, which triggers discrete actions almost instantaneously. Some examples include mechanical devices like gear assemblies [56, 57], impact print hammers [51, 124], walking robots [52], boiler tube assemblies [44, 93], metal cutters [130], vehicle suspensions, drilling and moling [63, 131], many-body interaction systems involving friction, etc. Mechanical components in such devices can impact each other due to limited clearance or loosened joints due to corrosion, abrasion, friction, and aging. This results in undesirable vibrations detrimental to the device, reducing its life expectancy. The most characteristic feature of such systems is the sudden changes to their motion caused by collisions and impacts. The timescales at which these occur are much smaller than the macroscopic timescale, due to which they appear almost instantaneous. Some other examples in engineering and science subjected to rapid changes, making them unpredictable, are electrical circuits like buck [138, 41, 19] and boost [8, 5, 9] converters comprising switches and physical systems pertaining to social, biological, chemical, and financial sciences. Sudden transitions in these systems also show similar large amplitude responses, and therefore a unified theory is required to determine when such undesired oscillations occur.

Nonlinear dynamical systems can phenomenologically model diverse engineering applications. A well-established bifurcation theory [47, 133, 132, 121] exists in the present literature, which provides insights into the topological changes occurring in nonlinear systems which model the physical system. This bifurcation theory comprises geometrical and intuitive approaches to predict when completely well-behaved systems become unstable and chaotic. However, the methodologies outlined in traditional bifurcation theory cannot be implemented to investigate systems subjected to instantaneous changes like impacts and collisions in mechanical

systems. Therefore, physical systems subjected to rapid changes are modeled using dynamical systems where the state variables evolve in the phase space until they are interrupted at discrete events. These events represent impacts, collisions, or sudden changes to the physical environment and are described using hyper-surfaces in the phase space. These hyper-surfaces, also known as discontinuity boundaries or switching manifolds, divide the phase space into sub-spaces. The state variables evolve in the respective sub-space governed by smooth functions with well-defined higher-order time derivatives until they encounter the discontinuity boundary resulting in a piecewise-smooth dynamical system.

Piecewise-smooth dynamical systems can effectively model mechanical systems and switching-electrical circuits mentioned earlier and provide insights regarding when such systems can become unstable and show large amplitude oscillations. Additionally, numerical investigations of piecewise-smooth systems reveal the occurrence of a wide range of rich dynamical behavior [30, 22, 54, 95, 108] not commonly observed in nonlinear dynamical systems governed by smooth functions of its arguments. Some of them include period-adding cascades [97, 89, 90, 99, 106, 37, 102], grazing bifurcations [22, 54, 7], sliding motion [31], chattering sequence [17], narrow-band and robust chaos [9, 7], coexisting attractors [14] etc. Collectively, such topological changes in the system's responses are called discontinuity-induced bifurcations (DIBs), which have also been experimentally observed in the respective physical system. Therefore, piecewise-smooth dynamical systems are crucial since they model various engineering applications subjected to sudden changes. Traditional bifurcation theory cannot model such a non-smooth system due to discontinuities in the phase space.

The following section discusses the main principles of piecewise-smooth dynamical systems, which lay the foundation over which most non-smooth systems are investigated to predict when instabilities occur, resulting in discontinuity-induced bifurcations.

1.2 Piecewise-smooth dynamical systems

Consider an arbitrary dynamical system comprising n state variables. These state variables represent some observable of a physical system, like, for example, the position of a moving body or current flowing in an electrical circuit. The state variables constitute a vector with components x_i of the vector $\mathbf{x}$, such that $\mathbf{x} \in \mathbb{R}^n$. The dynamics of the state $\mathbf{x}$ can be defined by a set of ODEs obeying,

$$\dot{\mathbf{x}} = \mathbf{F}_i(\mathbf{x}), \tag{1.1}$$

where overdot denotes the derivative with respect to time t. In non-smooth systems, the evolution of $\mathbf{x}$ depends on the respective region of the phase space it evolves in. Therefore, the phase-space can be further divided into sub-spaces, denoted by S_i. Fig. 1.1 is a schematic representation, in two dimensions, of the trajectory of $\mathbf{x}$ as it evolves in phase space. The subscript i in $\mathbf{F}_i$ denotes the velocity vector field $\mathbf{F}(\mathbf{x})$

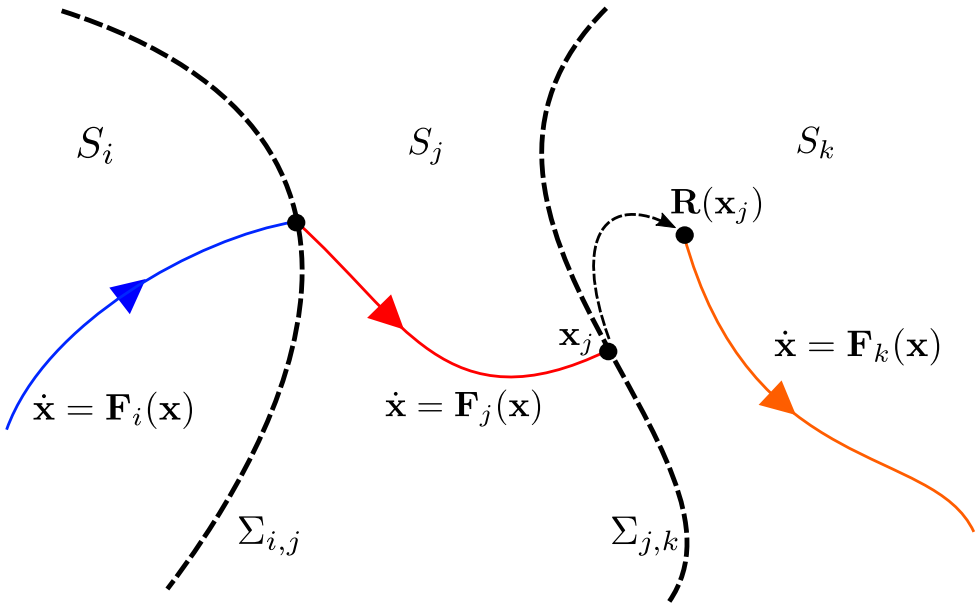

Figure 1.1: Schematic phase-portrait of a PWS system. The dashed lines $\Sigma_{i,j}$ (discontinuity boundary) separates the state-space into S_i and S_j where trajectories modeled as $\mathbf{x}$ evolves according to the respective vector fields $\mathbf{F}_i$. The evolution of trajectories are non-smooth on the barrier $\Sigma_{i,j}$. An example of hybrid system, typical to PWS systems, is shown where $\mathbf{x}_j \in \Sigma_{j,k}$ (see red curve impacts discontinuity barrier $\Sigma_{j,k}$) gets mapped to $\mathbf{R}(\mathbf{x}_j) \in S_k$.

defined in region S_i. The sub-space S_i and S_j are separated by a non-empty set $\Sigma_{i,j} := S_i \cap S_j$ known as a discontinuity boundary, discontinuity set, or switching manifold. This separating region, $\Sigma_{i,j}$ can be modeled by a scalar function $H_{i,j}(\mathbf{x})$ such that $\mathbf{x} \in \Sigma_{i,j} : H_{i,j}(\mathbf{x}) = 0$. It is assumed that the trajectory of $\mathbf{x}$ defined by $\mathbf{F}_i$ is well-behaved or smooth away from $\Sigma_{i,j}$. The term smooth implies that all higher-order derivatives of $\mathbf{x}$ with respect to t exist and are finite. However, when $\mathbf{x}$ interacts with $\Sigma_{i,j}$, there is a sudden change in the trajectory of $\mathbf{x}$. This transition occurs in a time scale smaller than the macroscopic time scale where the evolution of $\mathbf{x}$ is smooth when away from the discontinuity boundary $\Sigma_{i,j}$ and is assumed to occur instantaneously. Hence, the higher-order derivatives in $\mathbf{x}$ at $\Sigma_{i,j}$ are unequal when evaluated at $\mathbf{x} \in S_i$ and $\mathbf{x} \in S_j$. Such non-smooth systems are defined as piecewise-smooth (PWS) dynamical systems. Therefore,

Definition 1

Piecewise-smooth dynamical systems are governed by a finite set of ODEs,

$$\dot{\mathbf{x}} = \mathbf{F}_i(\mathbf{x}), \quad \text{for} \quad \mathbf{x} \in S_i, \tag{1.2}$$

S_i is the subspace into which the phase-space is partitioned. $\Sigma_{i,j}$ is the discontinuity boundary separating S_i and S_j, *i.e.*, $\Sigma_{i,j} := S_i \cap S_j \in \mathbb{R}^{n-1}$. Each velocity field F_i is smooth and defines a smooth trajectory $\mathbf{x}$ which evolves in the subspace S_i and is well-defined on both sides of $\Sigma_{i,j}$.

PWS systems are also defined for discrete-time dynamical systems comprising maps instead of ODEs. Observables in such systems are described by discrete variables $\mathbf{x}_k$ which belong to the set S_i where the map $\mathbf{F}_i$ applies. Therefore,

Definition 2

Piecewise-smooth maps are governed by a finite set of smooth maps. Here, the $(k+1)^{th}$ iterate of $\mathbf{x}_k$ is given by,

$$\mathbf{x}_{k+1} = \mathbf{F}_i(\mathbf{x}_k), \quad \text{for} \quad \mathbf{x}_k \in S_i, \tag{1.3}$$

S_i's are the subspaces into which the phase-space is partitioned. $\Sigma_{i,j}$ is the discontinuity boundary or border separating S_i and S_j, *i.e.*, $\Sigma_{i,j} := S_i \cap S_j \in \mathcal{R}^{n-1}$. Every function F_i is smooth and defines a smooth mapping of $\mathbf{x}_k \in S_i$ which is well-defined on both sides of $\Sigma_{i,j}$.

The discontinuity set $\Sigma_{i,j}$ separating the two sets S_i and S_j are known as discontinuity boundary or border. DIBs occur in PWS maps when the fixed point of the map interacts with the border $\Sigma_{i,j}$. Such bifurcations, in the literature pertaining to non-smooth dynamical systems, are collectively known as border-collision bifurcations [6]. A close connection exists between PWS systems governed by ODEs and discrete maps. For example, DIBs observed in PWS dynamical systems like grazing bifurcation, period-adding cascades, robust chaos, etc., can be invested using an equivalent map [8, 7] in a lower dimension, making the analysis more straightforward. This thesis primarily focuses on systems governed by ODEs; hence, PWS maps have not been considered. A brief literature review on PWS maps will be provided in Chapter 2. The following section discusses how PWS systems are classified.

1.3 Classification of piecewise-smooth systems

The non-smoothness, typical to PWS systems, arises due to discontinuity in the derivatives of the vector field, which governs the evolution of the state variables. Therefore, distinct types of PWS systems are classified according to the degree of smoothness (DOS) of the state $\mathbf{x}(t_i)$ when $\mathbf{x}$ interacts with the discontinuity boundary $\Sigma_{i,j}$ at the instant t_i. A Taylor series expansion of $\mathbf{x}(t) \in \mathcal{R}^n \in S_i$ at the instant of impact with $\Sigma_{i,j}$ or $\mathbf{x}_i$ about $t = t_i$ is

$$\begin{aligned}\mathbf{x}(t) &= \mathbf{x}_i + (t-t_i)\frac{d}{dt}\mathbf{x}(t_i) + \frac{(t-t_i)^2}{2!}\frac{d^2}{dt^2}\mathbf{x}(t_i) + \frac{(t-t_i)^3}{3!}\frac{d^3}{dt^3}\mathbf{x}(t_i) + \mathcal{O}(t^4) \qquad (1.4)\\ &= \mathbf{x}_i + (t-t_i)\mathbf{F}_i(\mathbf{x}_i) + \frac{(t-t_i)^2}{2!}\nabla\mathbf{F}_i^T(\mathbf{x}_i)\cdot\mathbf{F}_i(\mathbf{x}_i) + \frac{(t-t_i)^3}{3!}(\mathbf{A}_i + \mathbf{B}_i) + \mathcal{O}(t^4),\end{aligned}$$

where,

$$\mathbf{A}_i = \begin{pmatrix} \mathbf{F}_i(\mathbf{x}_i)\cdot \mathrm{He}(f_{i,1})\cdot\mathbf{F}_i(\mathbf{x}_i) \\ \mathbf{F}_i(\mathbf{x}_i)\cdot \mathrm{He}(f_{i,2})\cdot\mathbf{F}_i(\mathbf{x}_i) \\ \vdots \\ \mathbf{F}_i(\mathbf{x}_i)\cdot \mathrm{He}(f_{i,n})\cdot\mathbf{F}_i(\mathbf{x}_i) \end{pmatrix},$$
$$\mathbf{B}_i = \nabla\mathbf{F}_i^T(\mathbf{x}_i)\cdot\nabla\mathbf{F}_i^T(\mathbf{x}_i)\cdot\mathbf{F}_i(\mathbf{x}_i).$$

$\mathrm{He}(f_{i,j})$ is the Hessian matrix of the j^{th} component of $\mathbf{F}_i(\mathbf{x}_i)$. Eq. (1.4) was obtained using the chain rule *i.e.*, $\frac{d}{dt}\mathbf{x}_i = \mathbf{F}_i(\mathbf{x})$, $\frac{d^2}{dt^2}\mathbf{x}_i = \nabla\mathbf{F}_i^T(\mathbf{x}_i)\cdot\mathbf{F}_i(\mathbf{x}_i)$, etc. The DOS can be now defined as follows.

Definition 3

Degree of smoothness, α of a state $\mathbf{x}$ lying on the discontinuity boundary $\Sigma_{i,j}$ is the order of t in the Taylor series expansion of $\mathbf{x}_i \in S_i$ and $\mathbf{x}_j \in S_j$ about $t = 0$ up to which $\mathcal{O}(t^{\alpha-1})$ are equal.

PWS systems are categorized according to their DOS. In general, a wide range of non-smooth systems can be broadly segregated depending if their DOS is either zero (hybrid systems), one (Filippov systems) or two and more (piecewise-continuous systems). These are discussed next.

1.3.1 DOS 0: Hybrid systems

Hybrid systems are PWS systems with zero DOS. This implies that the first term in Eq. (1.4) *i.e.*, the impacting state $\mathbf{x} = \mathbf{x}_i$ is unequal before and after it interacts with the discontinuity boundary $\Sigma_{i,j}$. This is possible only when the impacting

state $\mathbf{x}_i$ gets mapped to a different state $\mathbf{x}_j$ defined using an impact law $\mathbf{R}(\mathbf{x}_i) = \mathbf{x}_j$. Therefore, hybrid systems are defined by both, a finite set of ODEs governed by Eq. (1.1) and discrete mappings of the state $\mathbf{x}_i \in \Sigma_{i,j}$. The mapping of $\mathbf{x}_i$ to $\mathbf{x}_j$ is defined by a vector $\mathbf{R}$, such that $\mathbf{x}_i \to \mathbf{R}(\mathbf{x}_i)$ when $\mathbf{x}_i \in \Sigma_{i,j}$. Here, the state $\mathbf{x}_i \in \Sigma_{i,j}$ approaching from S_i differs from $\mathbf{x}_j \in \Sigma_{i,j}$ approaching from S_j, *i.e.*, the t^0 term in Eq. (1.4).

To illustrate this, consider an example of a ball bouncing on a floor. The ball accelerates towards the floor due to gravity and, upon impact, bounces back until it reaches a maximum height, and the process repeats. The impact process can be a highly subtle mechanism involving the deformation of the ball, a normal reaction acting on it due to the floor getting deformed on a microscopic scale, followed by a restoring force from the ball acting on the floor which causes it to spring back up in the air. Instead, a very simplistic representation of the impact process using an impact law suffices when compared to experiments [120]. Therefore, the total time within which impact occurs can be approximated as an instantaneous process. Hence, the ball's impact on the floor causes an immediate change in velocity, accounting for some loss in energy. This loss in energy can be modeled by a coefficient of restitution $r \in \mathbb{R} : 0 \leq r \leq 1$. They can be dynamically modeled by a linear harmonic oscillator with an impact law. Such systems are known as impact oscillators and have been investigated in Chapter 3. Since the velocity changes instantaneously during an impact, this results in a sudden change to the state variable when observed in the phase space. Note that impact oscillators are a particular class of hybrid systems where the state $\mathbf{x}_i \in S_i$ gets mapped back to the same sub-space, *i.e.*, $\mathbf{x}_i \in S_i \to \mathbf{R}(\mathbf{x}_i) = \mathbf{x}_j \in S_i$. Fig. 1.2(a) and (b) is a schematic phase portrait of a hybrid and an impacting system.

1.3.2 DOS 1: Filippov systems

Filippov systems are PWS systems with a discontinuous velocity vector field at $\mathbf{x}_i \in \Sigma_{i,j}$. Here, $\mathbf{F}_i(\mathbf{x}_i) \neq \mathbf{F}_j(\mathbf{x}_i)$ when evaluated at $\Sigma_{i,j}$. The coefficient of $(t - t_i)^1$ in the Taylor series expansion of $\mathbf{x}_i$ and $\mathbf{x}_j$ (see Eq. (1.4)) are unequal and is, therefore, a system with degree of smoothness 1. Some examples of Filippov systems in engineering applications are many body mechanical systems with friction between them, stick-slip motions, switching circuits like boost and buck converters in power electronics, impact oscillators interacting with a deformable barrier, bilinear springs, etc. Due to the versatility of Filippov systems, their analysis is vital. Fig. 1.3(a) and (b) demonstrates two possible scenarios when $\mathbf{F}_i(\mathbf{x}_i) \neq \mathbf{F}_j(\mathbf{x}_i)$ at $\mathbf{x}_i \in \Sigma_{i,j} : H(\mathbf{x}_i) = 0$, where $H(\mathbf{x}_i) = 0$ denotes the discontinuity boundary $\Sigma_{i,j}$. Let the normal $\mathbf{n}$ to $H(\mathbf{x}_i)$ be $\mathbf{n} = \nabla H(\mathbf{x}_i)$. In Fig. 1.3(a), the condition $(\mathbf{n}^T \cdot \mathbf{F}_i(\mathbf{x}_i))(\mathbf{n}^T \cdot \mathbf{F}_j(\mathbf{x}_i)) > 0$ is demonstrated and corresponds to transversal interactions with $\Sigma_{i,j}$.

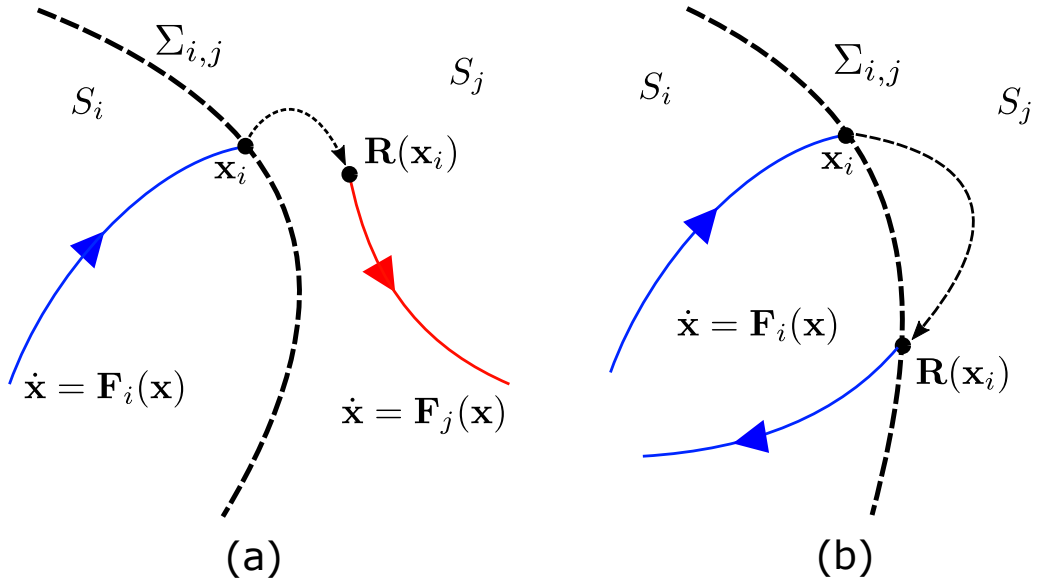

Figure 1.2: Schematic phase portrait of a (a) Hybrid system comprising of state jumps defined using ODEs and discrete maps, (b) Impact system where the trajectory $\mathbf{x}$ impacts barrier $\Sigma_{i,j}$ at $\mathbf{x}_i$, gets mapped using the impact rule $\mathbf{R}(\mathbf{x}_i)$ and returns to the same sub-space S_i.

During transversal interactions, the normal component of $\mathbf{F}_i(\mathbf{x}_i)$ and $\mathbf{F}_j(\mathbf{x}_i)$ along $\mathbf{n}$ point in the same direction. The vector fields therefore allow trajectories to cross the discontinuity barrier $\Sigma_{i,j}$. On the contrary, Fig. 1.3(b) demonstrates when sliding can occur. When in the sliding mode, the normal component of $\mathbf{F}_i(\mathbf{x}_i)$ and $\mathbf{F}_j(\mathbf{x}_i)$ along $\mathbf{n}$ point in the opposite direction, since $(\mathbf{n}^T \cdot \mathbf{F}_i(\mathbf{x}_i))(\mathbf{n}^T \cdot \mathbf{F}_j(\mathbf{x}_i)) < 0$. Hence, trajectories are attracted towards $\Sigma_{i,j}$ and can also evolve on $\Sigma_{i,j}$. This is the case of sliding motion and is commonly observed in systems that model Coulomb friction or stick-slip motions.

1.3.3 DOS 2: Piecewise-continuous systems

PWS systems where the coefficient of $(t-t_i)^2$ in the Taylor series expansion of $\mathbf{x}_i$ and $\mathbf{x}_j$ are unequal have a degree of smoothness 2 and are known as piecewise-continuous systems. Here, the Jacobian of the velocity field is unequal at the discontinuity boundary, *i.e.*, $\nabla\mathbf{F}_i(\mathbf{x}_i) \neq \nabla\mathbf{F}_j(\mathbf{x}_i)$ where $\mathbf{x}_i \in \Sigma_{i,j} : H(\mathbf{x}_i) = 0$. Fig. 1.4 shows the trajectory of a piecewise-continuous system in the local neighborhood of $\Sigma_{i,j}$.

1.4 Discontinuity-induced bifurcations

Bifurcations are essential events in dynamical systems and are accompanied by changes in the system's behavior. A bifurcation is said to occur when the topology of a given family of curves suddenly changes due to a smooth change in the parameter values of a system. PWS systems also show bifurcations and are different from

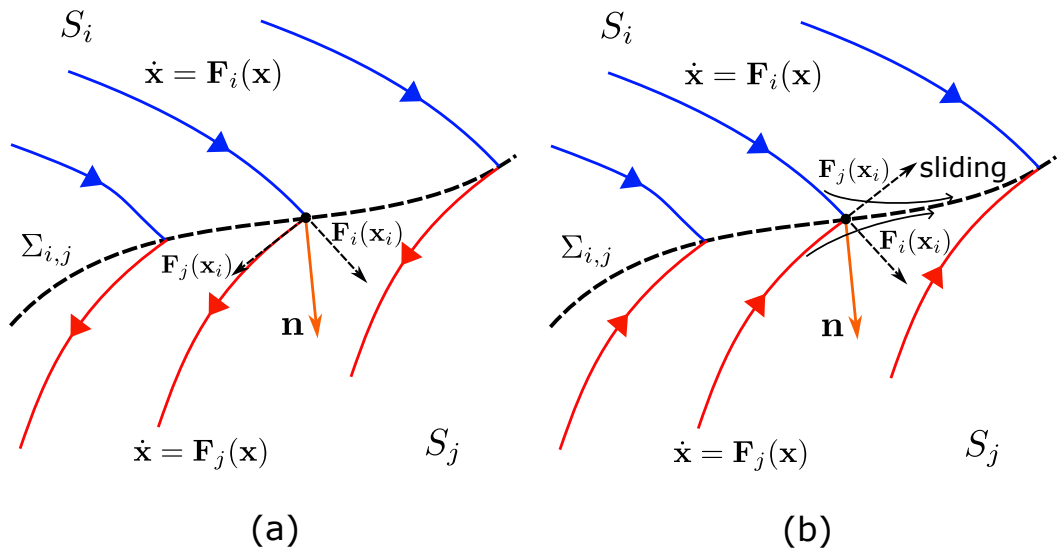

Figure 1.3: Evolution of trajectories for Filippov systems in the local neighborhood of a discontinuity barrier $\Sigma_{i,j}$ during impacts showing (a) transversal intersections (normal component of vector fields along $\mathbf{n}$ point in the same direction on either side of $\Sigma_{i,j}$) and (b) sliding (normal component of vector fields along $\mathbf{n}$ point opposite on either side of $\Sigma_{i,j}$ resulting in attraction of trajectories on $\Sigma_{i,j}$).

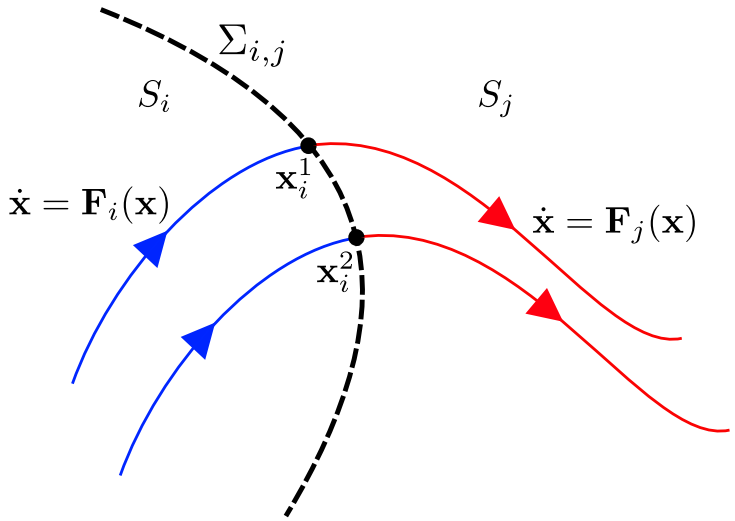

Figure 1.4: Schematic phase-portrait of a piecewise-continuous systems where the Jacobian or higher-order derivatives of $\mathbf{F}(\mathbf{x}_i)$ are unequal at $\Sigma_{i,j}$ when evaluated from either sides S_i and S_j.

the ones observed in dynamical systems governed by smooth ODEs. For example, stable periodic orbits of a PWS system can become unstable, resulting in period-adding cascades [14] of orbits separated by chaotic solutions over a wide range of parameters. Such topological changes are not observed for smooth systems since solutions become unstable by obeying a period-doubling route to chaos.

Various bifurcations occur in PWS systems, collectively called discontinuity-induced bifurcations (DIBs) [14]. A typical DIB observed when modeling mechanical and electrical systems is grazing bifurcations. A grazing bifurcation occurs when a

part of a stable orbit (limit cycle in phase space) interacts with the discontinuity boundary $\Sigma_{i,j}$ such that $\nabla H(\mathbf{x}_i)^T \cdot \mathbf{F}(\mathbf{x}_i) = 0$. This implies that the orbit locally grazes the discontinuity barrier since the vector field $\mathbf{F}(\mathbf{x}_i)$ lies on the tangent plane of $\mathbf{x}_i \in \Sigma_{i,j}$ and is normal to $\mathbf{n} = \nabla H(\mathbf{x}_i)$; see Fig. 2.2(a).

To illustrate grazing bifurcation occurs, consider the representative case of a Filippov system modeled using a bilinear harmonic oscillator subject to impact with a cushioned wall. This soft impact oscillator is externally excited by a periodic force $f \cos \omega t$ with amplitude f and time period $T = 2\pi/\omega$. The remaining details of this example are given in Chapter 6. Some results are presented next to demonstrate a DIB due to grazing incidence. In Fig. 1.5, the phase portrait of the soft impact oscillator is shown for varying amplitude f when $\omega = 0.8$ rad/s. Fig. 1.5(a) is the phase portrait corresponding to $f = 0.8$N after a time elapse of 300T to eliminate transient effects. Red points correspond to states (*i.e.*, displacement x and velocity $\dot{x}$) of the system measured stroboscopically at every $t \mod T = 0$. Since these points repeat every $2T$, the orbit or limit cycle shown is labeled as a period 2 or simply P2 orbit. When $f = 0.8605$N in Fig. 1.5(b), a part of the orbit grazes or touches the barrier $\Sigma_{1,2}$. When f is slightly increased, the P2 orbit becomes unstable and disappears as in Fig. 1.5(c) for $f = 0.861$N. At this instance, a new P1 orbit appears and remains stable as f is further increased. The occurrence of a bifurcation, as demonstrated here, immediately after the orbit grazes the discontinuity boundary is known as grazing bifurcation of limit cycles. Since an external force drives the impact oscillator, the phase-portrait and the time axis are shown in Fig. 1.6. The P2 orbit in Fig. 1.6(a) grazes $\Sigma_{1,2}$, represented by the plane, becomes unstable and disappears. A new stable P1 orbit appears when f is slightly increased to $f = 0.861$N, as shown in Fig. 1.6(b).

Hence, grazing incidence of orbits is often followed by a DIB, as shown in Fig. 1.5, where existing orbits become unstable, and a new orbit is born. Physical systems modeling impact oscillators also show grazing bifurcations followed by large amplitude oscillations (known as narrow-band chaos), as validated experimentally [7]. Such vibrational responses are undesirable in most engineering applications and require knowledge of how perturbations behave in the local neighborhood of an impacting orbit. Such investigations are conducted by constructing discontinuity mappings. This is discussed in the following section.

1.5 Discontinuity mappings

Discontinuity mappings are crucial for the investigations of periodic orbits for PWS systems. They provide insights regarding the behavior of perturbations in the local neighborhood of trajectories or orbits undergoing impacts with the discontinuity barrier. This is illustrated as follows. Consider the evolution of nearby two trajec-

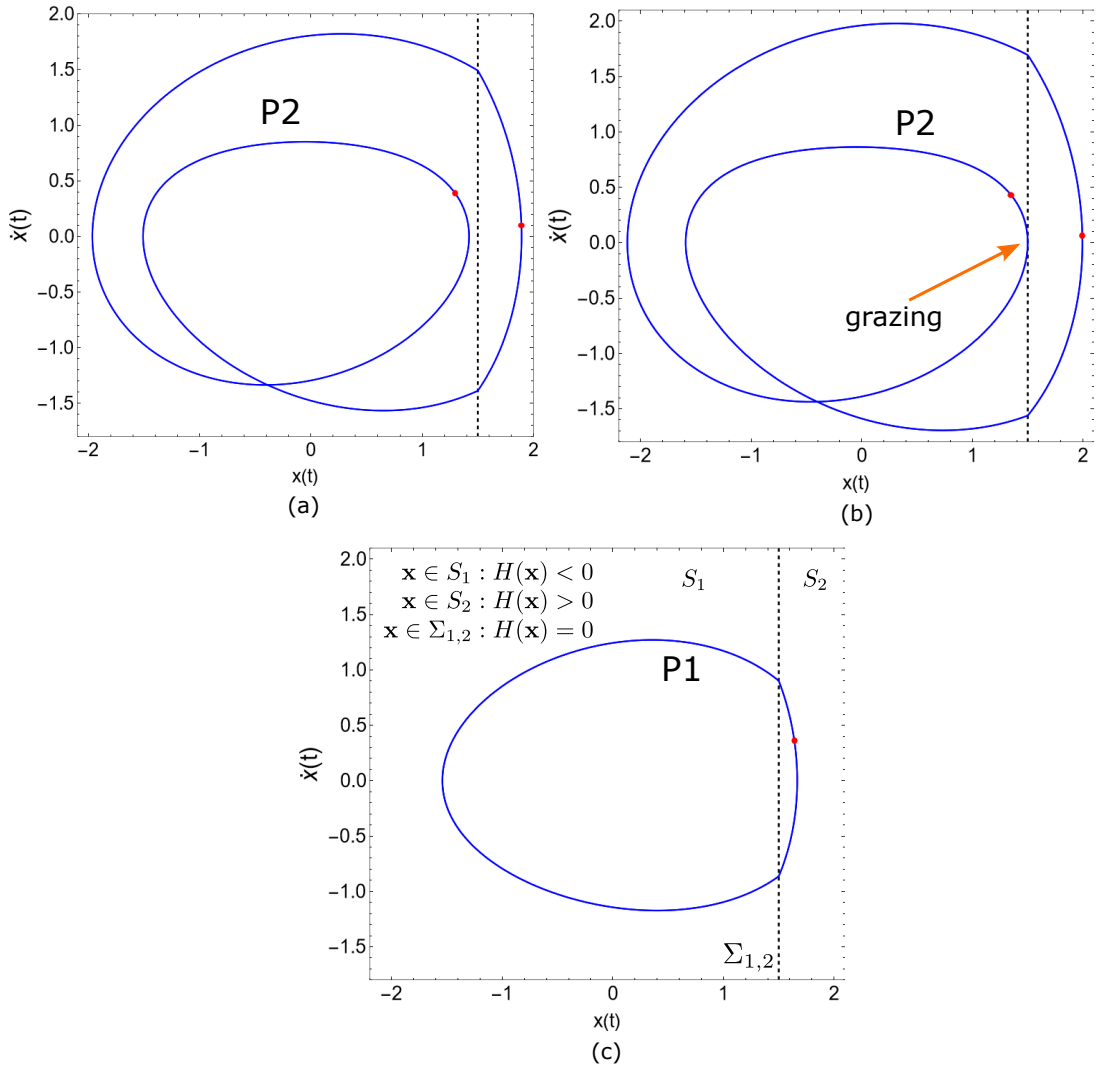

Figure 1.5: Phase portrait showing how a P2 orbit becomes unstable due to grazing phenomenon. A slight change in the parameter value results in the existing P2 orbit disappearing, giving birth to a new stable P1 orbit. The orbits shown here correspond to a (a) stable P2 orbit when $f = 0.8$N, (b) grazing orbit when $f = 0.8605$N and (c) stable P1 orbit appearing when $f = 0.861$N. The red points are the states x and $\dot{x}$ measured at stroboscopic intervals of $t \mod (T = 2\pi/\omega) = 0$.

tories $\mathbf{x}$ and $\mathbf{x} + \mathbf{y}$. The evolution of perturbations $\mathbf{y}$ in the local neighborhood of $\mathbf{x}$ is approximated by the variational equation, *i.e.*,

$$\dot{\mathbf{y}} \sim \nabla \mathbf{F}_i(\mathbf{x})^T \cdot \mathbf{y} + \mathcal{O}(||\mathbf{y}||^2), \quad \mathbf{x} \in S_i, \tag{1.5}$$

where $\nabla \mathbf{F}^T(\mathbf{x})$ is the Jacobian matrix. Figs. 1.7(a) and (b) are schematic phase portraits showing the evolution of $\mathbf{x}$ and $\mathbf{x} + \mathbf{y}$ in phase space for two systems with DOS 0 and DOS 1. Initially, both $\mathbf{x}$ and $\mathbf{x} + \mathbf{y}$ start from S_i before reaching $\Sigma_{i,j}$. However, both $\mathbf{x}$ and $\mathbf{x} + \mathbf{y}$ do not reach $\Sigma_{i,j}$ at the same instant. Let $\mathbf{x}$ reach $\Sigma_{i,j}$ at $\mathbf{x}_i$ for both the cases in Fig. 1.7(a) and (b). The key idea is to analytically estimate the flight time after which $\mathbf{x} + \mathbf{y}$ reaches $\Sigma_{i,j}$ at $\mathbf{x}_1$. Once this is determined, the

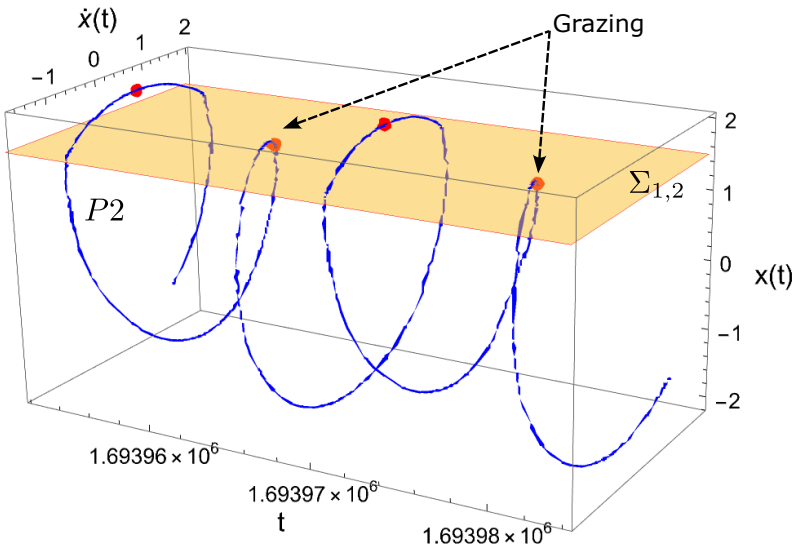

(a)

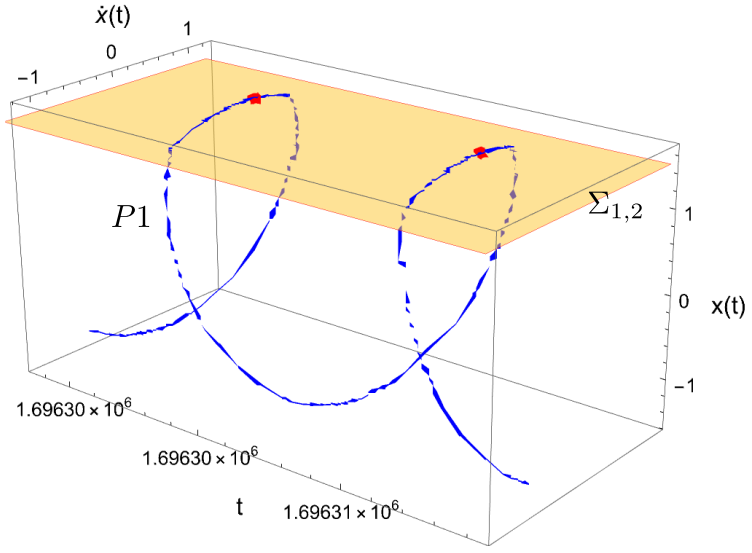

(b)

Figure 1.6: Phase portrait including the time axis of a (a) P2 orbit grazing the discontinuity barrier (yellow surface) at $f = 0.8605$N and (b) stable P1 orbit appearing when $f = 0.861$N. The P2 orbit becomes unstable and disappears at this instant. The red points are the states x and $\dot{x}$ measured at stroboscopic intervals of $t \mod (T = 2\pi/\omega) = 0$.

perturbation at the instant of impact $\mathbf{y}_-$ is adjusted or mapped, ensuring it reaches $\Sigma_{i,j}$ after the correct time difference. This adjustment of trajectories in the local linear neighborhood of the impacting state $\mathbf{x}_i$ is known as a transverse discontinuity mapping (TDM). In Fig. 1.7(a) corresponding to a hybrid system, $\mathbf{x}+\mathbf{y}$ reaches $\mathbf{x}_0$ when $\mathbf{x}$ impacts $\Sigma_{i,j}$ at $\mathbf{x}_i$. At this instant, $\mathbf{x}_i$ gets mapped according to an impact law given by $\mathbf{R}(\mathbf{x}_i)$. Since $\mathbf{x}_0$ is yet to reach $\mathbf{x}_1$, followed by the reset map $\mathbf{R}(\mathbf{x}_1)$ to continue from $\mathbf{x}_2$, the TDM maps $\mathbf{x}_0$ to reach $\mathbf{x}_2$ ensuring a mapping in zero time.

The details of the derivation of the TDM with higher-order corrections for hybrid systems of the impacting class are given in Chapter 3. Similarly, for Filippov type systems where the crossing of $\Sigma_{i,j}$ is allowed, the TDM is shown in Fig. 1.7(b). Here, the perturbed path $\mathbf{x}+\mathbf{y}$ reaches $\mathbf{x}_0$ when $\mathbf{x}$ reaches $\Sigma_{i,j}$ at $\mathbf{x}_i$. At this instant, the TDM maps $\mathbf{x}_0$ to $\mathbf{x}_2$ ensuring that the time taken to reach $\mathbf{x}_1$ from $\mathbf{x}_0$ is the same to reach $\mathbf{x}_1$ from $\mathbf{x}_2$. The flight time and the TDM with higher-order corrections are derived in Chapter 6, corresponding to Filippov systems.

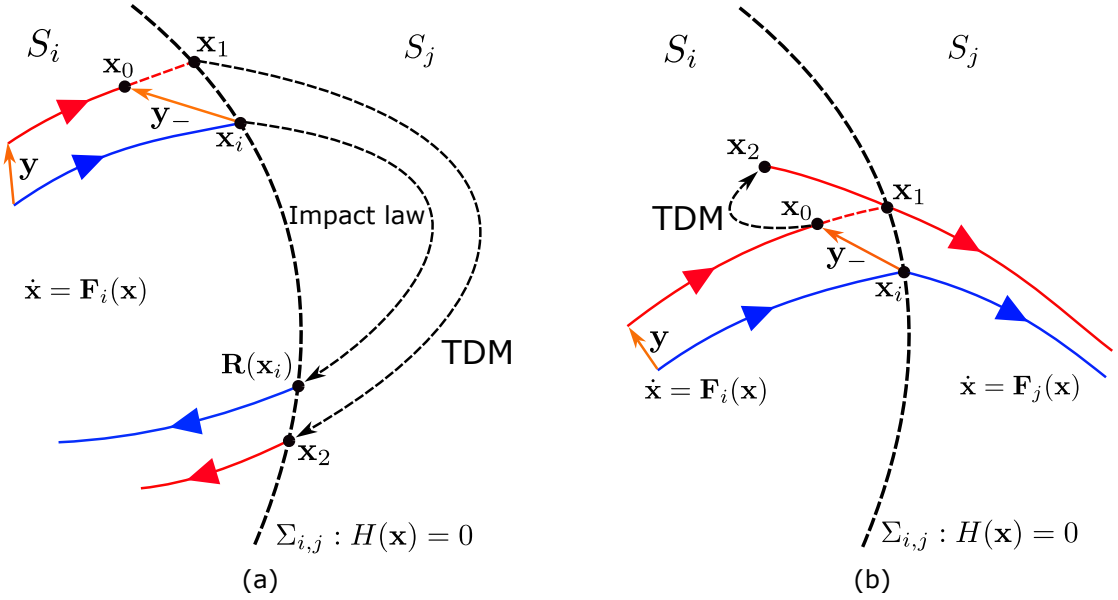

Figure 1.7: Phase portrait of two orbits $\mathbf{x}$ (blue curve) and a slightly perturbed orbit $\mathbf{x}+\mathbf{y}$ (red curve) to $\mathbf{x}$ undergoing transverse discontinuity mapping for (a) hybrid impacting and (b) Filippov systems. The TDM ensures that orbits in the local neighborhood (*i.e.*, $\mathbf{x}_i+\mathbf{y}_-$) to the impacting orbit (*i.e.*, $\mathbf{x}_i$) reaches $\Sigma_{i,j}$ at the correct instances post impact.

1.6 Motivation and thesis objectives

The present literature on piecewise-smooth systems relies on constructing discontinuity mappings using linearized approaches. Such approaches only consider the first-order terms of the Taylor expansion of orbits in the local neighborhood of an impacting state. The linearized methods result in a discontinuity mapping with a matrix form known as saltation matrices. These matrices, constructed using first-order approximations, do not depend on the magnitude of perturbations at the instant of impact. Additionally, the linearized saltation matrices do not consider all the parameters of the dynamical system, which can have important significance to the physical system they represent. This raises three important questions. First, do all orbits in the local neighborhood of an impacting state reach the discontinuity boundary? Secondly, is there an upper limit within which perturbations should lie,

ensuring that impacts do occur? Third, if higher-order corrections to the saltation matrix result in a vector equation, how can one construct a state-transition matrix compatible with the variational equation to further evaluate monodromy matrices for stability analysis?

This thesis addresses these questions by illustrating the limitations of the widely accepted first-order discontinuity mapping and saltation matrix for piecewise-smooth dynamical systems undergoing transverse interactions with the discontinuity boundary. The results in the thesis highlight the drawbacks of implementing a first-order approximation to the flight time and the transverse discontinuity mapping. A comparison of the higher-order corrections to the TDM with the widely accepted saltation matrix shows that impacts in the local neighborhood rely on the size of perturbations at the instant of impact. There are instances when perturbed trajectories $\mathbf{x}+\mathbf{y}$ will not show impact or cross the discontinuity boundary $\Sigma_{i,j}$ while the unperturbed path $\mathbf{x}$ crosses $\Sigma_{i,j}$. On the contrary, the first-order TDM predicts impacts under such circumstances. Comparison with numerical results indicates that the higher-order TDM correctly predicts impact occurrences that the first-order saltation matrix fails to capture. Therefore, the linearized TDM can incorrectly predict an impact and, consequently, the behavior of trajectories in the local linear neighborhood of $\Sigma_{i,j}$. Higher-order corrections to the TDM derived in this thesis, corresponding to hybrid and Filippov systems, can resolve these issues.

The thesis ends with an attempt to experimentally validate occurrences of discontinuity induced bifurcations typical to Filippov systems. A brief outline of how the thesis is structured is discussed next.

1.7 Thesis outline

This chapter introduces piecewise-smooth dynamical systems in general, their necessity in engineering applications, and limitations in the existing literature. The remainder of the thesis addresses some of these limitations for hybrid (DOS 0) and Filippov (DOS 1) systems and is structured as follows.

Chapter 2 first discusses the existing literature on PWS systems and discontinuity mappings, which are crucial during the investigation of discontinuity-induced bifurcations. Subsequently, methods for stability analysis using Floquet theory and Lyapunov exponents are presented next, which have been used to investigate in the following chapters to study discontinuity-induced bifurcations for hybrid and Filippov systems.

In ***Chapter 3***, a higher-order transverse discontinuity mapping for hybrid PWS systems is derived. The limitations of implementing a first-order saltation matrix are discussed and resolved by a higher-order TDM for two representative systems undergoing impacts with one (impact oscillator) and multiple barriers (pair-impact

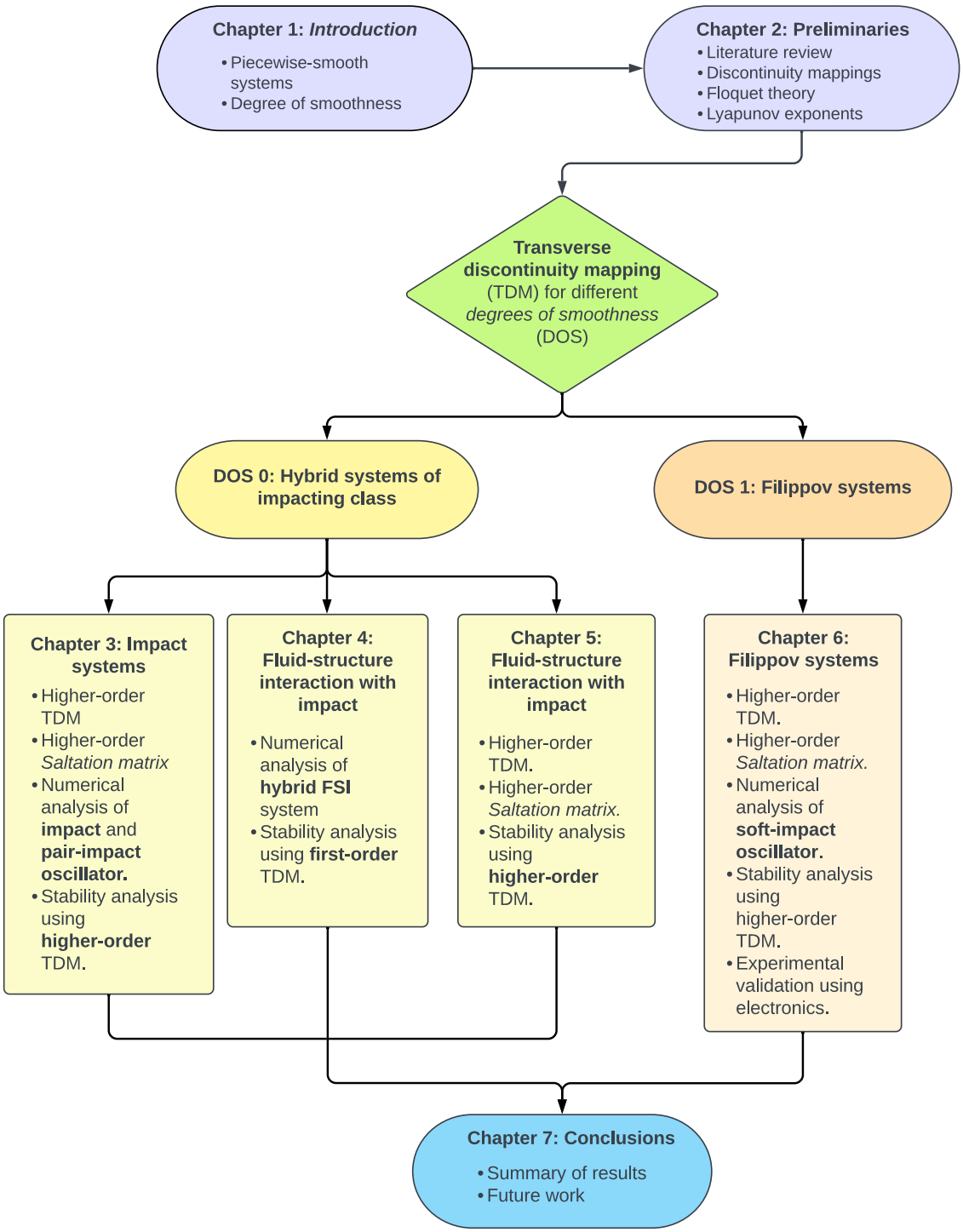

Figure 1.8: Outline of the thesis

oscillator). Next, a numerical method is proposed to obtain higher-order saltation and monodromy matrices and their Floquet multipliers and Lyapunov exponents. A stability analysis is carried out using the numerically obtained Floquet multipliers and Lyapunov exponents. Results are validated with the corresponding bifurcation diagrams obtained independently.

Chapter 4 presents a comprehensive numerical investigation of a 4 dimensional hybrid system with several bifurcation parameters. This chapter attempts

to phenomenologically model a fluid-structure interaction (FSI) system undergoing vortex-induced vibrations (VIV) in the presence of a rigid barrier. A detailed numerical analysis of the vibrational responses of the structure is investigated when subjected to impact with this rigid barrier. Next, stability analysis with first-order TDM is carried out using the methods developed in Chapter 3 to predict when discontinuity-induced bifurcations occur.

In ***Chapter 5***, the higher-order corrections to the transverse discontinuity mapping for the 4 dimensional hybrid FSI system investigated in Chapter 4 are presented. A comparison between the higher-order TDM with the widely accepted linearized TDM is discussed. The importance of higher-order corrections to the transverse discontinuity mapping is highlighted when the system size is large and comprises several parameters. Next, a numerical method to obtain a higher-order saltation matrix is presented.

In ***Chapter 6***, a higher-order transverse discontinuity mapping for Filippov systems has been derived. A comparison between the first-order saltation matrix with the proposed higher-order TDM for a representative case of a bi-linear oscillator (impact oscillator subject to impact with a deformable barrier) is carried out, illustrating the dangerous implications of constructing saltation matrices using linearized approaches. Next, a numerical method is proposed to obtain higher-order saltation and monodromy matrices and their Floquet multipliers and Lyapunov exponents for systems with DOS 1. A stability analysis is carried out using the numerically obtained Floquet multipliers and Lyapunov exponents. Results are validated with the corresponding bifurcation diagrams obtained independently. Next, experimental validation is provided for discontinuity-induced bifurcations observed in Filippov systems. An electronic circuit comprising two LCR circuits with a switching mechanism is investigated. This electronic circuit is equivalent to a mechanical system representing a Filippov system. The phase portraits recorded experimentally corroborate with the analytical and numerical predictions obtained independently using the proposed higher-order transverse discontinuity mapping.

Chapter 7 summarizes the key results from this thesis and the remaining limitations for possible future work.

Chapter 2

Literature review and mathematical preliminaries

This chapter is divided into two parts. The first section discusses the existing literature on PWS systems and various methods to construct a discontinuity mapping. Such discontinuity mappings are implemented to tend to the non-smooth transitions that occur in the phase space during interactions with the discontinuity barrier, following which traditional methods like stability analysis can be implemented to predict when discontinuity-induced bifurcations occur. The second part of this chapter describes methods to conduct stability analysis using Floquet theory and Lyapunov exponents implemented in this thesis to study the occurrences of discontinuity-induced bifurcations for piecewise-smooth hybrid and Filippov-type systems.

2.1 Literature review

An impact oscillator is the most simplistic phenomenological model of a mechanical system involving impacts or collisions between various components during its operation [129, 128]. They are modeled by linear harmonic oscillators subjected to piecewise-smooth external forces. The canonical form of a PWS impact oscillator is given in Eq. (2.1),

$$\ddot{x} + \xi\dot{x} + x = \begin{cases} F_1(x), & x \leq x_i \\ F_2(x), & x > x_i \end{cases} \tag{2.1}$$

where x is a harmonic oscillator modeling displacement of a moving mechanical device or charge across a capacitor in an LCR circuit. Accordingly, ξ denotes the viscous damping of the oscillator or resistance in the LCR circuit. The evolution of x in Eq. (2.1) is governed by the periodic force $F_1(x)$ or $F_2(x)$, depending on

whether $(x - x_i)$ is positive or negative in comparison to a predefined critical value x_i which represents the constraint after which impacts and collisions occur in the physical system. Shaw and Holmes [107] studied a single degree of freedom oscillator with a piecewise linear restoring force similar to Eq. (2.1). Next, they considered the limiting case when one of these forces became infinite, *i.e.*, the case of a hard collision in impact oscillators. Investigations revealed occurrences of DIBs and the existence of harmonic, sub-harmonic, and chaotic solutions. This work [107] showed that DIBs occurred due to the presence of singularities in the derivative of the Poincaré or return map. Shaw and Holmes [104] further investigated the limiting case of a periodically forced impact oscillator with large dissipation and an impact oscillator with multiple amplitude constraints [105]. A simple impact rule governs the partial inelastic impact of the oscillator. Therefore, the harmonic oscillator from Eq. (2.1) is now restricted in the region $(x - x_i) < 0$, *i.e.*,

$$\begin{aligned} & \ddot{x} + \xi\dot{x} + x = F(t), \quad x < x_i \\ \text{if,} \quad & x(t_-) = x_i, \quad \text{then,} \\ & x(t_+) = x(t_-) \quad \text{and} \quad \dot{x}(t_+) = -r\dot{x}(t_-) \end{aligned} \tag{2.2}$$

where t_- denotes the instant of impact with a barrier at $x = x_i$. During the impact, the velocity changes to $-r\dot{x}(t_-)$ instantaneously, and r is the coefficient of restitution. DIBs, in impact oscillators, occur when a part of the limit cycle grazes the discontinuity boundary with zero velocity *i.e.* when $x = x_i$ and $\dot{x} = 0$ simultaneously, resulting in a grazing bifurcation. To investigate this, Nordmark considered, in one of the pioneering works [85], a discrete-time mapping that could explain why orbits become unstable for grazing incidence. The discrete-time representation of the state x and $\dot{x}$ in Eq. (2.2) is given by x_n and y_n, and the mapping, known as Nordmark map, is defined as

$$\begin{aligned} x_{n+1} &= \alpha x_n + y_n + \rho, \quad x_n \leq 0 \\ y_{n+1} &= -\gamma x_n, \\ x_{n+1} &= \sqrt{x_n} + y_n + \rho, \quad x_n > 0, \\ y_{n+1} &= -\gamma r^2 x_n, \end{aligned} \tag{2.3}$$

where $F(t) = \sin\omega t$, $\gamma = e^{-c_1}$, $c_1 = 2\pi\xi/\omega$, $\alpha = 2e^{-c_1/2}\cosh\left(\sqrt{c_1^2 - 4c_2^2}/2\right)$ and $c_2^2 = 4\pi^2/\omega^2$. Interrelation between parameters of the Nordmark map (Eq. (2.3)) and the impact oscillator (Eq. (2.2)) can be found in [23] and are essentially related to the trace and determinant of the Jacobian matrix for the smooth part of the Nordmark map *i.e.*, $x_n \leq 0$. When the limit cycle is in the non-impacting region *i.e.*, $x_n \leq 0$, the Jacobian of the Nordmark map *i.e.*, $\partial x_{n+1}/\partial x_n$ is finite, indicating a stable orbit. However, when the limit cycle grazes the discontinuity boundary, trajectories

in the local neighborhood around $x_n = 0$ behave according to the Nordmark map. At this instant, the Jacobian is $\partial x_{n+1}/\partial x_n = 1/(2\sqrt{x_n})$. It is evident that in the limit of $x_n \to 0$, the Jacobian diverges. This phenomenon is known as the *square-root singularity*. Therefore, solutions that graze the switching manifold tend to diverge away since the square-root singularity stretches the phase space locally. At this point, the grazing limit cycle suddenly becomes unstable and disappears. This sudden change in the topology of the orbit is what is observed as a DIB. Nordmark further investigated occurrences of DIBs in impact oscillators for low-velocity incidences in [84]. Wai et al. [22] investigated, in great detail, different types of grazing bifurcations in impact oscillators by considering a sinusoidally excited harmonic oscillator in the presence of friction and subject to an impact with a rigid wall. They showed an equivalence between the physical parameters of this system and the Nordmark map (see Eq. (2.3)). The authors [22] introduced maximal orbits or limit cycles that cross the switching manifold once per time period, using which they investigated three possible DIB scenarios for the Nordmark map - (a) DIB from a stable period-1 orbit to a reversed infinite period adding cascade, (b) DIB from a stable period-1 orbit to a chaotic attractor and (c) collision of a maximal orbit with a stable period-1 orbit.

Nusse et al. [88] studied the bifurcation phenomena for piecewise-smooth maps. The bifurcations in such discrete-time non-smooth maps were also observed in continuous-time PWS hybrid systems. Their investigations showed that when fixed points of a PWS map crossed the discontinuity boundary or border, a new additional orbit was born, which may or may not be stable. This phenomenon was called a *border collision bifurcation* (BCB) and is a much richer class of bifurcation observed frequently in non-smooth systems. Nusse et al. [88] thoroughly investigated a wide variety of BCBs observed in two representative cases of a piecewise-linear map and the Hénon map. They generalized a class of piecewise-linear maps exhibiting period-2 to period-3 type BCB scenarios. Following the previous work, Nusse et al. [87] investigated a more general class of PWS maps comprising fractional powers of x_n (see Eq. (2.3)), like the square root singularity from the Nordmark map. The authors used the concept of orbit index introduced in [78] and [88] to study BCBs of a stable period-1 orbit to an arbitrary period-n orbit. An article by Wai et al. [23] summarises different types of universal behavior of grazing bifurcations in periodically forced impact oscillators. Wai et al. [23] have presented a wide range of BCB scenarios observed as the parameters α and γ are varied in the Nordmark map (see Eq. (2.3)).

Several authors [86, 22, 88] investigated a wide range of bifurcation scenarios that arise in the square-root map, a one-dimensional representation of the Nordmark

map, see Eq. (2.4),

$$x_{n+1} = \begin{cases} F_1(x_n) = \sqrt{\mu - x_n} + \nu\mu, & x_n < \mu \\ F_2(x_n) = \nu x_n, & x_n > \mu \end{cases} \tag{2.4}$$

where μ and ν are parameters. A BCB in the fixed points for the map Eq. (2.4) occurs at the point $x_n^* = \mu = 0$ while the slope of $F_1(x^*, \mu^*)$ and $F_2(x^*, \mu)$ is $-\infty$ and ν respectively. A wide range of DIBs is observed when μ increases beyond $\mu = 0$ depending on the slope ν. A summary can be found in the works of Bernardo et al. [14] and Nordmark [86]. The BCB in the square-root map can be segregated depending on the value of ν. To illustrate this, Fig. 2.1 presents a bifurcation diagram of the fixed points $x_{n+1} = x_{2000}$ obtained when the square-root maps converge after 2000 iterations. Note that fixed points repeating after m iterations are referred to as period m or Pm fixed points. The results are summarised as follows:

$\mathbf{2/3} < \nu < \mathbf{1}$: As μ increases through zero, there is a sudden transition to chaotic orbits with no stable attractors - this phenomenon is known as *robust chaos*, see Fig. 2.1(a) when $\nu = 0.80$.

$\mathbf{1/4} < \nu < \mathbf{2/3}$: As μ increases through zero, a range of m periodic orbits are observed, the periodicity of the orbits increase by one and between an m and $m+1$ period orbits exits chaotic attractors for a range of μ, see Fig. 2.1(b) when $\nu = 0.50$. This type of DIB, known as the period-adding cascade of attractors, is also commonly observed in impact oscillators as demonstrated in Chapters 3 and 4, see Fig. 2.1(c).

$\mathbf{0} < \nu < \mathbf{1/4}$: As μ increases, period-adding cascades of orbits are observed and $m \to \infty$ as $\mu = 0$. However, no chaotic attractors are observed between an m and $m+1$ orbit; see Fig. 2.1(d) when $\nu = 0.20$. Also, orbits with m and $m+1$ overlap, leading to multiple attractors for the same parameter values.

Nusse et al. [88] showed that any PWS map could be reduced to an equivalent canonical or *normal form* using suitable coordinate transformation into Eqs. (2.5)

$$\begin{pmatrix} x_{n+1} \\ y_{n+1} \end{pmatrix} = \begin{cases} \begin{pmatrix} \tau_i & 1 \\ -\delta_i & 0 \end{pmatrix} \begin{pmatrix} x_n \\ y_n \end{pmatrix} + \begin{pmatrix} 1 \\ 0 \end{pmatrix} \mu, & x_n \leq 0, \\ \begin{pmatrix} \tau_j & 1 \\ -\delta_j & 0 \end{pmatrix} \begin{pmatrix} x_n \\ y_n \end{pmatrix} + \begin{pmatrix} 1 \\ 0 \end{pmatrix} \mu, & x_n > 0, \end{cases} \tag{2.5}$$

where τ_i or τ_j and δ_i or δ_j are the trace and determinants of the Jacobian matrix evaluated on either side of a border $\Sigma_{i,j}$, see Eq. (1.3). Yuan et al. [138] studied various BCB scenarios arising in power electronics like current-feedback controlled buck converters. They showed that the governing dynamics of the buck converter could be reduced to the normal form of Eq. (2.5). Banerjee et al. [9] first showed a

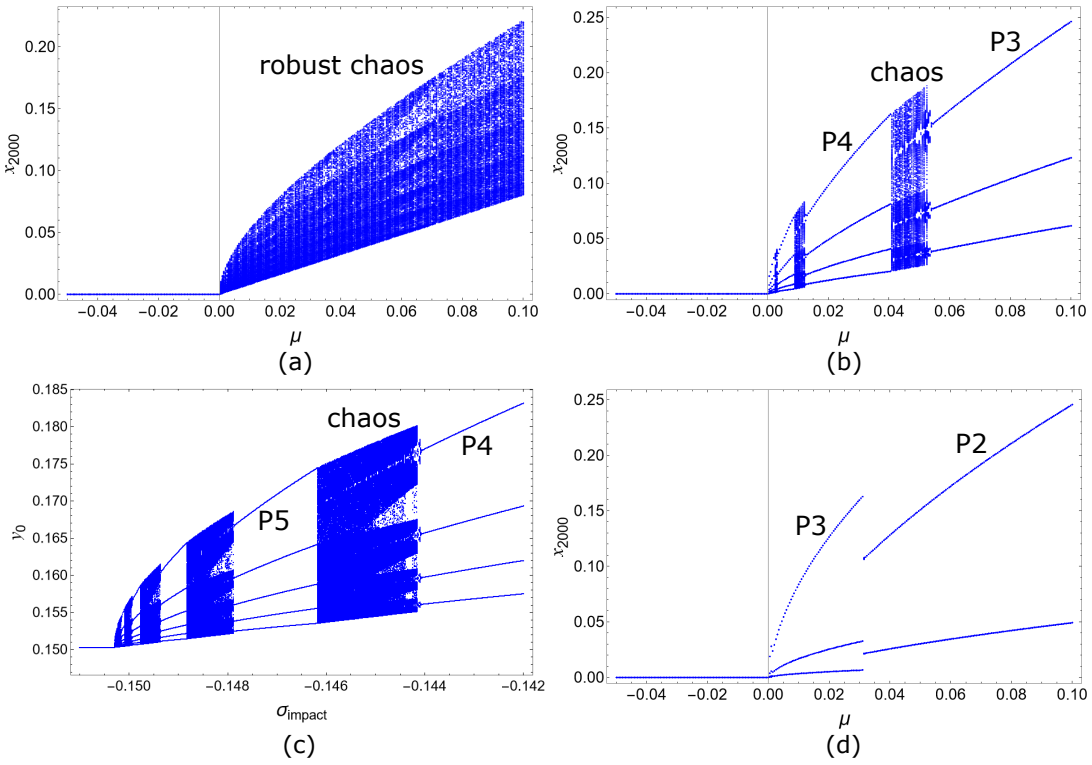

Figure 2.1: Bifurcation diagram showing BCB of fixed points $x_n = x_{2000}$ of the square-root map after 2000 iterations as the parameter μ is varied for (a) $\nu = 0.80$ for which only chaotic fixed points (also known robust chaos) is observed, (b) $\nu = 0.5$ where period-adding cascade of fixed points and separated by chaotic solutions are observed. (c) Amplitude y_0 vs. bifurcation parameter (barrier distance) where period-adding cascades separated by chaotic solutions are observed. These phenomena, observed in the case of square-root maps, are also found in impact oscillators governed by ODEs (further discussed in Chapter 4). (d) $\mu = 0.20$ for which only period adding fixed points are observed with coexisting attractors.

practical application of BCBs in electrical engineering. The authors derived conditions for which robust chaos was observed at the instant of BCB in the 2D normal form of Eq. (2.5). The robust chaos, as a result of BCB, has applications in areas like communications, chemical processes, etc., which require chaos as a reliable mode of operation. Next, Banerjee et al. [6] investigated the normal form of Eq. (2.5) by systematically carrying out a stability analysis of the eigenvalues of its Jacobian. The authors derived the necessary conditions in the parameter space of the normal form *i.e.*, τ and δ for which eleven different types of BCBs were observed. Hassouneh et al. [50] showed a new type of BCB for the 2D normal PWS map (Eq. (2.5)) called *robust dangerous border-collision bifurcation*. During a dangerous BCB, stable fixed points are born, but the orbits remain unbounded. The authors showed feedback control methods that could avoid a dangerous BCB. Ganguli and Banerjee [39] studied dangerous BCBs in 2D PWS maps and derived analytical conditions in the parameter space that leads to such BCBs. Their investigations showed that dangerous BCBs occur because when stable orbits are born, the basin of attraction

becomes infinitesimally small, resulting in unbounded orbits. Banerjee et al. [7] provided numerical and experimental evidence showing the occurrence of dangerous BCBs in impact oscillators due to which a *narrow-band chaos* can occur. Therefore, a close analogy exists between piecewise-smooth maps and piecewise-smooth dynamical systems, as both systems exhibit similar bifurcation behaviors.

Next, Foale and Bishop [34] studied the complexities in bifurcation scenarios observed in impact oscillators governed by a rigid impact law and a more natural, continuous impact process like a stiff spring. Since a grazing orbit can greatly change the topological behavior of a non-impacting stable solution, the authors compared the dynamics using other standard impact models like the Hertz model. Therefore, Foale and Bishop [35] modified the impact oscillator (see Eq. (2.2)) by considering a continuous function $f(x)$ modeling the impact phenomenon as,

$$\ddot{x} + \xi\dot{x} + f(x) = F(t), \tag{2.6}$$

$$f(x) = \begin{cases} x, & x < x_i \\ x + k(x - x_i)^{3/2}, & x \geq x_i \end{cases}$$

where k relates to the material properties of the impacting surface. The function $f(x)$ is smooth and depicts an additional force exerted on the oscillator during an impact. This additional force is proportional to the penetration depth $x - x_i$ raised to the power of 3/2. The authors found that both the continuous (Eq. (2.6)) and instantaneous (Eq. (2.2)) impact model qualitatively revealed similar behavior. If the square root term in the Nordmark map were smoothed off, the resulting bifurcation, at the instant of a low velocity impact, would lead to a new distant attracting solution.

Fredriksson and Nordmark [36] investigated the stability between impacting and non-impacting limit cycles in mechanical impact oscillators. The authors introduced a *discontinuity bypass mapping* for orbits in the local neighborhood of a grazing limit cycle. To illustrate this, consider a state $\mathbf{x}$, which represents the position and velocity of the impact oscillator defined in Eq. (2.2). Let the dynamics of $\mathbf{x}$ be governed by the velocity vector $\mathbf{F}(\mathbf{x})$, see Eq. (1.1). Let ϕ_t represent the evolution of state $\mathbf{x}$, initially at $\mathbf{x}_0$, after time t. Then, $\phi_t : \mathbf{x} \to \mathbf{x}(x_0, t)$. Next, consider a limit cycle that grazes the discontinuity boundary Σ as shown in Fig. 2.2. Let Σ be the set of all $\mathbf{x}$ such that $H(\mathbf{x}) = 0$, *i.e.*, $\Sigma = \{\mathbf{x} \in \mathbb{R}^2 : H(\mathbf{x}) = 0\}$. Then, $\nabla H(\mathbf{x}_i)$ represents a normal vector on $H(\mathbf{x}) = 0$ at the grazing point $\mathbf{x}_i$. Since, the orbit is grazing, the condition $\nabla H(\mathbf{x}_i)^T \cdot \mathbf{F}(\mathbf{x}_i) = 0$ is always true. In Fig. 2.2, a schematic phase portrait of a grazing orbit is shown. The state $\mathbf{x}_1$ reaches the grazing point $\mathbf{x}_i$ in time t_1 via ϕ_{t_1} where $H(\phi_{t_1}) = 0$ and $\dot{x} = 0$. Eventually, $\mathbf{x}_i$ will reach $\mathbf{x}_2$ after a time t_2. The mapping of the grazing orbit from $\mathbf{x}_1$ to $\mathbf{x}_2$ is written as the composition $\phi_{t_2} \circ \phi_{t_1}$. Fredriksson and Nordmark [36] investigated the composition, which takes

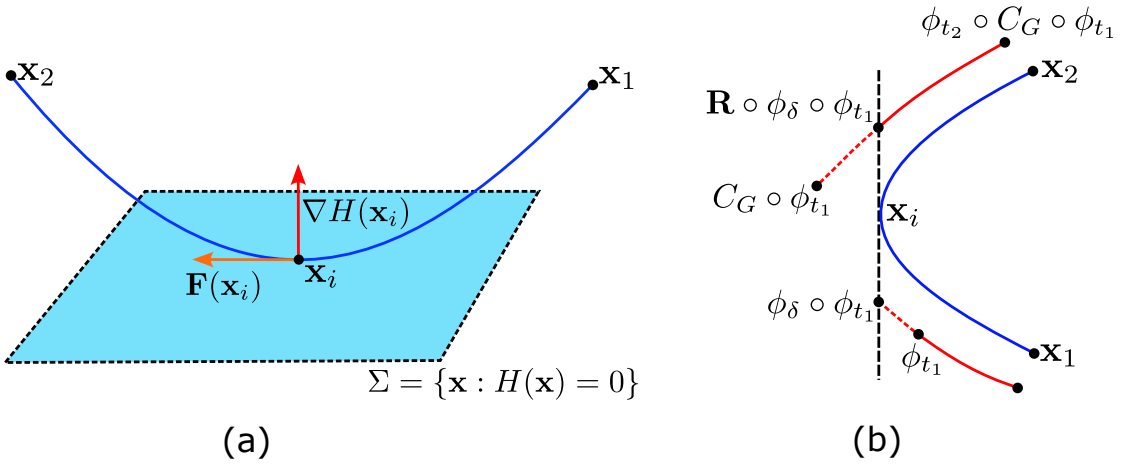

Figure 2.2: (a) An orbit grazing (blue curve) the discontinuity barrier at $\mathbf{x}_i$. At $\mathbf{x}_i$, the condition $\nabla H(\mathbf{x}_i)^T \cdot \mathbf{F}(\mathbf{x}_i) = 0$ is satisfied. (b) Phase-portrait showing discontinuity bypass mapping of orbits (red curve) in the local neighborhood of a grazing orbit (blue curve) at $\mathbf{x}_i$.

orbits in the local neighborhood of $\mathbf{x}_1$ to $\mathbf{x}_2$; see Fig. 2.2(b). This is achieved using a mapping $\phi_{t_2} \circ C_G \circ \phi_{t_1}$, where C_G is defined as,

$$C_G = \begin{cases} \phi_{-\delta} \circ \mathbf{R} \circ \phi_\delta, & H(\phi_{t_1}) \leq 0 \\ \mathbb{I}, & H(\phi_{t_1}) > 0 \end{cases} \tag{2.7}$$

The flow ϕ_δ takes impacting points in the local neighborhood of $\mathbf{x}_1$ on Σ; the map $\mathbf{R}$ is the impact map defined in Eq. (2.2). The flow $\phi_{-\delta}$ ensures that the composition in the local neighborhood of the grazing orbit occurs in zero-time. The authors approximated the discontinuity bypass mapping in Eq. (2.7) by Taylor expanding C_G near grazing incidence. This local analysis showed how orbits become unstable when C_G causes a one-dimensional stretching in the phase-space governed by the square root of the penetration depth *i.e.*, $\sqrt{-H(\mathbf{x})}$, a factor which can be found in the Nordmark map as well.

Based on the idea of a discontinuity bypass mapping, Fredriksson and Nordmark [37] derived a discontinuity mapping $\mathbf{D}$ for the impact oscillator with transverse interactions with the discontinuity barrier, see Fig. 2.3(a). The authors showed that for limit cycles impacting Σ with a non-zero velocity, *i.e.*, $\nabla H(\mathbf{x}_i)^T \cdot \mathbf{F}(\mathbf{x}_i) \neq 0$, the Jacobian derivative of the discontinuity mapping *i.e.*, $\mathbf{S} = \nabla \mathbf{D}^T$(known as the saltation matrix, $\mathbf{S}$) is given by,

$$\mathbf{S} = \nabla \mathbf{R}(\mathbf{x}_i)^T + \frac{(\mathbf{F}(\mathbf{R}(\mathbf{x}_i)) - \nabla \mathbf{R}^T(\mathbf{x}_i) \cdot \mathbf{F}(\mathbf{x}_i)) \otimes \nabla H(\mathbf{x}_i)}{\nabla H(\mathbf{x}_i)^T \cdot \mathbf{F}(\mathbf{x}_i)}. \tag{2.8}$$

Additionally, trajectories in the local neighborhood of an impacting orbit reach Σ

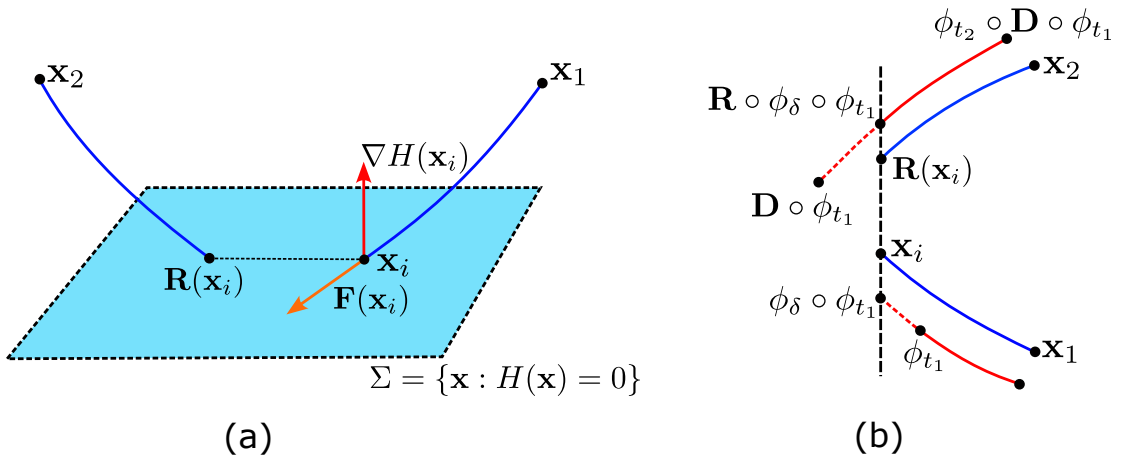

Figure 2.3: (a) An orbit impacting the discontinuity barrier transversally at $\mathbf{x}_i$ and getting mapped to $\mathbf{R}(\mathbf{x}_i)$ using an impact law. At $\mathbf{x}_i$, the condition $\nabla H(\mathbf{x}_i)^T \cdot \mathbf{F}(\mathbf{x}_i) \neq 0$ is satisfied. (b) Phase-portrait showing discontinuity mapping of orbits in the local neighborhood of an impacting orbit at $\mathbf{x}_i$.

after δs using ϕ_δ as

$$\delta = -\frac{\nabla H(\mathbf{x}_i)^T.\mathbf{y}}{\nabla H(\mathbf{x}_i)^T \cdot \mathbf{F}(\mathbf{x}_i)}, \tag{2.9}$$

where $\mathbf{y}$ denotes the perturbation or separation between impact state $\mathbf{x}_i$ and a nearby orbit in its local neighborhood. Both $\mathbf{S}$ and δ are only valid for transversal trajectories; the denominator is proportional to $\nabla H(\mathbf{x}_i)^T \cdot \mathbf{F}(\mathbf{x}_i)$ and hence diverges for grazing incidence.

Similarly, Filippov systems with discontinuous vector fields also show DIBs like grazing bifurcations. Such systems also require the methods discussed above to study the behavior of trajectories in the local neighborhood of a grazing orbit. Dankowicz and Nordmark [26] derived a discontinuity mapping for orbits in the vicinity of a grazing limit cycle for systems described by two different vector fields. Let two different vector fields describe a PWS system as

$$\dot{\mathbf{x}} = \begin{cases} \mathbf{F}_i(\mathbf{x}), & H(\mathbf{x}) > 0, \\ \mathbf{F}_j(\mathbf{x}), & H(\mathbf{x}) < 0, \end{cases} \tag{2.10}$$

where the $H(\mathbf{x})$ is a scalar function which defines a discontinuity boundary $\Sigma_{i,j}$ such that $\Sigma_{i,j} = \{\mathbf{x} : H(\mathbf{x}) = 0\}$. To illustrate the local analysis proposed by the authors [26], consider the phase portrait of an orbit grazing $\Sigma_{i,j}$ at $\mathbf{x}_i$ shown in Fig. 2.4(a). The state $\mathbf{x}$ evolves using Eq. (2.10) and, therefore, is governed by $\mathbf{F}_i(\mathbf{x})$ if $H(\mathbf{x}) < 0$ or $\mathbf{F}_j(\mathbf{x})$ if $H(\mathbf{x}) \geq 0$. The discontinuity boundary $\Sigma_{i,j}$ is defined as before, *i.e.*, $\Sigma_{i,j} = \{\mathbf{x} : H(\mathbf{x}) = 0\}$. Let $\phi_i(\mathbf{x}_0, t)$ and $\phi_j(\mathbf{x}_0, t)$ denote the evolution of $\mathbf{x}$ governed by $\mathbf{F}_i(\mathbf{x})$ and $\mathbf{F}_j(\mathbf{x})$ and initiated from $\mathbf{x}_0$ in time t. Let local trajectories from S_i impact $\Sigma_{i,j}$ at $\mathbf{x}_2$ to reach $\mathbf{x}_0$. The discontinuity mapping maps $\mathbf{x}_0$ to $\mathbf{x}_4$ in

zero-time while other intermediate states are mapped according to Eqs. (2.11),

$$\begin{aligned}\mathbf{x}_2 &= \phi_i(\mathbf{x}_0, t_1 - t_2), \\ \mathbf{x}_3 &= \phi_j(\mathbf{x}_2, t_3), \\ \mathbf{x}_4 &= \phi_i(\mathbf{x}_3, -(t_1 - t_2 + t_3)), \\ &= \phi_i(\phi_j(\phi_i(\mathbf{x}_0, t_1 - t_2), t_3), t_2 - t_1 - t_3),\end{aligned} \tag{2.11}$$

where $\mathbf{x}_0$ reaches $\mathbf{x}_1$ defined as $\mathbf{x}_1 = H_{min} = H(\mathbf{x}_1) = 0$ in time t_1, $\mathbf{x}_2$ reaches $\mathbf{x}_1$ in time t_2 and $\mathbf{x}_2$ reaches $\mathbf{x}_3$ in time t_3 following the dashed path. Dankowicz and

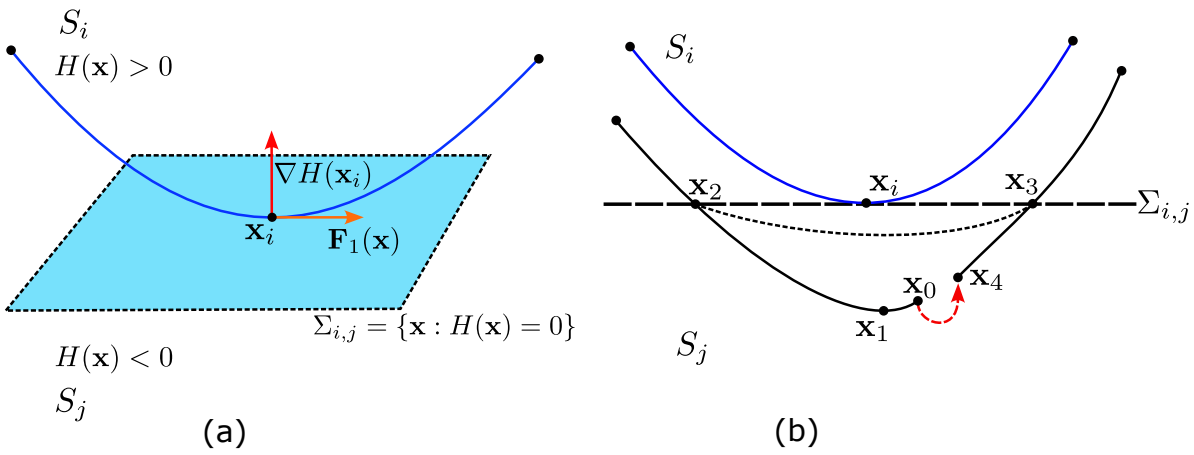

Figure 2.4: (a) Schematic of a grazing orbit for a Filippov system. The blue trajectory grazes on $\Sigma_{i,j}$ at $\mathbf{x}_i$. (b) Cross-section showing discontinuity mapping of $\mathbf{x}_0$ to $\mathbf{x}_4$ in zero-time. The discontinuity mapping ensures that orbits and states (*i.e.*, $\mathbf{x}_2$) in the local neighborhood of an grazing orbit at $\mathbf{x}_i$ gets mapped in the correct instances when reaching $\Sigma_{i,j}$.

Nordmark [26] derived that the mapped state post impact from $\mathbf{x}_0$ to $\mathbf{x}_4$ is equal to,

$$\mathbf{x}_4 = \mathbf{x}_i + 2\sqrt{\frac{2}{a}}\mathbf{G}(\mathbf{x}_i)\Big(- \frac{\partial H}{\partial \mathbf{x}_i} \cdot \mathbf{x}_i + \frac{1}{3}\mathbf{z}^2\Big)\mathbf{z} + h.o.t, \tag{2.12}$$

where $\mathbf{G} = \mathbf{F}_j(\mathbf{x}_i) - \mathbf{F}_i(\mathbf{x}_i)$, $a = \frac{d^2H(\mathbf{x}_i)}{dt^2}$ and $\mathbf{z} = \sqrt{-\frac{\partial H}{\partial \mathbf{x}} \cdot \mathbf{x}}$. The Jacobian derivative of the discontinuity mapping (Eq. (2.12)) is proportional to $\mathbf{x}_i^{-1/2}$ and therefore diverges for grazing impacts when $\mathbf{x}_i = 0$. The square-root singularity, mentioned earlier, is observed for Filippov systems similar to the Nordmark map found in impacting oscillators. Hence, grazing orbits in Filippov systems become unstable due to local stretching of the phase-space, resulting in DIBs.

To generalize the methods discussed above, Bernardo et al. [28] derived a Poincaré map comprising discontinuity mappings for grazing orbits for an arbitrary n-dimensional PWS system for vector fields that may or may not be continuous at the grazing point. This was achieved using two different types of mapping - a *zero-*

time discontinuity mapping or ZDM and a *Poincaré-section discontinuity mapping* or PDM. To illustrate this, consider a PWS system governed by Eqs. (2.10) such that no sliding is allowed, *i.e.*, the vector fields are never simultaneously attracting or repelling on the discontinuity boundary or $(\nabla H(\mathbf{x}_i)^T \cdot \mathbf{F}_i(\mathbf{x}_i))(\nabla H(\mathbf{x}_i)^T \cdot \mathbf{F}_j(\mathbf{x}_i)) \geq 0$. Let an orbit graze $\Sigma_{i,j}$ at $\mathbf{x}_i$ as shown in Fig. 2.5. Orbits near $\mathbf{x}_i$ will reach $\Sigma_{i,j}$ at different instants of time. Using the same notation, let $\phi_i(\mathbf{x}_0, t)$ and $\phi_j(\mathbf{x}_0, t)$ denote evolution or flow of $\mathbf{x}$ initially at $\mathbf{x}_0$ and governed by $\mathbf{F}_i(\mathbf{x})$ and $\mathbf{F}_j(\mathbf{x})$ in time t. Let $\mathbf{x}_0$ denote a state in the local neighborhood of $\mathbf{x}_i$ which evolves to $\mathbf{x}_2$ in time δ_0. Assume that $\mathbf{x}_2$ reaches $\mathbf{x}_3$ in time δ_2 governed by $\mathbf{F}_j(\mathbf{x})$, eventually stopping in a local neighborhood at $\mathbf{x}_6$. The correct flow of the perturbed orbit between two local neighborhoods from $\mathbf{x}_0$ to $\mathbf{x}_6$ can be achieved using a ZDM or a PDM. To illustrate this, consider the following intermediate states. Let $\mathbf{x}_2$ evolve to reach $\mathbf{x}_1$ in time δ located on a new Poincaré section Π_N perpendicular to $\Sigma_{i,j}$ such that $\Pi_N = \{\mathbf{x} : \nabla H(\mathbf{x}_1)^T \cdot \mathbf{F}_i(\mathbf{x}_1) = 0\}$. The state $\mathbf{x}_3$ is back interpolated in time $-\delta_3$ to reach $\mathbf{x}_5 \in \Pi_N$ and $-(\delta_0 + \delta_2)$ to reach $\mathbf{x}_4$. Therefore, the ZDM is defined as the mapping of $\mathbf{x}_0$ to $\mathbf{x}_4$ whereas the PDM is defined as the mapping of $\mathbf{x}_1$ to $\mathbf{x}_5$ on Π_N. The respective intermediate flows are given by,

$$\begin{aligned} &\mathbf{x}_2 = \phi_i(\mathbf{x}_0, \delta_0) \qquad \mathbf{x}_1 = \phi_i(\mathbf{x}_2, \delta) \\ &\mathbf{x}_3 = \phi_j(\mathbf{x}_2, \delta_2) \qquad \mathbf{x}_4 = \phi_i(\mathbf{x}_3, -(\delta_0 + \delta_2)) \qquad \mathbf{x}_5 = \phi_i(\mathbf{x}_3, -\delta_3) \end{aligned} \tag{2.13}$$

The flow which defines the ZDM and PDM are,

$$\begin{aligned} &\mathbf{x}_0 \to \mathbf{x}_4 = \phi_i((\phi_j(\phi_i(\mathbf{x}_0, \delta_0), \delta_2), \delta_2), -(\delta_0 + \delta_2)) \\ &\mathbf{x}_1 \to \mathbf{x}_5 = \phi_i(\phi_j(\phi_i(\mathbf{x}_1, -\delta), \delta_2), \delta_3) \end{aligned} \tag{2.14}$$

The ZDM and PDM have their own merits. ZDM is applicable for PWS systems governed by vector fields with explicit dependence on time, *i.e.*, for non-autonomous PWS systems. Since the state $\mathbf{x}$ depends on time, the discontinuity mapping should preserve time. Hence a zero-time mapping serves the purpose. Similarly, the investigation of periodic limit cycles in PWS systems governed by autonomous vector fields requires Poincaré maps to be defined at clever locations to simplify their analysis. Hence, the PDM defined in Eq. (2.14) can effectively map orbits locally near a grazing flow in such scenarios. Bernardo et al. [28] proved that both ZDM and PDM comprises a square-root singularity for Filippov systems *i.e.*, $\mathbf{F}_i(\mathbf{x}_i) \neq \mathbf{F}_j(\mathbf{x}_i)$ and a 3/2-type singularity for piecewise-smooth systems *i.e.*, $\mathbf{F}_i(\mathbf{x}_i) = \mathbf{F}_j(\mathbf{x}_i)$ but $\nabla \mathbf{F}_i(\mathbf{x}_i) \neq \nabla \mathbf{F}_j(\mathbf{x}_i)$ or $\nabla^2 \mathbf{F}_i(\mathbf{x}_i) \neq \nabla^2 \mathbf{F}_j(\mathbf{x}_i)$ at the discontinuity boundary. The existence of singularities due to terms having fractional powers of the penetration depth $H(\mathbf{x})$ in the discontinuity maps leads to unstable orbits for which DIBs are

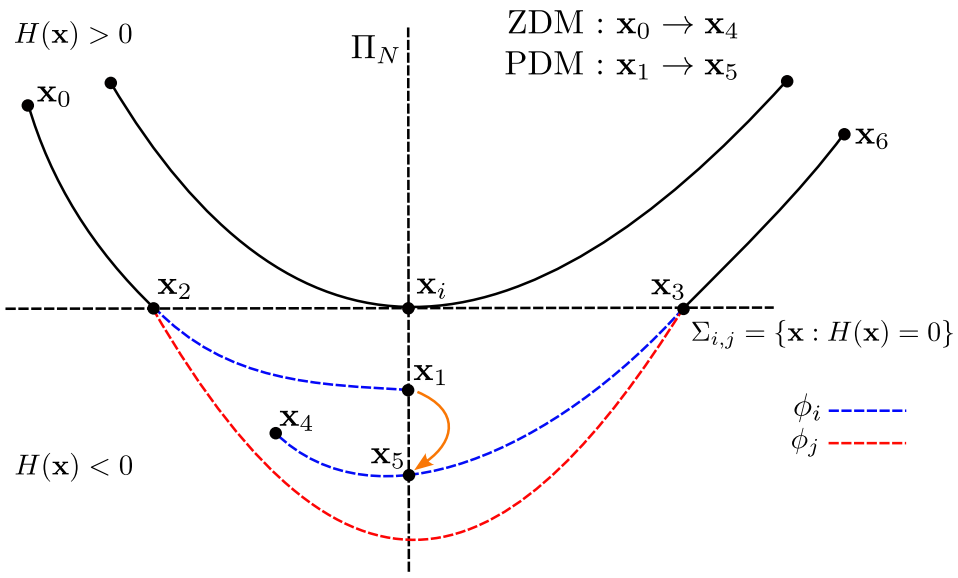

Figure 2.5: Schematic of two nearby orbits of a PWS system. The first orbit grazes $\Sigma_{i,j}$ at $\mathbf{x}_i$. A second orbit near $\mathbf{x}_i$ is initiated from $\mathbf{x}_0$ to reach $\mathbf{x}_2$. The blue and red dashed line corresponds to the flows ϕ_i and ϕ_j in the region $H(\mathbf{x}) < 0$. The orange arrow shows the mapping of $\mathbf{x}_1$ to $\mathbf{x}_5$ using the PDM while the mapping of $\mathbf{x}_0$ to $\mathbf{x}_4$ is the ZDM defined by Eqs. (2.12).

observed.

Next, based on their previous work, Bernardo et al. [31, 61] derived the ZDM for PWS systems (see Eqs. (2.10)) with the possibility that the vector fields can be simultaneously attracting or repelling on the discontinuity boundary. This allows vector fields to obey $(\nabla H(\mathbf{x}_i)^T \cdot \mathbf{F}_i(\mathbf{x}_i))(\nabla H(\mathbf{x}_i)^T \cdot \mathbf{F}_j(\mathbf{x}_i)) \leq 0$, resulting in sliding motion. Bernardo et al. [31] investigated four different possibilities of sliding motion - sliding bifurcation of type I and II, grazing-sliding bifurcation, and multi-sliding bifurcation scenarios. The authors showed that the ZDM for the case of grazing-sliding bifurcation is a piecewise-linear map due to which a stable orbit can become chaotic or show period-adding bifurcations. A summary of the normal forms for all types of PWS systems showing grazing bifurcations can be found in the letter by Bernardo et al. [29].

Based on the construction of saltation matrices for impacting systems (see Eqs. (2.2)) by Fredriksson and Nordmark [37], Leine [68] derived a discontinuity mapping for Filippov systems with transverse interactions with the discontinuity boundary. To illustrate this, consider an orbit, governed by Eqs. (2.10), initiated from $\mathbf{x}_0$ reach the discontinuity boundary $\Sigma_{i,j}$ at $\mathbf{x}_i$, as shown in Fig. 2.6. A second orbit initiated from $\tilde{\mathbf{x}}_0$ lying in the local neighborhood of $\mathbf{x}_0$ reaches $\mathbf{x}_1$ in the same time as $\mathbf{x}_0$ reaches $\mathbf{x}_i$. Both the orbits are initially in the region $H(\mathbf{x}) > 0$ and therefore evolves according to the vector field $\mathbf{F}_i(\mathbf{x})$. Since $\mathbf{x}_0$ and $\tilde{\mathbf{x}}_0$ reaches $\Sigma_{i,j}$ at different instants of time, it is incorrect to evolve both the trajectories using $\mathbf{F}_j(\mathbf{x})$ while $\mathbf{x}_1$ is still in the region $H(\mathbf{x}) > 0$. The transverse discontinuity mapping derived by Leine

[68] resolves this. Let δ be the time taken for $\mathbf{x}_1$ to reach $\mathbf{x}_3$ on $\Sigma_{i,j}$. The TDM maps $\mathbf{x}_1$ to $\mathbf{x}_2$ in a way such that $\mathbf{x}_2$ governed by $\mathbf{F}_j(\mathbf{x})$ reaches $\mathbf{x}_3$ on $\Sigma_{i,j}$ in the same time as $\mathbf{x}_1$ governed by $\mathbf{F}_i(\mathbf{x})$ would take to reach $\mathbf{x}_3$ on $\Sigma_{i,j}$, *i.e.*, δ. Therefore perturbations, at the instant of an impact, in the local neighborhood are mapped from $\mathbf{y}_-$ to $\mathbf{y}_+$ using the jacobian derivative of the TDM $\mathbf{S}$ (known as saltation matrix). Hence,

$$\mathbf{y}_+ = \mathbf{S} \cdot \mathbf{y}_-, \tag{2.15}$$

the saltation matrix is defined as,

$$\mathbf{S} = \mathbb{I} + \frac{(\mathbf{F}_j(\mathbf{x}_i) - \mathbf{F}_i(\mathbf{x}_i)) \otimes \nabla H(\mathbf{x}_i)}{\nabla H(\mathbf{x}_i)^T \cdot \mathbf{F}_i(\mathbf{x}_i)} \tag{2.16}$$

and the time difference between two near-by orbits to reach $\Sigma_{i,j}$ is given by,

$$\delta = -\frac{\nabla H(\mathbf{x}_i)^T . \mathbf{y}}{\nabla H(\mathbf{x}_i)^T \cdot \mathbf{F}_i(\mathbf{x}_i)}, \tag{2.17}$$

where $\mathbf{y}$ are perturbations separating near-by trajectories.

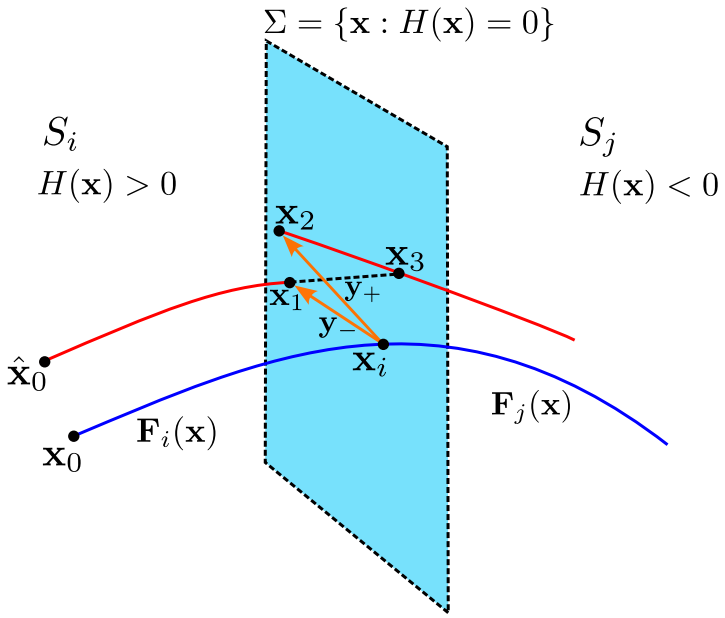

Figure 2.6: Schematic of two nearby orbits of a PWS Filippov system. The blue orbit impacts $\Sigma_{i,j}$ at $\mathbf{x}_i$. A second perturbed orbit near $\mathbf{x}_i$ is initiated from $\hat{\mathbf{x}}_0$ to reach $\mathbf{x}_1$. The orange arrow shows the mapping of perturbation $\mathbf{y}_-$ to $\mathbf{y}_+$ mapping $\mathbf{x}_1$ to $\mathbf{x}_2$ using the Saltation matrix defined by Eqs. (2.16).

DIBs also occur for PWS systems where the discontinuity boundary is perturbed by random amplitude noise [110, 109, 111]. Staunton and Piiroinen [113, 114] investigated the behavior of the dynamics of the Nordmark map due to an additive Gaussian white noise. To analyze the bifurcations and stability of noisy PWS systems, Staunton and Piiroinen [116] derived a stochastic zero-time discontinuity mapping

(SZDM) for Filippov systems with an oscillating stochastic discontinuity boundary. Later, Staunton and Piiroinen [115] extended the derivations of the SZDM for hybrid systems and PWS systems with higher-order discontinuities subjected to a stochastically oscillating discontinuity boundary.

Therefore, discontinuity mappings are crucial for investigating piecewise-smooth dynamical systems since they contain information regarding when discontinuity-induced bifurcations occur. Such mappings define the behavior of orbits in the local neighborhood of impacting states and can be implemented to perform stability analysis of orbits undergoing grazing bifurcations. This is usually achieved by calculating an orbit's global state transition matrix or Monodromy matrix [82]. The Monodromy matrix comprises products of state transition matrices (STMs) and discontinuity mappings multiplied in the order of events. Ma et al. [76] investigated the stability of a grazing orbit of a bi-linear oscillator undoing soft impact. The authors [76] calculated the Monodromy matrix of this system implementing the saltation matrix Eq. (2.16) at the instant of an impact. Their investigations showed that the eigenvalues of the Monodromy matrix diverge near a grazing impact. This is because the trace of the Jacobian of the respective system becomes infinite, implying a square-root singularity at the grazing point. Following their previous work, Ma et al. [77] investigated four configurations of the soft impact oscillator undergoing a grazing impact. They studied various types of singularities in the respective normal forms of a grazing orbit. A comprehensive derivation of the ZDM for the case of soft-impact oscillator, along with experimental validations mentioned above, can be found in the works of Kundu et al. [64]. Additionally, a comprehensive explanation of both PWS dynamical systems and PWS maps was written by Bernardo et al. [14]. This book, known as the Bristol book in literature, is an excellent resource on PWS systems. It provides an introduction for the readers to non-smooth systems, covering discrete time PWS maps (normal forms of the square-root maps, 2D PWS map, etc.), PWS flows (piecewise continuous, Filippov systems, etc.), hybrid systems (impact oscillators), etc. with detailed derivations and analysis of normal forms for discrete PWS maps and discontinuity maps for PWS flows like the TDM, ZDM and PDM. A more updated review of PWS systems and some existing problems on non-smooth systems can be found in the work by Belykh et al. [10].

This thesis highlights the limitations of implementing saltation matrices and discontinuity mappings derived from a first-order linearized approximation. Such lower-order approximations of the discontinuity mapping can result in incorrect predictions of the behavior of trajectories in the local neighborhood of an impacting orbit. The higher-order corrections to the discontinuity mapping presented in this thesis can resolve the existing limitations of the widely accepted first-order approaches. With the higher-order corrections to the existing theory around discontinuity mapping, stability analysis of PWS systems becomes more accurate. The following section

discusses traditional methods like Floquet theory and Lyapunov exponent, which can be implemented to investigate the stability of impacting orbits in PWS systems.

2.2 Stability analysis

One of the primary applications of discontinuity mapping is in the stability analysis of limit cycles for PWS systems. This is because periodic orbits can become unstable and disappear due to grazing incidence when subjected to changes in the system parameters. The saltation matrix for hybrid and Filippov systems can provide insights into how eigenvalues behave at the instant of grazing incidence. Several numerical methods or tools have been developed [79, 122] to obtain unstable and stable branches of solutions for PWS systems using the saltation matrix. This section discusses two standard methods - Floquet multipliers and Lyapunov exponents, to determine the stability of dynamical systems governed by smooth vector fields. With the aid of the TDM derived in this thesis, the existing theory can be extended for non-smooth PWS systems, discussed later in Chapters 3 - 6.

2.2.1 Floquet multipliers

Consider a state-space representation of an arbitrary dynamical system of size n. The state $\mathbf{x} \in \mathbb{R}^n$ evolves in time governed by the vector field $\mathbf{F}(\mathbf{x})$ as,

$$\frac{d\mathbf{x}}{dt} = \mathbf{F}(\mathbf{x}). \tag{2.18}$$

The vector field may or may not have explicit dependence on t, *i.e.*, non-autonomous or autonomous dynamical system. For non-autonomous systems governed by a vector field $\mathbf{F}(\mathbf{x}, t)$, a new variable $s = t$ can be defined such that $\dot{s} = 1$. Therefore, $\mathbf{x} \in \mathbb{R}^n$ can be written as $\mathbf{x}' \in \mathbb{R}^{n+1}$ accounting for the new time variable s. Let $\mathbf{x}_0$ denote a periodic solution of the system with time period T. To determine the stability of the solution $\mathbf{x}_0$, consider a slight disturbance or perturbation $\mathbf{y}$ to $\mathbf{x}_0$, *i.e.*, $\mathbf{x} = \mathbf{x}_0 + \mathbf{y}$. The dynamics of $\mathbf{y}$ can be obtained by substituting $\mathbf{x}_0 + \mathbf{y}$ in Eq. (2.18), followed by a Taylor expansion of $\mathbf{F}(\mathbf{x})$ about $\mathbf{x}_0$ upto first order to get,

$$\begin{aligned} \dot{\mathbf{x}}_0 + \dot{\mathbf{y}} &= \mathbf{F}(\mathbf{x}_0 + \mathbf{y}) \\ &= \mathbf{F}(\mathbf{x}_0) + \nabla \mathbf{F}(\mathbf{x}_0)^T \cdot \mathbf{y} + \mathcal{O}(||\mathbf{y}||^2) \end{aligned} \tag{2.19}$$

where $\dot{()}$ denotes derivative with respect to t. Since $\mathbf{x}_0$ is a periodic solution of Eq. (2.18), $\mathbf{y}$ evolves as,

$$\begin{aligned}\dot{\mathbf{y}} &= \nabla\mathbf{F}(\mathbf{x}_0)^T \cdot \mathbf{y} + \mathcal{O}(||\mathbf{y}||^2), \\ &\approx \mathbf{A}(\mathbf{x}_0, t) \cdot \mathbf{y},\end{aligned} \tag{2.20}$$

where $\mathbf{A} = \nabla\mathbf{F}(\mathbf{x}_0)^T$ is the Jacobian matrix and repeats itself with period T. The linear equation of Eq. (2.20) has n independent solution $\mathbf{y}_1, \mathbf{y}_2 ... \mathbf{y}_n$, known as the fundamental set of solutions. The fundamental set of solutions can be expressed compactly using the fundamental solution matrix $\mathbf{Y}$ such that each column entry is $\mathbf{y}_i$, *i.e.*,

$$\mathbf{Y} = [\mathbf{y}_1 \quad \mathbf{y}_2 \quad \mathbf{y}_3 \quad ... \quad \mathbf{y}_n], \tag{2.21}$$

where $\mathbf{Y}$ obeys,

$$\dot{\mathbf{Y}} = \mathbf{A}(\mathbf{x}_0, t) \cdot \mathbf{Y}. \tag{2.22}$$

Rescaling t to $\tau = t + T$, Eq. (2.22) becomes,

$$\begin{aligned}\frac{d\mathbf{Y}}{d\tau} &= \mathbf{A}(\mathbf{x}_0, \tau - T) \cdot \mathbf{Y}, \\ &= \mathbf{A}(\mathbf{x}_0, \tau) \cdot \mathbf{Y},\end{aligned} \tag{2.23}$$

using the property that $\mathbf{A}(\mathbf{x}_0, \tau - T) = \mathbf{A}(\mathbf{x}_0, \tau)$. Hence, Eqs. (2.23) infers that $\mathbf{Y}(\tau) = [\mathbf{y}_1(\tau) \quad \mathbf{y}_2(\tau) \quad \mathbf{y}_3(\tau) \quad ... \quad \mathbf{y}_n(\tau)]$ also comprises of fundamental set of solutions. However, since Eqs. (2.20) can have a maximum of n independent set of solutions, $\mathbf{Y}(\tau)$ can be expressed as a superposition or linear combination of $\mathbf{y}_i$s in Eq. (2.21). Therefore, $\mathbf{Y}(t + T)$ can be expressed as,

$$\mathbf{Y}(t + T) = \mathbf{Y}(t) \cdot \mathbf{\Phi}, \tag{2.24}$$

where $\mathbf{\Phi} \in \mathbb{R}^{n \times n}$ is a matrix. Note that $\mathbf{\Phi}$ is not unique and depends on initial $\mathbf{Y}(t)$. If initially at $t = 0$, $\mathbf{Y}(0) = \mathbb{I}_{n \times n}$, an identity matrix, then Eq. (2.24) reduces to,

$$\mathbf{Y}(T) = \mathbf{\Phi}, \tag{2.25}$$

where $\mathbf{\Phi}$ is known as the monodromy matrix. The monodromy matrix can be interpreted as a map which takes a state $\mathbf{x}(t)$ to $\mathbf{x}(t + T)$. If $\mathbf{x}(t)$ lies on a Poincaré section, then the monodromy matrix is the Poincaré map if the state returns to the Poincaré section after time T. More importantly, the eigenvalues of the monodromy matrix can determine the stability of the periodic solution $\mathbf{x}_0$. To illustrate this, consider the transformation $\tilde{\mathbf{Y}} = \mathbf{Y} \cdot \mathbf{P}$, where $\mathbf{P} \in \mathbb{R}^{n \times n}$ is an invertable matrix with each column entry as the eigenvectors of $\mathbf{\Phi}$. Rewriting Eq. (2.24) in terms of

$\tilde{\mathbf{Y}}$ and multiplying by $\mathbf{P}$ from the left hand side gives,

$$\begin{aligned}\tilde{\mathbf{Y}}(t+T) &= \tilde{\mathbf{Y}}(t)\cdot\mathbf{P}^{-1}\cdot\mathbf{\Phi}\cdot\mathbf{P} \\ &= \tilde{\mathbf{Y}}(t)\cdot\mathbf{J},\end{aligned} \tag{2.26}$$

where $\mathbf{J} = \mathbf{P}^{-1}\cdot\mathbf{\Phi}\cdot\mathbf{P}$ is a diagonal matrix obtained using properties of a similarity transformation. If $\mathbf{p}_i$ are the eigenvectors of $\mathbf{\Phi}$ with eigenvalues ρ_i such that $\mathbf{\Phi}\cdot\mathbf{p}_i = \rho_i\mathbf{p}_i$, then,

$$\mathbf{J} = \begin{pmatrix} \rho_1 & 0 & 0 & 0 \\ 0 & \rho_2 & 0 & 0 \\ \vdots & 0 & \ddots & \vdots \\ 0 & 0 & \dots & \rho_n \end{pmatrix}. \tag{2.27}$$

The eigenvalues ρ_i are known as Floquet multipliers and provides insights regarding the orbital convergence or divergence of perturbations in the local neighborhood of $\mathbf{x}_0$. Since Eq. (2.26) in the component form is $\tilde{\mathbf{y}}_i(t+T) = \rho_i\tilde{\mathbf{y}}_i(t)$, after N periods, the perturbed state becomes $\tilde{\mathbf{y}}_i(t+NT) = \rho_i^N\tilde{\mathbf{y}}_i(t)$. Therefore, in the limit of $N\to\infty$,

$$||\tilde{\mathbf{y}}_i(t+NT)|| = \begin{cases} 0, & \text{if} \quad ||\rho_i|| < 1, \\ \infty, & \text{if} \quad ||\rho_i|| > 1. \end{cases} \tag{2.28}$$

Thus if one of the Floquet multipliers have a norm greater than unity, perturbations $\mathbf{y}$ will grow away from the local neighborhood of $\mathbf{x}_0$. This implies that the orbit $\mathbf{x}_0$ is unstable. Fig. 2.7 illustrates the evolution of a periodic orbit $\mathbf{x}_0(0)$ and a slightly perturbed orbit $\mathbf{x}_0(0)+\mathbf{y}(0)$ after one time period T. At $\mathbf{x}_0$, the directions $\hat{\epsilon}_1$, $\hat{\epsilon}_2$ and $\hat{\epsilon}_3$ correspond to the directions of $\tilde{y}_1$, $\tilde{y}_2$ and $\tilde{y}_3$ with eigenvalues ρ_1, ρ_2 and ρ_3. The Floquet multipliers denote the orbital divergence or convergence (local stretching or shrinking) of a perturbed orbit $\mathbf{x}(T)+\mathbf{y}(T)$ along the directions $\hat{\epsilon}_i$. The stability of orbits depends on Eq. (2.28).

Further, an important observation can be made for autonomous dynamical systems. Differentiating Eq. (2.18) with respect to time gives at $\mathbf{x}_0$,

$$\ddot{\mathbf{x}} = \mathbf{A}(\mathbf{x}_0, t)\cdot\dot{\mathbf{x}}. \tag{2.29}$$

Hence, Eq. (2.29) satisfies Eq. (2.20), indicating that $\dot{\mathbf{x}}$ is also a solution of Eq. (2.22). Therefore, $\mathbf{x}_0$ can be expressed as a linear combination of $\mathbf{y}_i$s as,

$$\dot{\mathbf{x}}_0 = \mathbf{Y}(t)\cdot\alpha, \tag{2.30}$$

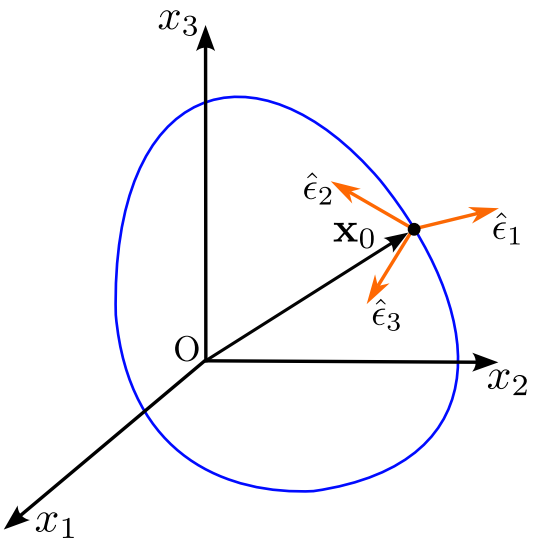

Figure 2.7: Schematic of a periodic orbit $\mathbf{x}(t) = [x_1, x_2, x_3] \in \mathbb{R}^3$ in phase-space illustrating that Floquet multipliers determine the orbital divergence, in the local neighborhood, of a periodic solution $\mathbf{x}_0$ along directions $\hat{\epsilon}_1$, $\hat{\epsilon}_2$ and $\hat{\epsilon}_3$.

where α is a vector. Due to periodicity of $\dot{\mathbf{x}}_0(t+T) = \dot{\mathbf{x}}_0(t)$,

$$\begin{aligned} \dot{\mathbf{x}}_0(t+T) &= \mathbf{Y}(t+T) \cdot \alpha, \\ \dot{\mathbf{x}}_0(t) &= \mathbf{Y}(t+T) \cdot \alpha, \\ \mathbf{Y}(t) \cdot \alpha &= \mathbf{Y}(t+T) \cdot \alpha. \end{aligned} \tag{2.31}$$

Substituting $t = 0$ above, using the property $\mathbf{Y}(0) = \mathbb{I}_{n\times n}$, Eq. (2.31) becomes,

$$\begin{aligned} \mathbf{Y}(T) \cdot \alpha &= \alpha \\ \mathbf{\Phi} \cdot \alpha &= \alpha. \end{aligned} \tag{2.32}$$

Therefore, for autonomous systems, one of the eigenvalues of the Monodromy matrix will always be unity. Geometrically, this implies that perturbations along the direction of the solution *i.e.*, $\dot{\mathbf{x}}_0$ or $\mathbf{x}_0$, accompanied by Floquet multiplier equal to 1, will remain the same, *i.e.*, no stretching or shrinking along $\mathbf{x}_0$. This is also valid for PWS systems and is a litmus test to ensure correct Floquet multipliers are evaluated. Chapter 4 verifies this result by evaluating the monodromy matrix for the respective autonomous PWS dynamical system investigated. However, the Floquet theory described above is only valid for periodic systems. The following section illustrates methods to perform a stability analysis of aperiodic dynamical systems by evaluating Lyapunov exponents.

2.2.2 Lyapunov exponents

Lyapunov exponents measure the exponential divergence or convergence of a perturbed orbit initiated from the local neighborhood of a limit cycle. As previously discussed, consider two nearby trajectories $\mathbf{x}$ and $\mathbf{x}+\mathbf{y}$ of an arbitrary dynamical system of size n governed by Eqs. (2.18) and Eqs. (2.20). The stability of the solution $\mathbf{x}_0$ depends on the behavior of the perturbed orbit $\mathbf{x}+\mathbf{y}$, and hence on the perturbation $\mathbf{y}$. The perturbation $\mathbf{y}$ evolves according to the Jacobian of $\mathbf{F}(\mathbf{x})$ evaluated at $\mathbf{x}_0$. Therefore, using linear algebra, the solution of $\mathbf{y}$ is,

$$\begin{aligned}\mathbf{y}(t) &= c_1\mathbf{u}_1 e^{\lambda_1 t} + c_2\mathbf{u}_2 e^{\lambda_2 t} + \ldots + c_n\mathbf{u}_n e^{\lambda_n t}, \\ &= \sum_{i=1}^{n} c_i\mathbf{u}_i e^{\lambda_i t},\end{aligned} \tag{2.33}$$

where $\mathbf{u}_i$ are the eigenvectors of the Jacobian $\mathbf{A}(\mathbf{x}_0)$ with eigenvalues λ_i. Since $\mathbf{y}$ is a linear combination of the eigenvectors $\mathbf{u}_i$, its eigenvalues determine the exponential rate at which the perturbation gets stretched or shrunk along $\mathbf{u}_i$. This is illustrated in Fig. 2.8. Consider the phase-portrait of two nearby trajectories $\mathbf{x}$ and $\mathbf{x}+\mathbf{y}$. Let the eigenvectors of $\mathbf{A}(\mathbf{x}_0)$ be $\mathbf{u}_1$ and $\mathbf{u}_2$ with eigenvalues $\lambda_1 < 0$ and $\lambda_2 > 0$. Since $\lambda_1 < 0$ and $\lambda_2 > 0$, the resultant vector rotates in time and aligns towards $\mathbf{u}_2$. This is because the components of $\mathbf{y}$ along $\mathbf{u}_1$ shrinks while that along $\mathbf{u}_2$ gets stretched. As a result, the perturbation $\mathbf{y}$ grows along $\mathbf{u}_1$ exponentially, which implies $\mathbf{x}_0$ is unstable.

Next, to systematically measure the exponential divergence or convergence along $\mathbf{u}_i$s, consider an orthogonal set of perturbations ϵ_i to the state $\mathbf{x}_0$ with an initial norm of $r_0 << 1$. This is illustrated using a 2D phase portrait shown in Fig. 2.9(a). After a short time τ, perturbations lying on the sphere of diameter r_0 evolve according to Eq. (2.20) and becomes a wiggly shape similar to a distorted circular amoeba. At this instant, the perturbations $\epsilon_1(\tau)$ and $\epsilon_2(\tau)$ lie on the wiggly shape as shown in Fig. 2.9(b). In the next step, the distorted shape is approximated by an ellipse on which the perturbations $\epsilon_1(\tau)$ and $\epsilon_2(\tau)$ lie as shown in Fig. 2.9(c). Next, the existing ellipse is approximated by a new ellipse with the major axis aligned along ϵ_1. This implies that the old ellipse (shown as blue dashed ellipse) approximating the distorted shape in Fig. 2.9(b) has been slightly rotated to accommodate ϵ_1 as shown in Fig. 2.9(c) (shown as black dashed ellipse). Now the main idea is to measure the growth rate along of ϵ_1 along $\mathbf{w}_1 = \epsilon_1(\tau)$ and ϵ_2 along $\mathbf{w}_2$, the projection of $\epsilon_2(\tau)$ on the perpendicular direction of $\epsilon_1(\tau)$, see Fig. 2.9(d). This new vector $\mathbf{w}_2$ perpendicular to $\epsilon_1(\tau)$ or $\mathbf{w}_1$ contains the minor axis and therefore, the growth rates approximate how perturbations lying initially on an orthogonal sphere of hyper-radius r_0 becomes a hyper-ellipsoid. The new directions $\mathbf{w}_1$, $\mathbf{w}_2$...$\mathbf{w}_n$ for $\mathbf{y} \in \mathbb{R}^n$, is

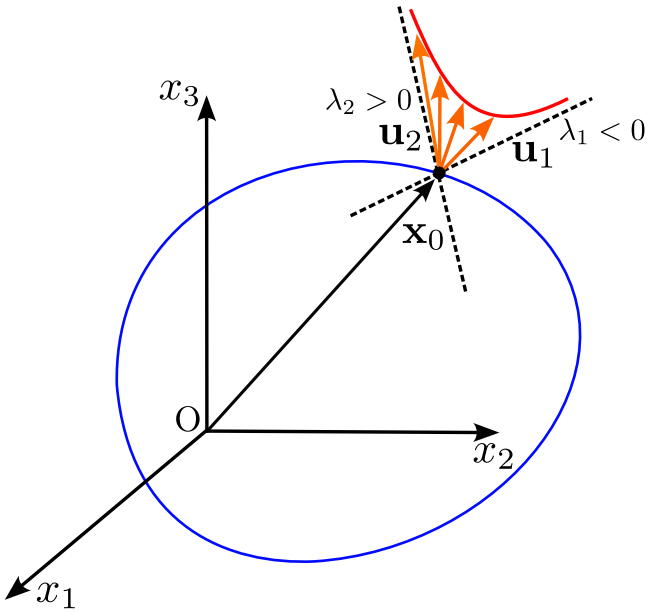

Figure 2.8: Schematic of a periodic orbit $\mathbf{x}(t) = [x_1, x_2, x_3] \in \mathbb{R}^3$ in phase-space illustrating exponential divergence of perturbations, in the local neighborhood, of a periodic solution $\mathbf{x}_0$. Since, eigenvalues of $\mathbf{u}_1$ and $\mathbf{u}_2$ are $\lambda_1 < 0$ and $\lambda_2 > 0$, perturbations shrinks along $\mathbf{u}_1$ and gets stretched along $\mathbf{u}_2$, eventually diverging away from unstable orbit $\mathbf{x}_0$.

given by,

$$\mathbf{w}_1 = \mathbf{e}_1 \tag{2.34}$$

$$\mathbf{w}_2 = \mathbf{e}_2 - \left(\epsilon_2(\tau) \cdot \frac{\epsilon_1(\tau)}{||\epsilon_1||}\right)\frac{\epsilon_1(\tau)}{||\epsilon_1||}$$

$$\mathbf{w}_3 = \mathbf{e}_3 - \left(\epsilon_3(\tau) \cdot \frac{\epsilon_1(\tau)}{||\epsilon_1||}\right)\frac{\epsilon_1(\tau)}{||\epsilon_1||} - \left(\epsilon_3(\tau) \cdot \frac{\epsilon_2(\tau)}{||\epsilon_2||}\right)\frac{\epsilon_2(\tau)}{||\epsilon_2||}$$

$$\vdots$$

$$\mathbf{w}_n = \mathbf{e}_n - \Sigma_{i=1}^{n-1}\left(\epsilon_n(\tau) \cdot \frac{\epsilon_i(\tau)}{||\epsilon_i||}\right)\frac{\epsilon_i(\tau)}{||\epsilon_i||}$$

(2.35)

and the growth rate are the norms of $\mathbf{w}_i$. Once the growth rates are recorded, the new directions $\mathbf{w}_i$ are renormalized to ϵ_i with norm r_0 and the process repeats within every time interval of τ.

The vectors $\mathbf{w}_i$ can be easily obtained using a QR decomposition in any algebraic software like Matlab or Mathematica. The growth rates $r_i^j = ||\mathbf{w}_i||$ at the j^{th} instant after $j\tau$s gives a measure of the evolution of perturbed ellipses in the local neighborhood of $\mathbf{x}_0$. The exponential growth rate of perturbations along $\mathbf{w}_i$s can be approximated as $r_i^j e^{\lambda_i^j \tau}$ where λ_i^j is defined as the Lyapunov exponent along $\mathbf{w}_i$

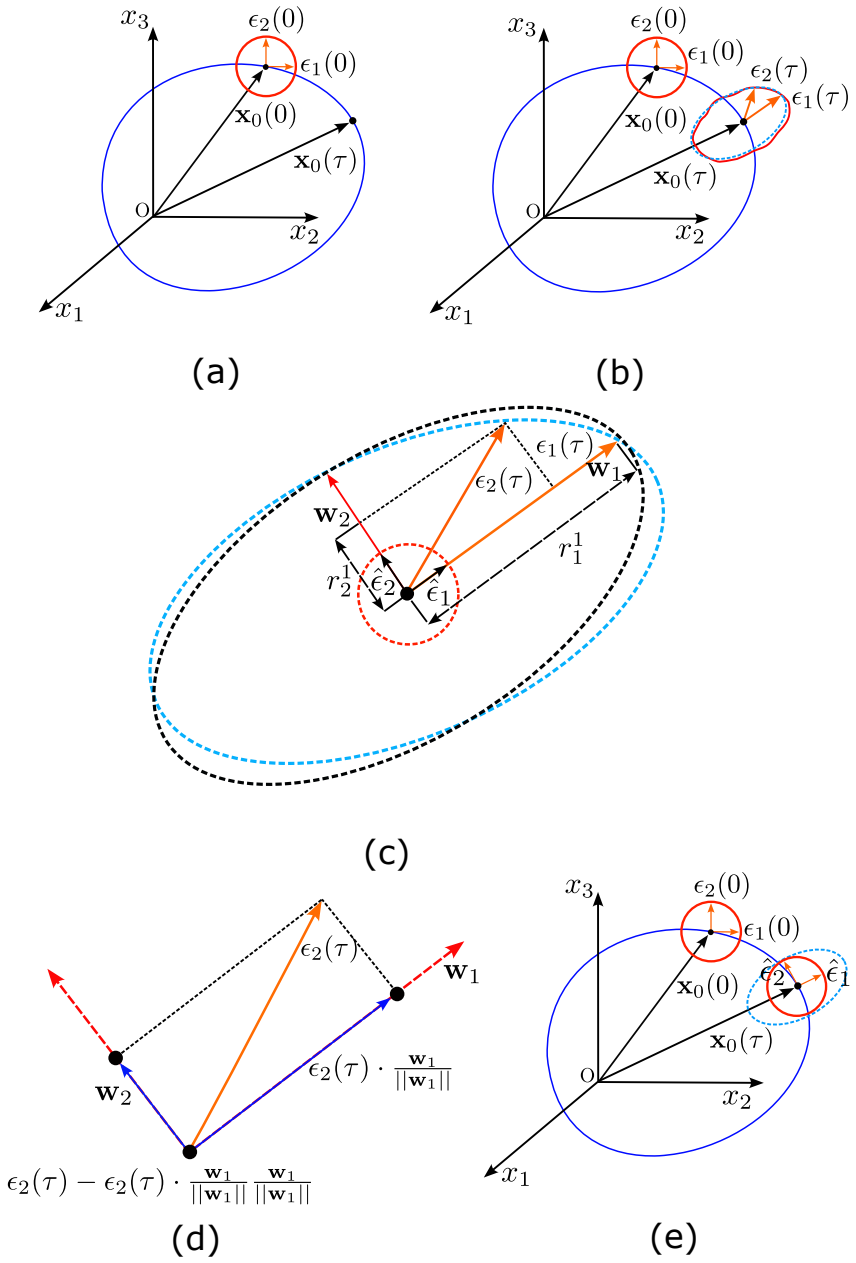

Figure 2.9: Schematic of an orbit $\mathbf{x}(t) = [x_1, x_2, x_3] \in \mathbb{R}^3$ showing (a) Two orthogonal perturbations ϵ_1 and ϵ_2 with norm r_0 initiated local to $\mathbf{x}_0$, (b) Perturbations $\epsilon_1(0)$ and $\epsilon_2(0)$ initially lying on the circle evolve to $\epsilon_1(\tau)$ and $\epsilon_2(\tau)$. Perturbations on the initial circle gets deformed and is approximated by an ellipse shown as blue dashed line.(c) The approximated ellipse containing $\epsilon_1(\tau)$ and $\epsilon_2(\tau)$ is replaced by a new ellipse, shown as black dashed line, such that the major axis aligns with $\epsilon_1(\tau)$. Projections of $\epsilon_1(\tau)$ along $\mathbf{w}_1$ and $\epsilon_2(\tau)$ along the minor axis $\mathbf{w}_2$ is recorded to evaluate Lyapunov exponents along $\mathbf{w}_1$ and $\mathbf{w}_2$. (d) Schematic showing how projection of $\epsilon_2(\tau)$ is measured along $\mathbf{w}_2$ using the QR decomposition. (e) The directions $\mathbf{w}_1$ and $\mathbf{w}_2$ are the new orthogonal perturbations $\hat{\epsilon}_1$ and $\hat{\epsilon}_2$ with norm r_0 and the process is repeated.

after j cycles of τ. From the recorded values of r_i^j for N cycles of τ, the average

Lyapunov exponent along $\mathbf{w}_i$ is defined as,

$$\lambda_i = \frac{1}{\tau N} \sum_{j=1}^{N} \ln \frac{r_i^j}{r_0}. \tag{2.36}$$

Note that the direction of ϵ_1 has remained the same but only renormalized. After a large number of renormalizations, $\mathbf{e}_1$ aligns itself along the eigenvector $\mathbf{u}_k$ of $\mathbf{A}(\mathbf{x}_0)$ with the largest eigenvalue. Therefore, λ_1, also known as the largest Lyapunov exponent determines if $\mathbf{x}_0$ is stable or unstable depending on whether $\lambda_1 < 0$ or $\lambda_1 > 0$. The remaining values of $\lambda_{i \neq k}$ measure the exponential growth rates along orthogonal directions of $\mathbf{u}_k$. All λ_is collectively form the Lyapunov spectrum and determine if perturbations to an orbit $\mathbf{x}_0$ grow away or towards it.

The tools for stability analysis discussed here holds for systems governed by vector fields which are smooth functions of its arguments. The following chapters extend these concepts to the domain of PWS hybrid and Filippov systems by incorporating a higher-order transverse discontinuity mapping.

Chapter 3

Higher-order transverse discontinuity mapping of hybrid dynamical systems

This chapter demonstrates the hazards of locally linearising the discontinuity mappings in a hybrid PWS dynamical system near discontinuities and how it leads to incorrect estimates of impact occurrences for transversal interactions with the discontinuity boundary. A higher-order formulation of the TDM overcomes this shortcoming, allowing for correct estimation of impact occurrences, state transitions, and, consequently, its trajectories. A generalized closed form expression of higher-order TDMs and the respective higher-order state transition matrices during instantaneous reversals governed by an impact law is derived. The difference in flight times of two closely initiated trajectories in state space to the impacting surface is estimated up to $\mathcal{O}(2)$. The higher-order corrections proposed are superior in estimating the dynamic state of the impacting system compared to widely accepted first-order approaches [37, 14]. The approach also avoids incorrect prediction of impact, which can happen when using first-order Saltation matrices. In this regard, two algorithms are proposed to estimate the Lyapunov spectrum and Floquet multipliers for piecewise-smooth hybrid systems of the impacting class. Stability analyses are carried out using the proposed higher-order approach for representative cases of a hard impact oscillator and a pair impact oscillator, respectively. The system's stability is investigated via Floquet multipliers and the Lyapunov spectrum. These agree with the corresponding bifurcation diagrams of the systems under consideration.

3.1 Introduction

Floquet theory [82] for stability analysis of piecewise-smooth dynamical systems requires calculations of state transition matrices at instants of impact. This is done

using linearized saltation matrices, which are obtained by retaining only the first-order terms in the Taylor expansion of the state at the instant of impact. Such an analysis is helpful to quantify stability in the infinitesimally close neighborhood quite well. However, there are instances where the well-known saltation matrix incorrectly predicts the occurrence of an impact, affecting the state of stability [122]. This can occur when the duration between two consecutive impacts is significant in comparison to the time period of excitation or where the magnitude of the perturbed trajectory in the local neighbourhood is slightly increased (but is still in $\sim \mathcal{O}(10^{-3})$). As the separation between nearby trajectories grows, the errors in the linearized discontinuity mapping of the perturbed saltating trajectory can be significant, rendering the stability analysis inadequate. This chapter highlights this issue and then resolves it by proposing a generalized framework with higher order terms. A first order variational equation governing the flow in the smooth part of the sub-space is usually sufficient. However, in the case of non-smooth mapping, a linearized approximation at the regions where there are abrupt changes in the vector field, this first-order approximation fails by being unable to correctly identify the instances of impacts. The limitation and erroneous use of this widely accepted first-order linearization near impacts can only be resolved if a generalized framework can be established using higher order terms, reconciling with a variational approach in the smooth regions of dynamics, which will lead to the correct mapping of impact states to the time instants of when they occur. These limitations have been overlooked mainly because the existing literature focuses strongly on discontinuity mappings near grazing. To establish this generalized framework, some of the above-mentioned terms along with some contextual remarks is discussed next.

Piecewise-smooth (PWS) systems refer to continuous or discrete time dynamical systems where the state space is compartmentalized into subspaces by instantaneous changes in dynamics. These abrupt transitions occur in time scales significantly less than the time scales of the dynamics of the system and are thus represented by discontinuous boundaries. The dynamics of the vector field within each subspace obey different functional forms [14, 10]. A sub-class of such systems is hybrid dynamical systems, where the transitions at the barriers are governed by re-initialization rules of state [127]. Such systems often show rich phenomenological behaviour which is atypical of its smooth counterpart [30, 22, 54, 95, 108]. Rich dynamic behaviour of non-smooth systems includes the occurrence of discontinuity induced bifurcations (DIBs), that occur due to the interaction of the trajectories with the boundary. This interaction with the boundary is known as impact and leads to occurrences like grazing [7], sticking-sliding [31], chattering [17] and period-adding cascades [97, 89, 90, 99, 106, 37, 102]. Parametric investigations of DIBs have revealed unconventional routes to chaos, like via grazing [85, 14].

Stability analyses of PWS systems yield insights into the implications of the

occurrence of impacts on the system dynamics. Measures like Lyapunov exponents (LE) [92, 96, 11, 13], entropy measures [12, 123] and Floquet multipliers [33, 82] qualitatively predict the asymptotic stability of smooth dynamical systems. However, when the dynamics is piecewise-smooth, these stability analyses need to account for the switch in dynamics at instants of impacts. Then the fundamental solution matrix describing the attractor comprises of multiplication of exponential matrices corresponding to the evolution through the smooth part of the subsystems and saltation matrices corresponding to the transitions through switching conditions, multiplied in the sequence of their occurrence. This was addressed by Coleman *et al.* [24] and later taken up by Leine *et al.* by obtaining invariants of the fundamental solution matrix (FSM) for Hill's equation [67]. Serveta *et al.* studied the stability of impact oscillators by implementing contact models between an oscillator and an interacting movable barrier. Similar methods, especially applicable for stability analysis of PWS hybrid systems, exist in literature [65, 79].

Numerical approaches to obtain the LE spectrum by evaluating Jacobians from the functional form of the governing equations or by reconstruction of state space from time histories exist for smooth systems [101, 136]. However, this is not straightforward for a non-smooth system as the Jacobian matrix of such systems is ill conditioned, resulting in large and unacceptable errors in computational estimations of LEs. De Souza *et al.* [27] proposed an algorithm to compute the LE spectrum for impacting systems by analytically reducing the state equations to a transcendental map whose eigenvalues represent the LE spectrum. Jin *et al.* [55] obtained the LE spectrum for an impacting system by studying the dynamics on a suitable Poincaré section, where the Jacobian matrix near impact was evaluated. The work by Stefanski [117] proposed computing the state difference vector between the dynamics of a pair of coupled PWS systems and established its synchronization state to compute the largest Lyapunov exponent. Stefanski [119] subsequently estimated the dominant LE of two closely spaced PWS systems when one of the systems is perturbed. This method is suitable for systems with both discontinuities as well as time delays. Stefanski also [118] presented a method where the LE spectrum is computed for non-smooth systems by circumventing discontinuities by considering the value of the function at its previous time-step and continuing integration of the perturbed trajectory until it encounters a discontinuity. Balcerzak *et al.* [4] computed LEs applicable to continuous-time dynamical systems as well as discrete maps by estimating the Jacobi matrix at the instant of impact. A method based on the scalar product of a system's perturbation and its derivative also exists [25]. Müller ([80]) evaluated the LE spectrum for a generalised dynamical system with discontinuities using a linearized approximation of the transitions at the instant of discontinuities. Li *et al.* [70] analytically derived the LE of a non-smooth dynamical system by evaluating the transfer matrix before, after and during the instant of a

impact at a discontinuous boundary.

Existing literature indicates that investigations of PWS systems fundamentally rely on their linearization at the instants of impact. This necessitates the need for investigating dynamics at impact with higher-order corrections. Yin *et al.* [137] studied bifurcations of an impact oscillator at near-grazing dynamics using higher order zero-time discontinuity mapping (ZDM). Trajectories undergoing transverse interactions are modeled here via a transverse discontinuity mapping (TDM), which is a more generalized case and has been overlooked despite its potential to address the limitations of local linearization. Here, the trajectories undergo impact with non-zero velocities and in such cases, two closely spaced trajectories might exponentially diverge on interaction with a barrier [18]. At some parameter value, the time difference between two consecutive impacts might be large. As a consequence of such an impact, the separation between two closely spaced trajectories will grow in time. This effect becomes more pronounced when the underlying dynamics for the chosen parameter is chaotic. The assumption of linearization in the neighbourhood of an impact will fail here, especially when the separation becomes larger than the radius of convergence of the respective linearization [1]. Additionally, there exists a time difference between the instant of impact for two nearby perturbed trajectories in the state space. In general, TDM defined by the saltation matrix at the instant of impact relies on a linearized derivation of this time difference [14]. This linearization of the TDM, even for most simplistic cases like the impact oscillator, is not a function of crucial system parameters like damping and external forcing frequency, which results in incorrect prediction of the mapped state following an impact. Note that alternate methods of obtaining the time taken for an impact oscillator to reach the discontinuity barrier exist due to several works of Luo et al. [75, 74, 72, 73]. Luo et al. [75] derived the exact analytical solution of an impact oscillator executing one and two paired impacts, which relates the time taken for orbits to reach the discontinuity barrier as functions of the position and velocity of the previous impact as the new initial condition. This method by Luo et al. [75], which can be used to obtain the exact analytical solution for the most simplistic case of an impact oscillator, becomes cumbersome for complicated piecewise-smooth systems with several degrees of freedom. In contrast, this chapter aims to obtain the time difference between impacts for an arbitrary and generalized PWS system where the exact analytical solution is unknown; this approach can be implemented to cater to a wide range of hybrid PWS systems executing multiple impacts.

In this chapter, the time difference between perturbed trajectories at the instant of impact with higher-order corrections has been derived. The proposed corrections to the time difference takes into account the functional form of the driving force and system parameters for a PWS system with transversal impact. This generalised approach therefore decides the order in which the saltation matrix is multiplied while

calculating the global state transition matrix for any chosen orbit. This cannot be done with the current linearized approach. The higher-order corrections derived in this chapter thus correctly identifies the occurrence of an impact by considering the initial separation between two trajectories, where a linearized approach concludes no impact has taken place. This has a direct consequence on the prediction of stability of the dynamical system and its behavior. Stability analysis of any periodic orbit relies on the Monodromy matrix and its eigenvalues. The possibility of an impact, as predicted by the higher-order TDM defines the order in which the saltation matrix is applied. The Monodromy matrix, and hence its eigenvalues can drastically change by the inclusion of a state transition matrix at the instant of impact. Therefore, a totally different conclusion regarding the stability of an orbit can be interpreted if a first order linearization is used as compared to the proposed approach.

A TDM governed by a linearized saltation matrix defines a map or a reset condition for trajectories under transverse impacts. Typically, PWS systems undergo several impacts before attaining a steady state. Therefore, errors in the linearized TDM will accumulate every time a mapping occurs, ultimately leading to an incorrect prediction of the steady state. This is also a motivation of the proposed method using a TDM of the perturbed trajectory with higher-order terms. The growth or decay in the evolution of disturbances in initially perturbed trajectories is quantified using the LE spectra. The proposed methodology to evaluate the LE spectra does not require prior knowledge of the analytical solution at the instant of impact, as opposed to the case for transcendental maps. The compatibility of numerically obtained higher-order STM with the variational approach is essential to obtain the monodromy matrix for a given orbit correctly. A computational approach to obtain the saltation matrix with higher-order corrections is presented to facilitate this. Floquet analysis has been carried out to demonstrate the efficacy of the method. The results obtained are compared with the corresponding bifurcation diagram for verification. The approach presented in this chapter can also be used as a benchmark tool to study long-time dynamics of the steady state for arbitrary PWS systems where the exact analytical solution near the discontinuity boundary is unknown. The derivations presented here apply to autonomous and non-autonomous hybrid systems with higher dimensions and multiple barriers. Applications of higher-order correction terms to transverse discontinuity mappings (saltation matrices) can be applied to diverse fields. For example, in robotics, control theory is implemented for stability analysis of systems like legged robots where robotic arms are subjected to impacts with the environment. The quadratic form of saltation matrices is implemented in state prediction algorithms like Kalman filters and Linear Quadratic Regulators (LQR) [60]. Kong et al. [59] showed improvements in the prediction of states and their covariance while implementing a Kalman filter using the quadratic form of the saltation matrix in comparison to the linearized form of the saltation

matrix comprising only the Jacobian of the reset map or Jacobian of the Reset Kalman Filter (JRKF). Kong et al. [59] proposed an approach that uses the saltation matrix to construct the Salted Kalman Filter (SKF), naturally extending the concept of Kalman filters to hybrid dynamical systems. Additional correction terms to the transverse discontinuity mapping presented in this chapter can be directly implemented in SKF for improved predictions of covariance post-impact.

The chapter is structured as follows. In Section 3.2, a discrete mapping of state transitions at the instant of impact for a hybrid system is derived. This mapping takes into account the second order terms in expansions. Section 3.3 introduces two hybrid oscillators with 1 and 2 discontinuity boundaries respectively and presents their stability analysis when viscous damping is varied. Results obtained from $\mathcal{O}(1)$ and $\mathcal{O}(2)$ approximations are compared and discussed. Section 3.4 extends the implementation of the derived TDM shown in Sec. 3.2 to numerically obtain the Lyapunov spectrum. Section 3.5 describes the numerical evaluation of higher-order saltation matrices using the proposed TDM, followed by an eigenvalue analysis of the monodromy matrix obtained therein. The stability of these hybrid systems under consideration is analyzed by obtaining the corresponding Floquet multipliers. The results are corroborated with respective bifurcation diagrams. Section 3.6 summarises the principal outcomes of this study.

3.2 Mathematical formulation

The generalized form of a dynamical system represented by states $\mathbf{x}(t)$, where $\mathbf{x} \in \mathbb{R}^n$, and its corresponding variational form can be written in the state space formulation as Eq. (3.1)

$$\begin{aligned} \frac{d\mathbf{x}}{dt} &= \mathbf{F}(\mathbf{x}), \\ \frac{d\mathbf{y}}{dt} &\approx \nabla\mathbf{F}(\mathbf{x})^T \cdot \mathbf{y} + \mathcal{O}(||\mathbf{y}||^2) \end{aligned} \tag{3.1}$$

where $\mathbf{y}$ is a perturbation to the system $\mathbf{x}$ post transients and $\nabla\mathbf{F}(\mathbf{x})^T$ is the Jacobian matrix. The variational form that governs the dynamics of nearby perturbed trajectories is generally derived with a linearized approximation. For a non-autonomous system with explicit time dependence, *i.e.*, $\mathbf{F}(\mathbf{x}, t)$, an additional phase variable can be defined, say s, to the state vector $\mathbf{x}$ such that $\dot{s} = 1$. Now, the non-autonomous system can be represented using Eq. (3.1) where the new state $\mathbf{x}'$ is $n + 1$ dimensional. Therefore, the following derivations are applicable to both autonomous and non-autonomous systems. However, for PWS systems, nearby perturbed trajectories reach the discontinuity boundary at different instants of time (see Fig. 3.1). The difference in the flight times can lead to estimation of erroneous trajectories

after an implementation of a linearized TDM at the instant of impact. This carries significance when the separation between trajectories is greater than the radius of convergence of $\mathbf{F}(\mathbf{x})$. To obtain the evolution of perturbed trajectories near impact, taking higher-order terms into consideration is thus necessary.

The evolution of two closely spaced trajectories is depicted in the simplistic case of a 2-dimensional state space (Fig. 3.1). Two closely spaced points $\mathbf{x}_p$ and $\hat{\mathbf{x}}$ are initiated at the Poincaré section Σ_1 where they start evolving from the same instant. Here, $\hat{\mathbf{x}}$ represents a perturbed trajectory from $\mathbf{x}_p$, *i.e.* $\hat{\mathbf{x}} = \mathbf{x}_p + \mathbf{y}$, where $\mathbf{y}$ is an infinitesimal perturbation to the original system at the beginning of its evolution, denoted by Eq. (3.1). After evolving in time, at $t = t_0$, the orbit $\mathbf{x}_p$ impacts the hard surface, Σ_2 at $\mathbf{x}_i$. At this instant, when the path described by $\mathbf{x}$ impacts the surface $\Sigma_2 = \{\mathbf{x}_i \in \mathbb{R}^n : H(\mathbf{x}_i) = 0\}$, the trajectory gets mapped to $\mathbf{R}(\mathbf{x}_i)$. Here, $\mathbf{R}(\mathbf{x})$ represents a restitutive law governing the state of the trajectory at impact whereas $H(\mathbf{x}) = 0$ models the impacting condition. The reset map $\mathbf{R}(\mathbf{x})$ is a typical example of a non-smooth event that arises in systems exhibiting switchings. Applying the map $\mathbf{R}(\mathbf{x}_0)$ to the perturbed trajectory $\hat{\mathbf{x}}(t_0) = \mathbf{x}_0$ at the instant of impact t_0 will result in an incorrect prediction of state, as it does not lie on the impacting surface Σ_2 at that instant. Thus the difference in the flight times of the two paths $\mathbf{x}_i$ and $\mathbf{x}_0$ is to be taken into account. The corresponding expression for the flight time is described below. Using the flight time difference, a TDM is derived which maps the point $\mathbf{x}_0$ to $\mathbf{x}_4$. The readers are advised to note that $\mathbf{x}_4$ now lies in the forbidden region $H(\mathbf{x}) < 0$ but eventually evolves in time to reach the barrier at $H(\mathbf{x}_3) = 0$. Post impact, the perturbed trajectory when initiated at $\mathbf{x}_4$, would take the same flight time to arrive at $\mathbf{x}_3$ on Σ_2 as the perturbed trajectory at $\mathbf{x}_0$ would take to reach $\mathbf{x}_2$, followed by the mapping $\mathbf{R}(\mathbf{x}_2)$ on Σ_2 to reach $\mathbf{x}_3$. This ensures that local trajectories obey a zero time mapping to the barrier and the time difference is preserved. The mapping of the perturbed path $\mathbf{x}_0$ to $\mathbf{x}_4$ at the instant of impact of the actual trajectory is shown in Fig. 3.1. This discrete mapping accounts for the state transition at impact and is expressed in terms of a saltation matrix in the linearized form. The corresponding equation governing the saltation matrix incorporating higher-order terms is presented next. If t_0 represents the instant of impact of the actual trajectory, a Taylor expansion of $\mathbf{x}(t)$ about $t = t_0$ and $\mathbf{F}(\mathbf{x})$ about $\mathbf{x} = \mathbf{x}_0$ up to $\mathcal{O}(2)$ gives Eqs. (3.2 and 3.3)

$$\mathbf{x}(t) = \mathbf{x}(t_0) + \Delta t\ \mathbf{F}(\mathbf{x}_0) + \frac{1}{2}\Delta t^2\ \nabla\mathbf{F}(\mathbf{x}(t_0))^T \cdot \mathbf{F}(\mathbf{x}(t_0)) + \mathcal{O}(3) \tag{3.2}$$

$$\mathbf{F}(\mathbf{x}) = \mathbf{F}(\mathbf{x}_0) + \nabla\mathbf{F}(\mathbf{x}_0)^T \cdot \mathbf{\Delta x} + \frac{1}{2}\begin{bmatrix}\mathbf{\Delta x}^T \cdot H_1 \cdot \mathbf{\Delta x} \\ \mathbf{\Delta x}^T \cdot H_2 \cdot \mathbf{\Delta x}\end{bmatrix} + \mathcal{O}(3) \tag{3.3}$$

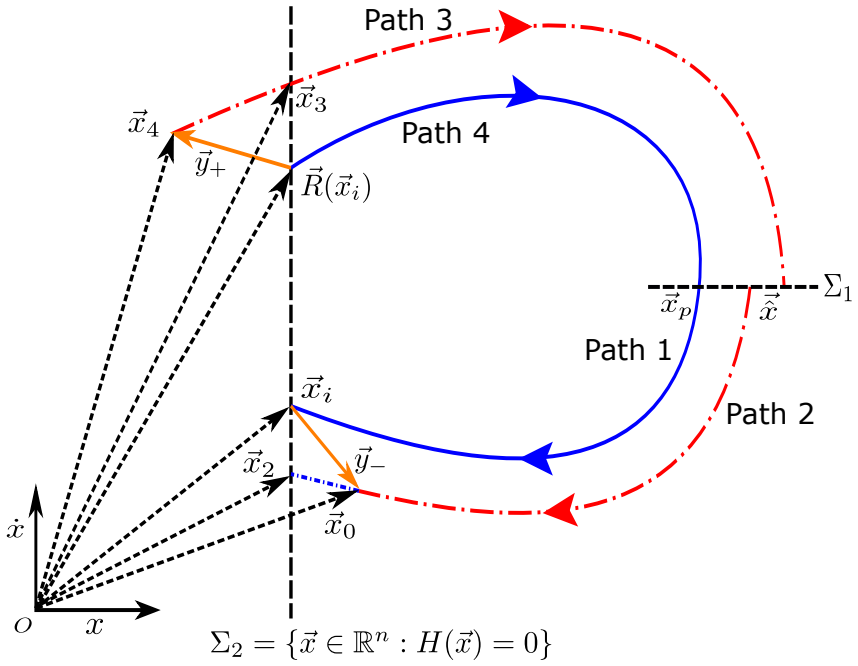

Figure 3.1: A schematic of phase portraits of two nearby trajectories exhibiting impact at Σ_2. The blue line shows the actual trajectory. The red dashed line denotes the perturbed trajectory. The horizontal black dashed line Σ_1 denotes the section from which both the trajectories are initiated and Σ_2 denotes the discontinuity boundary. The amber line denotes the perturbation vector.

Here, H_is denote the Hessian matrices of each component $f_i(\mathbf{x})$ of $\mathbf{F}(\mathbf{x})$ *i.e.*, H_i defined as the Jacobian of $\nabla f_i(\mathbf{x})$ or $\nabla(\nabla f_i(\mathbf{x}))^T$. Let δ be the time taken for the perturbed trajectory $\hat{\mathbf{x}}$ to reach impact surface Σ_2 from $\mathbf{x}(t_0) = \mathbf{x}_0$ to $\mathbf{x}(t_0+\delta) = \mathbf{x}_2$. Therefore, $\mathbf{x}_2$ is approximated by taking a Taylor expansion of $\hat{\mathbf{x}}$ along path 2 about $t = t_0$ (*i.e.*, $\mathbf{x}(t_0) = \mathbf{x}_0$) evaluated at $t = t_0 + \delta$ up to $\mathcal{O}(2)$ giving

$$\mathbf{x}_2 = \mathbf{x}_0 + \delta\ \mathbf{F}(\mathbf{x}_0) + \frac{1}{2}\delta^2\ \nabla\mathbf{F}(\mathbf{x}_0)^T \cdot \mathbf{F}(\mathbf{x}_0) + \mathcal{O}(3) \tag{3.4}$$

$\mathbf{F}(\mathbf{x}_0)$ in Eq. (3.4) is approximated by a Taylor expansion of $\mathbf{F}(\mathbf{x})$ along path 1 about $\mathbf{x}_i$ and evaluated at $\mathbf{x} = \mathbf{x}_0$. Retaining terms up to $\mathcal{O}(2)$, $\mathbf{x}_2$ becomes Eq. (3.5)

$$\mathbf{x}_2 = \mathbf{x}_0 + \delta\ [\mathbf{F}(\mathbf{x}_i) + \nabla\mathbf{F}(\mathbf{x}_i)^T \cdot \mathbf{y}_-] + \frac{1}{2}\delta^2\ \nabla\mathbf{F}(\mathbf{x}_i)^T \cdot \mathbf{F}(\mathbf{x}_i) + \mathcal{O}(3) \tag{3.5}$$

where $\mathbf{y}_-$ is the perturbed vector at the instant of impact (*i.e.* $\mathbf{x}_0 = \mathbf{x}_i + \mathbf{y}_-$). Then, the equation for the impacting surface $H(\mathbf{x})$ expanded about the state at impact $\mathbf{x}_i$ up to $\mathcal{O}(2)$ and evaluated at $\mathbf{x} = \mathbf{x}_2$ is given by Eq. (3.6).

$$\begin{aligned} H(\mathbf{x}_2) = \ & H(\mathbf{x}_i) + \nabla H(\mathbf{x}_i)^T \cdot (\mathbf{x}_2 - \mathbf{x}_i) \\ & + \frac{1}{2}(\mathbf{x}_2 - \mathbf{x}_i)^T \cdot \nabla(\nabla H)^T \cdot (\mathbf{x}_2 - \mathbf{x}_i) + \mathcal{O}(3) \end{aligned} \tag{3.6}$$

Using Eq. (3.5) in Eq. (3.6) and $H(\mathbf{x}_i) = H(\mathbf{x}_2) = 0$ (since $\mathbf{x}_i$ and $\mathbf{x}_2$ lie on the impacting surface Σ_2), the time difference in impact between two closely spaced trajectories, *i.e.* δ can be solved up to $\mathcal{O}(2)$. The result is a quadratic equation in δ given by Eq. (3.7).

$$\begin{aligned}\delta^2\Big(&\nabla H(\mathbf{x}_i)^T \cdot \nabla \mathbf{F}(\mathbf{x}_i)^T \cdot \mathbf{F}(\mathbf{x}) + \mathbf{F}(\mathbf{x}_i)^T \cdot \nabla(\nabla H(\mathbf{x}_i))^T \cdot \mathbf{F}(\mathbf{x}_i)\Big) \\ &+ \delta\Big(2\nabla H(\mathbf{x}_i)^T \cdot \mathbf{F}(\mathbf{x}_i) + 2\nabla H(\mathbf{x}_i)^T \cdot \nabla \mathbf{F}(\mathbf{x}_i)^T \cdot \mathbf{y} + \mathbf{y}^T \cdot \nabla(\nabla H(\mathbf{x}_i))^T \cdot \mathbf{F}(\mathbf{x}_i) \\ &+ \mathbf{F}(\mathbf{x}_i)^T \cdot \nabla(\nabla H(\mathbf{x}_i))^T \cdot \mathbf{y}\Big) + \mathbf{y}^T \cdot \nabla(\nabla H(\mathbf{x}_i))^T \cdot \mathbf{y} + 2\nabla H(\mathbf{x}_i)^T \cdot \mathbf{y} \\ &+ \mathcal{O}(3) = 0 \end{aligned} \tag{3.7}$$

The mapping of $\mathbf{x}_0$ to $\mathbf{x}_4$ at the instant of impact must satisfy $\mathbf{x}_4(t_0 + \delta) = \mathbf{x}_3$ where $\mathbf{x}_3 = \mathbf{R}(\mathbf{x}_2)$; see Fig. 3.1. This ensures that any perturbed trajectory initiated at $\hat{\mathbf{x}}(t)$ is correctly mapped on the impact surface Σ_2 to $\mathbf{x}_3$ at time $t_0 + \delta$. This is a parallel occurrence to the instance when the system at $\mathbf{x}_i$ impacts Σ_2 at $t = t_0$. The functional form of $\mathbf{x}_4$ is approximated by expanding $\mathbf{x}_3$ along path 3 about $t = 0$. Thus in the absence of Σ_2, $\mathbf{x}_4$ would naturally evolve to $\mathbf{x}_3$ after time δ. Thus $\mathbf{x}_4$ is obtained by expanding and evaluating $\mathbf{x}_3$ backwards in time $t = -\delta$ as described in Eq. (3.8)

$$\mathbf{x}_4 = \mathbf{x}_3 - \delta\ \mathbf{F}(\mathbf{x}_3) + \frac{1}{2}\delta^2\ \nabla \mathbf{F}(\mathbf{x}_3)^T \cdot \mathbf{F}(\mathbf{x}_3) + \mathcal{O}(3) \tag{3.8}$$

where $\mathbf{x}_3 = \mathbf{R}(\mathbf{x}_2)$. Expanding $\mathbf{R}(\mathbf{x})$ about $\mathbf{x}_i$ gives Eq. (3.9)

$$\mathbf{R}(\mathbf{x}) = \mathbf{R}(\mathbf{x}_i) + \nabla \mathbf{R}(\mathbf{x}_i)^T \cdot \boldsymbol{\Delta}\mathbf{x} + \frac{1}{2}\begin{bmatrix}\boldsymbol{\Delta}\mathbf{x}^T \cdot \tilde{H}_1 \cdot \boldsymbol{\Delta}\mathbf{x} \\ \boldsymbol{\Delta}\mathbf{x}^T \cdot \tilde{H}_2 \cdot \boldsymbol{\Delta}\mathbf{x}\end{bmatrix} + \mathcal{O}(3) \tag{3.9}$$

where $\boldsymbol{\Delta}\mathbf{x} = \mathbf{x} - \mathbf{x}_i$ and $\tilde{H}_i$ are the Hessian matrices of each component $r_i(\mathbf{x})$ of $\mathbf{R}(\mathbf{x})$. These Hessian matrices are defined as the Jacobian of $\nabla r_i(\mathbf{x})$ or $\nabla(\nabla r_i(\mathbf{x}))^T$. An approximation of $\mathbf{R}(\mathbf{x}_2)$ using Eq. (3.5) up to $\mathcal{O}(2)$ results in the following expression; see Eq. (3.10).

$$\begin{aligned}\mathbf{R}(\mathbf{x}_2) = \ &\mathbf{R}(\mathbf{x}_i) + \nabla \mathbf{R}(\mathbf{x}_i)^T \cdot \Big(\mathbf{y}_- + \delta \mathbf{F}(\mathbf{x}_i) + \delta \nabla \mathbf{F}(\mathbf{x}_i)^T \cdot \mathbf{y}_- \\ &+ \frac{1}{2}\delta^2 \nabla \mathbf{F}(\mathbf{x}_i)^T \cdot \mathbf{F}(\mathbf{x}_i)\Big) + \frac{1}{2}\begin{bmatrix}[\mathbf{y}_- + \delta \mathbf{F}(\mathbf{x}_i)]^T \cdot \nabla(\nabla r_1)^T \cdot [\mathbf{y}_- + \delta \mathbf{F}(\mathbf{x}_i)] \\ [\mathbf{y}_- + \delta \mathbf{F}(\mathbf{x}_i)]^T \cdot \nabla(\nabla r_2)^T \cdot [\mathbf{y}_- + \delta \mathbf{F}(\mathbf{x}_i)]\end{bmatrix} \\ &+ \mathcal{O}(3) \end{aligned} \tag{3.10}$$

where r_1 and r_2 are the components of the map $\mathbf{R}(\mathbf{x})$. Terms up to $\mathcal{O}(2)$ is taken in $\boldsymbol{\Delta}\mathbf{x} = \mathbf{x}_2 - \mathbf{x}_i$. One can then evaluate $\mathbf{F}(\mathbf{x}_3)$ as mentioned in Eq. (3.8) as an expansion of $\mathbf{F}(\mathbf{x})$ along path 4 about $\mathbf{R}(\mathbf{x}_i)$. Taking terms upto $\mathcal{O}(1)$ in $\mathbf{F}(\mathbf{x})$ yields

Eq. (3.11)

$$\mathbf{F}(\mathbf{x}_3) = \mathbf{F}(\mathbf{R}(\mathbf{x}_i)) + \nabla\mathbf{F}(\mathbf{R}(\mathbf{x}_i))^T \cdot \Big(\nabla\mathbf{R}(\mathbf{x}_i)^T \cdot \mathbf{y}_- + \delta\ \nabla\mathbf{R}(\mathbf{x}_i)^T \cdot \mathbf{F}(\mathbf{x}_i)\Big) + \mathcal{O}(2) \tag{3.11}$$

Now, substituting the expressions for $\mathbf{R}(\mathbf{x}_2)$, $\mathbf{F}(\mathbf{x}_3)$ in Eq. (3.8), the mapping of the perturbed trajectory initiated at $\mathbf{x}_0$ to $\mathbf{x}_4$ at the instant of impact up to $\mathcal{O}(2)$ can be analytically found. The resultant mapping is given by the following expression in Eq. (3.12).

$$\begin{aligned}
\mathbf{x}_4 = \mathbf{R}(\mathbf{x}_i) &+ \nabla\mathbf{R}(\mathbf{x}_i)^T \cdot \mathbf{y}_- + \delta\nabla\mathbf{R}(\mathbf{x}_i)^T \cdot \mathbf{F}(\mathbf{x}_i) - \delta\mathbf{F}(\mathbf{R}(\mathbf{x}_i)) \\
&+ \delta\nabla\mathbf{R}(\mathbf{x}_i)^T \cdot \nabla\mathbf{F}(\mathbf{x}_i)^T \cdot \mathbf{y}_- + \frac{1}{2}\delta^2\nabla\mathbf{R}(\mathbf{x}_i)^T \cdot \nabla\mathbf{F}(\mathbf{x}_i)^T \cdot \mathbf{F}(\mathbf{x}_i) \\
&- \delta\nabla\mathbf{F}(\mathbf{R}(\mathbf{x}_i))^T \cdot \nabla\mathbf{R}(\mathbf{x}_i)^T \cdot \mathbf{y}_- - \delta^2\nabla\mathbf{F}(\mathbf{R}(\mathbf{x}_i))^T \cdot \nabla\mathbf{R}(\mathbf{x}_i)^T \cdot \mathbf{F}(\mathbf{x}_i) \\
&+ \frac{1}{2}\delta^2\nabla\mathbf{F}(\mathbf{R}(\mathbf{x}_i))^T \cdot \mathbf{F}(\mathbf{R}(\mathbf{x}_i)) \\
&+ \frac{1}{2}\begin{bmatrix}[\mathbf{y}_- + \delta\mathbf{F}(\mathbf{x}_i)]^T \cdot \nabla(\nabla r_1)^T \cdot [\mathbf{y}_- + \delta\mathbf{F}(\mathbf{x}_i)] \\ [\mathbf{y}_- + \delta\mathbf{F}(\mathbf{x}_i)]^T \cdot \nabla(\nabla r_2)^T \cdot [\mathbf{y}_- + \delta\mathbf{F}(\mathbf{x}_i)]\end{bmatrix} + \mathcal{O}(3)
\end{aligned} \tag{3.12}$$

Defining $\mathbf{y}_-$ and $\mathbf{y}_+$ as the perturbation vector between path 1 and path 2 before and after impact, the relations $\mathbf{x}_4 - \mathbf{R}(\mathbf{x}_i) = \mathbf{y}_+$ and $\mathbf{x}_0 - \mathbf{x}_i = \mathbf{y}_-$ hold true. The proposed higher-order correction maps $\mathbf{x}_i$ to $\mathbf{R}(\mathbf{x}_i)$, $\mathbf{x}_0$ to $\mathbf{x}_4$ and $\mathbf{y}_-$ to $\mathbf{y}_+$.

To obtain the aforementioned $\mathcal{O}(1)$ mapping, *i.e.* the well known saltation matrix at the instant of impact, only the 1^{st} order terms in the Eq. (3.7) can be retained. This simplification leads to the following expression in δ; see Eq. (3.13).

$$\delta = -\frac{\nabla H(\mathbf{x}_i)^T \cdot \mathbf{y}_-}{\nabla H(\mathbf{x}_i)^T \cdot \mathbf{F}(\mathbf{x}_i)} \tag{3.13}$$

This system was analytically formulated in [37]. A substitution of Eq. (3.13) in Eq. (3.12) and retention of terms up to $\mathcal{O}(1)$ yields Eq. (3.14)

$$\mathbf{x}_4 = \mathbf{R}(\mathbf{x}_i) + \nabla\mathbf{R}(\mathbf{x}_i)^T \cdot \mathbf{y}_- + \frac{\Big(\mathbf{F}(\mathbf{R}(\mathbf{x}_i)) - \nabla\mathbf{R}(\mathbf{x}_i)^T \cdot \mathbf{F}(\mathbf{x}_i)\Big)}{\nabla H(\mathbf{x}_i)^T \cdot \mathbf{F}(\mathbf{x}_i)}\nabla H(\mathbf{x}_i)^T \cdot \mathbf{y}_- \tag{3.14}$$

One can define a first-order state transition matrix (STM) $\mathbf{S}_1$ that governs the mapping of $\mathbf{y}_-$ to $\mathbf{y}_+$. This STM can be expressed succinctly as Eq. (3.15)

$$\mathbf{y}_+ = \mathbf{S}_1 \cdot \mathbf{y}_- \tag{3.15}$$

On substituting the above expression in Eq. (3.14) and the relation between $\mathbf{x}_4$ and $\mathbf{R}(\mathbf{x}_i)$, one can obtain the expression for this state transition matrix, also known as

the saltation matrix ([2]), as Eq. (3.16)

$$\mathbf{S}_1 = \nabla \mathbf{R}(\mathbf{x}_i)^T + \frac{\Big(\mathbf{F}(\mathbf{R}(\mathbf{x}_i)) - \nabla \mathbf{R}(\mathbf{x}_i)^T \cdot \mathbf{F}(\mathbf{x}_i)\Big)}{\nabla H(\mathbf{x}_i)^T \cdot \mathbf{F}(\mathbf{x}_i)} \nabla H(\mathbf{x}_i)^T \tag{3.16}$$

The numerical evaluation of the saltation matrix using the obtained higher order approximation is discussed next by mapping $\mathbf{x}_0$ to $\mathbf{x}_4$.

3.3 Piecewise-smooth hybrid systems

The derived Eq. (3.7) and Eq. (3.12) are implemented to perform stability analysis of vibro-impacting oscillators with hard stops. Two representative cases possessing single and multiple barriers, respectively, are considered. The corresponding Floquet multipliers and Lyapunov characteristic exponents are obtained taking into consideration the $\mathcal{O}(2)$ terms. The obtained values are validated with respective bifurcation diagrams.

3.3.1 Impact oscillator

Figure 3.2 represents an classical harmonic oscillator with mass m, damping constant c and stiffness k subjected to an external harmonic forcing of frequency ω. The corresponding non-dimensionalized governing equation for undamped oscillator with unit mass and unit stiffness is described in Eq. (3.17).

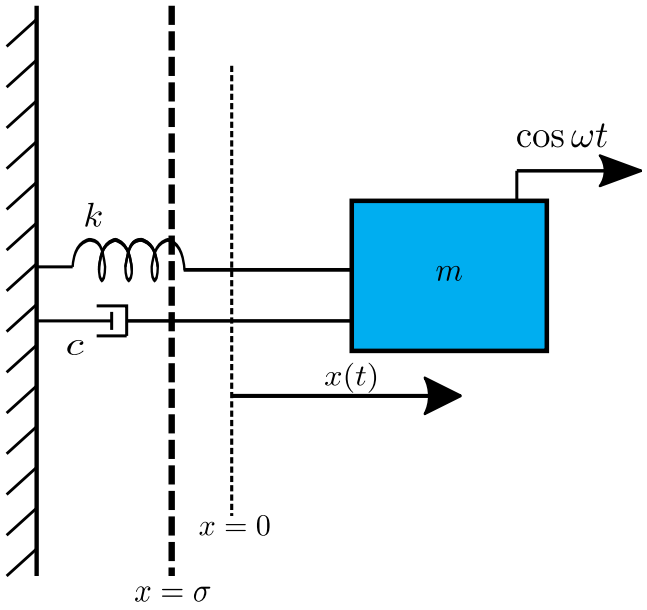

Figure 3.2: Schematic of a body with mass m excited by an periodic force applied externally. The oscillations are modeled by a linear harmonic oscillator. The body undergoes impact a with barrier placed at $x = \sigma$ after which its velocity is reversed instantaneously.

$$\ddot{x} + x = \cos(\omega t), \qquad (3.17)$$
$$\text{if, } x(t_-) = \sigma;\ \dot{x}(t_+) = -r\dot{x}(t_-),$$

where the undeformable impacting barrier [27] is placed at $x(t_0) = \sigma$. At the instant of impact $t = t_0$, the oscillator undergoes an instantaneous reversal of velocity which is modelled as $\dot{x}(t_+) = -r\,\dot{x}(t_-) = -rv_-$. Here, t_+ and t_- are the instants before and after a collision and r depicts the coefficient of restitution. The dynamics of a perturbed trajectory can be expressed in the state-space form and evaluated using Eqs. (3.7) and (3.12). First order non-smooth mapping is compared with that of the second order. Two closely spaced trajectories are initiated, post transient effects, and these trajectories evolve according to the variational form away from the barrier. The integration is performed in Mathematica using its inbuilt ODE solver, NDSolve. For event detection *i.e.,* when $x(t_-) = \sigma$, an event detection routine is implemented. Up to 15 digits of accuracy were considered to precisely detect the instances when an impact occurred. To demonstrate the conditions where a first-order approximation in δ is incorrect, the case of a damped impact oscillator with an additional damping term $2\xi\dot{x}$ on the left hand side of Eq. (3.17) is considered next. The $\mathcal{O}(1)$ and $\mathcal{O}(2)$ approximations of δ, using Eqs (3.17) and (3.7), are provided in Eq. (3.18).

$$\delta_1^\xi = -\frac{y_1}{v_-}, \qquad (3.18)$$
$$\delta_2^\xi = -\frac{v_- + y_2}{-\sigma - 2\xi v_- + \cos(\omega t_0)} + \frac{v_- + y_2}{-\sigma - 2\xi v_- + \cos(\omega t_0)}\sqrt{1 - 2\frac{(-\sigma - 2\xi v_- + \cos(\omega t_0))y_1}{(v_- + y_2)^2}}$$

Here, the superscript ξ corresponds to the case of non-zero damping and y_i are the components of the perturbation $\vec{y}$ when Eq. (3.17) is expressed in state space form, *i.e.* Eq. (3.1). The corresponding figures, Fig. 3.3(a), Fig. 3.3(c) and Fig. 3.3(e) are the phase-portraits of x and $\dot{x}$ for three nearby trajectories $\mathbf{x}$ and $\mathbf{x} + \mathbf{y}$ where $\mathbf{y}(0) = r_0/\sqrt{2}[1, 1]$ undergoing impact at $\sigma = -0.105$, $\sigma = -0.11$ and -0.1288 respectively. A magnified region of the respective phase-portraits near the discontinuity barrier is shown in Figs. 3.3(b), (d) and (f).

Transient effects are disregarded by rejecting the initial 1000 impacts to ensure the formation of a periodic orbit. The initial separation, $|\mathbf{y}(0)|$, between the trajectories is taken as $r_0 = 0.0095$ in Fig. 3.3(a), $r_0 = 0.007$ in Fig. 3.3(c) and 0.0018 in Fig. 3.3(e) with $\xi = 2.0$, $\omega = 1.8$ and $r = 0.8$. In all three cases, while the trajectory $\mathbf{x}$ undergoes an impact at σ, the perturbed trajectory $\mathbf{x}+\mathbf{y}$ misses the barrier as verified by the respective magnified phase-portraits of the true solution shown in Figs. 3.3(b), (d) and (f). However, a linearized approximation using $\mathcal{O}(1)$ incorrectly predicts an impact after $\delta_1^\xi = 0.086$, $\delta_1^\xi = 0.0754$ and $\delta_1^\xi = 0.037$. The saltation matrix,

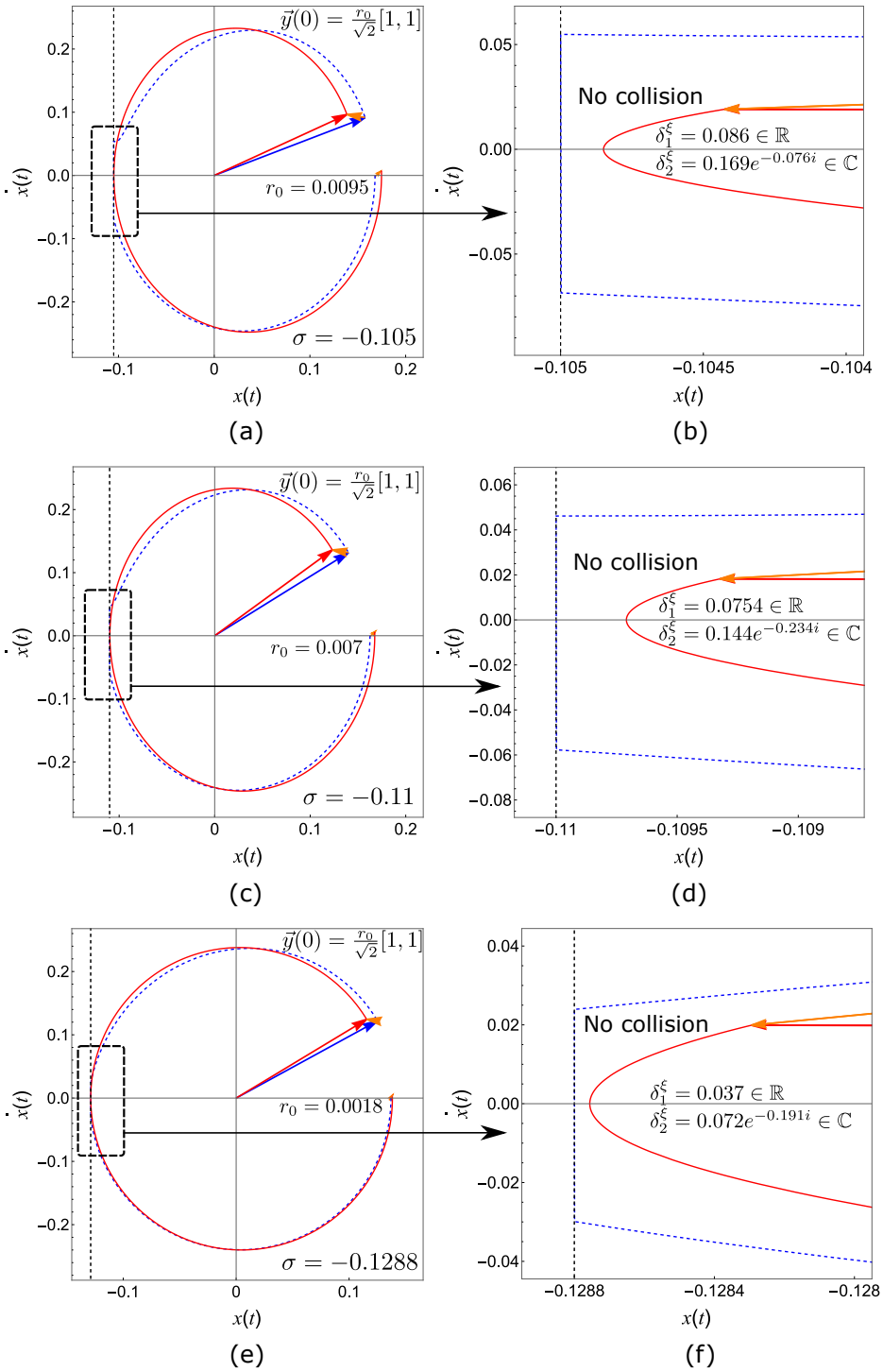

Figure 3.3: Phase portrait of two nearby trajectories $\mathbf{x}$ and $\mathbf{x}+\mathbf{y}$ shown in blue and red with initial perturbation $\mathbf{y} = r_0/\sqrt{2}[1,1]$ and barrier placed at (a) $\sigma = -0.105$ (c) $\sigma = -0.110$ and (e) $\sigma = -0.1288$ and their respective zoomed phase portraits at (b), (d) and (f). Here, $\xi = 2.0$, $\omega = 1.8$ and $r = 0.8$. In all three cases, $\delta_1^\xi \in \mathbb{R}$ while $\delta_2^\xi \in \mathbb{C}$ *i.e.*, there are no real roots satisfying $H(\mathbf{x}) = 0$. The zoomed phase-portraits verify that perturbations do not impact σ as predicted correctly by $\delta_2^\xi \in \mathbb{C}$.

derived using local linearizations, is compatible with the variational equation and yet in this case, yields an incorrect prediction of the perturbed state. The $\mathcal{O}(2)$ terms in Eqs. (3.7) and (3.18) returns an imaginary root for all three cases, leading

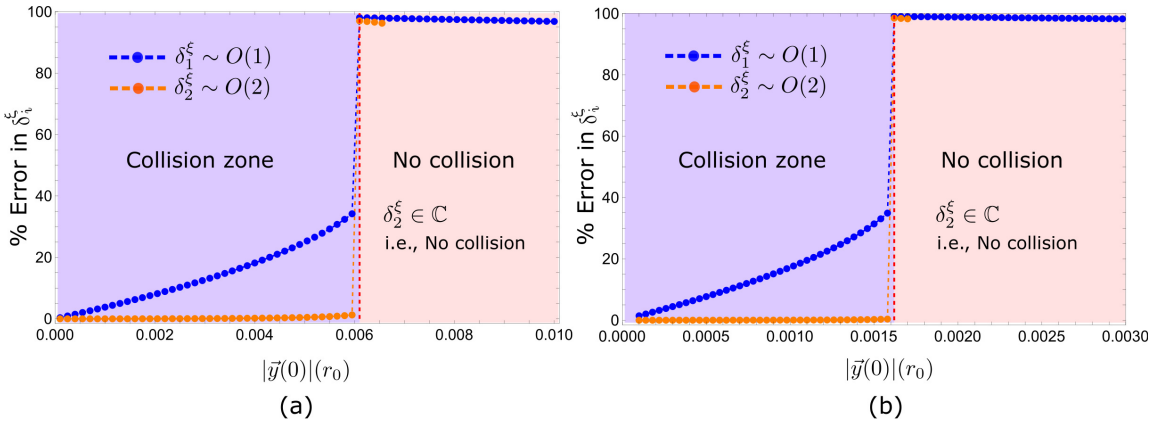

Figure 3.4: Percentage error in δ_i^ξ vs initial separation $||\mathbf{y}(0)|| = r_0$ for barrier placed at (a) $\sigma = -0.11$ (b) $\sigma = -0.1288$. Blue and red regions are no collision and collision zones obtained from exact numerical results. Here, $\xi = 2.0$, $\omega = 1.8$ and $r = 0.8$.

to a logical conclusion that there is no interaction with Σ_2. This is because no real root exists which satisfies $H(\mathbf{x}+\mathbf{y}) = 0$ for the chosen orbit. When compared with the true solutions, the perturbed trajectory, governed by the variational equation, is observed to miss the barrier $H(\mathbf{x}+\mathbf{y}) \in \mathbb{C}$; see Figs. 3.3(b), (d) and (f). Thus the higher-order approximation correctly predicts the behavior of perturbed orbits near a barrier, while the first-order TDM fails to do so. Mathematically, it is apparent since δ_2^ξ in Eq. (3.18) considers crucial system parameters like ξ, σ, ω and t_0 at the instant of an impact in contrary to δ_1^ξ, which is independent of these terms.

In Fig. 3.4, the error in estimation of δ is shown as the initial separation between the trajectories is varied when the barrier is placed at (a) $\sigma = -0.11$ and (b)$\sigma = -0.1288$. The purple and pink regions correspond to the numerically obtained collision and no collision zones respectively. In the collision zone, the error between $\mathcal{O}(1)$ and $\mathcal{O}(2)$ diverges as the separation increases. Improvements up to 35 percent were obtained while using the higher-order terms in δ. In the no collision zone, the higher-order terms yielded imaginary values, while the first order terms incorrectly predicted collisions with the border at finite times. It is to be noted that the perturbations are of order of $\mathcal{O}(10^{-3})$. This is a major improvement in comparison to the linearized approximation of how perturbed orbits would behave near an impact. Results relying on incorrect prediction of the state in the event of an impact would drastically alter the outcome of the global dynamics, especially for chaotic systems which is typical in such impact problems.

Figure 3.5 highlights the dependence of crucial parameters like damping ξ in the higher-order flight time δ_2^ξ which is absent in the first-order flight time δ_1^ξ; compare Eqs. (3.18). Fig. 3.5(a) compares the percent error of flight time δ^ξ estimated by the first-order and higher-order expressions of Eqs. (3.18) for varying damping with $\omega = 1.8$, $r = 0.8$ and barrier at $\sigma = -0.105$. Fig. 3.5(b) compares the

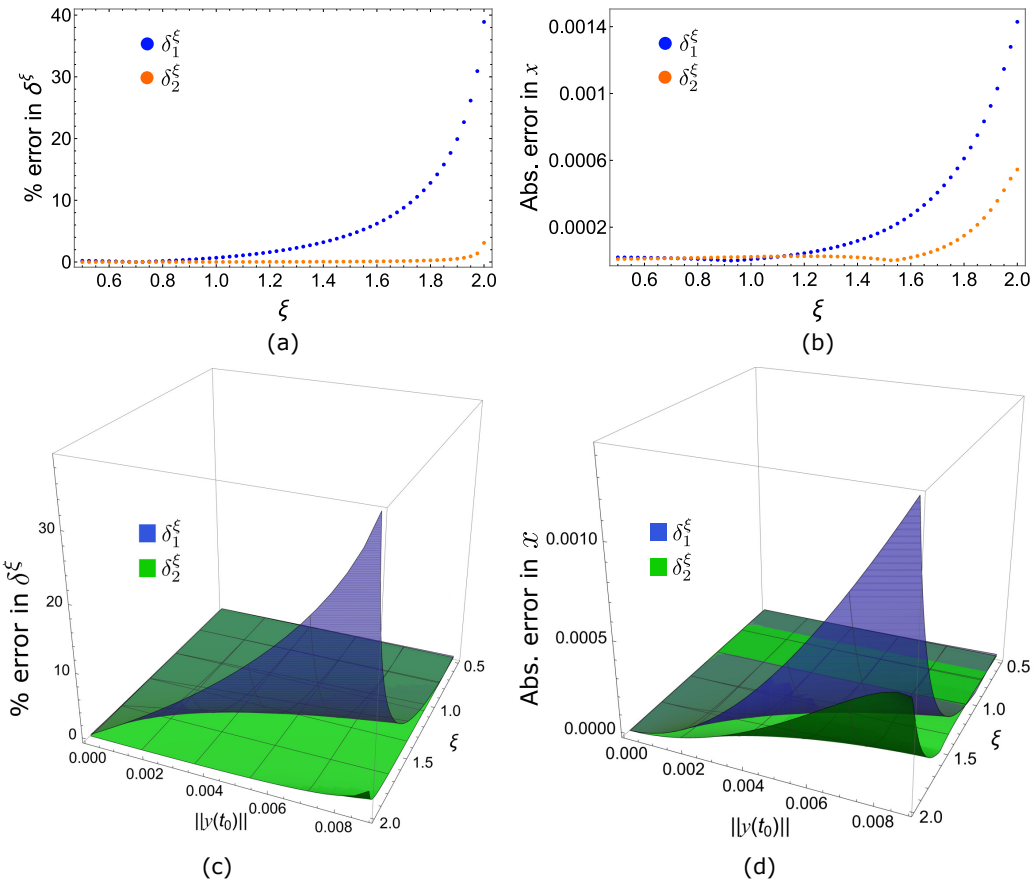

Figure 3.5: Comparison of first-order and higher-order flight time δ_i^ξ results with $\omega = 1.8$, $r = 0.8$ and barrier at $\sigma = -0.105$. Figures represent (a) percentage error in δ_i^ξ and (b) absolute error in position or first-component of state $\mathbf{x}_3$ for varying damping parameter ξ and initial separation $||\mathbf{y}(t_0)|| = 0.0089$ and, (c) percent error in δ_i^ξ and (d) absolute error in position x of state $\mathbf{x}_3$ for varying damping parameter and initial separation $||\mathbf{y}(t_0)||$.

absolute error in the estimation of the position of the oscillator (the first component of the mapped state $\mathbf{x}_3$) after a time elapse of the flight time at the instant of impact with the discontinuity barrier for varying damping. For both the figures, transients have been eliminated by discarding 1000 impacts, after which the flight time has been estimated between two trajectories with the initial separation of $r_0 = ||\mathbf{y}(t_0)|| = 0.0089$. Similarly, Figs. 3.5(c) and (d) compare the percent error of flight time and the absolute error in the position of the mapped state $\mathbf{x}_3$ by varying the damping parameters and for various initial separation $||\mathbf{y}(t_0)||$. Results imply that the higher-order flight time estimate (see Eqs. (3.18)) considers the damping parameter ξ, which improves the accuracy of the estimated flight times and mapped states. On the contrary, the first-order flight time does not depend on crucial system parameters like damping, which reduces the accuracy of the conventional first-order approaches. The accuracy of the higher-order flight time estimate becomes more significant when the separation between trajectories is increased and ranges in the order of unity, as discussed below.

Next, an undamped impact oscillator (Eqs. (3.17)) is considered. The expressions in Eqs. (3.19) correspond to the approximation of the flight times of the perturbed trajectory to Σ_2 after the primary trajectory has impacted this surface. The entity δ_1 in Eq. (3.19) depicts the linearized expression of Eq. (3.7), *i.e.,* Eq. (3.13). The variables δ_2 and δ_3 in Eq. (3.19) are obtained from Eq. (3.7) by expanding the discriminant up to $\mathcal{O}(1)$ and $\mathcal{O}(2)$ respectively. Meanwhile, δ_4 is numerically obtained from Eq. (3.7) considering only the positive root in δ.

$$\delta_1 = -\frac{y_1}{v_-}, \tag{3.19a}$$

$$\delta_2 = -\frac{y_1}{v_- + y_2}, \tag{3.19b}$$

$$\delta_3 = -\frac{y_1}{v_- + y_2} - \frac{(-\sigma + \cos(\omega t_0))y_1^2}{2(v_- + y_2)^3}, \tag{3.19c}$$

$$\delta_4 = -\frac{v_- + y_2}{-\sigma + \cos(\omega t_0)} + \frac{v_- + y_2}{-\sigma + \cos(\omega t_0)}\sqrt{1 - 2\frac{(-\sigma + \cos(\omega t_0))y_1}{(v_- + y_2)^2}}. \tag{3.19d}$$

To demonstrate the accuracy of the proposed higher-order corrections to the TDM, the flow of two trajectories is shown in the phase-space, separated by a perturbation $\|\mathbf{y}\| = 1$ (Fig. 3.6). This approach follows that the fundamental solution matrix is constructed by initially considering a unit sphere of perturbed vectors, ensuring that the initial fundamental solution matrix is an identity matrix. The trajectory shown in blue depicts the dynamics at $\omega = 2.0$, $\sigma = 0.0$ and $r = 0.8$ after 1000 impacts have been discarded. The perturbed trajectory shown in red evolves according to the Jacobian of the respective dynamical system[33]. At the instant of impact at $t = t_0$, the perturbed trajectory gets mapped in accordance with the derived $\mathcal{O}(1)$ and $\mathcal{O}(2)$ TDM. In principle, from the instant of impact to the instant when $t = t_0 + \delta$, the perturbed trajectory should lie on the discontinuity boundary $H(\mathbf{x}) = 0$ if accurately mapped. In Fig. 3.6(a) the trajectories at the instant of impact after the application of TDM, when mapped using $\mathcal{O}(1)$ time difference and TDM (*i.e.*, Eq. (3.13) and Eq. (3.16)), are shown. Fig. 3.6(b) corresponds to the trajectories after the application of TDM after elapsed time δ *i.e.*, when $t = t_0 + \delta$. The mapped perturbed vector does not lie on the discontinuity boundary, depicting the inaccuracy of the widely used first-order mapping. The effect of incorporating a second-order formulation is highlighted next. An improvement in mapping is observed in Fig. 3.6(c) - (d) where the mapping is done using an $\mathcal{O}(1)$ time difference and an $\mathcal{O}(2)$ TDM, *i.e.* using Eq. (3.13) and Eq. (3.12). This further reduces when one uses a $\mathcal{O}(2)$ approximation in δ and a $\mathcal{O}(1)$ TDM as derived in Eq. (3.7) and Eq. (3.16); See Figs. 3.6(e) - (f). The perturbed trajectory reaches the discontinuity boundary after $t = t_0 + \delta$ using $\mathcal{O}(1)$ TDM in this case. It can be thus inferred that the $\mathcal{O}(2)$ in δ renders a

significant improvement. A mapping $\mathcal{O}(2)$ in δ as well as the saltation will lead to a more accurate estimate of the state post impact. Using $\mathcal{O}(2)$ corrections to the TDM to calculate the higher-order Saltation matrix has been presented later in Sec. 3.5.

In Fig. 3.7, errors in time estimates δ_i, from in Eq. 3.19 is shown and compared. The percent error is computed by numerically integrating two closely separated trajectories interacting with the barrier Σ_2. Results indicate that the prediction of the flight time δ using higher order terms is more accurate in comparison to $\mathcal{O}(1)$. This is because the flight time prediction using $\mathcal{O}(2)$ *i.e.,* δ_4 in Eqs. (3.19)(d), takes into account the functional form of the driving force $\cos(\omega t)$ evaluated at t_0.

Figure 3.8 compares the errors in position (first component of $\mathbf{x}_3$) estimated after a long time integration of the impact oscillator with $\omega = 2.0$, $r = 0.8$ and $\sigma = 0.0$, as the separation between trajectories is varied. Fig. 3.8(a) shows the absolute error in position after implementing the first-order and higher-order TDM (Eqs. 3.16 and Eqs. 3.18) during 5 impacts when the impact oscillator is integrated up to $n = 5$ time periods ($T = 2\pi/\omega$) post transient effects. Similarly, Fig. 3.8(b) compares the absolute error in the position component of $\mathbf{x}_3$ while varying the initial separation $||\mathbf{y}(t_0)||$ and applying the first-order and higher-order TDM for $n = 1$ to 5 impacts with the discontinuity boundary. The exact solution of the perturbed trajectory should reach the discontinuity barrier at $x = \sigma = 0.0$ after a time elapse of δ^ξ post impact with Σ_2. The higher-order flight time δ_2^ξ accurately predicts the true position and state $\mathbf{x}_3$ for all impacts in comparison to δ_1^ξ as demonstrated in Figs. 3.8.
In Fig. 3.9, the error in estimation of one of the state variables, here $\dot{x}$ or velocity component of $\mathbf{x}_3$, is shown. As before, $\mathcal{O}(1)$ refers to the mapping of the perturbed trajectory obtained using the linearized saltation matrix presented in Eq. (3.16) and $\mathcal{O}(2)$ represents the proposed mapping with higher-order corrections derived in Eq. (3.12). The errors are evaluated using combinations of the flight time expressions for δ as described in Eq. (3.19) with different orders of mapping of $\mathbf{x}_4$. The numerical values obtained indicate that the error is the least and of the order of 10^{-3} when a combination of δ_4 and $\mathbf{x}_4$ from Eq. (3.12) is used.

A general hybrid dynamical system attains its steady state after multiple impacts. Therefore, if an analytical framework is used, these errors will add up, leading to a completely different trajectory. This ultimately leads to an incorrect prediction of the stability of the steady state. Additionally, the higher the magnitude of initial perturbation, the more errors one introduces in the reset state on using a lower order approximation. This is presented in Fig. 3.10. The error in the estimation of $\dot{x}$ or velocity component of a perturbed trajectory, introduced at an instant of impact when $\mathbf{y}_+$ is mapped in accordance with a linearized TDM and with the proposed higher order corrections is shown as a function of separation between two adjacent trajectories. The linearized mapping is given by δ_1 in Eq. (3.19) and S in Eq. (3.16)

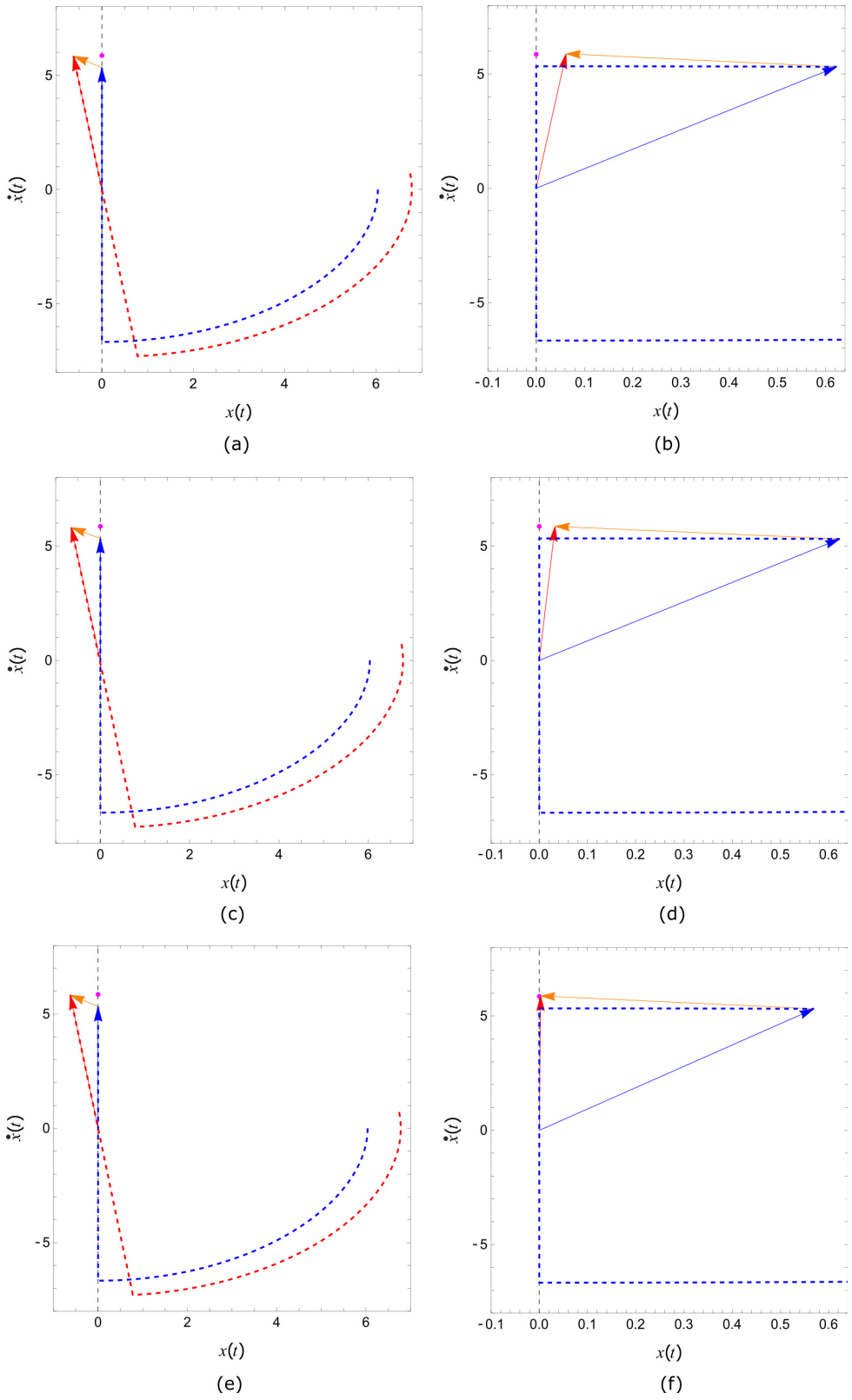

Figure 3.6: Two trajectories in the phase-space, shown in blue and red dashed lines, are separated initially by a perturbation $\|\mathbf{y}\| = 1.0$. The magenta dot depicts the numerically obtained state to which $\mathbf{x} + \mathbf{y}$ gets mapped after $t = t_0 + \delta$. The discontinuity boundary is shown as a black dashed line. Trajectories at instant of impact $t = t_0$ with $\mathbf{y}$ mapped using: $\mathcal{O}(1)$ in δ and $\mathcal{O}(1)$ in saltation terms (a) before impact, (b) after impact; $\mathcal{O}(1)$ in δ and $\mathcal{O}(2)$ in saltation terms (c) before impact, (d) after impact; $\mathcal{O}(2)$ in δ and $\mathcal{O}(1)$ in saltation terms (e) before impact, (f) after impact. Results correspond to $\omega = 2.0$, $\xi = 0.0$, $r = 0.8$ and $\sigma = 0.0$.

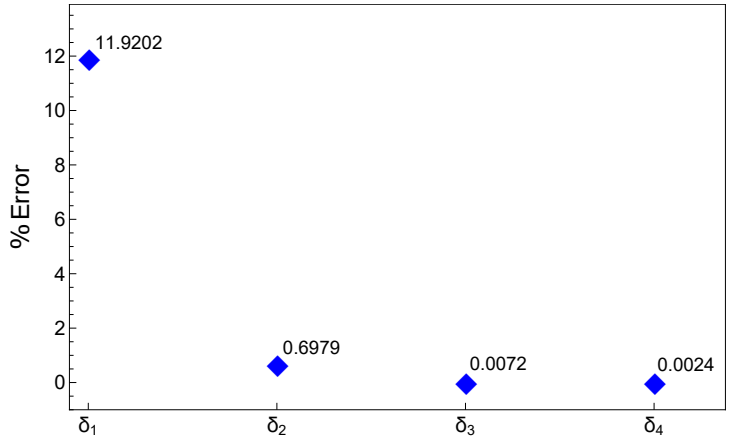

Figure 3.7: Percent errors in prediction of flight time *i.e.*, δ_is as defined in Eq. (3.19), in comparison to the numerically obtained flight times. The computations are carried out for forcing frequency, $\omega = 2.0$ with a barrier at $\sigma = 0.0$ and $r = 0.8$. The initial separation between trajectories is $\|\mathbf{y}\| = 0.1$.

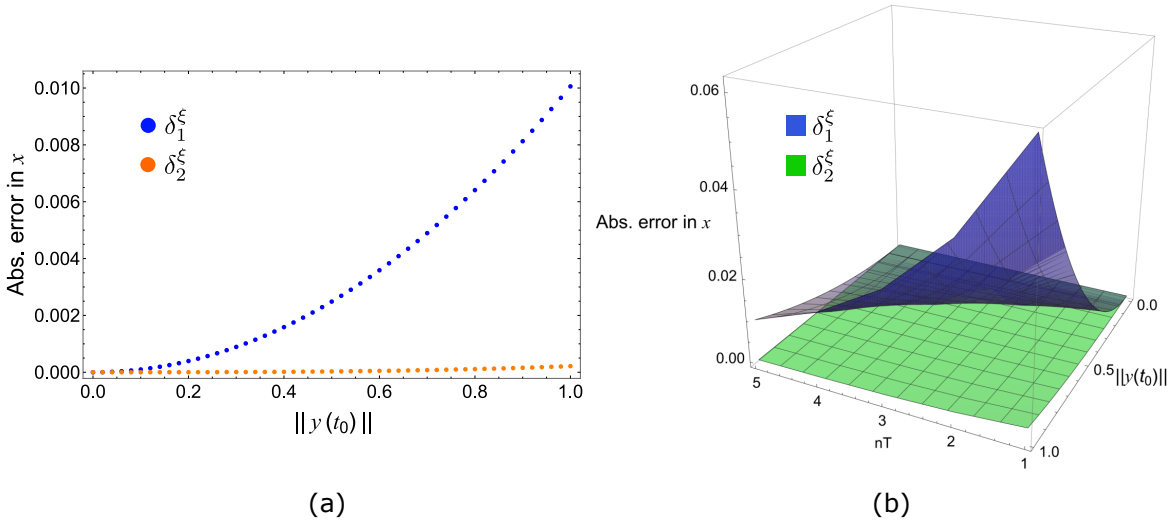

Figure 3.8: Comparison of absolute error in position or first-component of $\mathbf{x}_3$ using first-order and higher-order flight time estimate δ_i^ξ for (a) varying separation $||\mathbf{y}(t_0)||$ after long-time integration of 5 time periods and (b) varying separation $||\mathbf{y}(t_0)||$ and integrating the impact oscillator for $n = 1$ to 5 impacts with σ. Results are shown for $\omega = 2.0$, $r = 0.8$ and $\sigma = 0.0$.

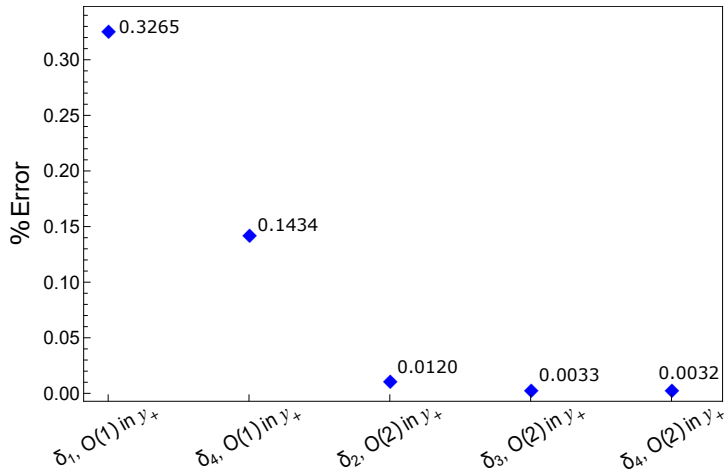

Figure 3.9: Comparison of errors in predicted $\mathbf{y}_+$ for different combinations of δ_is and $\mathcal{O}(1)$, $\mathcal{O}(2)$ mapping of $\mathbf{y}_+$ with respect to the numerical obtained exact values for $\omega = 2.0$, $r = 0.8$ and $\sigma = 0.0$. Initial separation between trajectories is $\|\mathbf{y}\| = 0.1$.

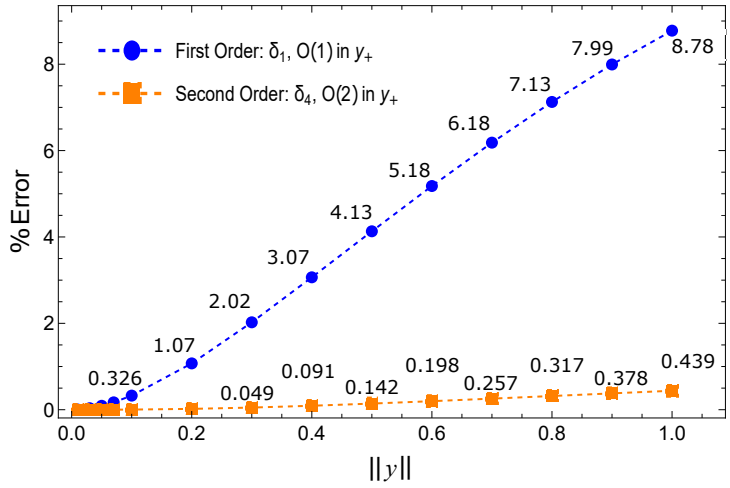

Figure 3.10: Comparison of percent error in velocity component of $\mathbf{x}_3$ or $\dot{x}$ at the instant of impact when $\mathbf{y}_+$ is mapped using $\mathcal{O}(1)$ vs $\mathcal{O}(2)$ TDM by varying separation between trajectories $\|\mathbf{y}\|$. Results are shown for $\omega = 2.0$, $r = 0.8$ and $\sigma = 0.0$.

whereas the $\mathcal{O}(2)$ correction is given by δ_4 in Eq. (3.19) and Eq. (3.12). Errors are plotted for various initial separations between the perturbed trajectory and the primary trajectory at the instant of impact. Results indicate that the errors introduced in the prediction of the state using the derived TDM are lower in comparison and therefore the proposed TDM can accurately predict the long time dynamics of hybrid systems.

3.3.2 Pair impact oscillator

A mechanical oscillator undergoing impact with two rigid undeformable barriers, modeled as a pair impact oscillator, is considered next [48]. The schematic of this dynamical system shown in Fig. 3.11. The model considers a typical mass-cart

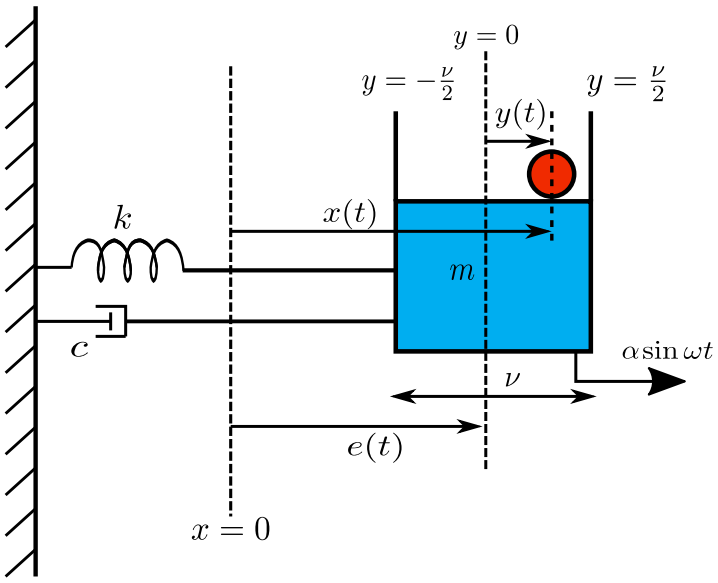

Figure 3.11: Schematic of a point mass object (shown in red) placed on a mass-cart system excited externally by a periodic force. The point mass object undergoes impacts on either sides of the cart walls when $y = \pm\nu/2$.

system executing periodic motion, where $x(t)$ and $y(t)$ describe the displacement of the object with respect to the stationary frame and the frame of reference, respectively. The term $e(t) = \alpha \sin(\omega t)$ describes the periodic motion of the cart excited externally with frequency ω. The dynamic response of the mass-cart is represented by $x(t) = y(t) + e(t)$ and Eq. (3.20).

$$\begin{aligned} \ddot{y} &= \alpha\omega^2 \sin(\omega t), \\ \text{if, } y(t_-) &= \pm\frac{\nu}{2};\ \dot{y}(t_+) = -r\dot{y}(t_-) \end{aligned} \tag{3.20}$$

The width of the cart is expressed by ν. Naturally, the motion of this point mass object will be obstructed at either walls of the cart when $y(t_-) = \pm\nu/2$. Here, an instantaneous velocity reversal occurs and is defined in Eq. (3.20) where t_- and t_+ denote instants before and after impact. As defined for the impact oscillator, r represents a coefficient of restitution.

The discontinuity mapping is derived for this system along similar lines as Eq. 3.7 and Eq. 3.12. The stability analyses for the impact and pair-impact oscillator is considered next by investigating the Lyapunov spectrum. Additionally, an algorithm to calculate the spectrum using the proposed higher-order mapping framework is proposed. The proposed form is applicable to any generalized PWS hybrid system transversally interacting with a discontinuity boundary . The stability of a hybrid dynamical system was previously assessed through analytical solution of the smooth trajectories between impacts [14]. The merit of the proposed algorithm in this chapter lies in the fact that it does not require any prior knowledge of the analytical solution of the system near the discontinuity boundary.

3.4 Lyapunov exponents

The stability analysis of the impact and pair-impact oscillator, defined in section 3.3, is taken up next. When the system under consideration encounters an impact, the perturbed vectors are mapped in the state space using higher-order corrections following Eqs. (3.7) and (3.12). The results are validated by the comparing numerically obtained stroboscopic bifurcation diagrams. Here, the amplitude of the oscillators at steady state are observed when forcing frequency is the bifurcation parameter. The Lyapunov characteristic exponents (LE) of the dynamical system measure the exponential divergence between two closely spaced trajectories [121]. For a dynamical system of order $\mathbb{R}^n$, the exponential divergence along the i^{th} orthogonal eigenvector is defined as Eq. 3.21

$$\lambda_i = \frac{1}{\tau N} \sum_{n=1}^{N} \log\left(\frac{r_n}{r_0}\right). \tag{3.21}$$

The i^{th} LE in Eq. (3.21) is evaluated by measuring the growth of the variation in the i^{th} direction after every time period $\tau = 2\pi/\omega$ *i.e.,* in a stroboscopic fashion. Since the state is of the order $\mathbb{R}^n$, there are n independent solutions of the corresponding variational form. Therefore, any arbitrary solution can be decomposed along these n eigenvectors. To measure the i^{th} LE along an eigenvector, a QR decomposition (QRD) is carried out using the Gram-Schmidt process. The process yields n orthogonal perturbed vectors, which can be encapsulated in a hypersphere of dimension n. The growth or decay of this hypersphere along the trajectory over time is an indicator of the stability of the dynamical system. The LE along an eigendirection is calculated by numerically integrating each of these orthogonal vectors and measuring the change in magnitude of these vectors after a time interval of τ. r_0 and r_n in Eq. (3.21) are the initial and final magnitudes of the perturbed vector after elapsed time τ.

However, for chaotic systems, the perturbed vectors might quickly diverge from the actual trajectory and the linearized variational form might not be able to capture the actual dynamics of the perturbed trajectory. Therefore, the initial perturbed hypersphere is kept small in its radius centered on the trajectory by using a scaling factor r_0 in Eq. (3.21). Furthermore, to obtain accurate values of LE, λ_i in Eq. (3.21) has been averaged out over several computations and it is ensured that the actual trajectory is on the invariant set by disregarding the transient cycles of oscillations. The necessary steps to implement this method has been described in Appendix A.

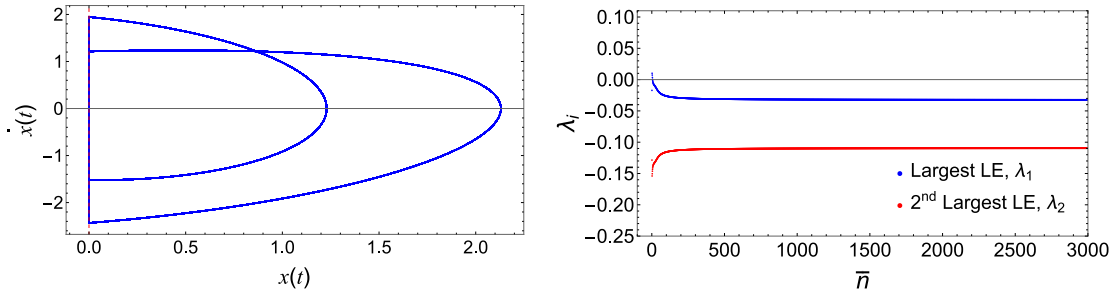

(a) (b)

Figure 3.12: (a) Phase portrait of the impact oscillator exhibiting period 2 oscillations. (b) The corresponding LE spectrum depicting a stable orbit. Here, $\omega = 1.0$ and $r = 0.8$.

3.4.1 Impact oscillator

The hybrid impact oscillator described in Eq. (3.17) is investigated for its stability. The external frequency, ω is taken to be the bifurcation parameter. The exponential divergence between perturbed trajectories is calculated every $2\pi/\omega$. First, a hypersphere of radius $r_0 = 0.001$ is initialised. After one cycle of evolution, a QRD and re-scaling in r_0 is carried out. Figures 3.12(a) and 3.12(b) show the phase portraits and the LE spectrum respectively for $\omega = 1.0$. Similar plots for $\omega = 1.1$ with $r = 0.8$ are presented in Fig. 3.13. For $\omega = 1.0$, the oscillator has a period-2 or P2 limit cycle while for $\omega = 1.1$, the dynamics in the state space is chaotic. The periodicity of an impact oscillator is computed as the number of times the trajectory crosses the Poincaré section $\dot{x} = 0$, provided $\ddot{x} > 0$. The LE spectrum is plotted against the strobe count $\bar{n}$. The largest LE (LLE) is observed to be positive for $\omega = 1.1$. The LEs are calculated by integrating Eqs. (3.17) using NDSolve along with the inbuilt event detection functionality in Mathematica. At the instant of impact when $H(\mathbf{x}) = 0$, the perturbed trajectory is mapped according to Eqs. (3.7) and (3.12) using $\mathbf{y}_+ = \mathbf{x}_4 - \mathbf{R}(\mathbf{x}_i)$. For the hard vibro-impact oscillator constrained by hard barriers, these expressions are as per Eq. (3.22).

$$\delta = -\frac{v_- + y_2}{-\sigma + \cos(\omega t_0)} + \frac{v_- + y_2}{-\sigma + \cos(\omega t_0)}\sqrt{1 - 2\frac{(-\sigma + \cos(\omega t_0))y_1}{(v_- + y_2)^2}}, \tag{3.22a}$$

$$\mathbf{y}_+ = \begin{bmatrix} y_1 + \delta v_-(1+r) + \delta y_2(1-r^2) + \dfrac{\delta^2}{2}(-\sigma + \cos(\omega t))(1-r) \\ -\delta^2 r^2(-\sigma + \cos(\omega t)) \\ \\ -r y_2 - \delta(-\sigma + \cos(\omega t))(1+r) + \delta y_1(1+r) \\ +\delta^2(1+r)(v_- + \dfrac{1}{2}\omega \sin(\omega t)) \end{bmatrix}_{2\times 1} \tag{3.22b}$$

where y_i are the components of the perturbed vector and v_- is the velocity, $\dot{x}$ at the instant of impact, t_0.

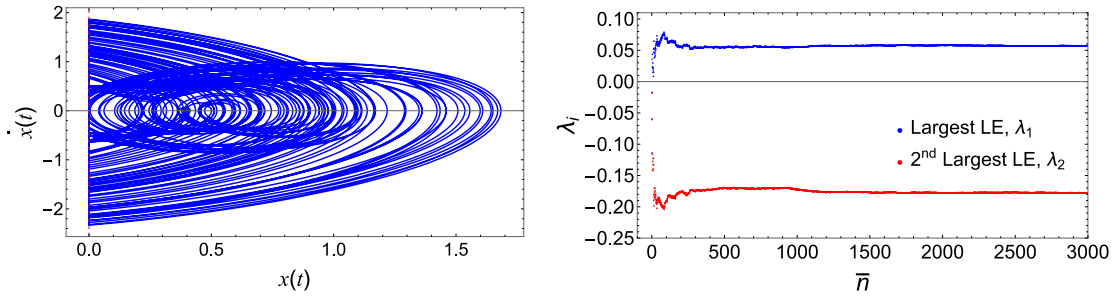

(a) (b)

Figure 3.13: (a) Phase portrait of an impact oscillator when $\omega = 1.1$ and $r = 0.8$. (b) The corresponding LE spectrum showing an unstable orbit.

Fig. 3.14(a) shows a bifurcation diagram of oscillator amplitude plotted against the non-autonomous harmonic frequency ω. The amplitude of the impact oscillator is observed when the condition $\dot{x} = 0$ is satisfied at every ω. The integration is performed for a total of 6000 impacts and amplitudes for the first 3000 impacts are discarded to eliminate any transient effects. Fig. 3.14(b) shows the LE spectrum plotted against ω. It is observed that the LE spectrum is in agreement with the bifurcation plot. The positive values of LE corresponds to chaotic trajectories and the LLE becomes zero at the parameter of occurrence of a period doubling. Dashed vertical lines are shown in figure for comparing the bifurcation diagram with the corresponding LEs to highlight some of the aperiodic chaotic solutions. Similarly, Fig. 3.15 and Fig. 3.16 depict the bifurcation diagrams and the corresponding LE spectrum for ω ranging between $0.35 \leq \omega \leq 1.3$ and $2.5 \leq \omega \leq 3.5$, respectively. It is observed that the calculated LE spectra depict the true underlying behaviour of the steady states.

3.4.2 Pair impact oscillator

Stability analysis of the pair-impact oscillator described in Sec. 3.3 is carried out next. The cart is assumed to have a width of $\nu = 2.0$, oscillating with a frequency of $\omega = 1.0$. The point mass moves freely on this cart unless it impacts the cart wall at $\nu = \pm\nu/2$. At this instant of impact there is an instantaneous reversal of velocity with a coefficient of restitution $r = 0.7$ as per Eq. (3.20). Figures 3.17 and 3.18 show the state space trajectories and both the LEs for two amplitudes $\alpha = 1.0$ and $\alpha = 1.5$. For $\alpha = 1.0$, the orbit is stable with negative LEs while $\alpha = 1.5$ results in a chaotic orbit with positive LLE. For this system, the mapped entities can be analytically expressed as Eq. (3.23). Here, y_i are the components of the perturbed

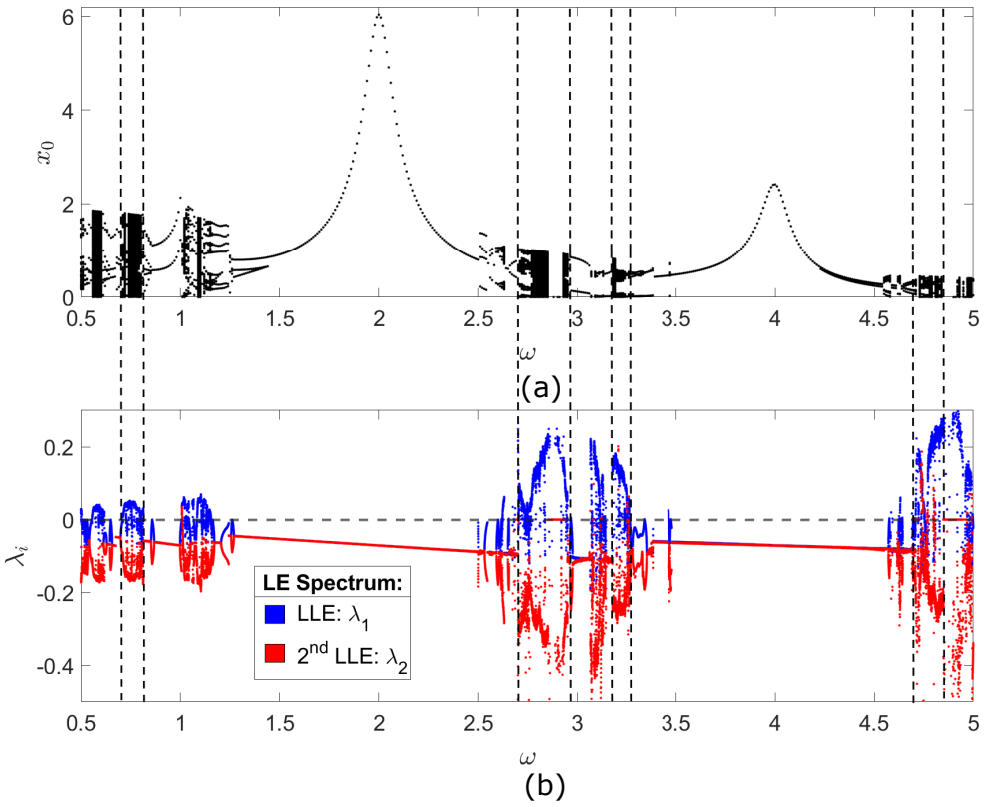

Figure 3.14: (a) Bifurcation diagram of stroboscopic displacement x_0 of the impact oscillator at steady state, *i.e.,* after discarding 6000 impacts, when $\dot{x} = 0$. (b) The corresponding LE spectrum for $0.5 \leq \omega \leq 5.0$ and $r = 0.8$.

vector and as before v_- is the velocity $\dot{x} = 0$ at instant of impact, t_0.

$$\delta = -\frac{v_- + y_2}{\alpha\omega^2 \sin(\omega t)} + \frac{v_- + y_2}{\alpha\omega^2 \sin(\omega t)} \sqrt{1 - 2\frac{(\alpha\omega^2 \sin(\omega t))y_1}{(v_- + y_2)^2}}, \tag{3.23a}$$

$$\mathbf{y}_+ = \begin{bmatrix} y_1 + \delta v_-(1+r) + \delta y_2(1-r^2) + \dfrac{\delta^2}{2}\alpha\omega^2 \sin(\omega t)(1-r) \\ -\delta^2 r^2 \alpha\omega^2 \sin(\omega t) \\ \\ -r y_2 - \delta\alpha\omega^2 \sin(\omega t)(1+r) - \dfrac{\delta^2}{2}\alpha\omega^3 \cos(\omega t)(1+r) \end{bmatrix}_{2\times 1} \tag{3.23b}$$

Fig. 3.19(a) shows a bifurcation diagram where the impact velocity at steady state is plotted against the corresponding oscillation amplitude α. Here, the velocity of the point mass $\dot{y}$ is recorded at the instant of impact when $y = \pm\nu/2$ for varying α. The bifurcation parameter α ranges from 0.5 to 2.0. In Fig. 3.19(b), the LE spectrum against α is shown by integrating for 6000 impacts. The LEs for the first 3000 impacts has been discarded in the computations. Positive values of LLEs indicate that the underlying orbit is chaotic for the corresponding oscillation amplitude, α.

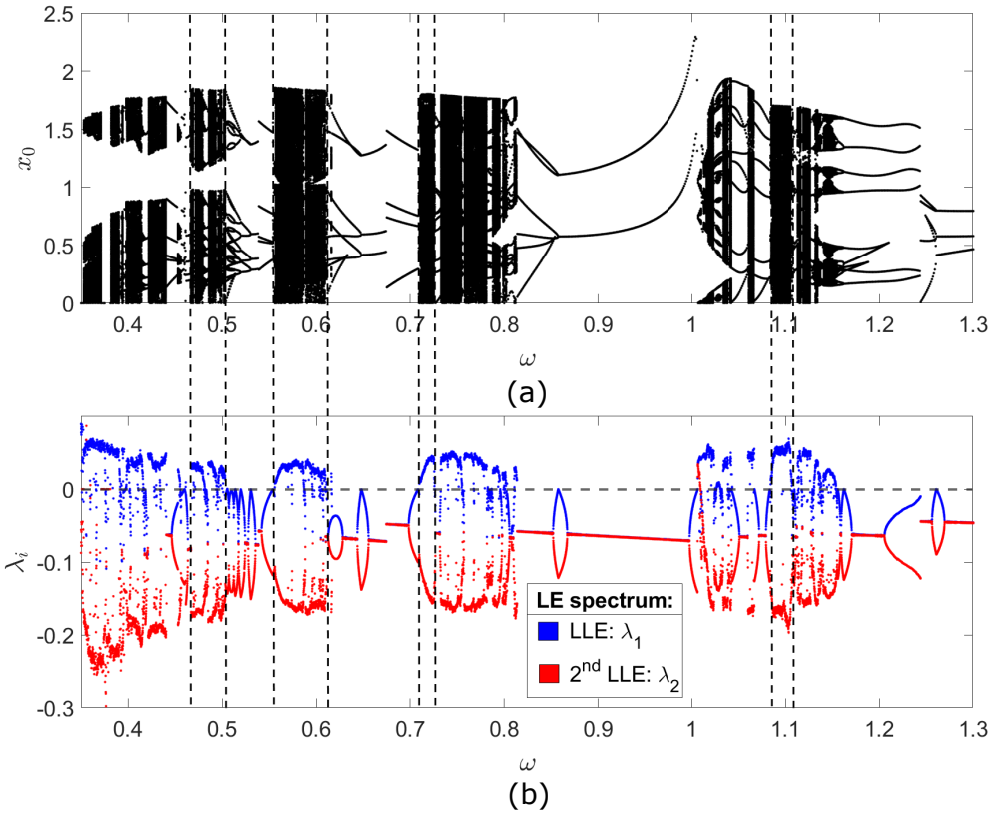

Figure 3.15: (a) Bifurcation diagram of stroboscopic displacement x_0 of the impact oscillator after discarding 6000 impacts when $\dot{x} = 0$. (b) LE spectrum for $0.35 \leq \omega \leq 1.3$ and $r = 0.8$.

3.5 Floquet multipliers

Stability of attractors in hybrid systems considered in Sec 3.3 is investigated via eigenvalue analysis of the global STM for a periodic orbit. This is also described as the monodromy matrix. According to Floquet theory [33], eigenvalues of the monodromy matrix determine the stability of a limit cycle. This analysis is applicable to periodically repetitive dynamics where the Jacobian is periodic. The eigenvalues or characteristic multipliers [82] determine the behaviour in the local linear neighbourhood of steady states in the state space. However, for hybrid dynamical systems, the monodromy matrix cannot be directly evaluated by integrating the variational form with initial conditions corresponding to an orthogonal basis. This is due to the presence of discrete jumps occurring in the state space near the discontinuity boundaries. A direct implementation of this leads to incorrect prediction of the state. In order to obtain the correct monodromy matrix, a saltation matrix that defines the state transition between the jumps is to be evaluated. In most studies, the saltation matrix is calculated using the form described in Eq. (3.16). Retaining $\mathcal{O}(2)$ terms leads to difficulty in writing the saltation terms in the form of a matrix.

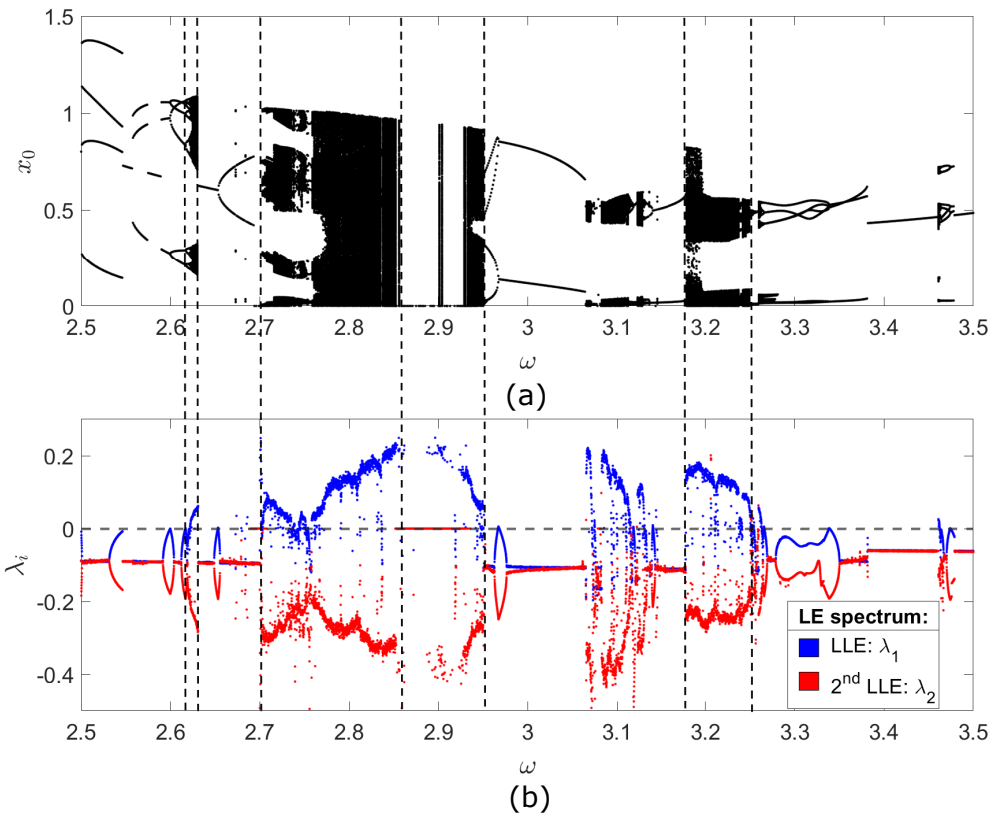

Figure 3.16: (a) Bifurcation diagram of stroboscopic displacement x_0 of the impact oscillator at steady state when $\dot{x} = 0$, after discarding 6000 impacts. (b) The corresponding LE spectrum. Here, $2.5 \leq \omega \leq 3.5$ and $r = 0.8$.

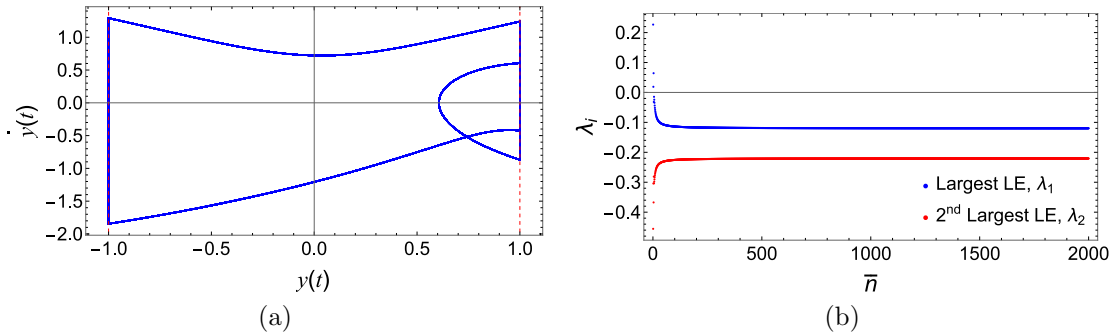

Figure 3.17: (a) Phase portrait of a pair impact oscillator for $\alpha = 1.0$, $\omega = 1.0$ and $r = 0.8$. The red dashed lines denote the presence of un-deformable surfaces $\Sigma_{2a} : (y = \nu/2)$ and $\Sigma_{2b} : (y = -\nu/2)$ (b) The corresponding LE spectrum depicting a stable orbit with negative LEs.

This is because the perturbed vector $\mathbf{y}_+$ gets mapped according to Eq. (3.12). A linear transformation between $\mathbf{y}_+$ and $\mathbf{y}_-$ cannot be written in a closed analytical form. To circumvent this representational issue, one can evaluate the saltation in matrix form via a numerical approach, as described below.

For an n^{th} order dynamical system $\mathbf{x} \in \mathbb{R}^n$, the variational equation whose

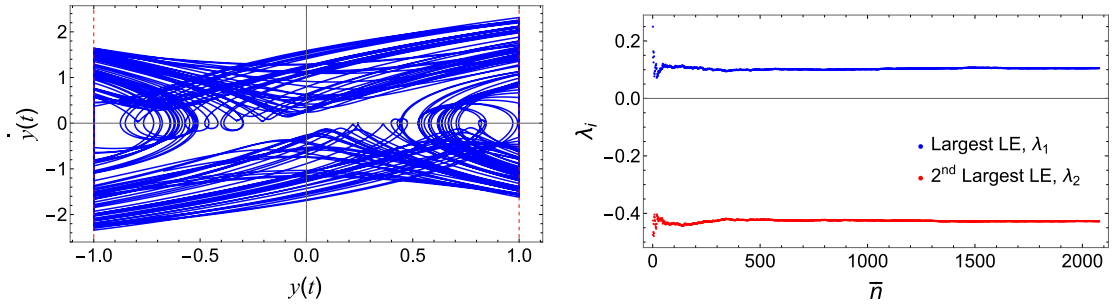

(a) (b)

Figure 3.18: (a) Phase portrait of a pair impact oscillator for $\alpha = 1.5$, $\omega = 1.0$ and $r = 0.8$. The red dashed lines denote impacting barriers placed at $\Sigma_{2a} : (y = \nu/2)$ and $\Sigma_{2b} : (y = -\nu/2)$. (b) The corresponding LE spectrum depicting an unstable orbit with a positive LE.

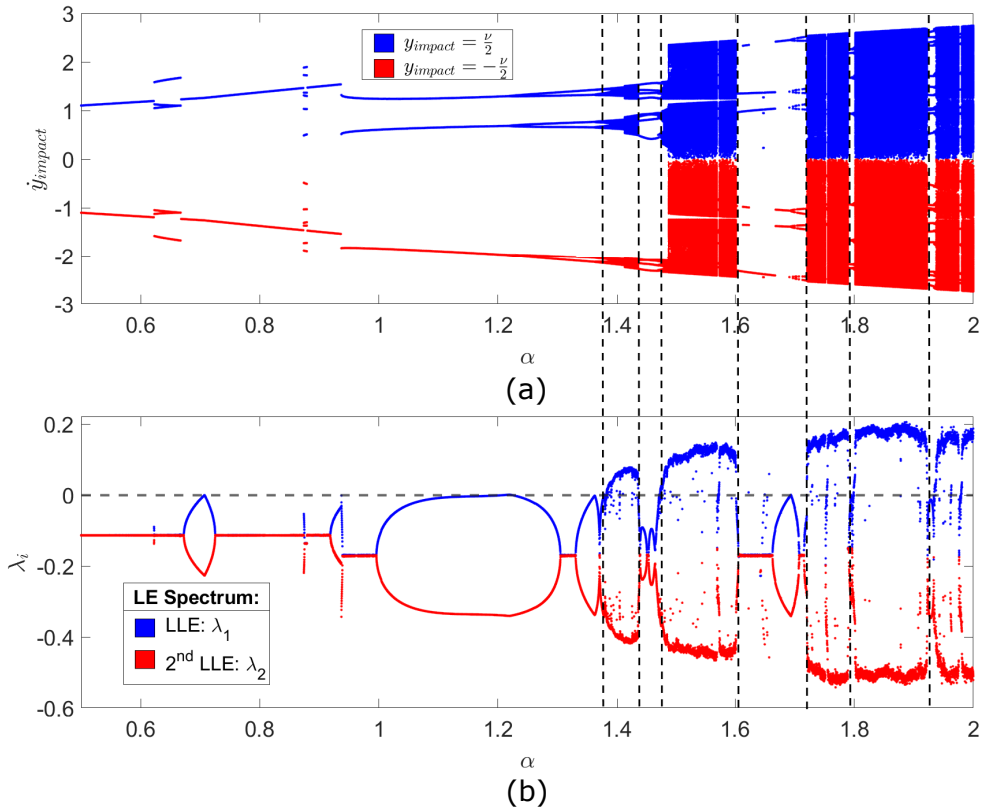

Figure 3.19: (a) Velocity $\dot{y}$ of steady state pair impact oscillator at instants of impact, *i.e.*, $y = \pm\nu/2$, presented as a function of the forcing amplitude α. The first 6000 impacts are discarded. (b) The corresponding LE spectrum. Here, $0.5 \leq \alpha \leq 2.0$, $\omega = 1.0$ and $r = 0.7$.

evolution is governed by terms in the Jacobian (Eq. (3.1)), is numerically integrated. The initial conditions are chosen along n orthogonal vectors and the perturbations are represented by $\mathbf{y}_i$. These vectors are expressed in the form of a matrix as in Eq.

(3.24).

$$\begin{aligned} \mathbf{Y}_{n\times n}(t) &= [\mathbf{y}_1\ \mathbf{y}_2\ \mathbf{y}_3 \dots \mathbf{y}_n], \\ \mathbf{Y}_{n\times n}(0) &= \mathbb{I}_{n\times n} \end{aligned} \tag{3.24}$$

The variational equation coupled to the system is integrated up to the instant of impact of the actual trajectory $\mathbf{x}$. Here, the vectors before and after impact, given by $\mathbf{Y}_{-,impact}$ and $\mathbf{Y}_{+,impact}$ can be expressed as Eq. (3.25).

$$\mathbf{Y}_{+,impact} = \begin{bmatrix} y_{+,1}^{(1)} & \dots & y_{+,n}^{(1)} \\ \vdots & \ddots & \vdots \\ y_{+,1}^{(n)} & \dots & y_{+,n}^{(n)} \end{bmatrix}_{n\times n}, \tag{3.25a}$$

$$\mathbf{Y}_{-,impact} = \begin{bmatrix} y_{-,1}^{(1)} & \dots & y_{-,n}^{(1)} \\ \vdots & \ddots & \vdots \\ y_{-,1}^{(n)} & \dots & y_{-,n}^{(n)} \end{bmatrix}_{n\times n} \tag{3.25b}$$

where $\mathbf{y}_j^{(i)}$ is the i^{th} component of j^{th} vector. A state transition matrix between perturbed vectors $\mathbf{y}_+$ and $\mathbf{y}_-$ at the instant of impact can be expressed as Eq. (3.26).

$$\mathbf{Y}_{+,impact} = \mathbf{S}_2 \cdot \mathbf{Y}_{-,impact} \tag{3.26}$$

Here, $\mathbf{S}_2$ is defined as the higher-order saltation matrix for a dynamical system. The subscript 2 denotes the evaluation of the variational form upto $\mathcal{O}(2)$, which is the entity of interest. Alternatively, this saltation matrix can be expressed as Eq. (3.27).

$$\mathbf{S}_2 = \mathbf{Y}_{+,impact} \cdot \mathbf{Y}_{-,impact}^{-1} \tag{3.27}$$

The RHS of Eq. 3.27 is required to be numerically evaluated. Eigenvalues of the monodromy matrix provide a representation of the local stability of periodic solutions. However, this is applicable only to dynamical systems where the Jacobian matrix has constants as entries or is periodic in time, ensuring that its entries are constant on any lower dimensional section taken along the limit cycle. The two impact oscillators considered in Sec. 3.3 are non-autonomous, with an external forcing period of $2\pi/\omega$. The periodicity of the underlying attractor is numerically determined by integrating the system until it undergoes 2000 impacts per impacting surface. The duration between the recurrence of state $\mathbf{x}$ across a well defined Poincaré section post transience yields the time period of oscillations. Once the time period is calculated, the monodromy matrix is evaluated, which is decomposed into product of STMs between the numerically obtained saltation matrices. The product is taken in the order of occurrence of events, making it essential to evaluate the flight times between impacts as well as the instances of impact. To effectively

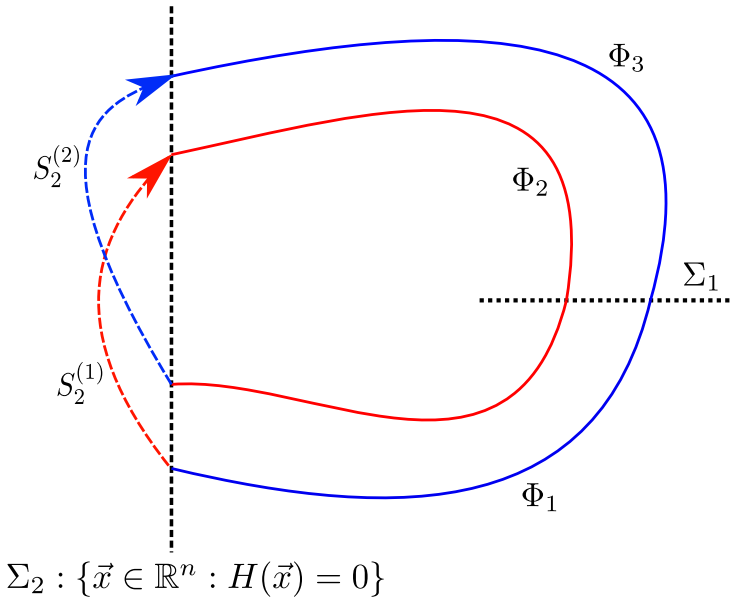

Figure 3.20: The schematic of a period 2 limit cycle undergoing two instances of instantaneous reversals at the instants of impact with Σ_2, depicted as black dashed line. The red solid line corresponds to flow governed by the STM Φ_2, the red dashed line corresponds to state transition at the instant of first impact (using numerically obtained saltation matrix $S_2^{(1)}$), the blue solid line corresponds to flow governed by STM Φ_1, the blue dashed line corresponds to state transition at the instant of second impact (using numerically obtained saltation matrix $S_2^{(2)}$).

demonstrate this, a period 2 limit cycle is considered (Fig. 3.20). Here, $\mathbf{\Phi}_1$, $\mathbf{\Phi}_2$ and $\mathbf{\Phi}_3$ are the state transition matrices obtained from the variational equations depicting the transitions from - (1) the Poincaré section Σ_1 to the first encounter with impact surface Σ_2, (2) mapped $\mathbf{y}_+$ to second encounter with Σ_2, (3) mapped $\mathbf{y}_+$ after second encounter with Σ_2 to Σ_1 respectively, eventually completing a limit cycle with time period T. $\mathbf{S}_2^{(1)}$ and $\mathbf{S}_2^{(2)}$ are the saltation matrices, the closed form expressions for which can be obtained from Eq. (3.27). These saltation terms map the perturbed vectors using Eq. (3.12) at the instant of impact. Therefore, the monodromy matrix $\mathbf{\Phi}$ for this limit cycle with period T, is a resultant of the matrix multiplication given by Eq. (3.28)

$$\mathbf{\Phi}(T) = \mathbf{\Phi}_3 \cdot \mathbf{S}_2^{(2)} \cdot \mathbf{\Phi}_2 \cdot \mathbf{S}_2^{(1)} \cdot \mathbf{\Phi}_1, \tag{3.28}$$

where the order of matrix dot product is important and the state transition matrices satisfy $\mathbf{\Phi}_1(0) = \mathbf{\Phi}_2(0) = \mathbf{\Phi}_3(0) = \mathbb{I}_{n\times n}$. For a hybrid dynamical system starting from an arbitrary Poincaré section Σ_1 and executing n impacts with the boundary Σ_2 and converging to an underlying attractor with period T, the monodromy matrix thus

takes the form represented in Eq. (3.29).

$$\mathbf{\Phi}(T) = \mathbf{\Phi}_n \cdot \prod_{i=1}^{n-1} \mathbf{S}_2^i \cdot \mathbf{\Phi}_i \tag{3.29}$$

where, $\mathbf{\Phi}_i$ is the STM from the Poincaré section Σ_1 to the discontinuous boundary Σ_2. $\mathbf{S}_2^i$ is the saltation matrix evaluated up to $\mathcal{O}(2)$ using Eq. (3.27) and $\mathbf{\Phi}_n$ is the final STM that takes the perturbed trajectory back to the Σ_1 within one time period T. To evaluate the saltation matrix $\mathbf{S}_2$ numerically, initial conditions for the set of orthogonal perturbed vectors in Eq. (3.24) are chosen as a hypersphere of radius r_0. A small number is assigned to r_0 to ensure the perturbations obey the dynamics in the local neighbourhood, governed by the Jacobian (Eqs. (3.24)). Two STMs $\mathbf{Y}_1$ and $\mathbf{Y}_2$ is defined in Eq. (3.30) where $\mathbf{Y}_1$ evaluates the saltation matrix and $\mathbf{Y}_2$ is the STM which maps the perturbed vectors at the instant of impact.

$$\begin{aligned} \mathbf{Y}_1(0) &= r_0 \mathbb{I}_{n\times n}, \text{ for evaluation of } \mathbf{S}_2^i, \\ \mathbf{Y}_2(0) &= \mathbb{I}_{n\times n}, \text{ for evaluation of } \mathbf{\Phi}_i \end{aligned} \tag{3.30}$$

The eigenvalues of the monodromy matrix, also known as the Floquet multipliers, are numerically obtained by solving Eq. (3.29). For a dynamical system of $\mathbb{R}^n$, complex conjugate pairs of eigenvalues exist for oscillatory solutions. Magnitudes of the eigenvalues are indicators of stability of an orbit under consideration. Periodic trajectories yield eigenvalues that lie within the unit circle in the Argand plane. Eigenvalues with magnitude greater than unity denote that perturbed trajectories from the periodic orbit diverges. For aperiodic solutions corresponding to exponentially diverging trajectories, the Floquet multipliers has been calculated from the monodromy matrix for a default time period of 100s *i.e.*, $\Phi(T = 100)$. Appendix B describes the method of obtaining higher-order saltation matrices along with the monodromy matrix and its subsequent Floquet multipliers by incorporating higher-order TDM.

3.5.1 Impact oscillator

Stability analysis of the impact oscillator (Eq. (3.17)) is evaluated by computing the period of the underlying attractor by integrating the system after 2000 impacts and observing the recurring times of return state x lying on the orbit at section $\dot{x} = 0$. For the chosen bifurcation parameter ω, the impact oscillator is expressed in the state space form (Eq. (3.1)) and is integrated for one period. At the instant of impact, the saltation matrix $\mathbf{S}_2$ (Eq. (3.27)) is numerically calculated using TDM defined by Eq. (3.22) for the impact oscillator. The monodromy matrix is evaluated using Eq. (3.29) followed by an eigenvalue analysis to determine the stability of the

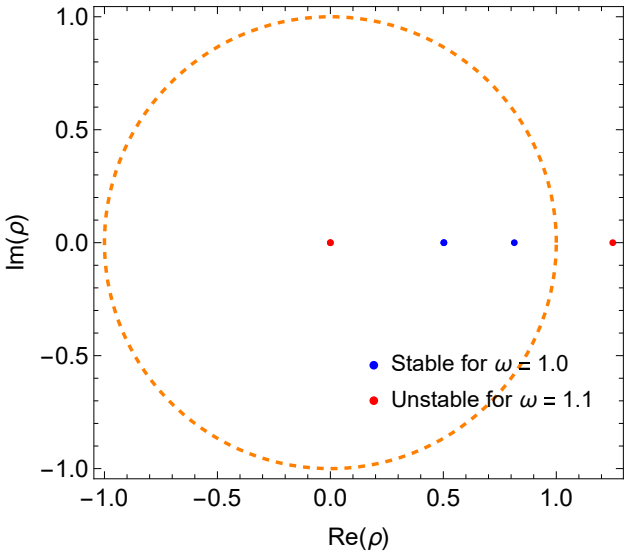

Figure 3.21: Floquet multipliers for the impact oscillator showing eigenvalues of a stable and an unstable periodic solution corresponding to $\omega = 1.0$ and $\omega = 1.1$ in red and blue respectively. The dashed orange circle of unit radius encloses eigenvalues corresponding to stable periodic solutions.

respective limit cycle for a given parameter ω. In Fig. 3.21, the eigenvalues of $\mathbf{\Phi}(T)$ are shown in the complex plane for external frequency ω of 1.0 and 1.1, respectively.

It is observed that the eigenvalues corresponding to $\omega = 1.0$ in Fig. 3.21 are within the unit circle $z = e^{i\theta}$. Therefore it is inferred that the respective limit cycle is stable. This inference is also backed by the phase portrait and the Lyapunov spectrum presented in Fig. 3.12. However, one of the eigenvalues for $\omega = 1.1$ is outside the unit circle and thus the perturbations grow along an eigen direction leading to divergence in trajectories. The underlying chaotic behaviour can be observed in Fig. 3.13. It is evident that the respective trajectory in the state space is aperiodic while the largest Lyapunov exponent is positive. In Fig. 3.22(b), the magnitude of both the Floquet multipliers against ω driving the impact oscillator is shown. A bifurcation diagram of the impact oscillator's amplitude at steady state against ω is shown in Fig. 3.22(a) for reference. Dashed vertical lines are shown for comparison between the bifurcation diagram and the corresponding LEs, highlighting some of the aperiodic chaotic solutions. The bifurcation parameter ω ranges from $0.5 \leq \omega \leq 5.0$ and the dashed horizontal line in Fig. 3.22(b) separates the stable region from trajectories diverging from the periodic limit cycle, while those greater than one correspond to divergent trajectories. Those below the dashed line of $\|\rho\| = 1$ correspond to stable trajectories for the respective ω. Fig. 3.23 depicts the real and imaginary part of the Floquet multipliers in the complex plane against ω. The blue cylinder of radius 1 in the figure depicts the stable region. All points within the cylinder represent the occurrence of stable limit cycles while the scattered

points lying outside this cylinder with $\|\rho\| \geq 1$ corresponds to diverging trajectories in the state space. Since trajectories near the periodic limit cycle exponentially diverge, eigenvalues corresponding to unstable limit cycles are scaled down to populate the plot within the defined range for easier visual representation (Figs. 3.22(b), 3.23).

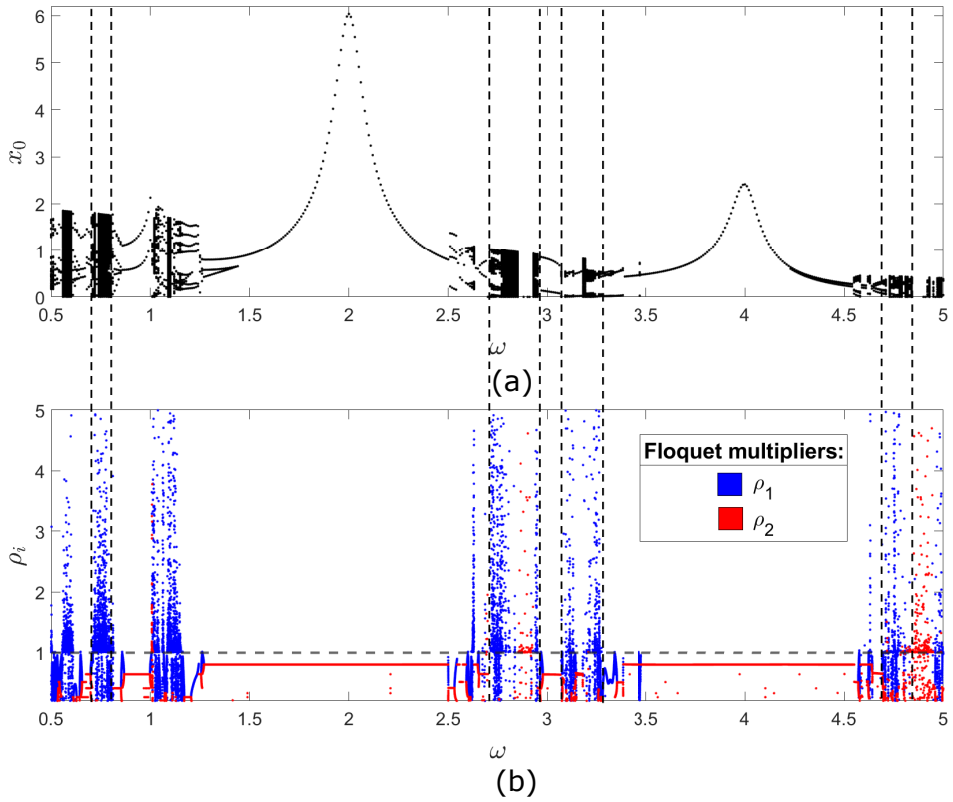

Figure 3.22: (a) Bifurcation diagram of stroboscopic displacement x_0 of the impact oscillator at steady state when $\dot{x} = 0$. Here, 6000 impacts are plotted. (b) The corresponding Floquet multipliers for $0.5 \leq \omega \leq 5.0$. Here, $r = 0.8$.

3.5.2 Pair impact oscillator

Stability analysis of the pair impact oscillator described by Eqs. (3.20) is computed after 4000 impacts since there are two impacting surfaces Σ_2 at $\pm\nu/2$. The bifurcation parameter is the amplitude α of the external periodic force which drives the cart with frequency $\omega = 1.0$. The time period of a periodic limit cycle for a given value of α is evaluated numerically from the recurring time when $\mathbf{y}$ (see Eq. (3.20)) intersects the Poincaré section $y = 0$. The saltation matrix is calculated using the TDM defined in Eq. (3.23) at the instant of impacts with either impacting surfaces. The monodromy matrix is evaluated numerically from the deduced STMs and saltation matrices as defined in Eq. (3.29). The eigenvalues of the obtained monodromy

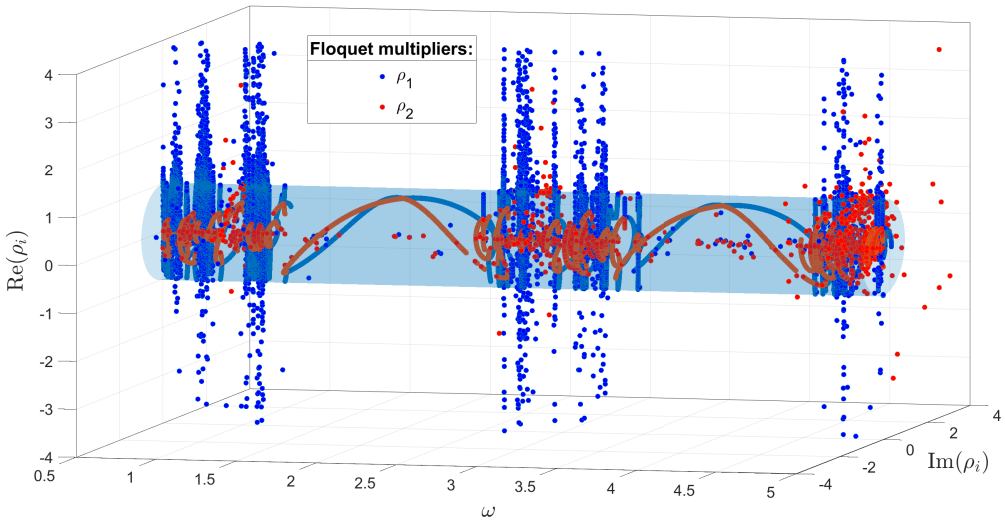

Figure 3.23: Floquet multipliers of the impact oscillator in the complex plane against the frequency of the harmonic excitation $0.5 \leq \omega \leq 5.0$ for $r = 0.8$. The blue cylinder of unit radius is the region enclosing Floquet multipliers corresponding to stable periodic solutions.

matrix $\mathbf{\Phi}$ are obtained for a given value of α, which is then used to deduce the stability of the attractors of the pair impact oscillator.

In Fig. 3.24, the Floquet multipliers of the pair impact oscillator for forcing amplitude of values 1.0 and 1.5 respectively is shown. The eigenvalues for $\alpha = 1.0$ is within the unit circle, implying the oscillator is stable. This is also confirmed by the observations from the phase-portrait and the respective Lyapunov spectrum (Fig. 3.17). However, one of the eigenvalues for $\alpha = 1.5$ is outside the unit circle and the corresponding limit cycle shows a diverging trajectory. This is also seen in Fig. 3.18 where the state space is chaotic and the LLE is positive.

In Fig. 3.25(b), the magnitude of Floquet multipliers for the pair impact oscillator against the bifurcation parameter α is shown. A bifurcation diagram of the velocity $\dot{y}$ at the instant of impact is shown against α for reference in Fig. 3.25(a). The dashed line where $\|\rho\| = 1$ separates the stable periodic limit cycles from the unstable diverging trajectories. $\|\rho\| \geq 1$ corresponds to values of α for which trajectories near the periodic limit cycle diverges according to Floquet theory. Figure 3.26 shows the real and imaginary parts of the Floquet multiplier ρ_i for different values of α. Eigenvalues that lie outside the cylinder with unit radius correspond to diverging trajectories for the respective α. Such eigenvalues with $\|\rho\| >> 1$ are scaled down for representation as described previously.

Pair-impact or vibro-impact oscillators are often being used as an excellent replacement as passive and adaptive controllers to reduce large-amplitude vibrations of the primary structure via nonlinear coupling [40, 71, 70]. In such devices, also known

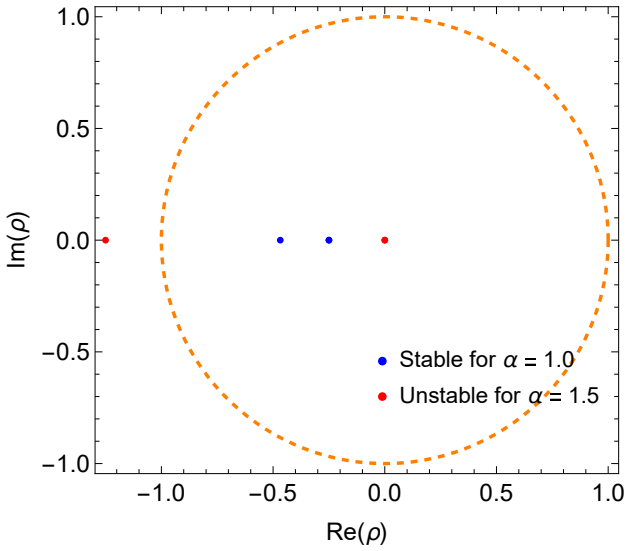

Figure 3.24: Floquet multipliers for the pair impact oscillator showing eigenvalues of a stable and an unstable periodic solution corresponding to $\alpha = 1.0$ and $\alpha = 1.5$, in blue and red respectively. The dashed orange circle is of unit radius.

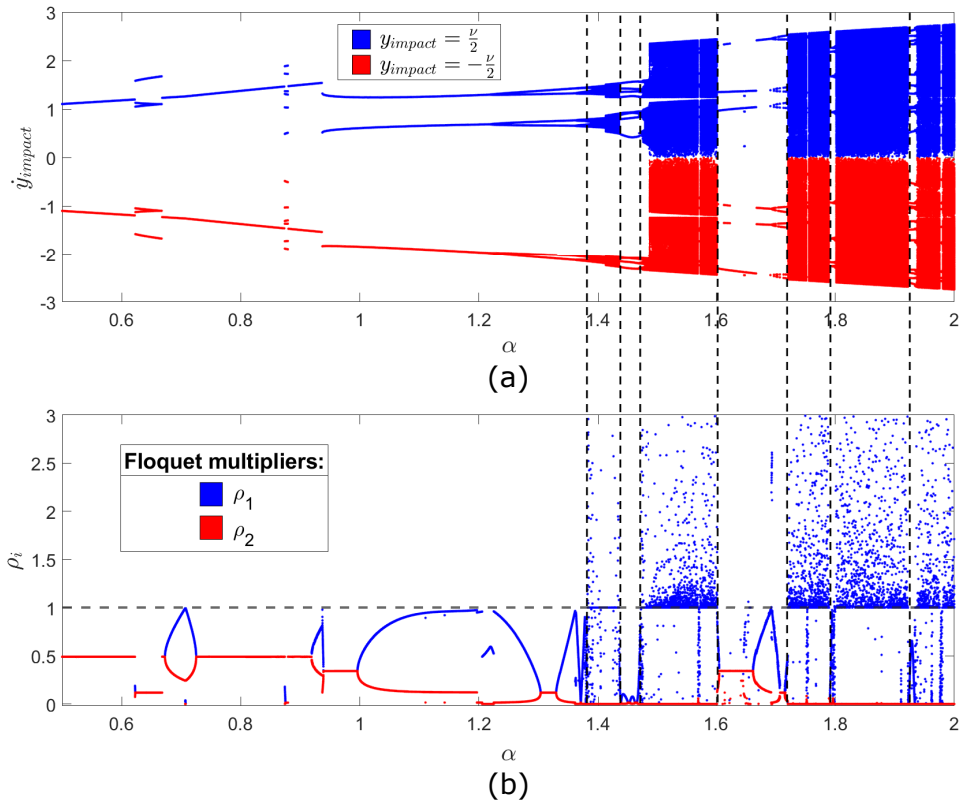

Figure 3.25: (a) Velocity $\dot{y}$ of the steady state pair impact oscillator at instant of impact, *i.e.*, $y = \pm\nu/2$. The initial 6000 impacts are disregarded in the computations. (b) The corresponding Floquet multipliers of pair impact oscillator for $0.5 \leq \alpha \leq 2.0$, $\omega = 1.0$ and $r = 0.7$.

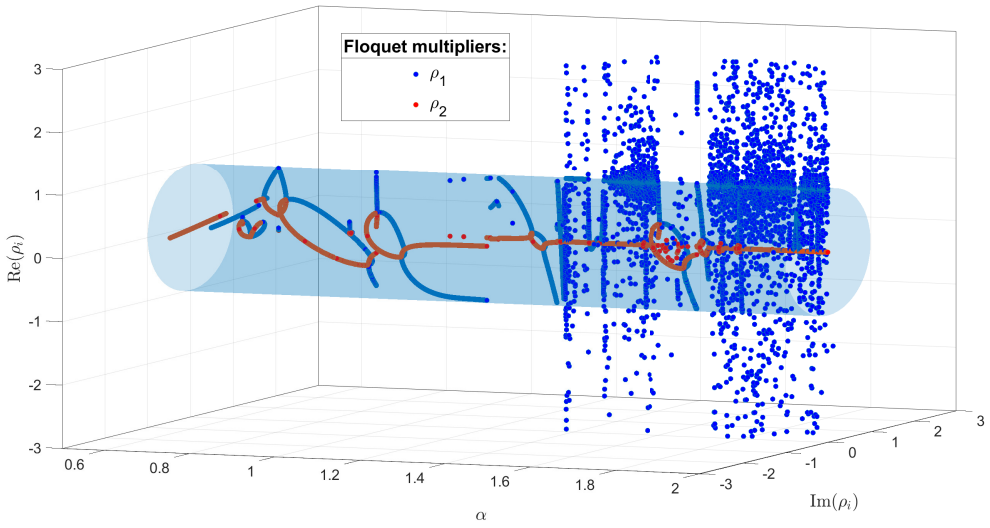

Figure 3.26: Floquet multipliers of the pair impact oscillator in the complex plane for $0.5 \leq \alpha \leq 2.0$, $\omega = 1.0$ and $r = 0.7$. The blue cylinder of unit radius is the region enclosing Floquet multipliers corresponding to stable periodic solutions for the respective α.

as a vibro-impact nonlinear energy sink (VINES), a pair-impact or vibro-impact oscillator is placed inside the primary structure and behaves as a coupled system [71]. Therefore, VINES act as passive absorbers by transferring the energy (also known as Targeted Energy Transfer, (TET) [126, 125]) from the primary structure to itself for a wide range of frequencies and perform better than conventional tuned-mass dampers [20]. Li et al. [71] showed that maximum reduction in vibrations of the primary structure via nonlinear TET occurs when the pair-impact oscillator shows steady state period one or P1 orbit. This phenomenon is known as $1:1$ resonance (two symmetric impacts between one time period) between the impact oscillator and the primary structure in the literature around VINES. Therefore, the higher-order TDM derived here can be implemented to predict the occurrence of impacts in devices like VINES correctly. Additionally, the algorithms developed in this chapter can be used to investigate the stability of P1 orbits in VINES devices via Floquet multipliers and Lyapunov exponents. Further, Li et al. [69] recently proposed a new electromagnetic energy harvesting system that can efficiently harvest energy from a VINES during a $1:1$ resonance. This is achieved by attaching an electromagnet on the primary structure with a cavity while a magnet replaces the vibro-impact oscillator. The primary goal is to store the energy in the electromagnet (based on Lenz's law [46]) surrounding the impact oscillator, which operates at $1:1$ resonance during which maximum TET occurs from the primary structure. Since the stability of a period one or P1 orbit is crucial in such vibrational energy harvesters (VEHs) like VINES, the higher-order flight time derived in the chapter can effectively detect

impact occurrence and further estimate the stability of P1 orbits, which show 1 : 1 resonance with the primary structure.

Next, the algorithms for Floquet and Lyapunov exponents are validated in a scenario where period-adding cascade of bifurcations is commonly observed in impact oscillators. A damped impact oscillator is considered, similar to Figs. 3.3 and 3.4. With a damping term of $2\xi\dot{x}$ on the left hand side in Eq. (3.17), the barrier distance is varied for fixed values of $\xi = 2.0$, $\omega = 1.8$ and $r = 0.8$. At the instant of a impact, the TDM for the damped impact oscillator is given by Eq. (3.31)

$$\mathbf{y}_+ = \begin{bmatrix} y_1 + \delta v_-(1+r) + \delta y_2(1-r^2) + \dfrac{\delta^2}{2}(-\sigma + \cos(\omega t))(1-r-2r^2) \\ \qquad - \; v_- \xi \delta^2 (1-r^2) \\ -r y_2 - r\delta(-\sigma - 2\xi v_- + \cos(\omega t)) - \delta(-\sigma + 2r\xi v_- + \cos(\omega t)) + \\ r\delta(y_1 + 2y_2\xi) + \dfrac{r\delta^2}{2}(v_- + 2\xi(-\sigma - 2\xi v_- + \cos(\omega t)) + \omega \sin(\omega t)) + \\ \delta(y_1 + 2r^2 y_2 \xi) + \delta^2(v_- + 2r^2\xi(-\sigma - 2\xi v_- + \cos(\omega t)) + \omega \sin(\omega t)) + \\ \dfrac{\delta^2}{2}(r v_- + 2r\xi(-\sigma + 2r\xi v_- + \cos(\omega t)) - \omega \sin(\omega t)) \end{bmatrix}_{2\times 1} \tag{3.31}$$

The TDM in Eq. (3.31) depends on system parameters like ξ and ω. The linearized saltation matrix is independent of the damping term ξ, which leads to an incorrect prediction of an impact while the higher-order approach rectifies this. Implementing Eq. (3.31), the exponents for two different ranges of barrier distance varying between $-0.1324 \leq \sigma \leq -0.10$ and $-0.1326 \leq \sigma \leq -0.1319$ are shown in Figs. 3.27(b) and 3.28(b). A comparison between numerically obtained exponents and amplitude responses is presented in Figs. 3.27(a) and 3.28 (a). Period-adding cascades of solutions separated by chaotic orbits was observed here with periodicity P# being defined as the number of intersections with a Poincaré section $\Sigma_1 : x = 0$ with $\ddot{x} < 0$. Results indicate that both Floquet multipliers are less than unity for a stable periodic orbit. Additionally, one of the Floquet multiplier approaches and becomes -1 at the exact location where a discontinuity-induced bifurcation to a higher periodic orbit occurs. This is apparent in Figs. 3.27 and 3.28. Floquet theory in only applicable for dynamical systems where the Jacobian matrix is periodic. Hence, to validate the presence of chaotic orbits observed in the amplitude response separating any two periodic orbits, the largest Lyapunov exponent is calculated and shown in Figs. 3.29 and 3.30. It was observed that the LLE is always negative for stable periodic orbits and approaches zero at the exact value where a discontinuity-induced bifurcation is observed in the amplitude response. Also, the LLE is always positive in a narrow range between two periodic solutions which indicates the presence of chaotic orbits sandwiched between the period-adding cascades observed here. A compari-

son with the bifurcations observed in amplitude response verifies this result. Thus the methodology proposed here implementing higher order corrections to the TDM can correctly predict the outcome of systems undergoing impact. Note that the proposed algorithms to calculate Lyapunov exponents and Floquet multipliers validate the accuracy of the numerically obtained higher-order saltation matrix, which can naturally be extended to include further higher-order corrections if necessary, depending on the application. Comparison of Floquet multipliers and bifurcation diagrams obtained using the first-order and higher-order TDM show similar results. This is primarily because the states predicted post-impact using the first and higher-order TDM differ due to different flight time estimates - yet the states are closer to the steady state limit cycle. Although the monodromy matrices calculated from different states post-impact differ, their eigenvalues are similar. A mathematical proof of this theorem can be found in Nayfeh and Balachandran [82].

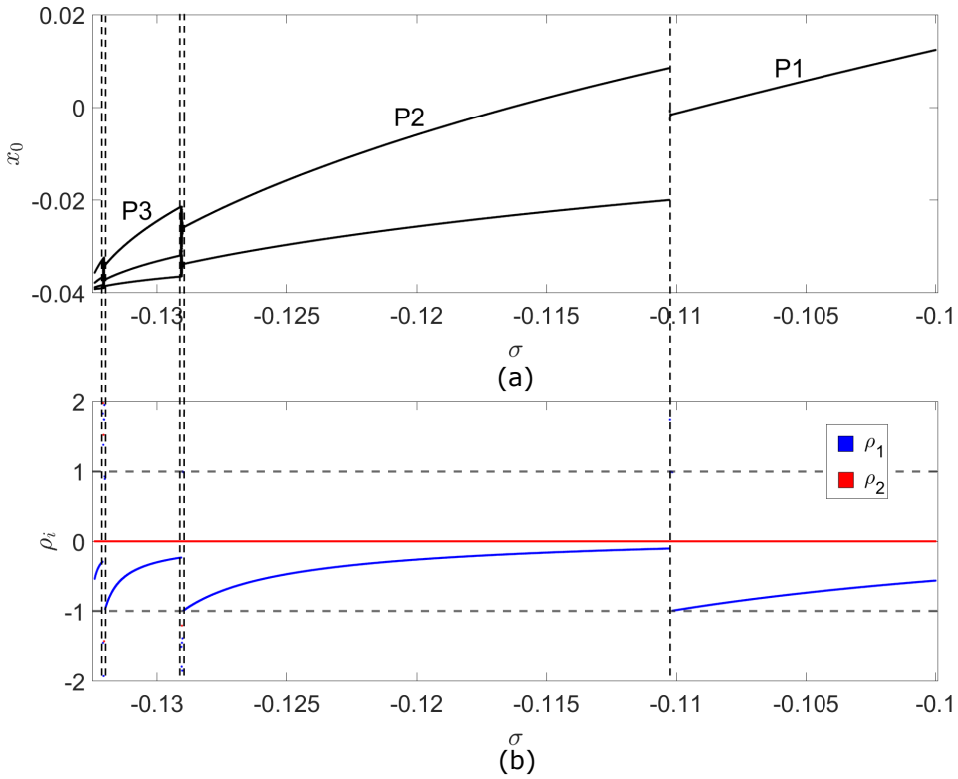

Figure 3.27: (a) Bifurcation diagram of stroboscopic displacement and (b) the corresponding Floquet multipliers for the damped impact oscillator vs barrier position ranging between $-0.1324 \leq \sigma \leq -0.10$, $\xi = 2.0$, $\omega = 1.8$ and $r = 0.8$. The bounded region $-1 \leq \rho \leq 1$ is the stable region.

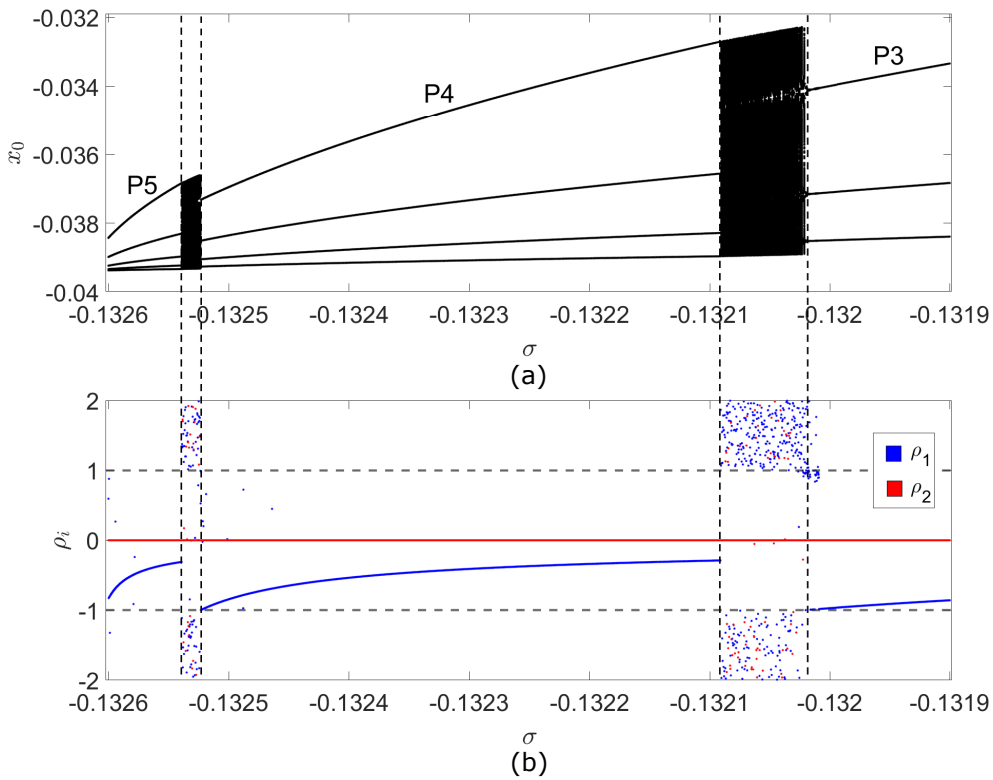

Figure 3.28: (a) Bifurcation diagram of stroboscopic displacement and (b) the corresponding Floquet multipliers for the damped impact oscillator vs barrier position ranging between $-0.1326 \leq \sigma \leq -0.1319$, $\xi = 2.0$, $\omega = 1.8$ and $r = 0.8$.

3.6 Conclusions

For a hybrid dynamical system of any order $\mathbb{R}^n$, a closed form expression of transverse discontinuity mapping (TDM) with higher-order corrections has been presented. This formulation is superior to the existing first order approach as it avoids incorrect identification of an impact, along with subsequent estimates of the state space of the system with implications on their stability. Additionally, the formulation establishes alignment with variational approach. Efficacy of the proposed approach is demonstrated by two examples. Stability of these hybrid systems encountering impact with immovable barrier(s) and mapped using higher-order saltation terms is investigated.

For perturbed trajectories in the vicinity of an invariant set, dynamics at the discontinuity boundary has been derived in closed form. This closed form with higher-order corrections to flight times of the perturbed trajectories at the instant of impact yields significantly better analytical estimates by incorporating system parameters and the functional form of the driving force of hybrid system under consideration. This explicit dependence on crucial parameters like the driving force is absent in a linearized approximation. As a result, the linearized approximations incorrectly predict a impact unlike what is demonstrated by numerical simulations.

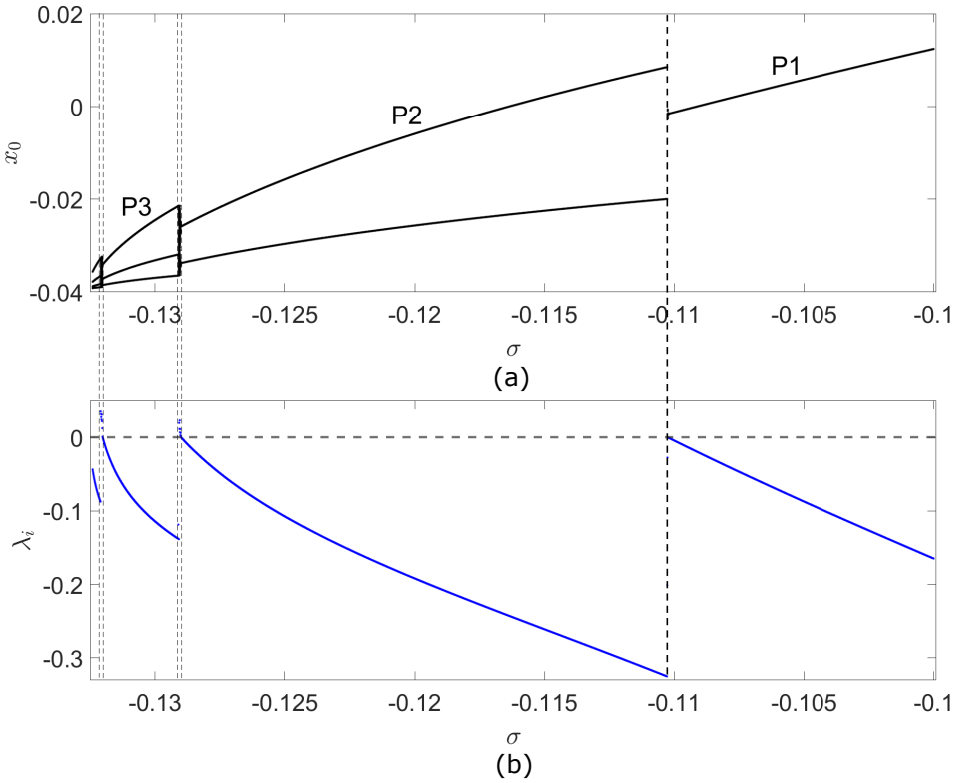

Figure 3.29: (a) Bifurcation diagram of stroboscopic displacement and (b) Largest Lyapunov exponent of the damped impact oscillator vs barrier position ranging between $-0.1324 \leq \sigma \leq -0.10$, $\xi = 2.0$, $\omega = 1.8$ and $r = 0.8$.

Moreover, results implementing the higher-order saltation terms are applicable when the initial separation between trajectories is such that it leads to a large difference in impact times. A higher periodic or aperiodic trajectory would be effectively analytically mapped with the help of the proposed formalism.

An algorithm to compute stability estimates using higher-order TDM to evaluate the LE spectra was proposed along with its implementation considerations. This method does not require any prior knowledge of the analytical solution at the instant of impact, unlike analytical forms in transcendental maps. With driving force frequency as the bifurcation parameter, bifurcation diagrams were obtained to corroborate stability estimates obtained for underlying attractors. The Lyapunov spectrum is observed to be consistent with the results obtained from bifurcation analysis, even when finer step sizes near bifurcation boundaries were examined.

A numerical approach to obtain the saltation matrix at the discontinuity boundary with higher-order corrections was proposed as well. Here, to accommodate second order terms within the matrix form, a numerical approach for matrix inversion is suggested. This formulation can be extended to even higher terms. Monodromy matrices for the hybrid systems under consideration were subsequently computed and an eigenvalue analysis provided the respective Floquet multipliers. The dynami-

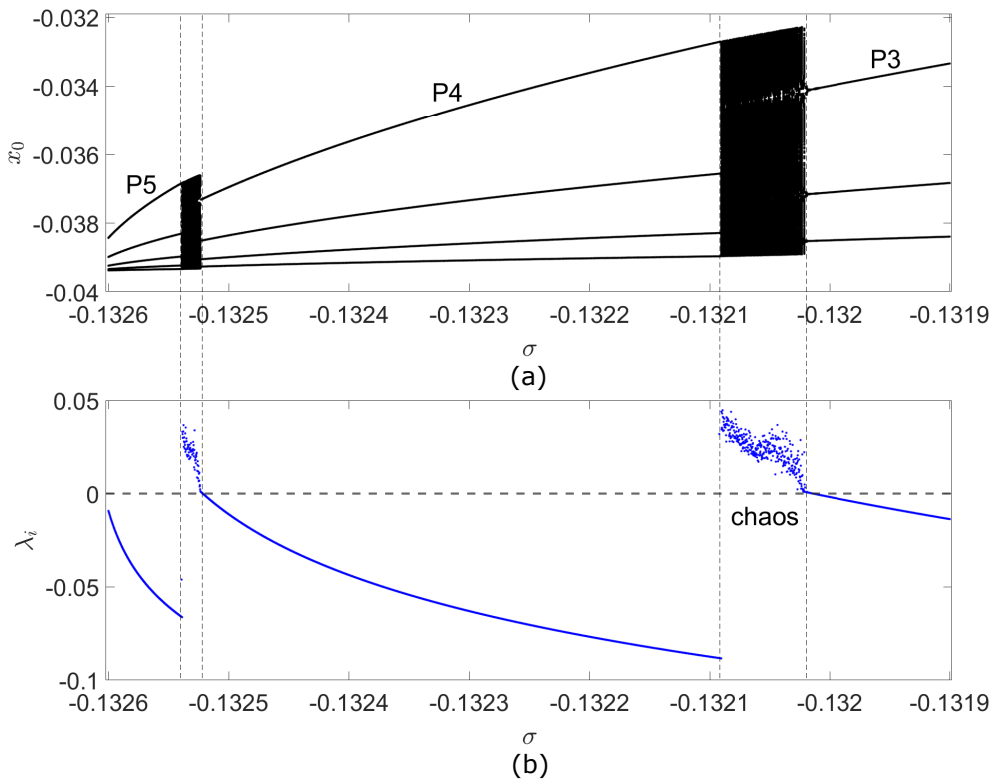

Figure 3.30: (a) Bifurcation diagram of stroboscopic displacement and (b) Largest Lyapunov exponent of the damped impact oscillator vs barrier position ranging between $-0.1326 \leq \sigma \leq -0.1319$, $\xi = 2.0$, $\omega = 1.8$ and $r = 0.8$.

cal behavior depicted via examination of the Floquet multipliers and the bifurcation diagram are in agreement with each other.

The results from this work are directly applicable for the study of complex higher periodic or aperiodic orbits in hybrid systems of any order $\mathbb{R}^n$. One can obtain analytically accurate estimates for trajectories interacting with the discontinuity boundary and quantify stability, especially near bifurcation regimes when one of the attractors loses stability and/or new stable states are born. A further extension of this work to Filippov systems has been presented in Chapter 6.

Chapter 4

Wake induced response of a hybrid fluid-structure interaction system

This chapter investigates the bifurcation behavior of wake-induced vibro-impacting systems considering fluid-structure interaction (FSI). The primary structure and the near wake dynamics are modeled as a harmonic oscillator and a Van der Pol oscillator, respectively, and are weakly coupled to each other. A non-deformable barrier obstructing the motion of the oscillator gives rise to the impacting dynamics. Instantaneous velocity reversal occurs when the structure impacts this barrier. Qualitative changes in the dynamical behavior of this system are investigated in the context of discontinuity-induced bifurcations resulting from the interaction of fluid flow and non-smoothness from the primary structure. Phenomenological behavior like the co-existence of attractors and period-adding cascades of limit cycles leading to chaos are examined. The existence of these phenomena is demonstrated via stability analysis using Floquet theory and associated Lyapunov spectra. A new approach to capture the impact dynamics of the hybrid system through a transverse discontinuity map is proposed. Orbits obtained using this new algorithm are demonstrated to accurately predict both stable and chaotic regimes as observed from the corresponding bifurcation diagrams. The effect of non-smoothness on the lock-in phenomenon in systems that involve FSI is studied for the first time.

4.1 Introduction

Vortex-induced vibration is commonly observed in nature as well as in various bluff-body-shaped engineering structures. Although the VIV characteristics of cylindrical structures are extensively studied in the literature [135, 134], the dynamical behaviour of such systems when impacting with rigid barriers is inadequately explored. Such a scenario can arise during lifetime operations of large submerged structures like trash racks of hydro-power stations and ship mooring lines, when

the structure undergoes large amplitude oscillations resulting in an impact with a nearby secondary structure. Such impacts are often due to loosened joints of lack of clearance. Consequently, there is a need to understand this dynamics. However, there is a shortage of literature on this subject.

Low-fidelity models are widely used to study vortex-induced dynamics in structures immersed in fluids [32]. Such models have been observed to effectively capture the qualitative aspects of various phenomena exhibited by two-way coupled fluid-solid systems. On the other hand, exhaustive sets of experiments pose a challenge in isolating the effects of a single parameter while direct numerical simulation (DNS) of the Navier-Stokes equations are computationally expensive [83]. For low order models, similar to the approach taken in this chapter, the near wake dynamics is typically described by a single variable that captures the fluctuating nature of vortex shedding and the associated periodic aerodynamic forces. This variable can be represented by the parameter of the non-dimensionalized Van der Pol oscillator that exhibits self-sustained limit-cycle oscillations (LCOs). With this low ordering modeling approach in mind, the idealized approximation of a bluff body immersed in fluid and executing VIV is a single-degree-of-freedom (SDOF) elastically linear harmonic oscillator coupled with a Van der Pol oscillator[32]. A detailed qualitative and quantitative review on phenomenological models and experimental studies on VIV can be found in [103, 38, 135, 134].

Many such phenomenological models have been developed since the concept of a wake oscillator was first introduced by Bishop and Hassan [15]. Balasubramanian and Skop [3] modelled the near wake dynamics interacting with a cylindrical bluff body using a coupled Van der Pol oscillator. Later, Skop [112] modified the wake oscillator by introducing a stall parameter. Other wake oscillator models like the Rayleigh oscillator were considered by Hartlen and Currie [49]; where the damping term was proportional to the velocity quadratically. Krenk and Nielsen [62] adapted this wake oscillator by considering a quadratic velocity damping in the coupled Van der Pol system *i.e.,* a combination of Rayleigh-Van der Pol wake oscillator. Recent developments of the wake oscillator model can be found in [91, 100].

VIV is characterized by the phenomenon of lock-in or synchronization, which occurs when the vortex shedding frequency approaches the structure's natural frequency resulting in large amplitude periodic oscillations. To accurately capture the lock-in phenomenon, modelling the coupling between the wake oscillator and the structural oscillator is crucial. Hartlen and Currie [49] initially considered a rather arbitrary velocity coupling between the two systems. Later, this velocity coupling was also adapted by Mureithi *et al.* [81] and Plaschko [98] . In 2004, Facchinetti *et al.* [32] proposed an acceleration coupling between the wake and structure oscillator to model the effect of the structure's motion on the wake dynamics.

Experiments conducted by Govardhan and Williamson [42, 43] reveal that the

amplitude response observed on varying the fluid-flow velocity of an elastically mounted cylinder undergoing VIV comprises of three different bifurcation branches depending on the mass ratio m^* (cylinder mass/fluid added mass) [42]. When the mass ratio of the FSI system is less than the critical value of 0.54, the lower branch ceases to exist and only a large amplitude response of the structure corresponding to the upper branch is observed for all higher values of U_r. Thus the upper branch continues indefinitely and the synchronization range extends to infinity. A comparison between the results obtained from the acceleration coupling model by Facchinetti *et al.* [32] with that of the experiments by Govardhan *et. al* [42] and Khalak *et. al* [58] show close qualitative agreements in the amplitude responses in this regime. Therefore, such phenomenological models can be used to qualitatively and quantitatively capture the essential physics underpinning the dynamics of VIV systems.

It is worth noting that the response dynamics of a VIV system subjected to the impacts with rigid barriers is yet to be explored. This study presents a numerical investigation of the effect of a rigid barrier obstructing the motion of a structure exhibiting VIV. A rigid barrier is considered with the assumption that the structural deformation due to such impacts is negligible. Dynamical systems with abrupt motion interactions are studied under the purview of piecewise-smooth (PWS) systems. To explore how non-smoothness impacts synchronization, regimes in which a lack of barriers result in a lock-in or synchronization have been examined.

PWS systems often exhibit contrasting bifurcation behaviour compared to smooth systems. This non-smooth transition divides the phase space into sub-spaces by what is known as the discontinuity boundary. An impact occurs when orbits in phase space interact with this boundary. A typical feature observed due to an impact is discontinuity-induced bifurcation (DIB), resulting in occurrences like grazing [7], sticking-sliding [31] and chattering [17] near the discontinuity boundary [14]. DIBs often lead to period adding cascades of steady states, interspersed with aperiodic or chaotic solutions or unconventional routes to chaos *i.e.*, via grazing [87, 22, 54, 89, 2, 21]. Understanding the dynamical behaviour of coupled fluid-solid systems in the existence of a barrier is thus crucial to their design and lifetime operations.

In this study, a non-smooth FSI system undergoing VIV with mass ratio $m^* = 0.52$ (below the critical value) is considered. A low order model proposed by Facchinetti *et al.* [32] has been adopted to capture the transition from the pre-lock-in lower amplitude response to the higher amplitude upper branch in the sustained lock-in regime for higher values of U_r. The structure is represented by a SDOF oscillator and the wake is modelled using a Van der Pol oscillator. The structure is coupled linearly to the wake variable and the effect of the the motion of the structure on wake dynamics is modelled via an acceleration coupling. Non-smoothness

manifests in this system due to the presence of a rigid barrier. Upon interaction with the structure, it leads to an instantaneous velocity reversal which is modeled via a restitutive law. A detailed numerical investigation of the amplitude response of the structure is carried out in this study. Rich dynamical behaviour like period-adding cascade of solutions separated by aperiodic chaotic solutions is anticipated here due to the presence of a non-smooth barrier. Stability analysis using Floquet theory is carried out to establish the presence of chaotic attractors [82], along with estimates of Lyapunov exponents. It is crucial to note that the numerical evaluation of the Floquet and Lyapunov spectrum is not straightforward here as compared to smooth systems [117, 4, 67]. This is because infinitesimally close trajectories do not interact with the border at the same time. There exists a time difference between such events and an incorrect mapping of the state at the instant of impact with the barrier will lead to an incorrect prediction of the state. Thus the variational equations, that form the underlying basis of the above-mentioned analyses, require careful consideration. The infinitesimally perturbed trajectories get mapped, at such instances, via a transverse discontinuity mapping (TDM) [80, 14, 24, 21, 137]. TDM implements a corrected state transition matrix at the instant of impact, which subsequently ensures that the nearby trajectories are mapped accurately. This chapter implements a $\mathcal{O}(1)$ TDM (also known as the saltation term) for transversal collisions with the discontinuity boundary. Using this approach, the Floquet and Lyapunov spectra are numerically obtained and the corresponding bifurcation behaviour is analyzed.

The remainder of this chapter is structured as follows. Section 4.2 discusses the FSI model undergoing motion in the presence of a rigid barrier, obstructing its motion. In Sec. 4.3 the bifurcation behaviour is described. Section 4.4 discusses stability analysis. The analytical form of the TDM at impact is derived and algorithmic details have been presented here. Section 4.5 summarizes the findings of this study.

4.2 Problem definition and governing equations

Figure. 4.1 depicts a SDOF cylinder of diameter D subjected to a cross flow velocity U. The structure exhibits limit-cycle oscillations due to its interaction with the surrounding wake. The motion of the structure is modelled as a linear oscillator $Y(\tau)$ and the periodic lift force acting on the structure is modeled using a Van der Pol oscillator $X(\tau)$ as given by Eq. (4.1).

$$\begin{aligned} mY'' + hY + \varrho Y' &= S, \\ X'' + \Omega_f^2 X + \epsilon\Omega_f(X^2 - 1)X' &= F. \end{aligned} \tag{4.1}$$

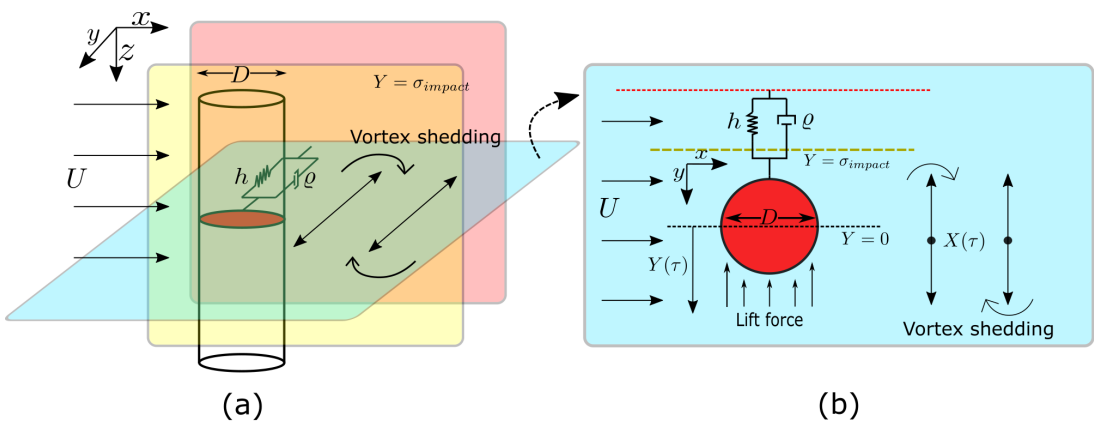

Figure 4.1: (a) A three-dimensional schematic representation of a cylinder of diameter D with uni-directional motion in the transverse cross-flow direction y. A rigid barrier shown in yellow is placed at $Y = \sigma$, obstructing the motion of the cylinder executing VIV. (b) A two-dimensional schematic representation depicting the setup. Lift force being exerted by the fluid on the cylinder in transverse direction to the flow.

The prime denotes a derivative with respect to the dimensional time τ. The mass of the oscillator m is composed of the mass of the cylinder m_s and the fluid-added mass m_f [16], defined as $m = m_s + m_f$. The fluid-added mass is a function of the added mass coefficient C_m, density of fluid ρ and D, defined as $m_f = C_m \rho D^2 \pi/4$. The damping coefficient of the oscillator ϱ comprises damping effects due to the structure r_s and fluid-added damping r_f. The fluid-added damping is a function of stall parameter γ, ρ, D and frequency Ω, defined as $r_f = \gamma \Omega \rho D^2$. In this case, where the structure is undergoing VIV due to cross-flow, Ω is the frequency of the periodic lift force Ω_f. The natural frequency of the structure is defined as $\Omega_s^2 = h/m$ where h is the stiffness of the oscillator. S depicts the lift force acting on the structure due to its interaction with the cross-flow fluid. The nonlinearity of the Van der Pol oscillator is governed by ϵ and F denotes the effects of the structure's motion on the wake dynamics. Using the non-dimensional mass ratio $\mu = m/\rho D^2$, the Strouhal number $S_t = \Omega_f D/2\pi U$, the damping ratio $\xi = r_s/2m\Omega_s$, dimensionless displacement of the structure $y = Y/D$, dimensionless time $t = \Omega_f \tau$, and $\delta = \Omega_s/\Omega_f$, $s = S/m\Omega_f D$, $f = F/D\Omega_f$, Eq. (4.1) can be non-dimensionalized as

$$\begin{aligned} \ddot{y} + \delta^2 y + (2\xi\delta + \frac{\gamma}{\mu})\dot{y} &= s, \\ \ddot{x} + x + \epsilon(x^2 - 1)\dot{x} &= f. \end{aligned} \tag{4.2}$$

The overdot denotes derivative with respect to t. The wake variable is defined as $x = 2C_L/C_{Lo}$, where C_L and C_{Lo} are the present and reference lift coefficients. s is redefined as $s = Mx$ where $M = C_{Lo}/16\pi^2 S_t^2 \mu$ is a scaling factor. Effects of structural motion on the wake dynamics are modelled using an acceleration coupling

[32] defined as $f = A\ddot{y}$.

When the structure interacts with a barrier located at $y(t_-) = \sigma$, it undergoes an instantaneous reversal of velocity at the instant of impact, where t_- and t_+ denote the instants immediately before and after impact, respectively. The instantaneous velocity reversal is defined using a coefficient of restitution r; see Eqs. (4.3) and (4.4).

$$\begin{aligned} y(t_-) &= \sigma, \\ \dot{y}(t_+) &= -r\dot{y}(t_-). \end{aligned} \tag{4.3}$$

and,

$$\begin{aligned} x(t_+) &= x(t_-), \\ \dot{x}(t_+) &= \dot{x}(t_-). \end{aligned} \tag{4.4}$$

The dynamics is governed by a smooth flow defined using Eqs. (4.2) and a discrete map at the instant of impact defined by Eqs. (4.3) and (4.4). PWS systems exhibiting such behaviour fall under the class of hybrid systems. The section below discusses the effects of an impact on the motion of the structure.

4.3 Bifurcation analysis

A detailed numerical investigation of Eqs. (4.2) along with explicit calculations of the non-smooth map that arises from the instantaneous reversal described in Eqs. (4.3) and (4.4) is presented here. The parameters considered corresponds with experiments [32, 42, 43] and are chosen as $\xi = 0.0052$, $\gamma = 0.8$, $\mu = 1.19381$ corresponding to $m^* = 0.52 < m^*_{crit}$, $A = 12$, $\epsilon = 0.3$, $S_t = 0.2$ and $r = 0.8$. Numerical integration has been carried out using adaptive time stepping based solver `NDSolve` in `Mathematica`. Since small perturbations can lead to diverse outcomes in non-smooth systems, these perturbations must be mapped to ensure that they have reached the barrier in the proper time. This is achieved via the discontinuity mapping. Bifurcation analysis is carried out by varying U_r and σ as the control parameters. In order to eliminate transience, the first 500 impacts have been discarded. A Poincaré surface of section Σ is defined at $\dot{y} = 0$ and the subsequent 200 impacts are observed. If the trajectory interacts with the Poincaré section N times, it is labelled as the period-N or PN orbit.

In Fig. 4.2, the amplitude response when the barrier is placed at $\sigma_{impact} = -0.150298$ with varying reduced velocity is shown. σ_{impact} corresponds to the grazing boundary when $U_r = 25$. Note that an infinitesimal change in the critical σ value may lead to a completely different orbit. Consequently, the value of σ_{impact} is consid-

ered up to six significant digits. Fig. 4.2(a) is the bifurcation diagram of structural displacement y_0 observed stroboscopically for varying reduced velocity ranging between $12 \leq U_r \leq 25.0$. The figure reveals the existence of period-adding cascades of orbits interspersed with bands of seemingly aperiodic responses. A zoomed section for the range $24.0 \leq U_r \leq 25.0$ is presented in Fig. 4.2(b) for clarity. Figs. 4.2(e) - 4.2(h) show P2, P3, P4 and P8 orbits for $U_r = 16$, 19, 21.5 and 24.8 respectively. The red dots highlight Poincaré points on Σ, which have been plotted in Fig. 4.2(a) and Fig. 4.2(b). In Fig. 4.2(c), simulations from multiple initial states reveal the presence of coexisting P1 and P2 attractors. Although no aperiodic band is observed in this window, such bands appear and get subsequently wider with the addition of periods in the cascade. In Fig 4.2(d) this aperiodic behaviour, as reflected in phase portrait, is shown for $U_r = 24.4$.

The coexistence of P1 and P2 attractors in Fig. 4.2(c) is further investigated by varying initial conditions while keeping U_r and σ fixed at 14.9 and -0.150298, respectively. In Fig. 4.3, the basins of attraction corresponding to P1 and P2 are shown. The placement of barrier at $\sigma_{impact} = -0.150298$ in Figs. 4.2 and 4.3 corresponds to the maximum amplitude of oscillations when $U_r = 25.0$. Thus, a barrier placed there would lead to grazing. A two-parameter bifurcation diagram is shown in Fig. 4.4. The initial states $y(0)$, $\dot{y}(0)$, $x(0)$ and $\dot{x}(0)$ for these simulations were taken to be 0.0, 0.0, 0.0 and 0.1 respectively. The dynamics was observed on the Poincaré section Σ. The results are then color coded according to the periodicity for a given set of chosen parameters (i.e., σ and U_r) post the transient cycles of 1000 impacts. Here, distinct regions of PN, aperiodic and no-impact *i.e,* P0 responses can be observed.

In Fig. 4.5, barrier distance σ is taken as the bifurcation parameter at a constant U_r of 25. Fig. 4.5(b) highlights the bifurcation behaviour when the oscillator is undergoing motion under pure compression *i.e.,* the barrier is placed such that the oscillator cannot reach its equilibrium position. Here, one can observe a period-adding cascade of orbits separated by bands of aperiodic solutions. In Fig. 4.5(a), the bifurcation behaviour for σ near the grazing condition (i.e., σ_{impact}) for $U_r = 25.0$ is shown. Higher period orbits are manifested when $\sigma \to \sigma_{impact}$. Fig. 4.5(g) is a zoomed section of the bifurcation diagram where the amplitude response in the vicinity of P1 and P2 orbits can be observed near $\sigma = -0.020$. A bifurcation branch of a P4 orbit sandwiched between two P2 orbits can be observed here. This bifurcation curve branches out at an acute angle, signifying the occurrence of a non-smooth transition. In Figs. 4.5(e) and 4.5(f), the periodic orbits in phase-space corresponding to P2 and P4 for $\sigma = -0.020$ and $\sigma = -0.0210$, respectively, are shown. Similarly, the periodic orbit in phase-space corresponding to a P6 orbit is shown in Fig. 4.5(c) for $\sigma = -0.149$. An aperiodic orbit in the phase-space, when the barrier is situated at $\sigma = -0.146$, is shown in Fig. 4.5(d).

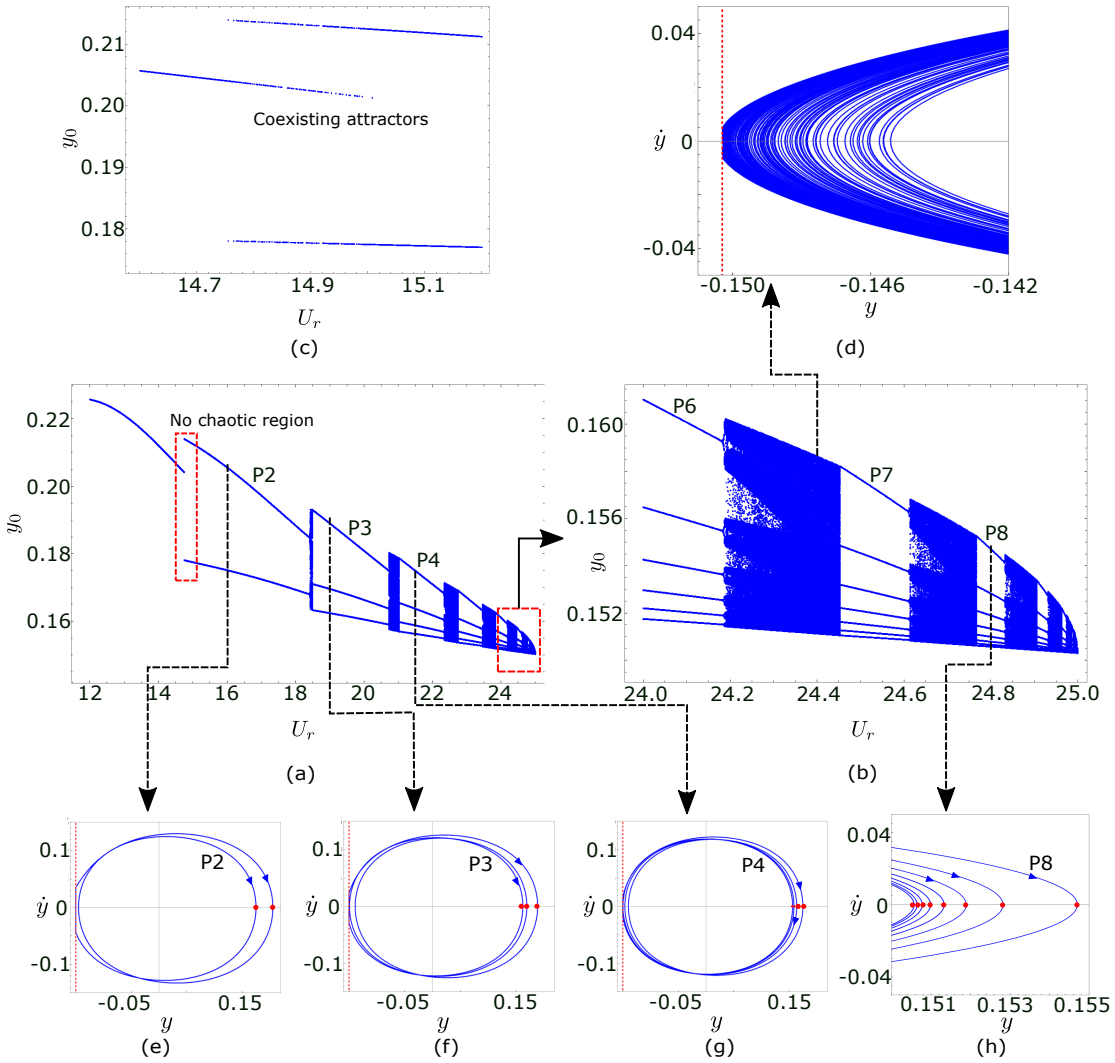

Figure 4.2: (a) Bifurcation diagram of the structure's amplitude response y_0 by varying reduced velocity U_r for $r = 0.8$ and $\sigma = -0.150298$. (b) Amplitude response y_0 for $24.0 \leq U_r \leq 25.0$. (c) Bifurcation diagram depicting the coexistence of P1 and P2 attractors. (d) A typical aperiodic trajectory in phase-space for $U_r = 24.4$. Periodic orbits: (e) P2 when $U_r = 16.0$, (f) P3 when $U_r = 19.0$, (g) P4 when $U_r = 21.5$, (h) P8 when $U_r = 24.8$. Dynamics between 500-700 impacts has been presented.

The aperiodic behaviour observed between the bifurcation branches of periodic orbits observed in Figs. 4.2 and 4.5 is investigated further. To establish that these aperiodic orbits are indeed chaotic, the dynamics on the Poincaré section Σ, governed by $\dot{y} = 0$, is examined. In Fig. 4.6(a), trajectories intersecting Σ for $U_r = 18.426$ and 18.494 with a barrier located at σ_{impact} and $r = 0.8$ are shown. To measure the dimension of the obtained Poincaré section [45], the correlation dimension ν has been calculated. This is done by counting the number of points $N(\epsilon_r)$ enclosed by a small circle of radius ϵ_r and letting the radius grow in size until it encloses the entire attractor. Since the points are clustered in different segments, multiple circles centered at different locations within the attractor are taken and the mean

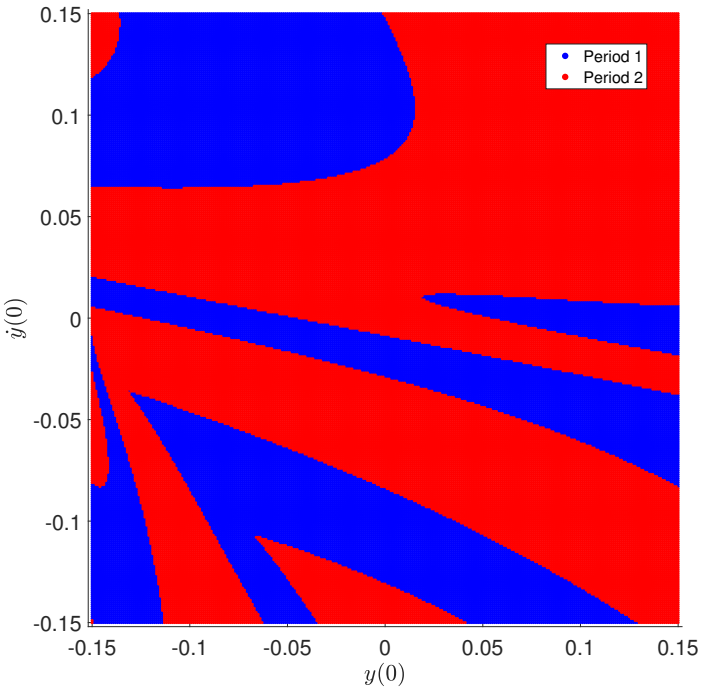

Figure 4.3: Basins of attraction for $U_r = 14.9$, $r = 0.80$ and $\sigma = -0.150298$.

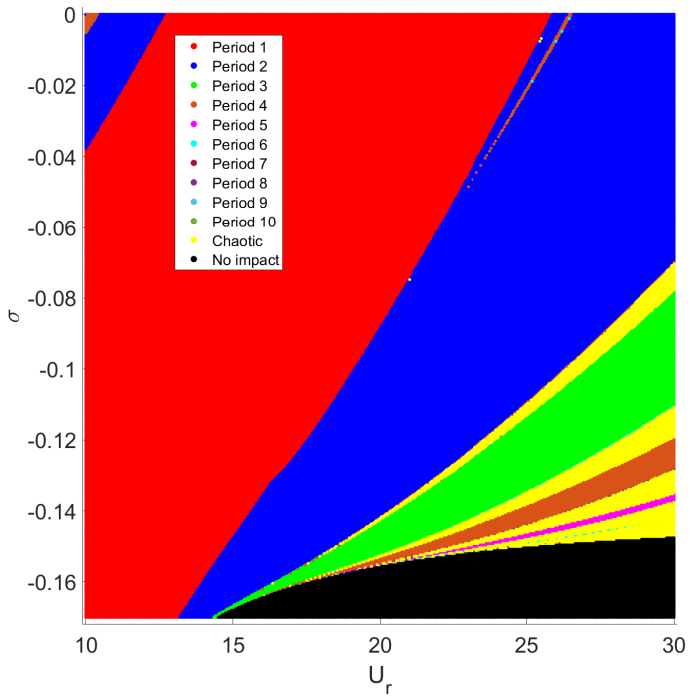

Figure 4.4: Periodicity in the dynamics of the structure's motion for $r = 0.8$. Periodicity has been calculated after 1000 impacts with a tolerance of 10^{-5}.

of dimensions at these locations is considered as the entity $C(\epsilon_r)$ such that $C(\epsilon_r) = \langle N(\epsilon_r) \rangle$. The correlation dimension can then be estimated using the expression in

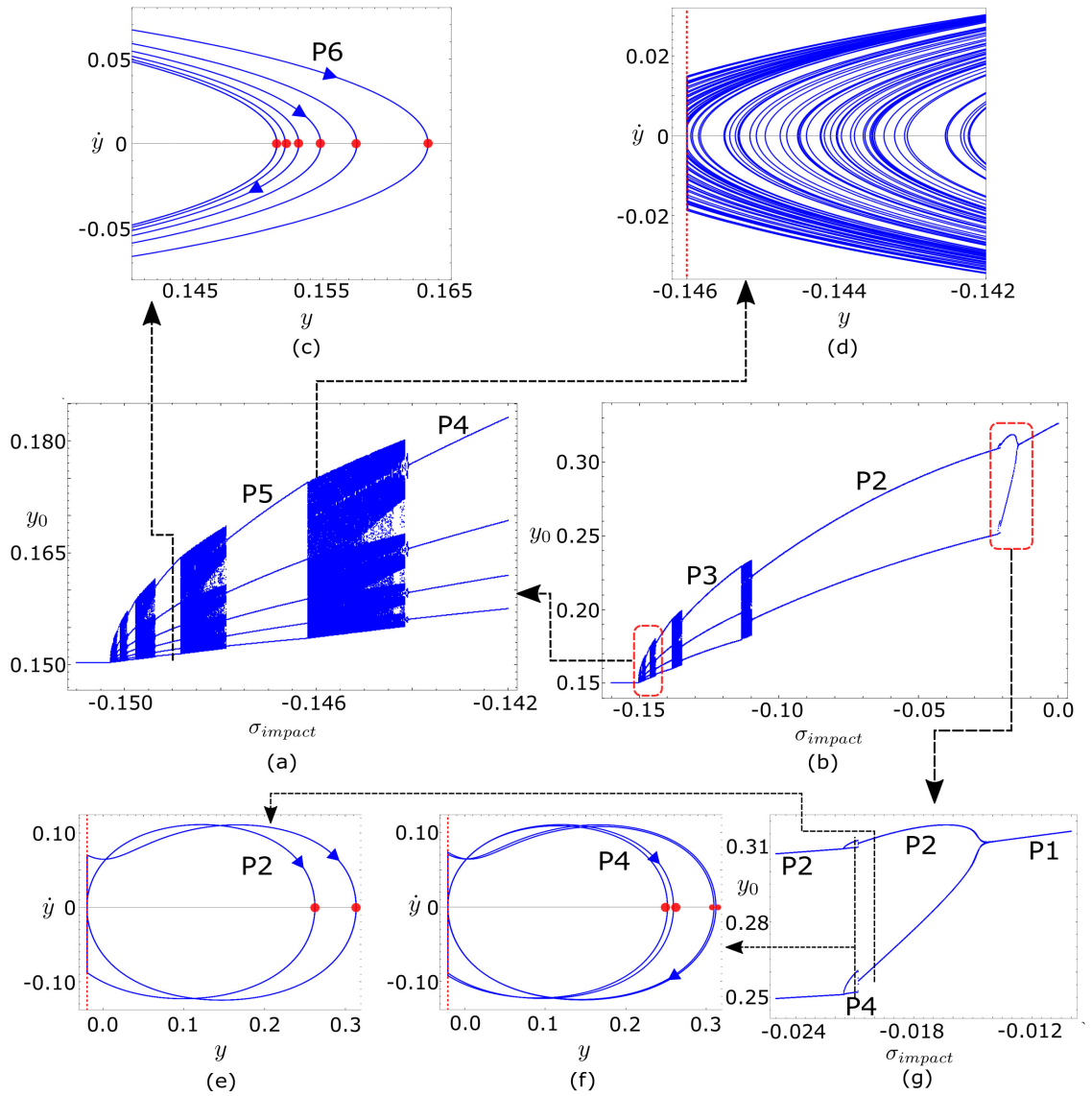

Figure 4.5: Bifurcation diagram depicting variation in structural amplitude y_0 as a function of σ ranging between (a) $-0.150298 \leq \sigma \leq -0.142$ (b) $-0.150298 \leq \sigma \leq 0$ for $r = 0.8$ and $U_r = 25.0$. Phase portraits of: (c) P6 orbit when $\sigma = -0.149$, (d) Aperiodic orbit when $\sigma = -0.146$, (e) P2 orbit when $\sigma = -0.020$, (f) P4 orbit when $\sigma = -0.021$. (g) Bifurcation diagram y_0 when σ ranges between $-0.024 \leq \sigma \leq -0.010$. Dynamics between 500-700 impacts are considered for these simulations.

Eq. (4.5)

$$C(\epsilon_r) \propto \epsilon_r^{\nu}. \tag{4.5}$$

The number of centres for evaluation of ν are chosen as multiples of 2 i.e. 2, 4, 6 . . . 12. The values of ν tends to converge for centres more than 10. In Fig. 4.6(a), the mean of $N(\epsilon_r)$ is estimated by considering 15 different centres that are circled in the figure. ϵ_r is varied from 0.0001 to 0.06 in steps of 10^{-4} to cover the entire finger-shaped attractor. The correlation dimension ν is then estimated from the slope of the log-log plot between ϵ_r and $C(\epsilon_r)$. A linear fit corresponding to obtained graph is

presented Fig. 4.6(b). Here, ν is estimated to be 2.4. Since ν is an non-integer value, the corresponding dynamics observed on the Poincaré section possess a fractal like structure, and hence, can be characterized as a strange attractor, indicative of the chaotic behaviour. In Fig. 4.6(c) Poincaré sections are shown for various reduced velocities and barrier at σ_{impact}. The corresponding correlation dimensions obtained have non-integer values as well. In Fig. 4.6(d) Σ corresponding to varying barrier distances with reduced velocity kept fixed at $U_r = 25.0$ have been presented. The values of U_r and σ chosen here correspond to the aperiodic regions in the bifurcation diagrams that separate the periodic orbits *i.e.,* between P2-P3, P3-P4 and P5-P6 orbits. For each of these Poincaré sections, the correlation dimensions obtained are non-integer values, thus verifying the existence of fractal-like strange attractors sandwiched between periodic solutions.

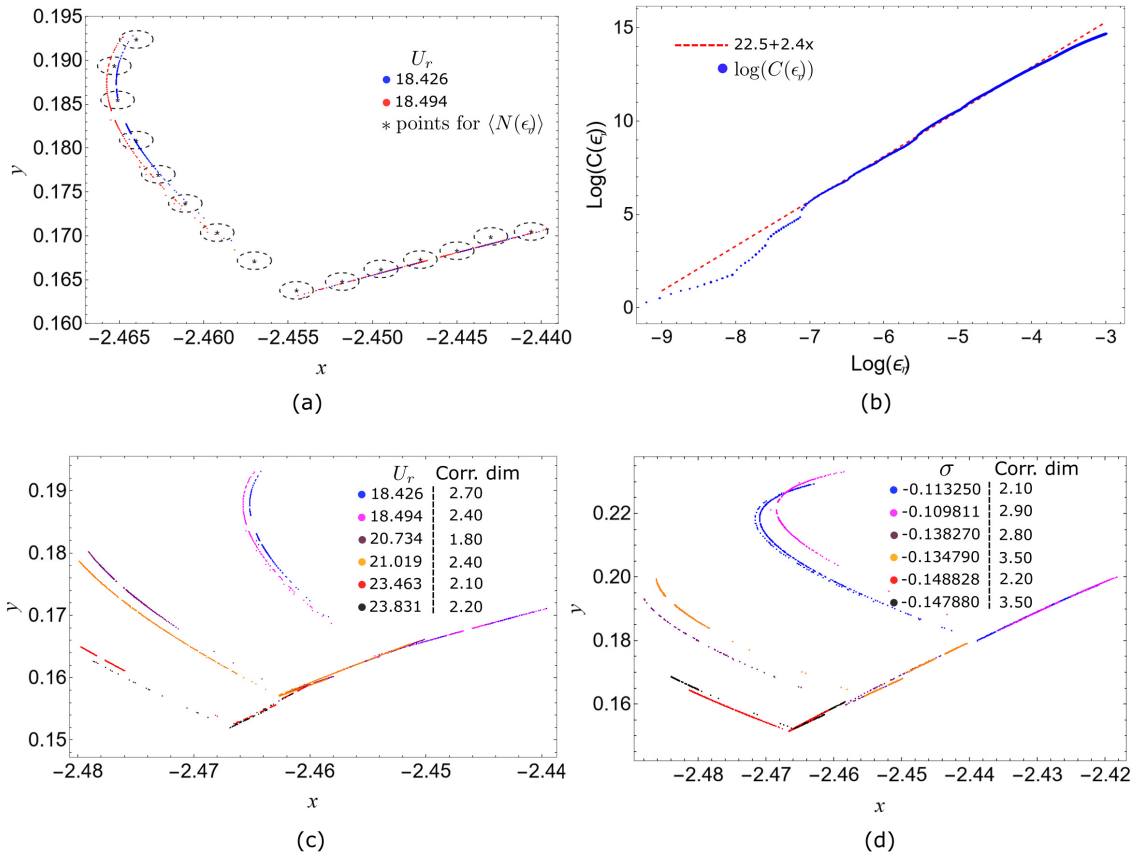

Figure 4.6: (a) Poincare section $\dot{y} = 0$ for $U_r = 18.426$ and 18.494. $N(\epsilon_r)$ is counted from the centre of circles shown; $C(\epsilon_r)$ defined as $\langle N(\epsilon_r)\rangle$. (b) Correlation dimension estimation from slope of $\log(C(\epsilon_r))$ vs $\log(\epsilon_r)$. Poincare section $\dot{y} = 0$ for (c) varying velocity U_r and barrier kept fixed at $\sigma = -0.150298$; (d) varying barrier distance σ with velocity fixed at $Ur = 25.0$.

The effect on the dynamics due to the variation of coefficient of restitution r is investigated next. In Fig. 4.7, the variation in amplitude response is shown against coefficient of restitution r, when the barrier is fixed at $\sigma = -0.021$ and

reduced velocity fixed at $U_r = 25.0$. The red dots shown in Figs. 4.5(f) and 4.7 correspond to the Poincaré points of a P4 orbit, when $U_r = 25.0$, $\sigma = -0.021$ and $r = 0.8$. The observed behaviour is similar to Fig. 4.5(g), where a P4 orbit is sandwiched between two P2 orbits. In Fig 4.8, a two-parameter bifurcation diagram is presented. Here, periodicity in dynamics is observed to follow a distinct adding pattern, separated by chaotic bands. The reduced velocity for these simulations is kept fixed at $U_r = 25.0$. The first 500 impacts have been discarded to eliminate transient effects and recurrence in a trajectory at the same point in the state space is considered when the Euclidean distance at the point of interest is close to the reference point within a tolerance of 10^{-5}. This is done to compute the periodicity of the orbits. In the observed period-adding cascade, higher period orbits tend to appear in the vicinity of the grazing region that corresponds to $\sigma = -0.150298$ for $U_r = 25.0$. A narrow region of P4 orbit is observed between two P2 regions; see Fig. 4.8. Using U_r as one of the bifurcation parameters, similar behaviour is observed. The stable behaviour here is examined by keeping the barrier fixed while varying the reduced velocity and coefficient of restitution. This is shown in Fig. 4.9. The barrier is kept fixed at $\sigma = -0.0210$, away from the grazing condition for $U_r = 25.0$. This distance corresponds to a value where P4 orbit was observed in Fig. 4.8 with $r = 0.8$ and $U_r = 25.0$.

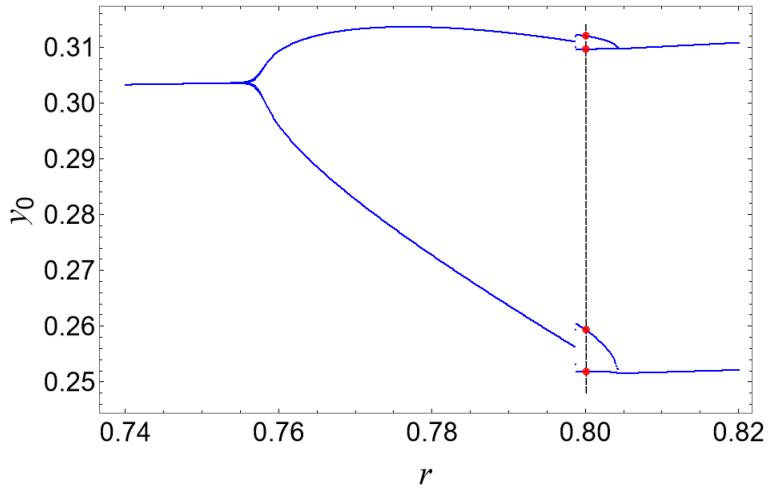

Figure 4.7: Bifurcation in amplitude of the structure for various values of coefficient of restitution. Here, reduced velocity fixed at $U_r = 25.0$ and with a barrier placed at $\sigma = -0.021$. The red dots correspond to Poincaré points for P4 shown in Fig. 4.5(g).

For the above simulations, the coupling and the wake parameters, A and ϵ, are taken as 12 and 0.3, respectively, such that $A/\epsilon = 40$. This ensures that the dynamical model is compatible with experimental observations in [32]. The parameter A determines the strength of coupling between the structure and associated wake dynamics, while ϵ controls the strength of non-linearity of the wake oscillator. In

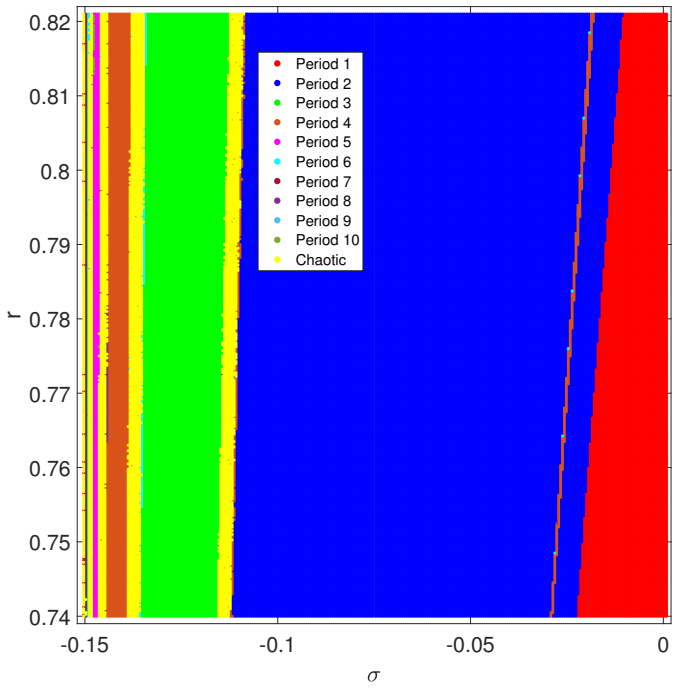

Figure 4.8: Two-parameter bifurcation diagram plotted between σ and r for reduced velocity $U_r = 25.0$.

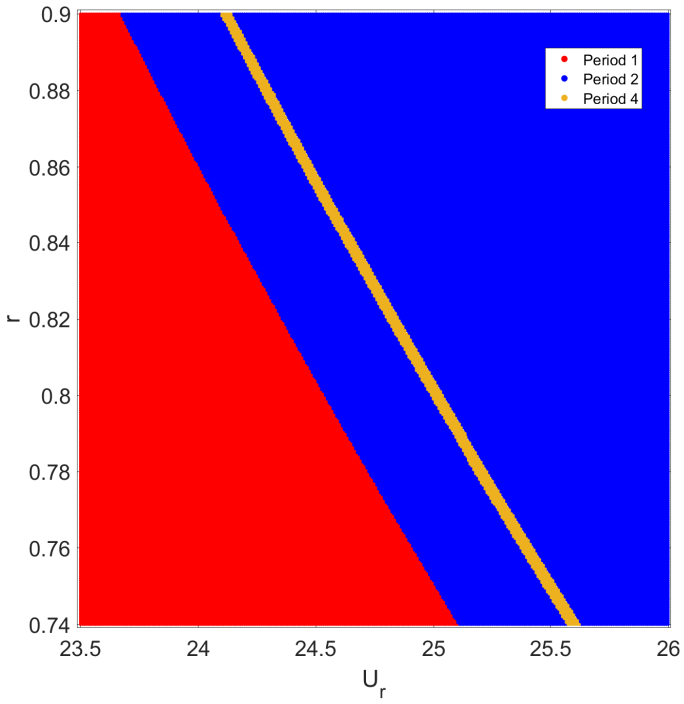

Figure 4.9: Two-parameter bifurcation diagram between U_r and r plotted for $\sigma = -0.0210$.

Fig. 4.10(a), the variation in amplitude response of the structure as a function of reduced velocity in the absence of a barrier is presented. The values of A and ϵ

are varied while ensuring that the ratio $A/\epsilon = 40$ is constant. It is observed that the amplitude of vibrations of the structure increases as the coupling parameter A increases. In Fig. 4.10(b), the amplitude response is shown in the absence of a barrier where A kept fixed at $A = 10$ and the ratio A/ϵ is varied. The ratio is kept close to 40 to ensure that observed dynamics correspond to the original physical system; see the models discussed by Facchinetti *et. al* [15, 32]. In this case, the amplitude response increases as the ratio A/ϵ is increased. The location of the rigid barrier is chosen such that, in the parameter regime of interest, the structure grazes the barrier for only one parameter. This implies that the vibration amplitude of the structure is the lowest in the domain of interest, ensuring that all other values of A and ϵ will undergo an impact with the rigid barrier transversally. This is further demonstrated graphically. In Fig. 4.10(c), the trajectories depicting the structure's oscillations are presented. The observations are made when the vibrations have attained a steady state for barrier placed at $\sigma = -0.13181$. The barrier, shown as an orange dashed line, corresponds to the grazing condition for $A = 10$ and $\epsilon = 0.25$ such that $A/\epsilon = 40$. The black curve in Fig. 4.10(c) grazes the barrier, while the blue and red curves interact with the barrier transversally. Similarly, in Fig. 4.10(d), the structur oscillations are shown when the barrier is located at $\sigma = -0.130979$, corresponding to the grazing condition for $A = 10$, and $\epsilon = 0.333$, such that $A/\epsilon = 30$. Thus, the black curve with $A/\epsilon = 30$ grazes the barrier while the blue and red curves corresponding to $A/\epsilon = 50$ and 40, respectively, impact the barrier transversally. A bifurcation analysis is subsequently carried out.

Figs. 4.11(a), (c) and (e) depict the dynamical change in the amplitude response of the structure as a function of reduced velocity. The initial 500 impacts are discarded to remove any transient effects and the ratio in all the cases is $A/\epsilon = 40$. The discontinuity boundary kept fixed at $\sigma = -0.13181$, which corresponds to the grazing condition for $A = 10$, $\epsilon = 0.25$ and $U_r = 25.0$. For $12 \leq U_r \leq 25.0$, only P1 and P2 orbits can be observed for $A = 14$ and $\epsilon = 0.35$; see Fig. 4.11(a). As the coupling parameter A reduces, the maximum amplitude of vibration of the structure reduces, thus leading to non-transversal interactions of trajectories with the boundary. As the value of A approaches 10 for which σ is near grazing value of -0.13181, higher period orbits separated by chaotic bands are observed; see Figs. 4.11(c) and (e). When $A = 10$ and $\epsilon = 0.25$ in Fig. 4.11(e), existence of higher periodic orbits is observed in the vicinity of $U_r = 25.0$ beyond which no impact with the barrier occurs. Similarly, in Figs. 4.11(b), (d) and (f), the amplitude response of the cylindrical structure is shown for $A/\epsilon = 50$, 40 and 30 ensuring $A = 10$. The barrier is situated at $\sigma = -0.130979$, corresponding to the grazing condition for $A = 10$, $\epsilon = 0.333$ and $U_r = 25.0$. Again a similar phenomenon is observed. With $A = 10$ and decreasing A/ϵ, the amplitude of oscillations of the structure decreases and the cylinder interacts with the barrier more non-transversally. A

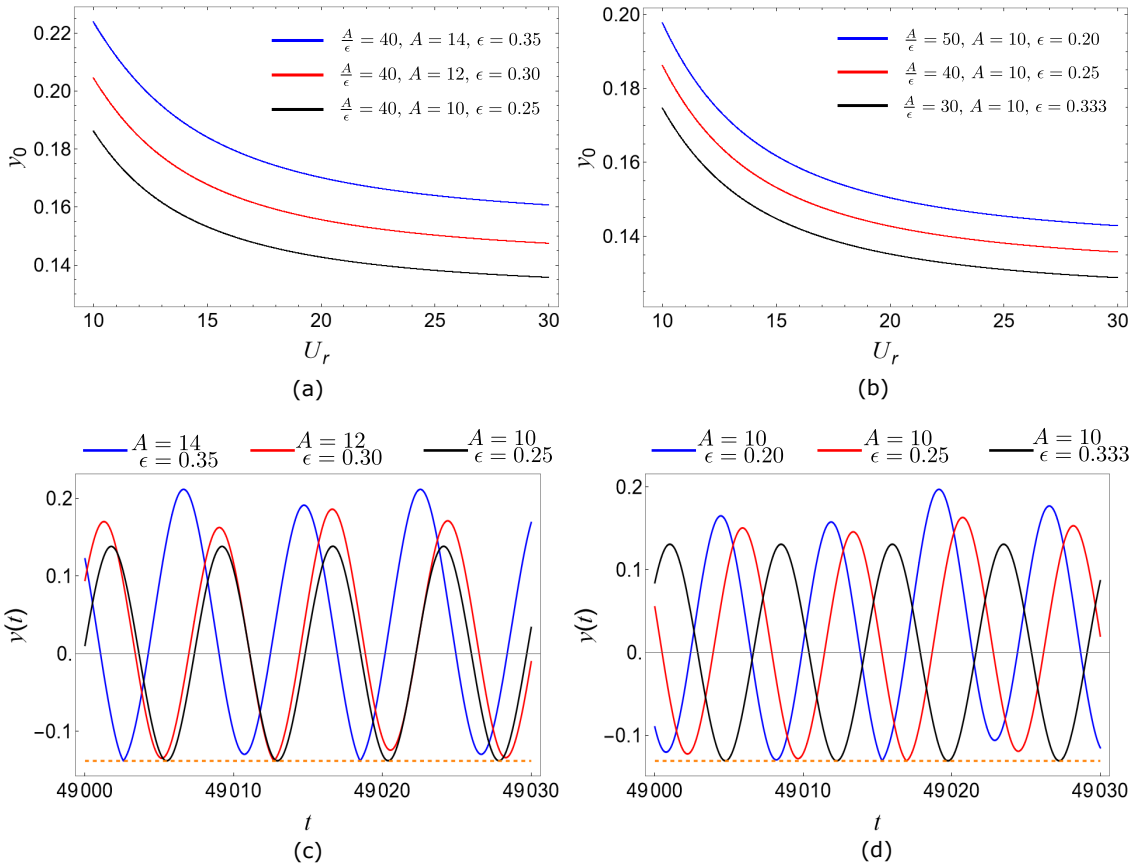

Figure 4.10: Amplitude response without barrier for (a) $A = 14$, 12 and 10 such that $A/\epsilon = 40$, (b) $A/\epsilon = 50$, 40 and 30. Structural displacement with barrier placed at (c) $\sigma = -0.13181$ by varying $A = 14$, 12 and, 10 ensuring $A/\epsilon = 40$. (d) $\sigma = -0.130979$ for $A/\epsilon = 50$, 40 and 30.

cascade of periodic orbits separated by chaotic behaviour is observed. As A, ϵ and U_r approach the grazing condition of $\sigma = -0.130979$, higher periodic orbits are observed with bands of chaotic solutions; see Fig. 4.11(f). However, in all of these results, no chaotic solutions are observed between P1 and P2 orbits.

The following section presents stability analysis of this non-smooth system using Floquet theory. Here, the methods and numerical algorithms are presented and inferences about the dynamical behaviour are drawn by correlating the results with the bifurcation studies presented above.

4.4 Stability analysis

Bifurcation diagrams presented above indicate that as parameters like U_r or σ is varied, existing orbits become unstable, resulting in newer periodic or aperiodic orbits. Hence, it is essential to carry out a stability analysis to investigate when an orbit might become unstable, therefore revealing routes to chaos. This sections considers two methods of investigating the stability of a limit cycle - an eigenvalue

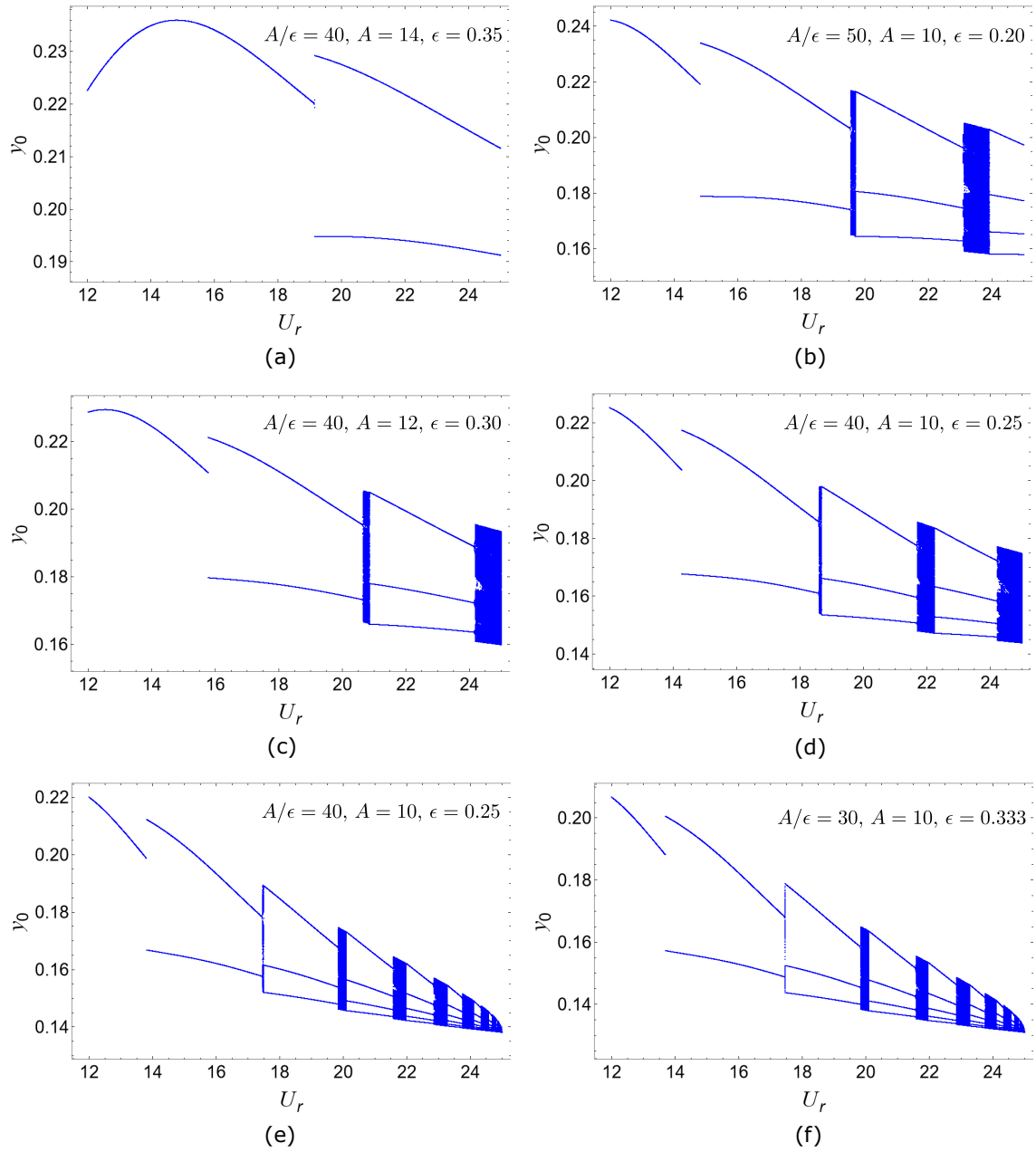

Figure 4.11: Bifurcation diagram with barrier placed at $\sigma = -0.13181$ for (a) $A = 14$ (c) $A = 12$ (e) $A = 10$ ensuring $A/\epsilon = 40$. Bifurcation diagram with barrier placed at $\sigma = -0.130979$ and $A = 10$ such that (b) $A/\epsilon = 50$, (d) $A/\epsilon = 40$ (f) $A/\epsilon = 30$.

analysis of the fundamental solution matrix of the orbit under consideration followed by evaluation of Lyapunov exponents.

4.4.1 Floquet multipliers

The stability of orbits obtained for various parameters of the FSI system undergoing impacts *i.e.*, Eq. (4.3) and Eq. (4.4) is investigated next. Since the system under consideration is piecewise-smooth and leads to orbiting steady states, a combination of Floquet theory along-with the consideration of discontinuity mappings are

taken into consideration while performing the stability analyses. For smooth systems, Floquet multipliers are the eigenvalues of the global state transition matrix (STM) for any given periodic orbit. However, in hybrid dynamical systems, there are discontinuous transitions in the phase-space at the instant of an impact. The Floquet multipliers jump at the instant of impact. Hence, the global STM or the monodromy matrix is composed of local STMs and STMs at the instant of impact, also known as the saltation matrices. These matrices are multiplied in the order of occurrence of dynamical evolution. The state transition of any perturbed trajectory at the instant of an interaction with the barrier is defined by a transverse discontinuity map (TDM). The approach for obtaining the complete monodromy matrix and the role of appropriately defining the TDM is presented next. In Fig. 4.12, the phase portrait of a P2 orbit of a hybrid system undergoing impact twice with a discontinuity boundary Σ_2, depicted by a black dashed line, is shown. The monodromy matrix $\mathbf{\Phi}(T)$ for this orbit of period T (time after which the orbit repeats itself) comprises products of several STMs applied in the correct order of events. Here, the orbit is initiated on the section Σ_1 and it traverses to the switching surface Σ_2 by state transition $\mathbf{\Phi}_1$. The state gets mapped by another transition matrix S_1 to a new state. The mapping of this state back to Σ_2 again is given by $\mathbf{\Phi}_2$. It undergoes a state transition S_2 and $\mathbf{\Phi}_3$ subsequently to land up at Σ_1 and the orbit repeats itself. Thus, over one cycle, the state transition matrix can be defined as

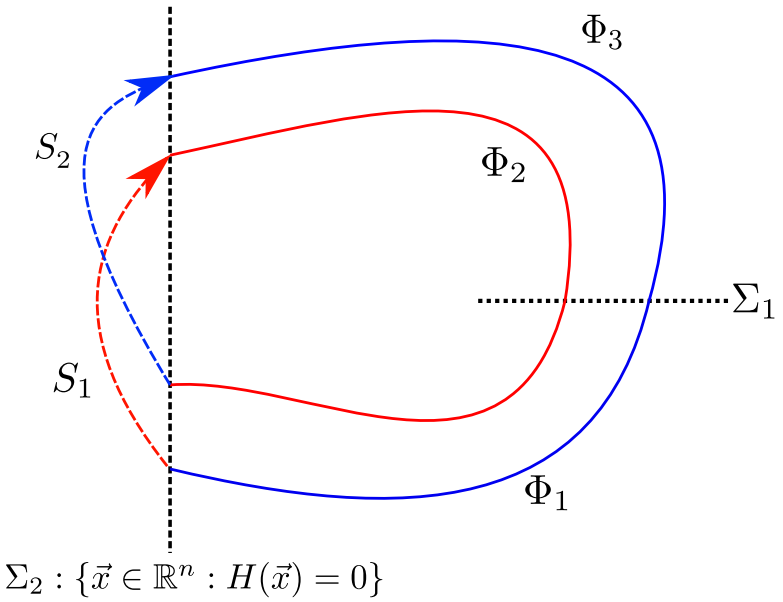

Figure 4.12: The schematic of a P2 limit cycle undergoing two instances of instantaneous reversals at the instants of impact with Σ_2, depicted as black dashed line. The red solid line corresponds to flow governed by the STM Φ_2, the red dashed line corresponds to state transition at the instant of first impact (using saltation matrix S_1), the blue solid line corresponds to flow governed by STM Φ_1, the blue dashed line corresponds to state transition at the instant of second impact (using saltation matrix S_2).

$$\mathbf{\Phi}(T) = \mathbf{\Phi}_3 \cdot \mathbf{S}_2 \cdot \mathbf{\Phi}_2 \cdot \mathbf{S}_1 \cdot \mathbf{\Phi}_1, \tag{4.6}$$

where $\mathbf{S}_i$ is the STM or saltation matrix at the instant of i^{th} impact. Similarly for a given solution obtained numerically with period T and n number of impacts, the monodromy matrix is defined by Eq. (4.7).

$$\mathbf{\Phi}(T) = \mathbf{\Phi}_n \cdot \prod_{i=1}^{n-1} \mathbf{S}_i \cdot \mathbf{\Phi}_i. \tag{4.7}$$

According to the Floquet theory, the monodromy matrix is evaluated by integrating the fundamental solution matrix over one complete orbit. This ensures that the time varying Jacobian over the limit cycle is now observed over one period, making the entries of the state transition matrix constant. Here, the saltation matrix describes the mapping of orbits in the local neighborhood at the instants when the dynamical system undergoes an impact with a discontinuity boundary. Consider an arbitrary dynamical system $\mathbf{x}$ with a small perturbation $\mathbf{y}$. The governing dynamics and its corresponding variational equations are presented in Eq. (4.8).

$$\begin{aligned} \dot{\mathbf{x}} &= \mathbf{F}(\mathbf{x}), \\ \dot{\mathbf{y}} &\approx \nabla \mathbf{F}(\mathbf{x})^T \cdot \mathbf{y} + \mathcal{O}(||\mathbf{y}^2||). \end{aligned} \tag{4.8}$$

Fig. 4.13 is a schematic representation of two perturbed trajectories obeying Eq. (4.8). The periodic trajectory of the primary system starts initially from $\mathbf{x}_p$ and undergoes impact at $H(\mathbf{x}_i) = 0$. Here, $H(\mathbf{x}) = 0$ is a scalar function that models the discontinuity boundary. However, any perturbed trajectory from this periodic orbit will not undergo an impact at the same instant when the primary orbit impacts the discontinuity boundary. Therefore, there exists a time difference between impacts for any two trajectories of a given hybrid system. To ensure that the perturbed trajectory is appropriately mapped at its instant of impact, a mapping of the perturbed trajectory at the instant of impact *i.e.*, $\mathbf{y}_-$ to $\mathbf{y}_+$ is performed. This mapping ensures that the perturbed trajectory will reach the discontinuity boundary after the time difference between the impact of the two trajectories has elapsed. The perturbed trajectory starts from $\hat{\mathbf{x}} = \mathbf{x}_p + \mathbf{y}_0$ and at the instant of impact of the primary trajectory (when $\mathbf{x}_0 = \mathbf{x}_i + \mathbf{y}_-$) gets mapped from $\mathbf{y}_-$ to $\mathbf{y}_+$ such that $\mathbf{x}_4 = \mathbf{R}(\mathbf{x}_i) + \mathbf{y}_+$. Here, $\mathbf{R}(\mathbf{x}_i)$ represents the mapping of the primary periodic orbit (*i.e.*, the impact of the structure with the barrier). The trajectory evolves from $\mathbf{x}_4$ and reaches $\mathbf{x}_3$ lying on the discontinuity boundary within the time difference as previously mentioned. This evolution can be interpreted as the perturbed trajectory $\mathbf{x}_0 = \mathbf{x}_i + \mathbf{y}_-$ undergoing impact at $H(\mathbf{x}_2) = 0$ after the time difference and getting mapped to $\mathbf{x}_3 = \mathbf{R}(\mathbf{x}_2)$. The above mapping of the perturbed trajectory is analytically modeled via a state transition matrix, also

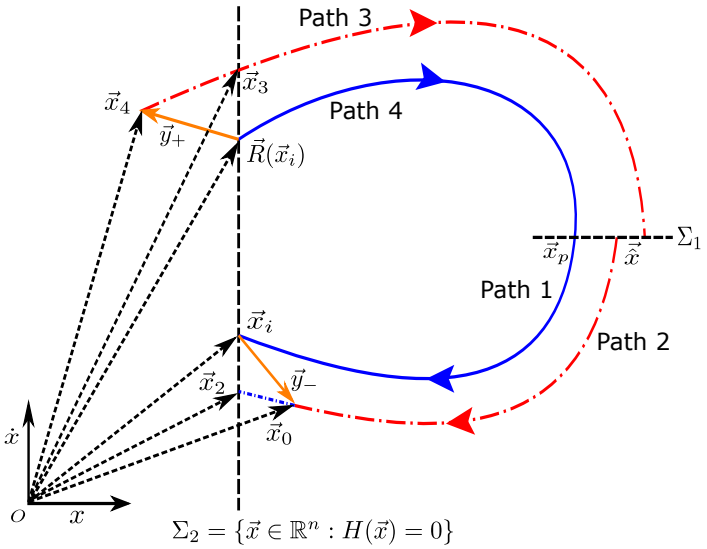

Figure 4.13: A schematic of the phase portrait of two nearby trajectories exhibiting impact at Σ_2. The blue line shows the actual trajectory. The red dashed line denotes the perturbed trajectory. This is a representative figure and is not to scale. The black dashed line Σ_1 denotes the Poincaré section from which both the trajectories are initiated and Σ_2 denotes the discontinuity boundary. The amber line denotes the perturbation vector y.

known as saltation matrix in literature [21]; see Eq. (4.9).

$$\mathbf{y}_+ = \mathbf{S}_i \cdot \mathbf{y}_-. \tag{4.9}$$

The saltation matrix $\mathbf{S}_i$ at i^{th} impact obtained by retaining only the first order terms of the Taylor series is presented in Eq. (4.10).

$$\begin{aligned} \mathbf{S}_i = \nabla \mathbf{R}(\mathbf{x}_i)^T \\ + \frac{\Big(\mathbf{F}(\mathbf{R}(\mathbf{x}_i)) - \nabla \mathbf{R}(\mathbf{x}_i)^T \cdot \mathbf{F}(\mathbf{x}_i)\Big)}{\nabla H(\mathbf{x}_i)^T \cdot \mathbf{F}(\mathbf{x}_i)} \otimes \nabla H(\mathbf{x}_i)^T \end{aligned} \tag{4.10}$$

where $\mathbf{x}_i$ represents the state of the dynamical system at the instant of impact, $\mathbf{R}(\mathbf{x}_i)$ is the reset map at the instant of impact, $\mathbf{F}(\mathbf{x})$ denotes the underlying vector field and $H(\mathbf{x}) = 0$ represents the discontinuity boundary where an impact or reset occurs.

For the given FSI system described by Eq (4.3) along-with Eq (4.4), the state space is 4 dimensional *i.e.*, $\mathbf{x} = [y\ \dot{y}\ x\ \dot{x}]$ and the dynamics evolves according to the vector field $\mathbf{F}(\mathbf{x})$ described by Eq. (4.11).

$$\mathbf{F} = \begin{bmatrix} \dot{y} \\ -\delta^2 y - \alpha \dot{y} + Mx \\ \dot{q} \\ -x - \epsilon(x^2 - 1)\dot{x} + A(-\delta^2 y - \alpha \dot{y} + Mx) \end{bmatrix}, \tag{4.11}$$

where $\alpha = (2\xi\delta + \gamma/\mu)$. The discontinuity barrier is defined using a scalar function $H(\mathbf{x}) = 0$ where $H(\mathbf{x}) = y - \sigma$. At the instant of impact a reset map $\mathbf{R}(\mathbf{x})$ is initiated such that $\mathbf{R}(\mathbf{x}) = [y \ -r\dot{y} \ x \ \dot{x}]$; r being the coefficient of restitution defined previously in Eq. (4.4). The analytical form of the saltation matrix given by Eq. (4.10) is represented in Eq. (4.12),

$$\mathbf{S}_i = \begin{bmatrix} -r & 0 & 0 & 0 \\ \frac{(1+r)}{\dot{y}}(-\delta^2 y + Mx) & -r & 0 & 0 \\ 0 & 0 & 1 & 0 \\ A\alpha(1+r) & 0 & 0 & 1 \end{bmatrix}. \tag{4.12}$$

The fundamental solution matrix $\mathbf{Y}(t)$ is numerically evaluated by considering an orthogonal set of perturbed vectors such that $\mathbf{Y}(0) = \mathbb{I}_{n\times n}$. Each perturbed vector is a column entry of $\mathbf{Y}$ and evolves using Eq. (4.8). Next, the periodicity of the FSI system is obtained numerically after discarding 500 impacts with the barrier to eliminate any transient effects. The monodromy matrix and its eigenvalues are evaluated after one time period from Eq. (4.7). The numerical procedure to evaluate the Floquet multipliers, using first-order saltation matrices, has been described in Appendix C.

In Fig. 4.14, the Floquet multipliers ρ_i of the monodromy matrix have been shown as the reduced velocity U_r is varied. A one to one correspondence is drawn with the dynamics observed on the bifurcation diagram. A barrier is placed at σ_{impact} (grazing condition for $U_r = 25.0$) with $r = 0.8$. The region ranging between $-1 \leq \rho_i \leq 1$ corresponds to a stable periodic orbit. The dashed vertical lines highlight the observed bands of chaotic orbits. Floquet multipliers are within the unit circle for stable orbits. As U_r is varied, the Floquet multiplier approaches -1, eventually resulting in a bifurcation to chaotic orbits at $\rho_i = -1$. Additionally, in the parameter region where a transition from P1 to P2 orbit is observed, the Floquet multipliers discontinuously jumps to a value with norm less than unity. This suggests a birth of a new stable periodic orbit. Eventually, the absolute value of the Floquet multipliers decreases to -1 before it approaches the next instant of a non-smooth bifurcation. Similarly, in Fig. 4.15, the Floquet multipliers are shown as the barrier distance is varied, while the reduced velocity is kept fixed at $U_r = 25.0$ and $r = 0.8$. Similar transitions in values of the Floquet multipliers are observed near bifurcation occurrences. This is clearly reflected in the bifurcation diagram as well. Moreover, it was also observed that one of the Floquet multiplier is always unity *i.e.* it lies on the unit circle. For an autonomous dynamical system, this implies that there is an eigendirection along that which there is no variation in the magnitude of perturbation *i.e.* the primary and the perturbed trajectory neither converge nor diverge from each other [82]. This also verifies that the TDM that correctly maps the

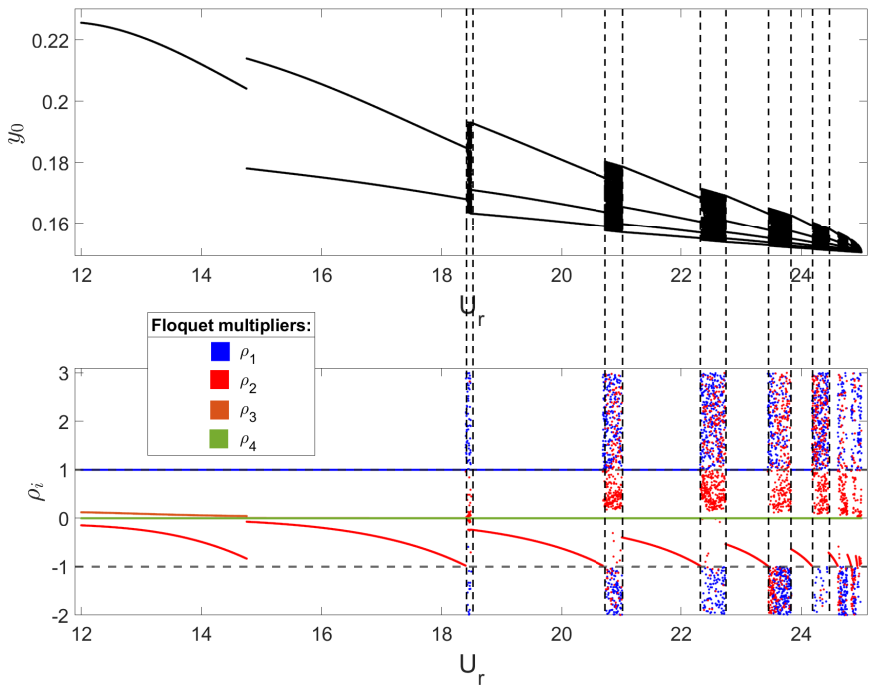

Figure 4.14: Floquet multipliers vs reduced velocity U_r for barrier placed at $\sigma = -0.150298$ and $r = 0.8$.

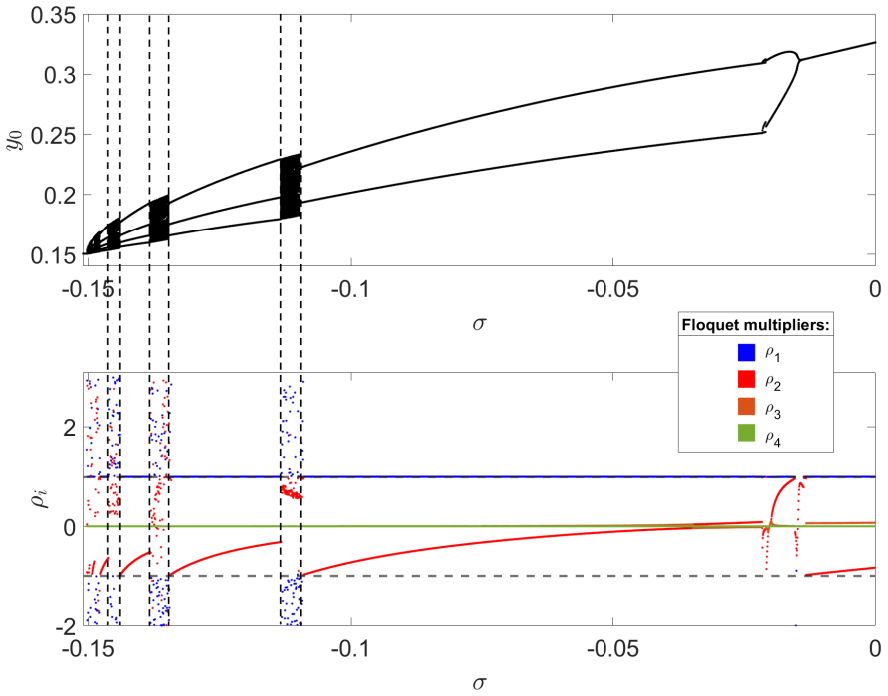

Figure 4.15: Floquet multipliers vs barrier distance σ when reduced velocity is $U_r = 25.0$ and $r = 0.8$.

perturbed trajectories at the instant of impact and the results verify the established Floquet theory. It is to be noted here that Floquet theory is not directly applicable

for aperiodic oscillatory responses. This is because, the trajectories do not recur and thus, the product of matrix multiplications blow up. This reflects in Fig. 4.14(b) as noisy bands of ρ_i with magnitude greater than unity. An alternate marker of chaotic dynamics is the presence of positive Lyapunov exponents. Lyapunov spectra is thus obtained below to analyze the observed aperiodic phenomena in this non-smooth system.

4.4.2 Lyapunov exponents

In this section, the stability of orbits is investigated by estimating the rate of exponential divergence of their nearby perturbed trajectories. The rates of exponential divergence or the Lyapunov exponents are computed as follows. Starting from a periodic orbit $\mathbf{x}_0$, an orthogonal set of perturbed trajectories are initialized. The initial magnitude of the perturbed trajectories is set to a small value of $r_0 = 0.0001$ units. This implies that the perturbed vectors lie on a hypersphere of radius r_0. Then, this hypersphere is allowed to evolve for the n^{th} time from t to $t + t_0$ after which, the growth rate r_n of all the perturbed trajectories is noted. The perturbed trajectories evolve according to the variational formalism of the dynamical system under investigation (see Eq. (4.8)). Each time the primary system undergoes an impact with the discontinuity boundary, the perturbed trajectory gets mapped by Eq. (4.9) in phase-space using the saltation matrix in Eq. (4.12). After a time interval of t_0, the initialized hypersphere has now evolved into a hyper-ellipsoid. The average largest Lyapunov exponent λ_1 is measured from the growth rate of the perturbations along the major axis of the hyper-ellipsoid using Eq. (4.13),

$$\lambda_i = \frac{1}{t_0 N} \sum_{n=1}^{N} \ln \frac{r_n}{r_0}. \tag{4.13}$$

At this instant, the set of perturbed vectors is once again orthogonalized using the Gram-Schmidt process with respect to one of the perturbed vectors (along eigenvector with the largest Lyapunov exponent), meanwhile ensuring the magnitude is again scaled down to r_0. This is achieved by performing a QR decomposition (QRD) followed by scaling of the vectors by r_0. Thus, once again an initial hypersphere of radius r_0 is obtained but the vectors now are oriented differently. This process is repeated and the growth rate is monitored and reset stroboscopically *i.e.* when $t\%t_0 = 0$. This step is followed by a QRD. The Lyapunov exponents along each orthogonal direction are thus obtained by evaluating steps 6-8 in Appendix D; also see Eq. (4.13).

In Fig. 4.16, the variation of the largest Lyapunov exponent (LLE) as a function of reduced velocity as well as the corresponding bifurcation diagrams are shown. The barrier is kept fixed at σ_{impact} and $r = 0.8$. The LLE has been computed stro-

boscopically at $t_0 = \pi$ for 800 impacts with the barrier. The LLE is a measure of the maximum rate of exponential divergence between two nearby perturbed trajectories. Positive values of LLE in Fig. 4.16 correspond to trajectories that diverge from each other; indicating the occurrence of chaos. This can also be verified from the corresponding bifurcation diagram. The dashed lines in the figure highlight the intervals within which chaotic orbits are observed. These regions also show a positive value of the LLE. Similarly, in Fig. 4.17, LLEs have been shown as the barrier distance is varied, ranging between $-0.150298 \leq \sigma \leq 0$. The flow velocity here is kept fixed at $U_r = 25.0$ and $r = 0.8$. The LLE is zero for all periodic orbits and suddenly jumps to positive values where chaotic orbits are observed in the corresponding amplitude response diagram.

Therefore, the TDM, using the derived saltation matrix, accurately determines the dynamical stability of the FSI system undergoing impacts. The algorithms presented above can also be adapted to consider higher order estimations of the TDM for better estimation of the states near an impact [21]. Furthermore, the proposed algorithms can be used to study non-smooth dynamical systems of different formalisms *i.e.*, the Filippov and piecewise continuous kind and can be extended to higher dimensions. The findings from the presented work are summarized in the section next.

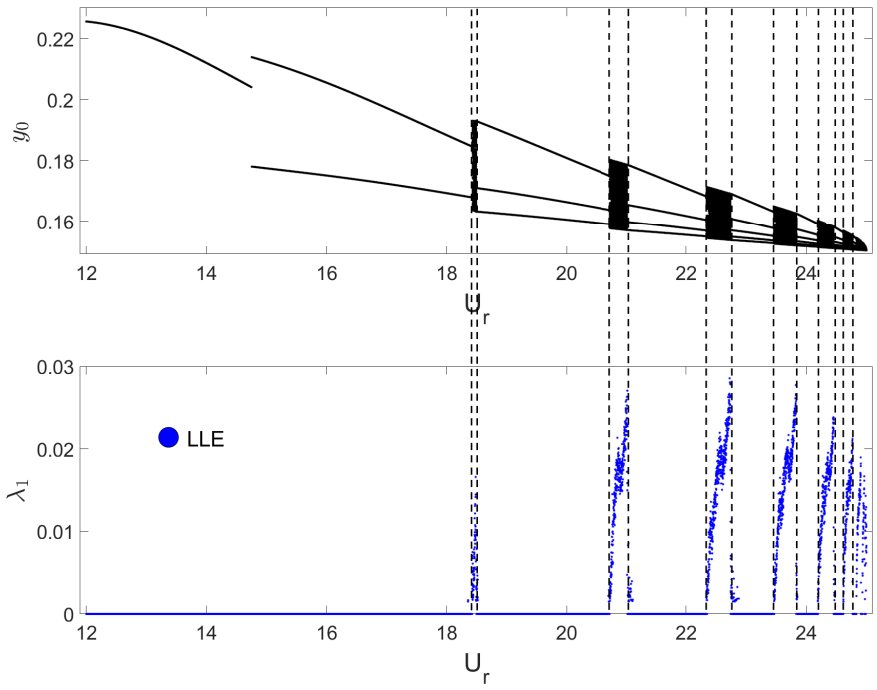

Figure 4.16: Largest lyapunov exponent vs reduced velocity U_r when barrier is placed at $\sigma = -0.150298$ and $r = 0.8$.

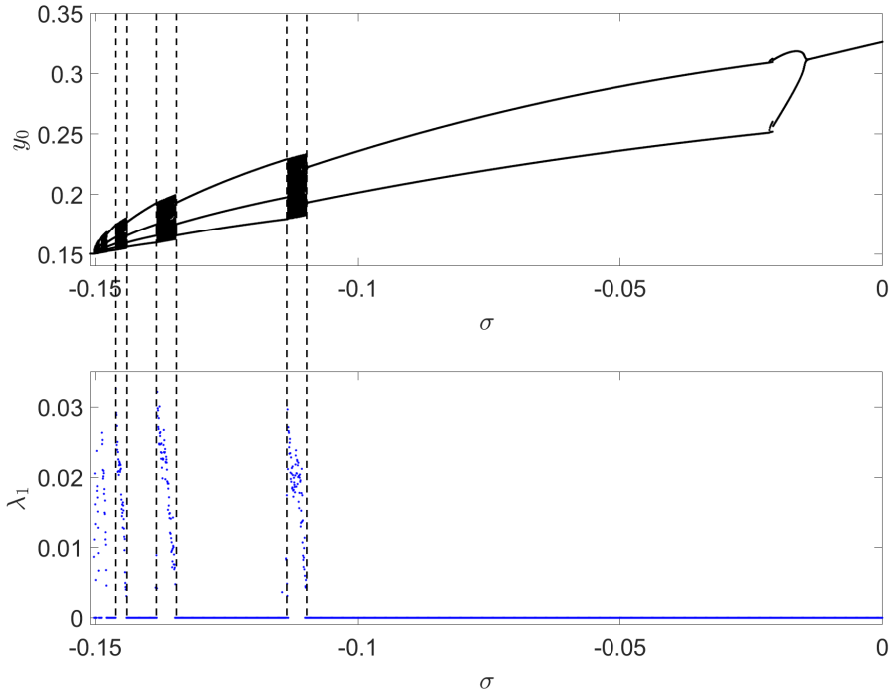

Figure 4.17: Largest lyapunov exponent vs barrier distance σ when reduced velocity is $U_r = 25.0$ and $r = 0.8$.

4.5 Conclusions

The effect of non-smooth impacts with a rigid barrier on the VIV characteristics of a SDOF cylindrical system is investigated in this chapter. A detailed study of the underlying dynamical bifurcations, followed by the stability analysis of the concerned FSI system undergoing vibro-impacts, is presented. Non-smooth dynamical phenomena like period adding, periodic bifurcation branches separated by chaotic orbits, and finger-shaped chaotic attractors are observed. Further, there are coexistence of P1 and P2 stable attractors with intertwined basins of attraction. By varying the coupling strength and non-linearity of the wake oscillator, cascades of higher periodic orbits were observed in the vicinity of the grazing condition.

Furthermore, algorithms for obtaining Floquet multipliers and Lyapunov spectra for non-smooth dynamical systems are proposed and demonstrated for the vibro-impact system under fluid flow. To capture the discontinuous jump of the orbits in phase-space in the presence of a non-smooth barrier, a discontinuity map was numerically estimated at the instant of impact. Results indicate that one of the Floquet multipliers approaches and exits the unit circle as the system loses stability. At this instant, the bifurcation diagrams showed the presence of large-amplitude chaotic oscillations. This was further backed up by a positive Lyapunov exponent obtained by incorporating the TDM at impacts. Additionally, jumps in the Floquet multipliers indicate the occurrence of a non-smooth bifurcation. The jumps occurred

when one of the orbits lost stability, and another came into existence upon variation of a system parameter; here, the barrier distance and reduced flow velocity. The Floquet spectra and the largest Lyapunov exponents, obtained using variational formalism and incorporating non-smooth saltation terms, agree with the numerically obtained bifurcation diagrams. Hence, the stability analysis can accurately predict when discontinuity-induced bifurcations occur, resulting in chaotic behavior of the structure. Such vibrations can be detrimental to the physical system and can be avoided by investigating impacting systems using the methods of saltation matrices presented above.

Chapter 5

Higher-order transverse discontinuity mapping of hybrid fluid-structure interaction system

This chapter compares the widely accepted saltation matrix and the higher-order transverse discontinuity mapping proposed in Chapter 3 for a hybrid PWS system of larger size. The time difference between impacts for two closely initiated trajectories predicted using $\mathcal{O}(1)$ and $\mathcal{O}(2)$ approximation becomes more prominent and sometimes erroneous when the respective PWS system has several parameters and more degrees of freedom. To demonstrate the usefulness of a higher-order TDM, a 4 dimensional hybrid system representing the simplest case of fluid-structure interaction undergoing impacts is studied. As discussed in Chapter 4, this model simulates a structure experiencing vortex-induced vibrations in a uniform flow. Non-smoothness manifests when a barrier obstructs the structure's motion, resulting in discontinuity-induced bifurcations like period-adding cascades and chaos. The derived TDM, compared to the first-order Saltation matrix, reveals significant improvements in the prediction of the dynamics and offers a better estimation of the states post-impact. Due to the quadratic nature of the time difference between impacts, as shown in Chapter 3, perturbations greater than a critical range in the local neighborhood will not impact the discontinuity barrier. The widely accepted linearized saltation matrix fails to capture this and incorrectly predicts impacts for all perturbations. This is rectified and validated numerically using the higher-order TDM to predict the outcome of trajectories in vibro-impact systems accurately.

5.1 Introduction

A large class of engineering systems undergo impact [85] and electrical switching [8], leading to hybrid dynamics *i.e.* differential equations with discrete algebraic reset

laws. Such systems exhibit a unique suite of bifurcations coined as DIBs, which do not arise in smooth dynamical systems. Additionally, further considerations are necessary to analyse such hybrid systems as the behaviour of trajectories near discontinuity boundaries needs to be appropriately modelled [14]. In a n-dimensional hybrid dynamical system $\dot{\mathbf{x}} = \mathbf{F}(\mathbf{x}, t, \mathbf{u})$, where $\mathbf{x} \in \mathbb{R}^n$ and $\mathbf{u}$ denotes parameters, the phase-space is divided into i smooth sub-spaces with vector field $\mathbf{F}_i \in \mathbf{F}$ separated by discontinuity boundaries $\mathbf{\Sigma}_i$. Trajectories at the discontinuity boundary often exhibit behaviours like grazing [85], sliding [31] and chattering [17]. As a consequence, period-adding cascades [97], quasi-periodicity or chaos [7] might occur. The dynamics of such systems sensitively depend on how the state $\mathbf{x}$ behaves near the barrier.

Infinitesimal perturbations $\mathbf{y}$ in the neighborhood of $\mathbf{x}$ are assumed to evolve according to the linearized form of the dynamics *i.e.,* the Jacobian $\nabla \mathbf{F}^T_{i,\mathbf{x}}(\mathbf{x})$, where T denotes transpose and subscript $\mathbf{x}$ denotes gradient with respect to $\mathbf{x}$. Since any two perturbed trajectories $\mathbf{x}$ and $\mathbf{x}+\mathbf{y}$ will undergo impacts at different instants of time, the difference being $\delta(t, \mathbf{x})$, it is incorrect to compute the evolution of $\mathbf{x}+\mathbf{y}$ in accordance with $\nabla \mathbf{F}^T_{j,x}(\mathbf{x})$ while it is still evolving in $\mathbf{F}_i$.

Therefore, a TDM is introduced to accurately map $\mathbf{x}+\mathbf{y}$ at the instant of an impact with the barrier. This map is thus a function of the underlying state $\mathbf{F}$ and separation $\mathbf{y}$ at the instant,t_0. Hence, δ at impact can be expressed as

$$\delta = A_{1\times 1} + \mathbf{B}_{1\times n}\mathbf{y}_{n\times 1} + \mathbf{y}^T_{n\times 1}\mathbf{C}_{n\times n}\mathbf{y}_{n\times 1} + \mathcal{O}(3) \tag{5.1}$$

where A, B and C are functions of t_0 and $\mathbf{u}$. In general, for hybrid systems like a hard impact oscillator, δ and hence, the TDM has been derived using a linear approximation [24, 2]. The linearized expressions of δ in Eq. (5.1) and the TDM, mathematically represented by saltation matrix $\mathbf{S}_1$, are

$$\begin{aligned} \delta_1 &= -\frac{\nabla H(\mathbf{x}_i)^T \cdot \mathbf{y}_-}{\nabla H(\mathbf{x}_i)^T \cdot \mathbf{F}(\mathbf{x}_i)} \\ \mathbf{S}_1 &= \nabla \mathbf{R}(\mathbf{x}_i)^T + \frac{(\mathbf{F}(\mathbf{R}(\mathbf{x}_i)) - \nabla \mathbf{R}^T(\mathbf{x}_i)\cdot \mathbf{F}(\mathbf{x}_i)) \otimes \nabla H(\mathbf{x}_i)}{\nabla H(\mathbf{x}_i)^T \cdot \mathbf{F}(\mathbf{x}_i)} \end{aligned} \tag{5.2}$$

where, $\mathbf{x}_i$ and $\mathbf{y}_-$ denote the trajectory $\mathbf{x}$ and perturbation $\mathbf{y}_-$ before impact, H models the barrier and $\mathbf{R}$ is a discrete map of $\mathbf{x}$ upon impact. Here, subscript x denotes gradient $\partial/\partial\mathbf{x}$. The linearized saltation matrix $\mathbf{S}_1$ is the state transition matrix due to transversal interaction of the trajectory, that maps the perturbation $\mathbf{y}$ as $\mathbf{y}_+ = \mathbf{S}_1 \cdot \mathbf{y}_-$, $-$ and $+$ denote $\mathbf{y}$ before and after an impact. It is observed that this linearized approximation in Eqs. (5.2) fails to accurately predict $\mathbf{y}$ at impact[21]. This is because of two underlying reasons. For the case of hard impact,

the linearized expressions of δ and $\mathbf{S}_1$ (Eqs. (5.2)) are independent of the functional form of the external forces and crucial system parameters which model the physical system. The inaccuracy of $\mathcal{O}(1)$ terms becomes more pronounced for a higher order hybrid system comprising of several system parameters $\mathbf{u}$. Secondly, in a chaotic regime, the perturbed paths exponentially diverge with a positive Lyapunov exponent. This results in a large value of $\mathbf{y}_-$. Here, δ approximated to $\mathcal{O}(\mathbf{y}_-)$ will result in an inaccurate prediction of the time difference between impacts. This error will get appended each time a barrier is encountered, thus leading to a completely different trajectory $\mathbf{x} + \mathbf{y}$.

To demonstrate this, a 4 dimensional FSI system undergoing vibro-impact is analyzed. Such low-fidelity models have been seen to qualitatively capture the phenomena exhibited in experiments designed to analyze VIVs [66, 62, 15]. Such phenomenological models can qualitatively replicate the events which would otherwise require complex experimental set-ups or computationally expensive direct numerical simulations (DNS) to be observed. Experiments conducted by Govardhan and Williamson [42, 43] reveal that the amplitude response of an elastically mounted cylinder undergoing VIV, recorded against reduced fluid-flow velocity U_r, comprises of three different bifurcation branches for high and low values of mass ratio m^* [42]. More quantitatively, for $m^* >> 1$ the vortex shedding frequency f is close to the natural frequency f_N of the structure, while for $m^* \propto \mathcal{O}(1)$, the reduced vortex shedding frequency f^* (f/F_N) increases indefinitely, leading to a persistent upper branch. They derived an empirical expression for f^* in the lower branch defined as $f^*_{lower} = \sqrt{(m^*+1)/(m^*-0.54)}$ revealing the existence of a critical mass ratio $m^*_{crit} = 0.54$ below which the lower branch frequency does not exist. When expressed in terms of the reduced fluid flow velocity [42], the lower branch starts at, *i.e.*, $U^*_{start} = 5.75\sqrt{(m^*+1)/(m^*-0.54)}$. Thus when $m^* \leq 0.54$, U^*_{start} tends to infinity. Hence, when m^* of an FSI system is below the critical value of 0.54, the lower branch ceases to exist. Only large amplitude response of the structure corresponding to the upper branch is observed for all values of U_r. The upper branch will continue indefinitely and the synchronization range extends to infinity. In this chapter, a non-smooth FSI system with mass ratio $m^* = 0.52$, below the critical value, undergoing VIV is considered. The smooth part of this FSI system comprises a cylindrical bluff body undergoing VIV after the onset of lock-in or synchronization. A low order model proposed by Facchinetti *et al.* [32], which models the initial to upper branch transition and remains indefinitely showing large amplitude response for higher values of U_r, has been adopted. The structure is represented by an elastically connected harmonic oscillator and the wake dynamics is modelled using a Van der Pol oscillator. The non-smooth part of this system comprises a rigid barrier which, upon interaction with the structure, leads to a velocity reversal at the instant of impact defined by Newton's restitutive law.

This 4 dimensional hybrid system exhibits DIBs leading to chaos for certain parameter regimes. A detailed numerical analysis is conducted by incorporating higher order terms to accurately estimate δ and subsequently the TDM of the perturbation $\mathbf{y}$ near impacts. The global state transition matrix of an orbit relies on δ and TDM at impact. Thus, a small error due to linear approximation at every occurrence of an impact will lead to an incorrect estimation of the monodromy matrix and subsequently, Floquet multipliers. A comparison of errors in estimation of δ using $\mathcal{O}(2)$ terms over $\mathcal{O}(1)$ is presented, revealing a significant improvement. Additionally, for certain perturbed trajectories, the $\mathcal{O}(2)$ terms of δ and TDM indicate that some trajectories slightly miss the barrier at a certain time instant, whereas $\mathcal{O}(1)$ estimates indicate that an impact will occur. Furthermore, a comparison with direct numerical simulations reveals that the $\mathcal{O}(2)$ accurately predicts the behaviour of this trajectory near the barrier.

This chapter is structured as follows. Section 5.2 presents the mathematical form of the low order phenomenological model of the 4 dimensional hybrid FSI system undergoing impacts with a rigid barrier. Section 5.3 presents the numerical results, showing the improvement in using a higher order TDM by retaining the $\mathcal{O}(2)$ terms in comparison with the linearized approximation of δ. The key findings of this work are summarized in Sec. 5.4.

5.2 Non-smooth FSI system

An elastically mounted cylinder of diameter D is immersed in a fluid medium with a uniform flow velocity U and density ρ. It can only oscillate in the transverse direction 5.1. The cylinder is vibrating under the influence of lift forces acting on it. The cylinder's motion $Y(t)$ is modelled by a harmonic oscillator and the self sustained lift forces $X(t)$ acting upon it are represented by a Van der Pol equation; See Eq. 5.3 [32].

$$\begin{aligned} mY'' + hY + \varrho Y' &= S \\ X'' + \Omega_f^2 X + \epsilon\Omega_f(X^2 - 1)X' &= F \end{aligned} \tag{5.3}$$

where, over prime represents derivative with respect to time t. The mass of the oscillator m is defined as $m = m_s + m_f$, where m_s and m_f are the mass of cylinder and fluid-added mass respectively. The fluid-added mass is defined as $m_f = C_m \rho D^2 \pi/4$ with constant added mass coefficient $C_m = 1$ for circular cross-section. h and ϱ represent stiffness and damping of the structural oscillator. ϱ is further defined as $\varrho = r_s + r_f$ where r_s, r_f are the damping of the cylinder and fluid-added damping defined as $r_f = \gamma\Omega_f\rho D^2$. γ is a stall parameter. The natural frequency of the

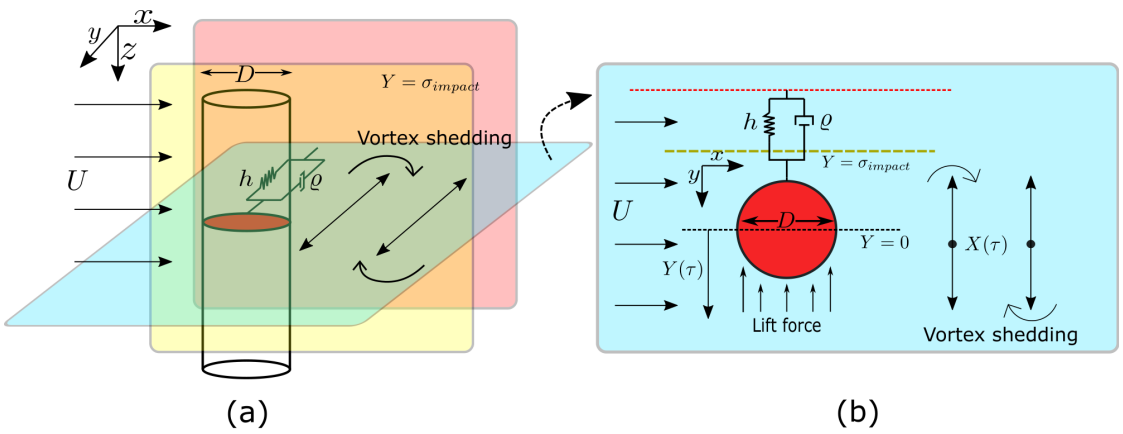

Figure 5.1: (a) Cylinder executing VIV in a transverse direction to the cross-flow fluid medium with velocity U. (b) Cross-section of FSI set-up. Cylinder undergoes impact with a barrier at $y = \sigma_{impact}$ followed by an instantaneous velocity reversal.

cylinder is defined as $\Omega_s^2 = h/m$. S represents the lift force on structure, Ω_f is the vortex shedding frequency of the wake, ϵ is the strength of non-linearity of the wake variable and F is the result of the structure's motion on the nearby fluid medium effecting the dynamics of the wake variable. Eqs. 5.3 can be expressed in a non-dimensional form as Eq. 5.4. Normalizing Y as $y = Y/D$, t as $\tau = \Omega_f t$, X as $x = X$ and $\delta = \Omega_s/\Omega_f$, Eqs. (5.3) is rewritten as [32]

$$\begin{aligned} &\ddot{y} + \delta^2 y + (2\xi\delta + \frac{\gamma}{\mu})\dot{y} = s, \qquad \text{if, } y(\tau_-) = \sigma \quad \dot{y}(\tau_+) = -r\dot{y}(\tau_-) \\ &\ddot{x} + x + \epsilon(x^2 - 1)\dot{x} = f, \qquad\qquad x(\tau_+) = x(\tau_-) \quad \dot{x}(\tau_+) = \dot{x}(\tau_-). \end{aligned} \tag{5.4}$$

where, the overdot represents the derivative with respect to τ, $\mu = m/\rho D^2$ is mass ratio, Strouhal number is $S_t = \Omega_f D/2\pi U$, damping ratio is $\xi = r_s/2m\Omega_s$, $s = S/m\Omega_f D$ and $f = F/D\Omega_f$. S is a function of vortex lift coefficient C_L, defined as $S = \rho U^2 D C_L/2$ [49]. The wake variable is expressed as $x = 2C_L/C_{Lo}$ where C_{Lo} is the reference lift coefficient, s is redefined as $s = Mx$ where $M = C_{Lo}/16\pi^2 S_t^2 \mu$ is a scaling factor. The structure's motion effects the wake dynamics via an acceleration coupling [32] and is defined as $f = A\ddot{y}$. When the structure interacts with a barrier located at $y(\tau_-) = \sigma$, it undergoes an instantaneous reversal in its velocity during an impact where τ_- and τ_+ denote the instants before and after impact. The instantaneous velocity reversal is defined using a coefficient of restitution r, see Eq. (5.4).

The amplitude response for the structure in a flow of velocity U_r due to the presence of this barrier is presented next and the fate of infinitesimally perturbed trajectories are examined by using higher order state transition matrices. An improvement in estimating the perturbed state from a periodic orbit during an impact with $\mathcal{O}(2)$ corrections in δ is discussed and compared with $\mathcal{O}(1)$ terms.

5.3 Numerical results

The hybrid FSI system modelled using Eq. 5.4 has been numerically integrated using an adaptive-step Runge-Kutta solver with an event detection routine. A barrier is placed at $\sigma = \sigma_g = -0.155638$, which is the calculated value for grazing condition at $U_r = 20$ [31]. Any value of $U_r > 20$ would lead to oscillations with no interaction with the barrier. This is because the amplitude of the upper branch [42] reduces as U_r increases. In Fig. 5.2., the amplitude response of the structure is plotted against reduced flow velocity U_r. Here, $\xi = 0.0052$, $\gamma = 0.8$, $\mu = 1.19381$ corresponding to $m^* = 0.52 < m^*_{crit}$, $A = 12$, $\epsilon = 0.3$, $S_t = 0.2$ and $r = 0.8$. The initial 800 transient cycles have been discarded during computations. The inset figure in Fig. 5.2(a) shows the cylinder's motion in phase-space where the periodic orbit intersects the Poincaré section $\dot{y} = 0$ twice and is thus a period 2 or P2 orbit. Similarly, the number of uni-directional intersections of the orbit with this Poincaré surface have been considered to determine its periodicity for a given U_r. The amplitude responses in Fig. 5.2(a) and 5.2(b) reveal a period adding cascade of attractors with chaotic orbits interspersed between them. As the value of U_r approaches the grazing condition, orbits with further higher periodicities are observed. A detailed bifurcation study of this 4D hybrid FSI system has been presented in Chapter 4.

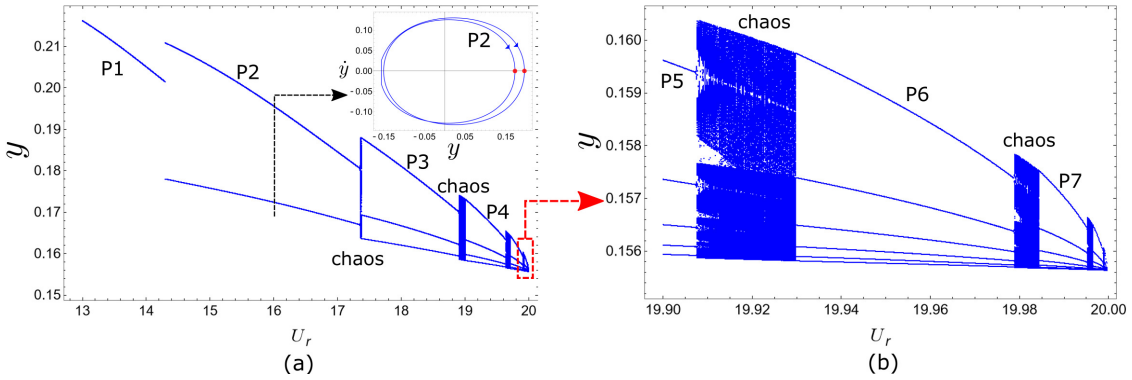

Figure 5.2: (a)Bifurcation diagram of amplitude response $y(\dot{y} = 0)$ against reduced velocity U_r. The inset figure depicts the phase portrait at $U_r = 16.0$. Two red dots depict the Poincaré points. (b)y vs U_r near grazing at $U_r = 20.0$.

The seemingly aperiodic bands appear due to the occurrence of DIBs. As chaotic trajectories are sensitively dependent on the initial conditions, it is essential to possess insights into the evolution of any perturbed trajectory in the vicinity of a barrier. Here, the dependence to initial conditions will also manifest in scenarios where a trajectory slightly missing the barrier would start interacting with it and getting reset to a completely new state upon the slightest change in initial conditions. Eq. 5.4 denotes the governing equations describing the evolution of state vector $\mathbf{x}$, while the perturbed state $\mathbf{y}$ evolves according to the Jacobian matrix of $\mathbf{F}(\mathbf{x})$. The barrier is modelled using a scalar function $H(\mathbf{x}) = y - \sigma = 0$. The reset map in Eq.

(5.4) is modelled by $\mathbf{R}(\mathbf{x})$. Fig. 5.3 depicts the schematic of a periodic trajectory $\mathbf{x}$ and its perturbation $\mathbf{y}$ as it evolves in the phase-space starting from Σ_1. The state $\mathbf{x}$ undergoes an impact at $\Sigma_2 = H(\mathbf{x}_i) = 0$ when it gets mapped to $\mathbf{R}(\mathbf{x}_i)$. At this instant, the perturbed state gets mapped from $\mathbf{x}_0$, before it impacts the barrier to $\mathbf{x}_4$ via a transverse discontinuity mapping (TDM). Therefore, the TDM maps the perturbed state $\mathbf{x}_0 = \mathbf{x}_i + \mathbf{y}_-$ to $\mathbf{x}_4 = \mathbf{R}(\mathbf{x}_i) + \mathbf{y}_+$, after the actual trajectory $\mathbf{x}$ impacts the barrier at $\mathbf{x}_i$, such that the mapped state $\mathbf{x}_4$ reaches Σ_2 at $\mathbf{x}_3$ after time δ. It is the same time δ that the trajectory $\mathbf{x}_i + \mathbf{y}_-$ would take if evolved from $\mathbf{x}_0$ to reach Σ_2 at $\mathbf{x_2}$. The analytical expressions for δ upto second order and the corresponding TDM with higher-order corrections is given by Eq. (5.5) and Eq. (5.6) below.

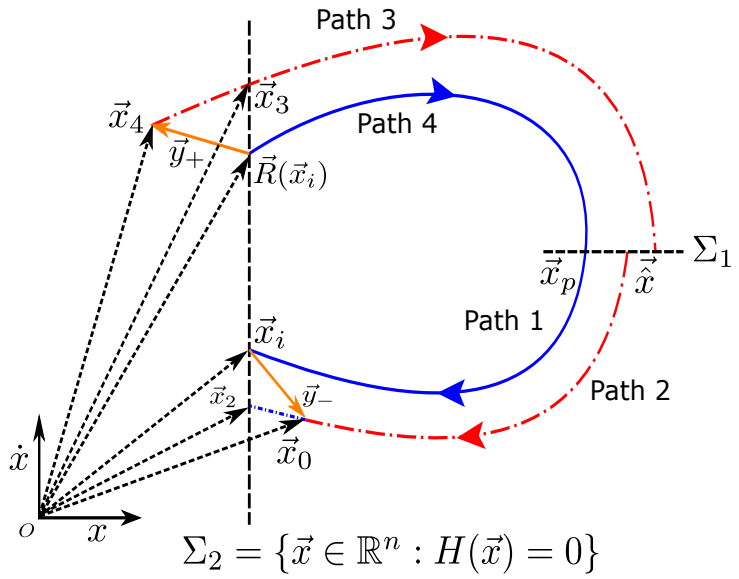

Figure 5.3: Schematic of two nearby trajectories shown in red and blue, impacting at Σ_2. The blue line is the actual trajectory $\mathbf{x}$ and the red dashed line denotes $\mathbf{x}+\mathbf{y}$. Both the orbits are initiated from the Poincaré section Σ_1 shown as black dashed line. The amber line represents the perturbation vector $\mathbf{y}$.

$$\begin{aligned}
&\delta^2\Big(\nabla H(\mathbf{x}_i)^T \cdot \nabla \mathbf{F}(\mathbf{x}_i)^T \cdot \mathbf{F}(\mathbf{x}) + \mathbf{F}(\mathbf{x}_i)^T \cdot \nabla(\nabla H(\mathbf{x}_i))^T \cdot \mathbf{F}(\mathbf{x}_i)\Big) \\
&\quad + \delta\Big(2\nabla H(\mathbf{x}_i)^T \cdot \mathbf{F}(\mathbf{x}_i) + 2\nabla H(\mathbf{x}_i)^T \cdot \nabla \mathbf{F}(\mathbf{x}_i)^T \cdot \mathbf{y} + \mathbf{y}^T \cdot \nabla(\nabla H(\mathbf{x}_i))^T \cdot \mathbf{F}(\mathbf{x}_i) \\
&\qquad + \mathbf{F}(\mathbf{x}_i)^T \cdot \nabla(\nabla H(\mathbf{x}_i))^T \cdot \mathbf{y}\Big) + \mathbf{y}^T \cdot \nabla(\nabla H(\mathbf{x}_i))^T \cdot \mathbf{y} + 2\nabla H(\mathbf{x}_i)^T \cdot \mathbf{y} \\
&\qquad + \mathcal{O}(3) = G(\delta, \mathbf{x}_i, \mathbf{y}_-) = 0
\end{aligned} \tag{5.5}$$

$$\begin{aligned}\mathbf{x}_4 = \mathbf{R}(\mathbf{x}_i) &+ \nabla\mathbf{R}(\mathbf{x}_i)^T \cdot \mathbf{y}_- + \delta\nabla\mathbf{R}(\mathbf{x}_i)^T \cdot \mathbf{F}(\mathbf{x}_i) - \delta\mathbf{F}(\mathbf{R}(\mathbf{x}_i)) \\ &+ \delta\nabla\mathbf{R}(\mathbf{x}_i)^T \cdot \nabla\mathbf{F}(\mathbf{x}_i)^T \cdot \mathbf{y}_- + \frac{1}{2}\delta^2\nabla\mathbf{R}(\mathbf{x}_i)^T \cdot \nabla\mathbf{F}(\mathbf{x}_i)^T \cdot \mathbf{F}(\mathbf{x}_i) \\ &- \delta\nabla\mathbf{F}(\mathbf{R}(\mathbf{x}_i))^T \cdot \nabla\mathbf{R}(\mathbf{x}_i)^T \cdot \mathbf{y}_- - \delta^2\nabla\mathbf{F}(\mathbf{R}(\mathbf{x}_i))^T \cdot \nabla\mathbf{R}(\mathbf{x}_i)^T \cdot \mathbf{F}(\mathbf{x}_i) \\ &+ \frac{1}{2}\delta^2\nabla\mathbf{F}(\mathbf{R}(\mathbf{x}_i))^T \cdot \mathbf{F}(\mathbf{R}(\mathbf{x}_i)) \\ &+ \frac{1}{2}\begin{bmatrix}[\mathbf{y}_- + \delta\mathbf{F}(\mathbf{x}_i)]^T \cdot \nabla(\nabla r_1)^T \cdot [\mathbf{y}_- + \delta\mathbf{F}(\mathbf{x}_i)] \\ [\mathbf{y}_- + \delta\mathbf{F}(\mathbf{x}_i)]^T \cdot \nabla(\nabla r_2)^T \cdot [\mathbf{y}_- + \delta\mathbf{F}(\mathbf{x}_i)]\end{bmatrix} + \mathcal{O}(3) \end{aligned} \tag{5.6}$$

where $\mathbf{y}_+$ and $\mathbf{y}_-$ denote the perturbed vector $\mathbf{y}$ before and after an impact. The detailed derivation of this TDM can be found in Chapter 3 and [21]. Note that the TDM maps the perturbed state from $H(\mathbf{x}_0) > 0$ to $H(\mathbf{x}_4) < 0$ which is forbidden since the dynamics is only restricted to the region $H(\mathbf{x}) \geq 0$. Therefore, it is essential that the flight time δ defined in Eq. (5.5) can accurately predict when perturbations reach $\mathbf{x}_3$ on the surface Σ_2.

The higher-order corrections to the flight time results in a quadratic equation in δ, *i.e.*, $G(\delta, \mathbf{x}_i, \mathbf{y}_-)$; see Eq. (5.5). Therefore, Eq. (5.5) can be expressed as,

$$G(\delta, \mathbf{x}_i, \mathbf{y}_-) = A\delta^2 + B\delta + C, \tag{5.7}$$

where, A, B and C are scalars defined as,

$$\begin{aligned} A &= \nabla H(\mathbf{x}_i)^T \cdot \nabla\mathbf{F}(\mathbf{x}_i)^T \cdot \mathbf{F}(\mathbf{x}) + \mathbf{F}(\mathbf{x}_i)^T \cdot \nabla(\nabla H(\mathbf{x}_i))^T \cdot \mathbf{F}(\mathbf{x}_i), \\ B &= 2\nabla H(\mathbf{x}_i)^T \cdot \mathbf{F}(\mathbf{x}_i) + 2\nabla H(\mathbf{x}_i)^T \cdot \nabla\mathbf{F}(\mathbf{x}_i)^T \cdot \mathbf{y} + \mathbf{y}^T \cdot \nabla(\nabla H(\mathbf{x}_i))^T \cdot \mathbf{F}(\mathbf{x}_i) \\ &\quad + \mathbf{F}(\mathbf{x}_i)^T \cdot \nabla(\nabla H(\mathbf{x}_i))^T \cdot \mathbf{y}, \\ C &= \mathbf{y}^T \cdot \nabla(\nabla H(\mathbf{x}_i))^T \cdot \mathbf{y} + 2\nabla H(\mathbf{x}_i)^T \cdot \mathbf{y}. \end{aligned} \tag{5.8}$$

The root $G(\delta, \mathbf{x}_i, \mathbf{y}_-) = 0$ provides the flight time δ after which perturbations reach the discontinuity barrier Σ_2. Note that the higher-order quadratic equation can return imaginary values of δ when no real roots exist. This implies that solutions satisfying $H(\mathbf{x} + \mathbf{y})$ do not exist, and hence perturbations do not reach the discontinuity barrier Σ_2. Hence no impacts should occur. This contradicts the widely accepted first-order approaches, which tell that impacts should occur for all values of perturbations; see Eq. (5.2). Furthermore, the higher-order corrections tell that only those perturbations bounded in the range and satisfying $B^2 - 4AC \geq 0$ can undergo impacts. Hence not all trajectories in the local neighborhood of an impacting orbit can reach the discontinuity barrier. Perturbations satisfying $B^2 \geq 4AC$ with real roots will undergo impacts with a flight time given by the positive root δ_+

satisfying $G(\delta_+, \mathbf{x}_i, \mathbf{y}) = 0$ where,

$$\delta_+ = -\frac{B}{2A}\left(1 - \sqrt{1 - \frac{4AC}{B^2}}\right). \tag{5.9}$$

This ensures that $\delta_+ \to 0$ when $\mathbf{y}_- \to 0$. Next, the predictions of the higher-order corrections to δ are validated by considering the representative case of a 4D hybrid FSI system of Eqs. (5.4).

The linearized and second order expressions of δ for the hybrid FSI system are given by,

$$\begin{aligned}
\delta_1 &= -y_1/\dot{y} \qquad (5.10)\\
\delta_+ &= -\frac{(\dot{y} + y_2)}{-\delta^2 y - \alpha\dot{y} + Mx} \\
&\quad + \frac{(\dot{y} + y_2)}{-\delta^2 y - \alpha\dot{y} + Mx}\sqrt{1 - \frac{2(-\delta^2 y - \alpha\dot{y} + Mx)y_1}{(\dot{y} + y_2)^2}}, \\
\delta_- &= -\frac{(\dot{y} + y_2)}{-\delta^2 y - \alpha\dot{y} + Mx} \\
&\quad - \frac{(\dot{y} + y_2)}{-\delta^2 y - \alpha\dot{y} + Mx}\sqrt{1 - \frac{2(-\delta^2 y - \alpha\dot{y} + Mx)y_1}{(\dot{y} + y_2)^2}}.
\end{aligned}$$

Here, δ_1, δ_+ and δ_- are the $\mathcal{O}(1)$ and $\mathcal{O}(2)$ expressions of δ. y_i denote the components of the perturbed state $\mathbf{y}_-$ during impact and $\alpha = (2\xi\delta + \gamma/\mu)$. It is evident from Eqs. 5.10 that the linearized approximation of δ oversimplifies the problem and does not consider the effect of system parameters. The expression for δ with second order terms retained takes into account the system parameters as well as the functional form of the underlying vector field $\mathbf{F}(\mathbf{x})$. For systems with larger size like the hybrid 4-D FSI model considered in this chapter, the accuracy of δ_1 deteriorates significantly, necessitating the retention of higher-order terms.

The implications of a quadratic equation like Eq. (5.7) is illustrated next. Fig. 5.4(a) is a surface plot of $G(\delta, y_1)$ vs δ and y_1 for $U_r = 14.0$ corresponding to a P1 orbit. The limit cycle, post transient effects, impacts the barrier at $\mathbf{x}_i = \{-0.15563, -0.03592, 1.79544, 2.92968\}$. A slightly perturbed orbit is initiated from $\mathbf{y}(0) = 0.0085/\sqrt{2}\{1, 1, 0, 0\}$ and reaches $\mathbf{y}(t_i) = \mathbf{y}_-$, when $\mathbf{x}_i$ impacts the discontinuity barrier, becoming $\mathbf{y}_- = \{0.00671, -0.00406, -0.07910, 0.05690\}$. The component y_1 is varied while keeping $||\mathbf{y}_-||$ fixed. Fig. 5.4(a) illustrates that the higher-order TDM only allows impacts for values of y_1 for which the surface $G(\delta, y_1)$ (green contour plot) intersects the plane $G(\delta, y_1) = 0$ (blue controur plot). The locus of the curve intersecting the plane is given by the higher-order flight time estimate of Eqs. (5.10) and is shown as blue (δ_+) and red (δ_-) points in Fig. 5.4(a). The imaginary and real values of higher-order δ_+ (shown as blue points) and first-order

δ_1 (shown as red points) for varying y_1 is shown in Fig. 5.4(b). The first-order δ_1 predicts that impacts occur for values of y_1 since it lies on the green plane where the imaginary part of δ_+ is zero as shown in Fig. 5.4(b). On the contrary, δ_+ predicts that impacts only occur for values of y_1 lying on the green plane.

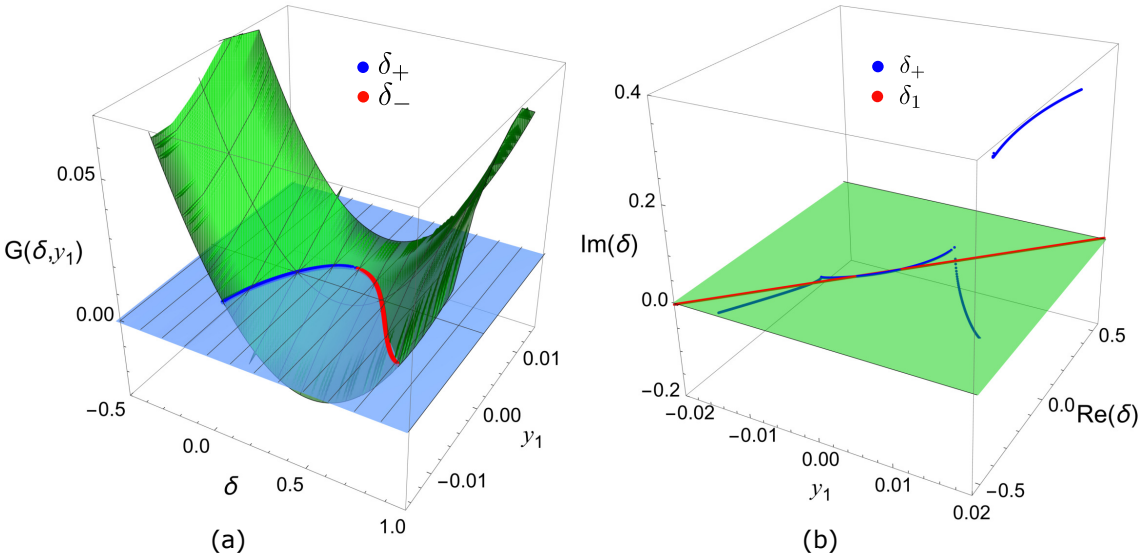

Figure 5.4: (a) Surface plot of $G(\delta, y_1)$ vs δ and y_1 for $U_r = 14.0$ at $\mathbf{x}_i = \{-0.15563, -0.03592, 1.79544, 2.92968\}$. The sky-blue plane corresponds to solutions satisfying $G(\delta, y_1) = 0$. The locus of the curve where $G(\delta, y_1)$ intersects the sky blue plane are shown as blue and red points and correspond to the positive and negative roots satisfying $G(\delta, y_1) = 0$; given by Eqs. (5.10). (b) Scatter plot of real and imaginary parts of the flight time δ vs y_1. The blue and red points correspond to higher-order (*i.e.*, δ_+) and first-order (*i.e.*, δ_1) estimates of the flight time defined in Eqs. (5.10). Note that the norm is fixed at $||\mathbf{y}_-|| = 0.097758$.

Similarly, for the same impact state $\mathbf{x}_i$ and $\mathbf{y}_-$ as in Figs. 5.4, Fig. 5.5(a) is a surface plot of $G(\delta, y_1)$ vs δ and y_1 for $U_r = 14.0$ as y_1 is varied keeping the second component y_2 of $\mathbf{y}_-$ fixed at $y_2 = -0.004063$. Fig. 5.5(a) illustrates that the higher-order TDM only allows impacts for values of y_1 for which the surface $G(\delta, y_1)$ (green contour plot) intersects the plane $G(\delta, y_1) = 0$ (blue controur plot). The locus of the curve intersecting the plane is given by the higher-order flight time estimate of Eqs. (5.10) and is shown as blue (δ_+) and red (δ_-) points in Fig. 5.5(a). The imaginary and real values of higher-order δ_+ (shown as blue points) and first-order δ_1 (shown as red points) for varying y_1 is shown in Fig. 5.5(b). The first-order δ_1 predicts that impacts occur for values of y_1 since it lies on the green plane where the imaginary part of δ_+ is zero as shown in Fig. 5.5(b). On the contrary, δ_+ predicts that impacts only occur for values of y_1 lying on the green plane.

Fig. 5.6 is a projected phase portrait of y and $\dot{y}$ for $U_r = 14.0$ corresponding to a P1 orbit when the barrier is placed at σ_g. The transients have been discarded after 1000 impacts. The evolution of perturbation vector $\mathbf{y}$ initiated from $\mathbf{y}(0) =$

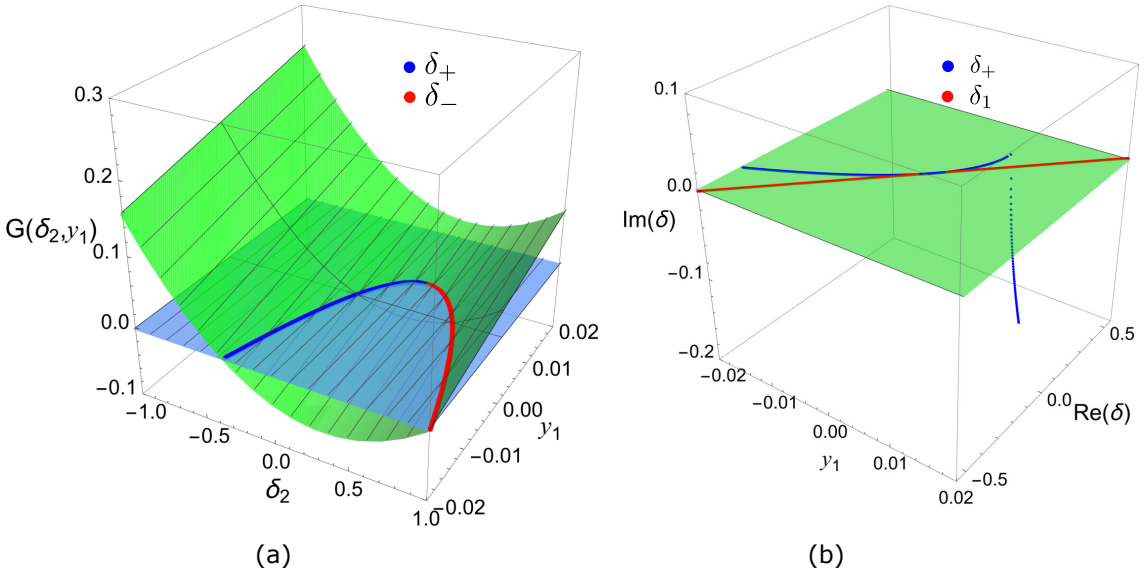

Figure 5.5: (a) Surface plot of $G(\delta, y_1)$ vs δ and y_1 for $U_r = 14.0$ at $\mathbf{x}_i = \{-0.15563, -0.03592, 1.79544, 2.92968\}$. The sky-blue plane corresponds to solutions satisfying $G(\delta, y_1) = 0$. The locus of the curve where $G(\delta, y_1)$ intersects the sky blue plane are shown as blue and red points and correspond to the positive and negative roots satisfying $G(\delta, y_1) = 0$; given by Eqs. (5.10). (b) Scatter plot of real and imaginary parts of the flight time δ vs y_1. The blue and red points correspond to higher-order (*i.e.*, δ_+) and first-order (*i.e.*, δ_1) estimates of the flight time defined in Eqs. (5.10). The second component of $\mathbf{y}_-$ is fixed at $y_2 = -0.004063$.

$r_0/\sqrt{2}[1, 1, 0, 0]$ where $r_0 = 0.0085$, is shown in Fig. 5.6(a) and when near the discontinuity barrier in (b). Figure 5.6(c) and (d) is the projected phase portrait of the perturbed trajectory initiated at $\mathbf{y}(0) = r_0/\sqrt{4}[1, 1, 1, 1]$, where $r_0 = 0.011$. As both states $\mathbf{x}$ and $\mathbf{y}$ evolve, $\mathbf{x}$ trajectory reaches the impacting surface first. At this instant, the perturbed vector is still evolving in the same sub-space. The linearized approximation δ_1 in Eq. (5.10) estimates the duration after which the collision of the perturbed trajectory takes place. The duration is estimated to be $\delta_1 = 0.1869$ for the first case and $\delta_1 = 0.1898$ for the second case. However, the numerical results show that the considered perturbed trajectories do not impact the discontinuity barrier at all. On incorporating the $\mathcal{O}(2)$ terms, the obtained δ_+s return imaginary roots implying no impacts should occur as validated numerically. Numerical results of exact solution indicate that the perturbed trajectory actually misses the barrier and does not intersect Σ_2. Thus, the higher-order estimation of $\delta = \delta_+$ provides a more accurate impact prediction of the perturbed state when the primary trajectory undergoes an impact. This validates the analytical and numerical predictions highlighted in Figs. 5.4 and 5.5.

The higher-order TDM predicts that not all perturbations in the local neighborhood of an impacting orbit should undergo impact with the discontinuity boundary contrary to the first-order saltation matrix which allows impacts for all perturba-

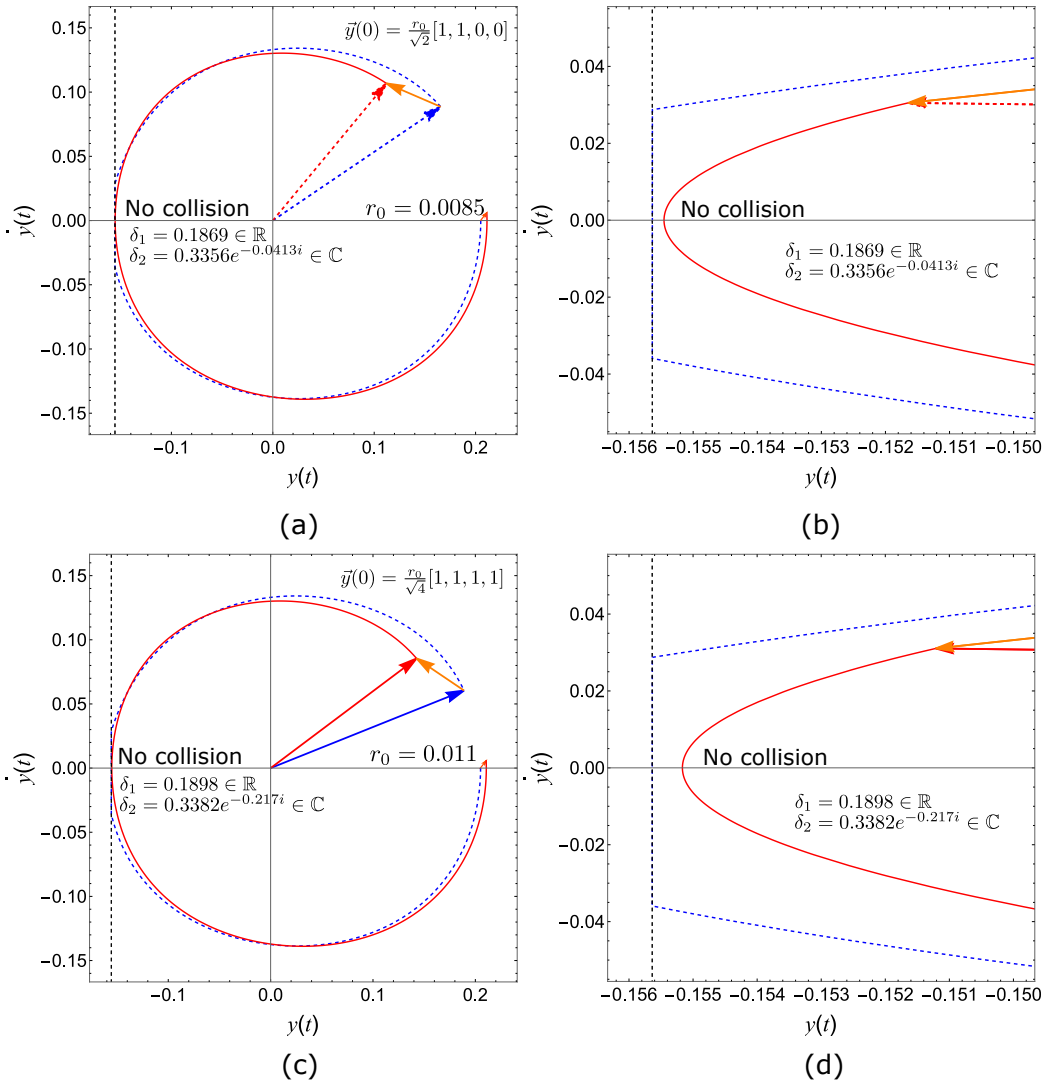

Figure 5.6: Trajectory $\mathbf{x}$ is shown in blue, $\mathbf{x}+\mathbf{y}$ is shown in red. The perturbation vector $\mathbf{y}$ is initiated as (a) $\mathbf{y}(0) = r_0/\sqrt{2}[1,1,0,0]$ and (c) $\mathbf{y}(0) = r_0/\sqrt{4}[1,1,1,1]$. $\delta_1 \sim \mathcal{O}(1)$ predicts when $\mathbf{x}+\mathbf{y}$ undergoes an impact. $\delta_2 \sim \mathcal{O}(2)$ predicts no impacts since $\delta_2 \notin \mathbb{R}$ *i.e.,* no real roots exist for $G(\delta, \mathbf{x}, \mathbf{y}) = 0$. This is validated numerically since $\mathbf{x}+\mathbf{y}$ does not impact for (b) $\mathbf{y}(0) = r_0/\sqrt{2}[1,1,0,0]$ and (d) $\mathbf{y}(0) = r_0/\sqrt{4}[1,1,1,1]$.

tions. Perturbations satisfying the condition $B^2 \geq 4AC$ in Eq. (5.7) should result in a real root implying impacts. For the hybrid 4-D FSI system investigated in this chapter, the boundedness is given by,

$$4(\dot{y} + y_2)^2 \geq 8(-\delta^2 y - \alpha\dot{y} + Mx)y_1, \tag{5.11}$$

which ensures that δ_+ will be real. Fig. 5.7(a) and (b) shows the imaginary value of δ_+ vs y_1 for the two cases of fixing $||\mathbf{y}_i||$ and y_2 demonstrated in Figs. 5.4(b) and 5.5(b) corresponding to P1 orbit when $U_r = 14.0$. In Fig. 5.7(a), when the norm kept is fixed at $||\mathbf{y}_-|| = 0.097758$, the higher-order flight time, given by Eq. (5.10), is real provided y_1 is bounded within $-0.0078 \leq y_1 \leq 0.0035$ as calculated using

Eq. (5.11). Similarly, in Fig. 5.7(b), with y_2 fixed at $y_2 = -0.004063$, impacts only occur when $y_1 \leq 0.0067$. The red point corresponds to $y_1 = 0.00671$ for which the perturbed vector $\mathbf{x} + \mathbf{y}$ does not reach and impact the barrier as verified in Fig. 5.6(b). On the contrary, the first-order flight time δ_1 incorrectly predicts impacts for all perturbations.

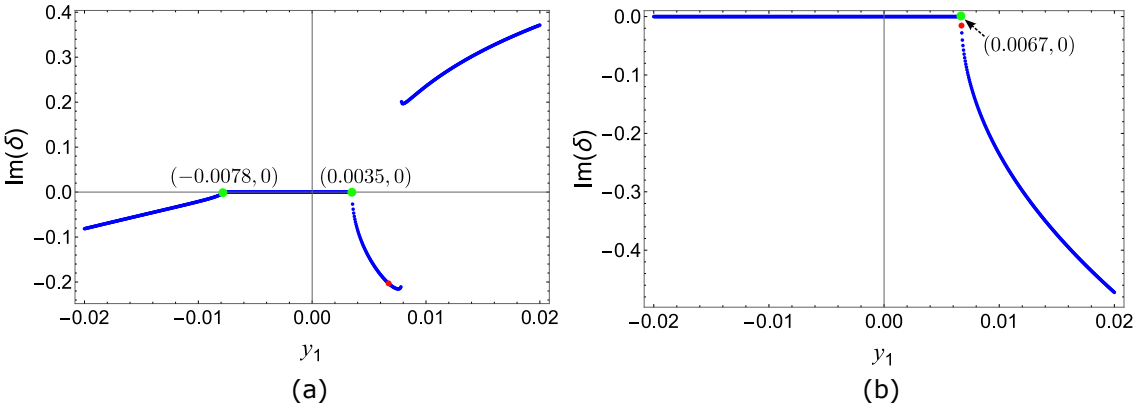

Figure 5.7: Imaginary part of higher-order flight time estimate δ_+ vs. first component of perturbation y_1 for $U_r = 14.0$. Figure shows (a) $\mathrm{Im}(\delta_+)$ vs. y_1 by fixing $||\mathbf{y}_-|| = 0.097758$ and (b) $\mathrm{Im}(\delta_+)$ vs. y_1 by fixing $y_2 = -0.004063$. The higher-order δ_+ predicts that impacts only take place in (a) when $-0.0078 \leq y_1 \leq 0.0035$ (green points) and (b) when $y_1 \leq 0.0067$ (green point) by solving the impact condition $B^2 - 4AC \geq 0$ from Eq. (6.11); see Eq. (6.22). The first-order δ_1 incorrectly predicts impacts for all values of y_1. The red point corresponds to value of δ_+ where no impact occurs for $\mathbf{y}_- = \{0.00671, -0.00406, -0.07910, 0.05690\}$ as verified in Figs. 5.6(b) and 5.6(d).

In Fig. 5.8, the error in δ as a function of the initial separation $\mathbf{y}_0$ is presented. Fig. 5.8(a) and 5.8(b) correspond to initial separation vector $\mathbf{y}(0) = 1/\sqrt{2}[1, 1, 0, 0]$ and $\mathbf{y}(0) = 1/\sqrt{4}[1, 1, 1, 1]$ respectively. Only the scaling factor r_0 is varied. The blue and pink regions are the collision and no collision regions, as obtained numerically. It is observed that as r_0 increases, the estimates diverge significantly. In the collision zone, δ_+ provides an improved estimate of the flight times in comparison to the δ_1. In the no collision zone, δ_1 incorrectly predicts a collision, returning a finite real value of δ. However, in this region, δ_+ predicts no collision with the barrier and returns an imaginary value. Similarly, in Fig. 5.9, the error in δ with respect to initial perturbation $\mathbf{y}_0$ scaled by a scalar value r_0 is presented. The four perturbed states lie orthogonally on a unit hyper-sphere scaled by r_0 in $4D$. Here, δ_+ is seen to provide a better estimate of δ when compared with numerical simulations.

The obtained higher-order correction to δ is used to calculate the improved saltation matrix $\mathbf{S}_2$. However, with the higher-order corrections, the TDM results in a vector equation having terms proportional to $\mathbf{y}$, δ_+^2, $\delta_+\mathbf{y}$ and $\mathbf{yy}$. Therefore, $\mathbf{S}_2$ cannot be straightaway expressed as a linear matrix transformation. Hence, to ob-

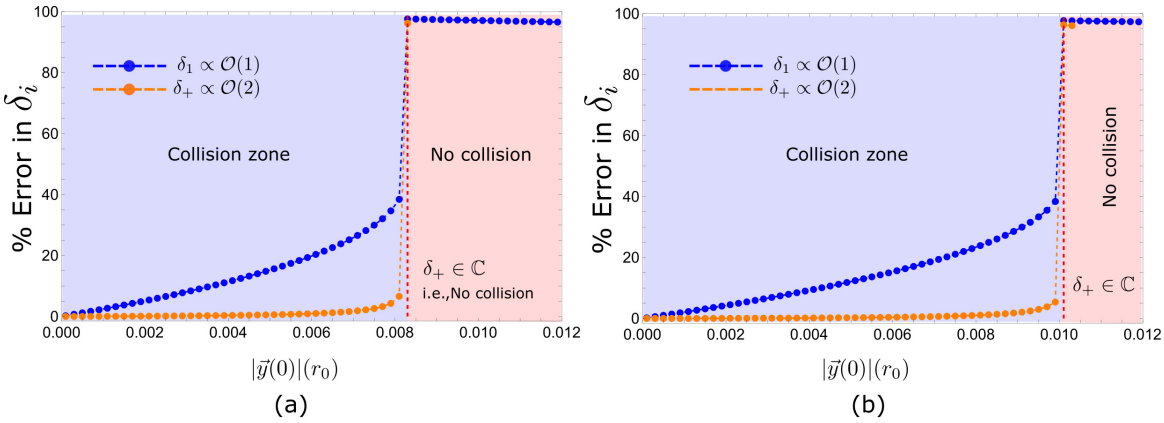

Figure 5.8: Percentage error in flight time δ_i (first-order δ_1 and higher-order δ_+; see Eqs. (5.10)) plotted for initial perturbation (a) $\mathbf{y}(0) = 1/\sqrt{2}[1,1,0,0]$, (b) $\mathbf{y}(0) = 1/\sqrt{4}[1,1,1,1]$, scaled by r_0. The blue and red regions are numerically obtained collision and no collision zones for the respective perturbed trajectories.

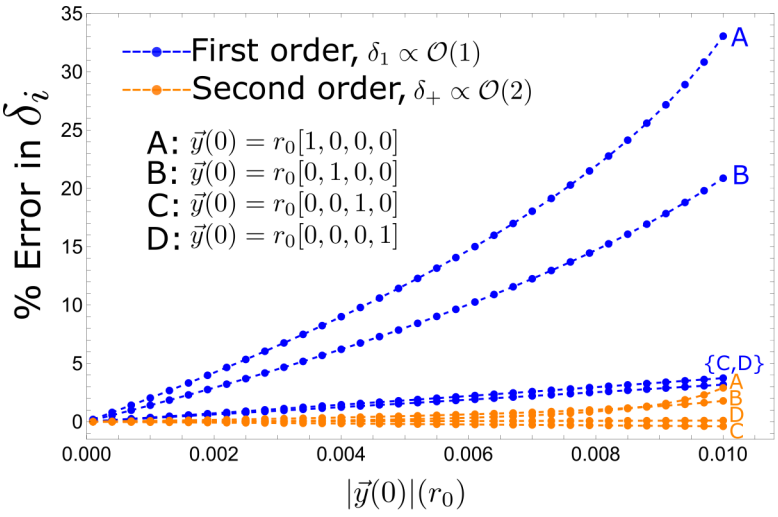

Figure 5.9: Percentage error in flight time δ_i (first-order δ_1 and higher-order δ_+; see Eqs. (5.10)) vs. varying initial separation $||\mathbf{y}(0)||$ for four orthogonal perturbations scaled by r_0.

tain the higher-order saltation matrix numerically, a set of orthogonal vectors lying on a 4D hyper-sphere of norm $r_0 \ll 1$ is considered. Each individual perturbed state $\mathbf{y}$, at the instant of impact, make the columns of a matrix $\mathbf{Y}(t_-)$ ensuring $\mathbf{Y}(0) = r_0\ \mathbb{I}_{n\times n}$, with $\mathbf{Y} \in \mathbb{R}^{n\times n}$. At impact, these perturbed paths are mapped, using the higher-order TDM, to $\mathbf{x}_4$ using Eqs. (5.5) and (5.6). The exact form of x_4 is given in Appendix E. Hence, at the instant of impact t_i, the matrix $\mathbf{Y}_+ = \mathbf{Y}(t_i)$ is calculated. The saltation matrix can be then numerically obtained by inverting the matrix $\mathbf{Y}_-$; see Eq.5.12.

$$\mathbf{S}_2^N = \mathbf{Y}_+ \cdot \mathbf{Y}_-^{-1} \tag{5.12}$$

To validate the proposed methodology of obtaining a higher-order saltation matrix, a P2 orbit, observed when $U_r = 14.0$ and $\sigma = \sigma_g$, is considered. The transients

are discarded by eliminating the initial 1000 collisions in computations. The $\mathcal{O}(1)$ saltation matrix (Eq. (5.2)) is found to be,

$$\mathbf{S}_1 = \begin{pmatrix} -0.8 & 0 & 0 & 0 \\ -4.76274 & -0.8 & 0 & 0 \\ 0 & 0 & 1 & 0 \\ 14.5549 & 0 & 0 & 1 \end{pmatrix} \tag{5.13}$$

Meanwhile, the numerically obtained $\mathcal{O}(2)$ saltation matrix, using the matrix inversion method of Eq. (5.12), by considering four orthogonally placed vectors on the hyper-sphere of radius $r_0 = 0.0001$, is calculated to be

$$\mathbf{S}_2 = \begin{pmatrix} -0.799939 & 0.001782 & -0.00002 & 0.00006 \\ -4.76258 & -0.795284 & -0.00005 & 0.00016 \\ -1.13 \times 10^{-10} & -4.547 \times 10^{-10} & 1 & -2.84 \times 10^{-14} \\ 14.5544 & -0.0144 & 0.00016 & 0.9995 \end{pmatrix}. \tag{5.14}$$

Both the estimated saltation matrices are in close agreement when compared term by term. However, in the case of dynamical systems with instantaneous reversals, a slight error in mapping the perturbed trajectories could lead to a completely different state, as demonstrated above. The higher-order flight time estimate resolves this by accurately predicting when impacts occur, which the linearized first-order saltation matrix fails to capture.

5.4 Conclusions

The well-known and widely used linearized discontinuity mapping for hybrid dynamical systems is observed to inaccurately predict impact occurrences of perturbed trajectories. Thus, an analytical expression of the TDM with higher-order corrections has been derived. To demonstrate the difference in estimating the perturbed states by the two approaches, a 4D FSI system undergoing hard impacts and possessing several system parameters is considered. Initially, the bifurcation behavior is studied. Period-adding cascades, interspersed by bands of chaos, are observed in the amplitude response. Investigations of flight times of the perturbed paths reveal that a $\mathcal{O}(2)$ TDM provides a better estimate of the state in comparison to a $\mathcal{O}(1)$ expression for TDM. This is because the closed-form expression of δ under a linearized approximation is not a function of the forcing function and crucial system parameters. This missing information is incorporated in the formulation when higher-order terms in δ are considered. Further, the higher-order flight time results in a quadratic equation for which the roots can become imaginary when perturbations become too large. This implies that impacts do not occur with the discontinuity barrier even

when the primary orbit reaches the barrier. This contradicts the first-order results, which tell that impacts occur for all values of perturbations. Comparison with the exact numerical solution indicates that the higher-order TDM correctly predicts when impacts will occur, while the first-order saltation matrix fails to do so. Further, the higher-order flight time provides a closed-form expression of the critical range within which perturbations should lie for impacts to occur. Next, a numerical technique to estimate a higher-order saltation matrix comprising higher-order flight time estimate δ_+ is proposed. The obtained results are in good agreement with the observations from numerical simulations.

Chapter 6

Higher-order transverse discontinuity mapping of Filippov systems

This chapter illustrates the dangers of linearizing transverse discontinuity mapping (TDM) in the local neighborhood of a piecewise-smooth (PWS) Filippov system executing transversal impacts with a discontinuity boundary. The widely accepted linearized state transition or saltation matrix can incorrectly predict impact occurrences in the local neighborhood. A higher-order approximation of the TDM rectifies this, accurately mapping trajectories undergoing impact transversally. A closed-form expression of the higher-order TDM is derived. The flight time to impact the discontinuity boundary is estimated using higher-order Taylor series expansions. The resulting expression of flight time is a quadratic function, which implies that impacts can only occur if perturbations are not too large, contrary to the first-order saltation matrix, which incorrectly predicts impacts for all perturbations. Additionally, the higher-order results provide accurate estimates of the mapped state post-impact compared to the first-order approaches. Two numerical techniques have been developed to estimate a higher-order saltation matrix and its consequent Floquet multipliers and Lyapunov exponents for a PWS system by implementing the derived higher-order TDM. The predictions of the proposed methodology are compared numerically on a representative case of a pre-compressed forced damped impact oscillator and validated experimentally on its equivalent analog circuit model comprising two LCR circuits with a switching mechanism. The experimental results validate occurrences of discontinuity-induced bifurcations in Filippov systems, as predicted numerically by the higher-order TDM. Further, the stability analysis of the respective soft impact oscillator is investigated using Floquet multipliers and Lyapunov exponents. The predictions agree with the corresponding forward and backward bifurcation diagrams obtained numerically and experimentally, verifying

that the proposed higher-order TDM can accurately predict when orbits become unstable during hysteresis, resulting in discontinuity-induced bifurcations.

6.1 Introduction

Discontinuity mappings are fundamental in the study of piecewise-smooth dynamical systems. Such mappings estimate how trajectories in the local neighborhood of an impacting orbit would behave in the vicinity of a discontinuity barrier. Stability analysis of such PWS systems via Floquet multipliers and Lyapunov exponents relies on how perturbed states are mapped using discontinuity mapping. However, the widely accepted mapping approaches are based on local linearizations in the Taylor expansion of an impacting orbit to predict the dynamics of perturbations during an impact. Such approximations are helpful for dynamical systems governed by smooth functions of their arguments. However, this approximation can fail for PWS systems with richer dynamics and sensitive dependence on initial conditions. For cases where the underlying dynamics are chaotic or for periodic systems with a large time period, the well-known saltation matrix can fail to predict impact occurrences. This occurs when nearby trajectories have an exponential orbital divergence, causing the perturbations to grow large (but still in $\mathcal{O}(10^{-2})$), rendering the linearized discontinuity mapping inadequate. These incorrect impact occurrences, which are based on the existing linearization approaches of the flow during an impact, can erroneously map orbits, leading to incorrect conclusions regarding the stability of the impacting orbit. This chapter highlights and resolves these issues by proposing a generalized method with higher-order corrections to the discontinuity mapping for transversal interactions with the discontinuity barrier for Filippov systems. These limitations have been overlooked since the existing literature focuses mainly on discontinuity mapping for grazing incidence. A summary of PWS systems and discontinuity mappings in the present literature is provided next.

For typical PWS systems, the state space is subdivided into regions where the dynamics are defined by a vector field local to the respective region. These sub-spaces are separated by a discontinuity barrier or switching manifold. Filippov systems constitute one of the primary types of PWS systems where the vector fields at the discontinuity boundary are not continuous; see Eqs. 6.1. Such discontinuities introduce much richer dynamics not observed in typical systems where the vector fields are always continuous. Such non-smooth systems often show several types of bifurcation under some parametric variation collectively known as discontinuity-induced bifurcations (DIBs). Some examples of DIBs found in PWS and Filippov systems are grazing[22, 54, 7], period-adding cascades of orbits [97, 89, 90, 99, 106, 37, 102], sticking-sliding [31], chattering [17], robust chaos [9] etc. Insights regarding the behavior of such systems can only be provided by investigating how perturbation

in the local linear neighborhood of an impacting orbit behaves. This is possible using discontinuity bypass mappings introduced by Fredriksson and Nordmark [36]. Fredriksson derived the discontinuity bypass mapping [36] for impact oscillators under grazing incidence. This work was motivated based on the normal form derivations by Nordmark [85, 84] for the case of an impact oscillator explaining the behavior of orbits under grazing incidence with the discontinuity barrier. Similarly, based on discontinuity mappings for grazing incidence, Fredriksson and Nordmark [37] derived the mappings for transverse interactions with the discontinuity barrier. Next, Dankowicz and Nordmark [26] derived the discontinuity mappings for PWS systems governed by discontinuous vector fields under grazing incidence. Bernardo et al. [28] introduced zero-time discontinuity mapping (ZDM) and Poincaré-section discontinuity mapping (PDM) to investigate how grazing orbits near the discontinuity barrier behave for PWS, piecewise-continuous (PWC), and Filippov systems. Later, Leine [68] derived a discontinuity mapping, also known as saltation matrix, for Filippov systems with transverse interactions with the discontinuity boundary. Yin *et al.* [137] studied bifurcations of an impact oscillator at near-grazing dynamics by deriving a higher-order ZDM. Therefore, the current literature mainly focuses on discontinuity mappings for orbits grazing the discontinuity barrier.

The existing literature mainly implements the widely accepted linearized approaches that only consider the first-order terms (terms proportional to the norm of the perturbations) in the Taylor expansions about an impacting orbit with transversal interactions with the switching manifold. Further, higher-order corrections of the discontinuity mappings have been considered for grazing incidence only. The transverse discontinuity mapping (TDM) takes care of interactions of orbits in the local linear neighborhood of the primary impacting trajectory and away from grazing incidence. In general, not all orbits will reach the discontinuity barrier simultaneously. A finite time difference or flight time exists, after which perturbations would eventually reach and cross the barrier for Filippov systems. The well-known saltation matrix approaches rely on a linearized derivation of this flight time. This first-order estimation results in a real fraction, implying that impacts occur for all values of perturbations. This assumption becomes more questionable when the orbital divergence between nearby trajectories is exponential. In such instances, the separation between orbits grows and becomes large; hence, the linearizations become insufficient to describe the governing dynamics. Additionally, the linearized approximations do not consider crucial system parameters even for the most simplistic case of a soft-impacting system modeled as a bilinear oscillator.

This chapter provides higher-order corrections to the TDM under a generalized scheme for PWS Filippov systems. The higher-order terms consider all crucial system parameters which determine the underlying dynamics. Using this approach, the higher-order flight time, which estimates when trajectories in the local neighbor-

hood of an impacting orbit reach the barrier, results in a quadratic function. This implies that the solution of the flight time can become imaginary, and therefore, not all perturbations will always undergo an impact with the discontinuity barrier. Thus, when perturbations become too large, orbits in the local neighborhood can miss the discontinuity barrier; this contradicts the first-order estimates, allowing impacts for all perturbation values. A comparison between the exact solution with the first-order vs. higher-order TDM reveals that the higher-order terms accurately predict the behavior of local perturbation; the first-order fails to capture this. The implications of predicting an incorrect impact have far-fetched consequences. The stability of a periodic orbit can be determined from an eigenvalue analysis (Floquet multipliers) of its monodromy matrix. Therefore, impact occurrences determine how monodromy matrices are constructed as they comprise products of fundamental solution matrices and state transition matrices (*i.e.*, saltation matrices) at impact occurrence. Hence, an impact vs. no impact can alter the monodromy matrix and its eigenvalues, ultimately leading to an incorrect conclusion regarding the orbit's stability. Additionally, while implementing a first-order linearized TDM, the errors accumulate when the respective orbit has multiple impacts with the discontinuity boundary due to a large time period. The higher-order approaches presented in this chapter are far superior in predicting the mapped state of perturbations during impacts with the discontinuity barrier, especially for orbits executing multiple impacts.

To validate the results of the TDM, including higher-order corrections, methods to conduct a stability analysis using Floquet theory and Lyapunov exponents have been discussed below. Since the monodromy matrix requires the state transition matrix to be defined at impact instances, a generalized method to numerically obtain the saltation matrix with higher-order corrections, ensuring compatibility with the variational equation, is provided. This is primarily because the TDM with higher-order corrections has been derived in the form of a vector; a closed-form analytical expression like the first-order saltation matrix is not possible. The prescribed method has been tested to investigate the dynamics of a soft-impact oscillator showing discontinuity-induced bifurcations (DIBs) under parametric changes. Next, a generalized scheme for determining the largest Lyapunov exponent and the Lyapunov spectrum is given. This method can determine the orbital convergence or divergence of nearby trajectories while the higher-order TDM maps perturbations at impact occurrences. The conclusions obtained by evaluating the Floquet and Lyapunov spectrum correspond well with the forward and backward bifurcation diagrams, correctly predicting when orbits become unstable during hysteresis. The approach presented in this chapter can also be used as a benchmark tool to study long-time dynamics of the steady state for arbitrary PWS Filippov systems where the exact analytical solution near the discontinuity boundary is unknown.

The derivations presented here apply to autonomous and non-autonomous Filippov systems with higher dimensions and multiple barriers.

Further, this chapter provides an experimental validation of occurrences of DIBs observed numerically for a representative Filippov system. This experiment is based on constructing an electronic system comprising two LCR circuits with a switching mechanism. The electronic analog switch resembles a discontinuity barrier, and the underlying dynamics of this electronic circuit are equivalent to the mechanical soft-impact oscillator investigated numerically. The experimentally obtained oscillatory responses, and subsequent phase portraits and bifurcation diagram, measured using a digital oscilloscope, validate occurrences of discontinuity-induced bifurcations, as predicted by a numerically obtained bifurcation diagram and from the stability analysis using the derived higher-order transverse discontinuity mapping.

The chapter is structured as follows. Section 6.2 presents a closed-form analytical expression of the transverse discontinuity mapping with higher-order corrections for piecewise-smooth Filippov systems. This TDM determines how trajectories in the local neighborhood of an impacting orbit should behave near the discontinuity barrier at the instant of an impact. Section 6.3 compares the proposed higher-order TDM with the existing and widely accepted first-order approaches using a saltation matrix. The comparison is examined on a representative system of a forced soft-impact oscillator undergoing impacts with a deformable barrier pre-compressed elastically to a fixed support. In Sec. 6.4, two methods are proposed to conduct a stability analysis for Filippov systems by implementing the higher-order TDM. First, a numerical method is presented to evaluate saltation matrices using the proposed higher-order TDM. The method is verified by conducting an eigenvalue analysis of the monodromy matrix obtained using the higher-order saltation matrices. The predictions given by the Floquet multipliers agree with the corresponding forward and backward bifurcation diagrams, further explaining when orbits become unstable during hysteresis. Next, the method is extended to calculate the largest Lyapunov exponent and Lyapunov spectrum using the higher-order TDM. This method does not require prior knowledge of the solution at the instant of an impact and can be extended to accommodate higher-order corrections like $\mathcal{O}(3)$ or higher. Section 6.5 describes an electronic analog circuit equivalent of the mechanical system investigated in Sec. 6.3, experimentally verifying the occurrence of DIBs for a pre-compressed soft impact oscillator. Sec. 6.6 summarises the principal outcomes of this chapter.

6.2 Transverse discontinuity map

An arbitrary PWS dynamical system of size n can be expressed as a vector $\mathbf{x} \in \mathbb{R}^n$ with components x_1, x_2 ... x_n representing the respective measurable quantities of

the physical system it models. The dynamics of $\mathbf{x}$ is either governed by the vector field $\mathbf{F}_i(\mathbf{x})$ or $\mathbf{F}_j(\mathbf{x})$ in the subspace S_i or S_j obeying

$$\dot{\mathbf{x}} = \begin{cases} \mathbf{F_i}(\mathbf{x}), & \text{if}, \mathbf{x} \in S_i \\ \mathbf{F_j}(\mathbf{x}), & \text{if}, \mathbf{x} \in S_j \end{cases} \tag{6.1}$$

where S_i or S_j partitions the phase-space into regions with varying vector fields $\mathbf{F}_i(\mathbf{x})$ or $\mathbf{F}_j(\mathbf{x})$. For non-autonomous systems with explicit time dependence *i.e.*, $\mathbf{F}_i(\mathbf{x}, t)$, a new phase variable $s = t$ can be defined such that $\dot{s} = 1$. Including s in $\mathbf{x}$ as an additional component, $\mathbf{x} \in \mathbb{R}^n$ becomes $\mathbf{x}' \in \mathbb{R}^{n+1}$. Therefore, the following theory holds for both autonomous and non-autonomous systems. To determine the stability of a periodic orbit $\mathbf{x}$ post transient effects and obeying Eq. (6.1), consider a secondary orbit $\tilde{\mathbf{x}} = \mathbf{x}_0 + \mathbf{y} \in S_i$ in the local neighborhood of $\mathbf{x}_0$. On substituting $\tilde{\mathbf{x}}$ in Eq. (6.1) and Taylor expanding $\mathbf{F}(\mathbf{x})$ about $\mathbf{x}_0$, the dynamics of $\mathbf{y}$ is given by,

$$\begin{aligned} \dot{\mathbf{x}}_0 + \dot{\mathbf{y}} &= \mathbf{F}_i(\mathbf{x}_0) + \nabla \mathbf{F}_i(\mathbf{x}_0)^T \cdot \mathbf{y} + \mathbf{O}(||\mathbf{y}||^2) \\ \dot{\mathbf{y}} &\approx \nabla \mathbf{F}_i^T(\mathbf{x}_0) \cdot \mathbf{y} \end{aligned} \tag{6.2}$$

where $\dot{()}$ denotes derivative with respect to time t, $\nabla \mathbf{F}_i^T(\mathbf{x})$ is the Jacobian matrix of $\mathbf{F}_i(\mathbf{x})$ and $\dot{\mathbf{x}}_0 = \mathbf{F}_i(\mathbf{x}_0)$ from Eq. (6.1). Since the evolution of $\mathbf{x}$ and $\tilde{\mathbf{x}}$ is piecewise-smooth and depends on the subspace from where they are initiated, both $\tilde{\mathbf{x}}$ and $\mathbf{x}$ reach the discontinuity boundary separating S_i from S_j at different instants. To obtain a closed-form expression of this time difference, consider the phase portrait of a 2D system showing the evolution of trajectories in Fig. 6.1. Two nearby trajectories $\mathbf{x}(0)$ and $\tilde{\mathbf{x}}(0) = \mathbf{x}(0) + \mathbf{y}(0)$ are initiated from the region S_i. Initially, $\mathbf{x}(0)$ is the periodic solution of Eq. (6.1) and $\tilde{\mathbf{x}}$ is a perturbed orbit from $\mathbf{x}_0$ with perturbation $\mathbf{y}(0)$. As $\tilde{\mathbf{x}}$ and $\mathbf{x}$ evolves in time, $\mathbf{x}(0)$ reaches $\mathbf{x}(t_i) = \mathbf{x}_i$ on the discontinuity boundary $\Sigma_{i,j} := S_i \cap S_j \in \mathbb{R}^{n-1}$ separating S_i from S_j at time $t = t_i$. The discontinuity boundary $\Sigma_{i,j}$ can be represented using a scalar function $H(\mathbf{x}) \in \mathbb{R}^1$ such that $\Sigma_{i,j} = \{\mathbf{x} \in \mathbb{R}^n : H(\mathbf{x}) = 0\}$. This implies that $S_i = \{\mathbf{x} \in \mathbb{R}^n : H(\mathbf{x}) > 0\}$ and $S_j = \{\mathbf{x} \in \mathbb{R}^n : H(\mathbf{x}) < 0\}$. At this instant, the vector field governing $\mathbf{x}_i$ changes from $\mathbf{F}_i(\mathbf{x})$ to $\mathbf{F}_j(\mathbf{x})$. However, the perturbed trajectory at $t = t_i$ has evolved to $\hat{\mathbf{x}}(t_i) = \mathbf{x}_0 \in S_i$ which is yet to reach $\Sigma_{i,j}$. At this instant, integrating $\mathbf{x}_0$ using the Jacobian of $\mathbf{F}_j(\mathbf{x})$ (see Eq. (6.2)) is incorrect since $\mathbf{x}_0 \in S_i$ will reach $\Sigma_{i,j}$ later in time at $t = t_i + \delta$, assuming δ to be the flight time of $\mathbf{x}_0$ to reach $\mathbf{x}_1 \in \Sigma_{i,j}$, see Fig. 6.1. A closed-form expression that estimates this time difference δ has been derived below. Next, to account for the discontinuities of the vector field in the local neighborhood of $\Sigma_{i,j}$, a transverse discontinuity mapping (TDM) is derived. This TDM is crucially dependent on δ and maps the state $\mathbf{x}_0$ to $\mathbf{x}_2$ ensuring that the time taken for $\mathbf{x}_0 \in S_i$ to reach $\mathbf{x}_1 \in \Sigma_{i,j}$ is the same for $\mathbf{x}_2 \in S_i$ to

reach $\mathbf{x}_1$ using the Jacobian of $\mathbf{F}_j(\mathbf{x})$. This guarantees a zero-time mapping of the perturbed trajectories ensuring that time is preserved. During the TDM of $\mathbf{x}_0$ to $\mathbf{x}_2$, the perturbation $\mathbf{y}_-$ is mapped to $\mathbf{y}_+$ using the Jacobian of the derived TDM. Using a linearised approximation, perturbations are mapped using a state transition matrix known in the literature as the saltation matrix. In the following section, the TDM of $\mathbf{x}$ and $\hat{\mathbf{x}}$ at the instant of an impact with the barrier $\Sigma_{i,j}$ has been derived implementing higher-order corrections to the saltating terms. A Taylor expansion

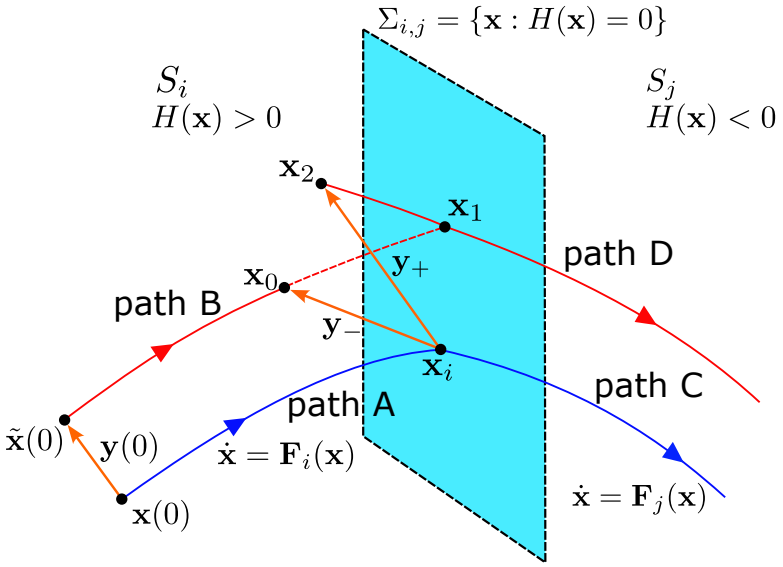

Figure 6.1: Schematic of two nearby trajectories $\mathbf{x}$ and $\tilde{\mathbf{x}} = \mathbf{x} + \mathbf{y}$ of a PWS system; shown as blue and red curves. The primary trajectory $\mathbf{x}$ impacts the discontinuity barrier $\Sigma_{i,j}$ at $\mathbf{x}_i$, when the perturbed trajectory has only reached $\mathbf{x}_0 \in S_i$. At this instant, the perturbation $\mathbf{y}_-$ gets mapped to $\mathbf{y}_+$ or $\mathbf{x}_0$ gets mapped to $\mathbf{x}_2$ using the TDM defined in Eqs. (6.9) and (6.16).

of $\mathbf{x}(t)$ and $\mathbf{F}(\mathbf{x})$ obeying $\dot{\mathbf{x}} = \mathbf{F}(\mathbf{x})$ about $t = t_0$ and $\mathbf{x}(t_0) = \mathbf{x}_0$ gives,

$$\mathbf{x}(t) = \mathbf{x}(t_0) + \Delta t\ \mathbf{F}(\mathbf{x}_0) + \frac{1}{2}\Delta t^2\ \nabla\mathbf{F}(\mathbf{x}(t_0))^T \cdot \mathbf{F}(\mathbf{x}(t_0)) + \mathcal{O}(\Delta t^3), \tag{6.3}$$

$$\mathbf{F}(\mathbf{x}) = \mathbf{F}(\mathbf{x}_0) + \nabla\mathbf{F}(\mathbf{x}_0)^T \cdot \boldsymbol{\Delta}\mathbf{x} + \frac{1}{2}\begin{bmatrix} \boldsymbol{\Delta}\mathbf{x}^T \cdot \mathrm{He}_1 \cdot \boldsymbol{\Delta}\mathbf{x} \\ \boldsymbol{\Delta}\mathbf{x}^T \cdot \mathrm{He}_2 \cdot \boldsymbol{\Delta}\mathbf{x} \end{bmatrix} + \mathcal{O}(\boldsymbol{\Delta}\mathbf{x}^3), \tag{6.4}$$

where He_is denote the Hessian matrices of each component $f_i(\mathbf{x})$ of $\mathbf{F}(\mathbf{x})$ *i.e.,* He_i defined as the Jacobian of $\nabla f_i(\mathbf{x})$ or $\nabla(\nabla f_i(\mathbf{x}))^T$ and $\boldsymbol{\Delta}\mathbf{x} = \mathbf{x} - \mathbf{x}_0$. Let δ be the time taken for $\mathbf{x}_0$ to reach $\mathbf{x}_1$ along path B as shown in Fig. 6.1. Since the primary trajectory initiated from $\mathbf{x}(0)$ reaches $\mathbf{x}(t_i) = \mathbf{x}_i$ after time t_i using path A, $\tilde{\mathbf{x}}(0)$ reaches $\tilde{\mathbf{x}}(t_i) = \mathbf{x}_0$. Therefore, $\tilde{\mathbf{x}}(t_i + \delta) = \mathbf{x}_1 \in \Sigma_{i,j}$ along path B. The state $\mathbf{x}_1$ can be approximated using a Taylor series expansion about $\mathbf{x}_0$ at time $t = \delta$ to obtain,

$$\mathbf{x}_1 = \mathbf{x}_0 + \delta\mathbf{F}_i(\mathbf{x}_0) + \frac{\delta^2}{2}\nabla\mathbf{F}_i^T(\mathbf{x}_0) \cdot \mathbf{F}_i(\mathbf{x}_0) + \mathcal{O}(\delta^3). \tag{6.5}$$

Using the expansion of Eq. (6.4), $\mathbf{F}_i(\mathbf{x}_0)$ can be approximated by Taylor expanding $\mathbf{F}_i(\mathbf{x})$ about the primary impact state $\mathbf{x}_i$ and evaluated at $\mathbf{x}_0 = \mathbf{x}_i + \mathbf{y}_-$, see Fig. 6.1. The state $\mathbf{y}_-$ is the perturbation of the perturbed trajectory $\tilde{\mathbf{x}}$ at the impact state $\mathbf{x}_i$. Therefore, $\mathbf{F}_i(\mathbf{x}_0)$ can be written as,

$$\mathbf{F}_i(\mathbf{x}_0) = \mathbf{F}_i(\mathbf{x}_i) + \nabla\mathbf{F}_i^T(\mathbf{x}_i)\cdot\mathbf{y}_- + \frac{1}{2}\begin{pmatrix}\mathbf{y}_-^T\cdot\mathrm{He}(f_1^i)\cdot\mathbf{y}_-\\ \mathbf{y}_-^T\cdot\mathrm{He}(f_2^i)\cdot\mathbf{y}_-\end{pmatrix} + \mathcal{O}(||\mathbf{y}_-||^3), \tag{6.6}$$

where $\mathrm{He}(f_1^i)$ and $\mathrm{He}(f_2^i)$ are the Hessian matrices of the scalar components of $\mathbf{F}_i(\mathbf{x})$. Substituting Eq. (6.6) in Eq. (6.5), $\mathbf{x}_1$ can be approximated as,

$$\begin{aligned}\mathbf{x}_1 = \mathbf{x}_0 + \delta\Big(\mathbf{F}_i(\mathbf{x}_i) + \nabla\mathbf{F}_i^T(\mathbf{x}_i)\cdot\mathbf{y}_-\Big) + \frac{1}{2}\delta^2\nabla\mathbf{F}_i^T(\mathbf{x}_i)\cdot\mathbf{F}_i(\mathbf{x}_i)\\ + \mathcal{O}(\delta^3, ||\mathbf{y}_-||^3, \delta^2||\mathbf{y}_-||, ||\mathbf{y}_-||^2\delta).\end{aligned} \tag{6.7}$$

The flight time δ for $\mathbf{x}_0$ to reach $\mathbf{x}_1$ is calculated next by solving for the root $H(\mathbf{x}_1) = 0$. A Taylor expansion of the scalar function $H(\mathbf{x})$ about $\mathbf{x}_i$ when evaluated at $\mathbf{x}_1$ gives,

$$H(\mathbf{x}_1) = H(\mathbf{x}_i) + \nabla H(\mathbf{x}_i)^T\cdot(\mathbf{x}_1-\mathbf{x}_i) + \frac{1}{2}(\mathbf{x}_1-\mathbf{x}_i)^T\cdot\mathrm{He}(H(\mathbf{x}_i))\cdot(\mathbf{x}_1-\mathbf{x}_i) + \mathcal{O}(||(\mathbf{x}_1-\mathbf{x}_i)||^3). \tag{6.8}$$

Since the states $\mathbf{x}_1$ and $\mathbf{x}_i$ lie on $\Sigma_{i,j}$, $H(\mathbf{x}_1)$ and $H(\mathbf{x}_i)$ vanishes using the definition of $\Sigma_{i,j} = \{\mathbf{x}\in\mathbb{R}^n : H(\mathbf{x}) = 0\}$. Finally, substituting Eq. (6.7) in Eq. (6.8) and using the expression $\mathbf{x}_0 = \mathbf{x}_i + \mathbf{y}_-$, the flight time δ is be solved analytically. The result is a quadratic equation in δ given in Eq. (6.9),

$$\begin{aligned}&\delta^2\Big(\nabla H(\mathbf{x}_i)^T\cdot\nabla\mathbf{F_i}(\mathbf{x}_i)^T\cdot\mathbf{F_i}(\mathbf{x}_i) + \mathbf{F_i}(\mathbf{x}_i)^T\cdot\nabla(\nabla H(\mathbf{x}_i))^T\cdot\mathbf{F_i}(\mathbf{x}_i)\Big)\\ &\quad+\delta\Big(2\nabla H(\mathbf{x}_i)^T\cdot\mathbf{F_i}(\mathbf{x}_i) + 2\nabla H(\mathbf{x}_i)^T\cdot\nabla\mathbf{F_i}(\mathbf{x}_i)^T\cdot\mathbf{y}_-\\ &\qquad+\mathbf{y}_-^T\cdot\nabla(\nabla H(\mathbf{x}_i))^T\cdot\mathbf{F_i}(\mathbf{x}_i) + \mathbf{F_i}(\mathbf{x}_i)^T\cdot\nabla(\nabla H(\mathbf{x}_i))^T\cdot\mathbf{y}_-\Big)\\ &\qquad+\mathbf{y}_-^T\cdot\nabla(\nabla H(\mathbf{x}_i))^T\cdot\mathbf{y}_- + 2\nabla H(\mathbf{x}_i)^T\cdot\mathbf{y}_-\\ &\qquad+\mathcal{O}(3) = G(\delta,\mathbf{x}_i,\mathbf{y}_-) = 0,\end{aligned} \tag{6.9}$$

where the quadratic expression is defined as $G(\delta,\mathbf{x}_i,\mathbf{y}_-)$. Retaining only linear terms in $\mathbf{y}_-$, the widely implemented first-order flight time δ_1 takes the form,

$$\delta_1 = -\frac{\nabla H(\mathbf{x}_i)^T\cdot\mathbf{y}_-}{\nabla H(\mathbf{x}_i)^T\cdot\mathbf{F_i}(\mathbf{x}_i)}. \tag{6.10}$$

As $G(\delta,\mathbf{x}_i,\mathbf{y}_-)$ is quadratic in δ, Eq. (6.9) can be expressed as,

$$G(\delta,\mathbf{x}_i,\mathbf{y}_-) = A\delta^2 + B\delta + C \tag{6.11}$$

where A, B and C are scalars defined as,

$$\begin{aligned} A &= \nabla H(\mathbf{x}_i)^T \cdot \nabla \mathbf{F_i}(\mathbf{x}_i)^T \cdot \mathbf{F_i}(\mathbf{x}_i) + \mathbf{F_i}(\mathbf{x}_i)^T \cdot \nabla(\nabla H(\mathbf{x}_i))^T \cdot \mathbf{F_i}(\mathbf{x}_i) \\ B &= 2\nabla H(\mathbf{x}_i)^T \cdot \mathbf{F_i}(\mathbf{x}_i) + 2\nabla H(\mathbf{x}_i)^T \cdot \nabla \mathbf{F_i}(\mathbf{x}_i)^T \cdot \mathbf{y}_- \\ &\quad + \mathbf{y}_-^T \cdot \nabla(\nabla H(\mathbf{x}_i))^T \cdot \mathbf{F_i}(\mathbf{x}_i) + \mathbf{F_i}(\mathbf{x}_i)^T \cdot \nabla(\nabla H(\mathbf{x}_i))^T \cdot \mathbf{y}_- \\ C &= \mathbf{y}_-^T \cdot \nabla(\nabla H(\mathbf{x}_i))^T \cdot \mathbf{y}_- + 2\nabla H(\mathbf{x}_i)^T \cdot \mathbf{y}_- \end{aligned} \tag{6.12}$$

The root $G(\delta, \mathbf{x}_i, \mathbf{y}_-) = 0$ or $H(\mathbf{x}_1) = 0$ implies that nearby trajectories undergo impacts with $\Sigma_{i,j}$ at time $t = t_i + \delta$. A comparison of Eqs. (6.9) and (6.10) raises two questions. First, can imaginary roots of Eq. (6.9) exist, implying that no impacts will occur, contradictory to the predictions of the widely accepted first-order approaches resulting in Eq. (6.10)? Secondly, should the perturbation $\mathbf{y}_-$ be within a critical range for which impacts will occur? This implies that perturbations larger than a critical value will not undergo impacts since $\delta \in \mathcal{C}$. Thus, the root of $G(\delta, \mathbf{x}_i, \mathbf{y}_-) = 0$ with the positive sign determines the flight time of impact in the local neighborhood of $\mathbf{x}_i$ and is given by,

$$\delta_+ = -\frac{B}{2A}\left(1 - \sqrt{1 - \frac{4AC}{B^2}}\right). \tag{6.13}$$

This ensure that $\delta_+ \to 0$ when $\mathbf{y}_- \to 0$. The critical range in $\mathbf{y}_-$ beyond which no impacts should occur and hence perturbations will miss $\Sigma_{i,j}$ is given by the condition $B^2 \geq 4AC$. Hence, when δ_+ is imaginary, no real roots exist which satisfy $H(\mathbf{x}_1) = 0$, and therefore perturbations do not reach and impact the discontinuity barrier $\Sigma_{i,j}$. On the contrary, the first-order approximation of $\delta = \delta_1$ (see Eq. (6.10)) is a real fraction that incorrectly predicts that impacts occur for all perturbations. This has been demonstrated in Sec 6.3.

Next, a Taylor expansion of $\mathbf{x}$ along path D about the point $\mathbf{x}(0) = \mathbf{x}_1$ and evaluated backwards in time at $t = -\delta_+$ gives the mapped state $\mathbf{x}_2$,

$$\mathbf{x}_2 = \mathbf{x}_1 - \delta_+ \mathbf{F}_j(\mathbf{x}_1) + \frac{\delta_+^2}{2}\nabla \mathbf{F}_j^T(\mathbf{x}_1) \cdot \mathbf{F}_j(\mathbf{x}_1) + \mathcal{O}(\delta_+^3) \tag{6.14}$$

The vector field $\mathbf{F}_j(\mathbf{x}_1)$ along path D is approximated using a Taylor expansion of $\mathbf{F}_j(\mathbf{x})$ about $\mathbf{x}_i$ and evaluated at $\mathbf{x}_1$. From Eq. (6.7) and the relation $\mathbf{x}_0 = \mathbf{x}_i + \mathbf{y}_-$, $\mathbf{F}_j(\mathbf{x}_1)$ can be expressed up to $\mathcal{O}(1)$ as,

$$\mathbf{F}_j(\mathbf{x}_1) = \mathbf{F}_j(\mathbf{x}_i) + \nabla \mathbf{F}_j^T \cdot (\mathbf{y}_- + \delta_+ \mathbf{F}_i(\mathbf{x}_i)) + \mathcal{O}(||\mathbf{y}_-||^2, \delta_+ ||\mathbf{y}_-||, \delta_+^2) \tag{6.15}$$

Finally, on substituting Eqs. (6.7) and (6.15) in Eq. (6.14), using the positive root

δ_+, the TDM from $\mathbf{x}_0$ to $\mathbf{x}_2$ can be expressed in terms of $\mathbf{y}_-$ and $\mathbf{y}_+$ as,

$$\begin{aligned}\mathbf{y}_+ = \mathbf{y}_- &+ \delta\Big(\mathbf{F}_i(\mathbf{x}_i) - \mathbf{F}_j(\mathbf{x}_i)\Big) + \delta\Big(\nabla\mathbf{F}_i^T(\mathbf{x}_i) - \nabla\mathbf{F}_j^T(\mathbf{x}_i)\Big)\cdot\mathbf{y}_- \\ &+ \frac{\delta^2}{2}\Big(\nabla\mathbf{F}_i^T(\mathbf{x}_i)\cdot\mathbf{F}_i(\mathbf{x}_i) - 2\nabla\mathbf{F}_j^T(\mathbf{x}_i)\cdot\mathbf{F}_i(\mathbf{x}_i) + \nabla\mathbf{F}_j^T(\mathbf{x}_i)\cdot\mathbf{F}_j(\mathbf{x}_i)\Big) \\ &+ \mathcal{O}(\delta^3, \delta^2||\mathbf{y}_-||, \delta||\mathbf{y}_-||^2) \end{aligned} \tag{6.16}$$

where $\mathbf{x}_2 = \mathbf{x}_i + \mathbf{y}_+$; see Fig. 6.1. Additionally, keeping only the linear order terms in Eq. (6.16) and using the $\mathcal{O}(1)$ approximation of δ (see Eq. (6.10)), the mapping of $\mathbf{y}_-$ to $\mathbf{y}_+$ can be expressed in a matrix form as,

$$\mathbf{y}_+ = \mathbf{S}_1 \cdot \mathbf{y}_- \tag{6.17}$$

where $\mathbf{S}_1$ is called the saltation matrix in literature [68] and is given by,

$$\mathbf{S}_1 = \mathbb{I}_{n\times n} + \frac{\big(\mathbf{F}_j(\mathbf{x}_i) - \mathbf{F}_i(\mathbf{x}_i)\big)}{\nabla H(\mathbf{x}_i)^T \cdot \mathbf{F}_i(\mathbf{x}_i)} \otimes \nabla H(\mathbf{x}_i). \tag{6.18}$$

The TDM defined by Eqs. (6.9) and (6.16) comprises higher-order corrections to the widely accepted first-order saltation matrix defined in Eqs. (6.10) and (6.18). The higher-order terms included using the proposed TDM can correctly predict impact occurrences of orbits in the local neighborhood of the discontinuity barrier, which the linearized saltation matrix fails to capture. Sec 6.3 illustrates this numerically on a pre-compressed impact oscillator executing soft impacts with a barrier. Additionally, providing a closed-form expression of the state transition of perturbations at the instant of impact in a matrix form is more complex. This is mainly because of two reasons. The TDM defined in Eq. (6.16) is a vector; hence the perturbation state $\mathbf{y}_-$ cannot be factored out. Secondly, the higher-order form of time of flight is quadratic and cannot be expressed in the product form with $\mathbf{y}_-$; this was achieved previously using linearized approximations, but the corresponding results are incorrect as illustrated in Sec. 6.3. Sec. 6.4 presents a numerical method to obtain a state transition matrix, similar to the saltation matrix but incorporating higher-order corrections. This state transition matrix, evaluated at the instant of impact, contributes to the monodromy matrix and is crucial when conducting stability analysis of limit cycles using Floquet theory.

6.3 Numerical results

This section demonstrates the failure to correctly predict impact occurrences when using a linearized TDM when keeping only the $\mathcal{O}(1)$ terms; see Eqs. (6.10) and (6.18). The higher-order TDM resolves this by considering the contributions made

by crucial system parameters missing in the first-order saltation matrix. To illustrate this, a periodically excited bilinear oscillator undergoing soft impacts with a deformable barrier is shown in Fig. 6.2.

To illustrate this, consider a body of mass $m = 1$Kg connected elastically to a wall as shown in Fig. 6.2. This mass is driven by a sinusoid with amplitude fm, forcing frequency $\omega = 0.8$Hz, and executes oscillations on a frictionless surface. The mass m comes in contact with a pre-compressed barrier when the relative distance between them is greater than $L_2 - L_1 = 1.5$m. At this instant, an additional restoring force acts on the object due to the barrier pressing against it until there is no more contact between them. The oscillatory behavior of m can be modeled as a bilinear spring with spring constants $k_1 = k_2 = 1.0$N/m and damping $\xi_1 = \xi_2 = 0.1$Ns/m.

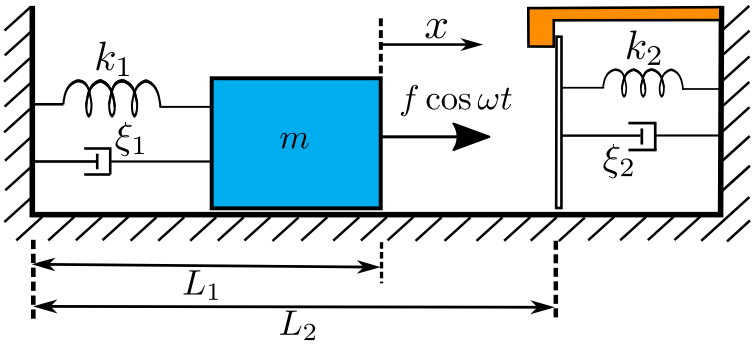

Figure 6.2: Schematic of a body of mass m undergoing oscillations due to an external force. The body is modeled as a harmonic oscillator, with stiffness k_1 and damping ξ_1, elastically connected to the left wall. The mass is excited externally by a period force with amplitude f and frequency ω. As the force f increases, the oscillations increase and eventually contact a pre-compressed deformable barrier or a soft wall. The wall is modeled as massless with stiffness k_2 and damping ξ_2. Upon contact, the pre-compressed wall exerts an additional restoring force on mass m, and the governing dynamics change instantaneously.

The resultant equations of motion can be expressed as a PWS system (see Eq. (6.1)) as,

$$m\ddot{x} = \begin{cases} f\cos\omega t - k_1 x - \xi_1 \dot{x}, & x < L_2 - L_1 \\ f\cos\omega t - (k_1 + k_2)x - (\xi_1 + \xi_2)\dot{x}, & x \geq L_2 - L_1 \end{cases} \tag{6.19}$$

Next, the orbital divergence of limit cycles has been investigated by integrating Eqs. (6.19) in Mathematica with an absolute tolerance up to 15^{th} decimal. The equations have been written as Eqs. (6.1) and (6.2). For the chosen problem, the discontinuity barrier $\Sigma_{i,j}$ is located at $x = 1.5$m since $H(\mathbf{x}) = x - (L_2 - L_1)$. The results have been recorded after 300 cycles of period $2\pi/\omega$ to eliminate any transient effects. In order to label the topology of various limit cycles observed, post-transients, the state $\mathbf{x}$ is recorded stroboscopically at every instant when t is a

multiple of the time period $T = 2\pi/\omega$ or when $t\%T = 0$. If the states repeat every Ts and $2T$s, it is labeled as a period 1 or P1 and period 2 or P2 orbit accordingly.

Consider the evolution of trajectories in the local neighborhood of a P1 orbit observed for $f = 0.57$N. Two nearby trajectories $\mathbf{x}$ and $\tilde{\mathbf{x}} = \mathbf{x} + \mathbf{y}$ with perturbation $\mathbf{y}$ are initiated from $\mathbf{x}(330818) = \{-1.275, -0.536\}$ and $\mathbf{y}(330818) = 0.1/\sqrt{2}\{1, 1\}$. At time $t_i = 330818$s, $\mathbf{x} = \mathbf{x}_i$ undergoes an impact with $\Sigma_{i,j}$ while $||\mathbf{y}_-|| = 0.0842268$. At this instant, the higher-order flight time δ for $\tilde{x}$ to reach $\Sigma_{i,j}$ can be evaluated from Eq. (6.9) and solving for $G(\delta, \mathbf{x}_i, \mathbf{y}_-) = 0$ or

$$\delta^2(f\cos\omega t - k_1\sigma - \xi_1 v) + 2\delta m(v + y_2) + 2my_1 = G(\delta, \mathbf{x}_i, \mathbf{y}_-) = 0, \tag{6.20}$$

where $\mathbf{x}_i = \{\sigma, v\}$ and y_1 and y_2 are the components of $\mathbf{y}_-$. Figure 6.3(a) presents a contour plot of $G(\delta, y_1)$ while varying between $-1.0 \leq \delta \leq 0.3$ and $-0.1 \leq y_1 \leq 0.1$. The values y_1 and y_2 are chosen such that the norm $||\mathbf{y}_-||$ is fixed at 0.0842268 according to the numerical integration. The blue and red plot points correspond to the positive and negative root satisfying $G(\delta_+, y_1) = 0$ and $G(\delta_-, y_1) = 0$ given by Eqs. (6.21). Hence the solutions given by the higher-order corrections lie on the blue plane and predict the flight time for $\tilde{\mathbf{x}}$ to reach $\Sigma_{i,j}$. In Fig. 6.3(b), the first-order prediction of flight time δ_1(see Eq. (6.10)) and the real and imaginary values of higher-order δ_+, the root with the positive sign for which $G(\delta_+, y_1) = 0$ are shown. For the system Eq. (6.19), the first and higher-order flight times are given by,

$$\begin{aligned}
\delta_1 &= -\frac{y_1}{v} \\
\delta_+ &= \frac{(v + y_2)}{\alpha_1}\left(-1 + \sqrt{1 - \frac{2\alpha_1 y_1}{(v + y_2)^2}}\right) \\
\delta_- &= \frac{(v + y_2)}{\alpha_1}\left(-1 - \sqrt{1 - \frac{2\alpha_1 y_1}{(v + y_2)^2}}\right)
\end{aligned} \tag{6.21}$$

where $\alpha_1 = f/m\cos\omega t - k_1/m\ \sigma - \xi_1/m\ v$. Note that the orbit, initiated from S_i, impacts $\Sigma_{i,j}$ and crosses into S_j. To calculate δ_+ when orbits evolve from S_j and therefore cross $\Sigma_{i,j}$ from S_j to S_i, replace α_1 in Eq. (6.21) by α_2 where $\alpha_2 = f/m\cos\omega t - (k_1 + k_2)\sigma/m - (\xi_1 + \xi_2)v/m$. The higher-order results in Fig. 6.3(a) indicate that not all values of y_1 will have a root, implying impacts do not occur for all orbits in the local neighborhood of $\mathbf{x}_i \in \Sigma_{i,j}$. The roots are given by the curve formed due to the intersection of $G(\delta, y_1)$ with the $G(\delta_+, y_1) = 0$ plane. The locus of points on this curve is given by Eq. (6.21), and only the positive root is physical since $\delta_+ \to 0$ when $\mathbf{y}_- \to 0$. Investigation of δ_+ in Fig. 6.3(b) reveals that impacts occur only for some values of y_1. This is because solutions, which lie on the green plane where the imaginary part of δ_+ vanishes, have a physical meaning implying

impacts occur at such instances. This result is in contradiction to the first-order flight time estimates (δ_1 in Eq. (6.21) is a real fraction) where solutions always lie on the plane for all values of y_1. Therefore, the instant of impact for local trajectories depends not only on the magnitude of perturbation at the instant of an impact but also on the individual components of the perturbation itself.

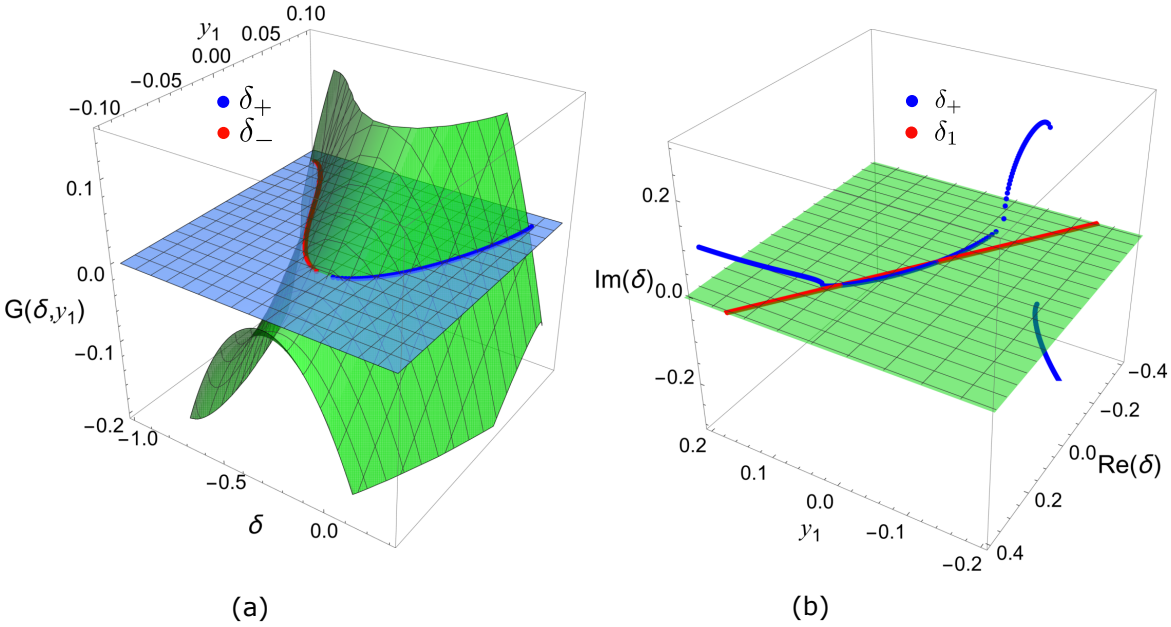

Figure 6.3: (a) Surface plot of $G(\delta, y_1)$ vs δ and y_1 for $f = 0.57$N at $\mathbf{x}_i = \{1.5, -0.349336\}$. The sky-blue plane corresponds to solutions satisfying $G(\delta, y_1) = 0$. The locus of the curve where $G(\delta, y_1)$ intersects the sky blue plane are shown as blue and red points and correspond to the positive and negative roots satisfying $G(\delta, y_1) = 0$; given by Eqs. (6.21). (b) Scatter plot of real and imaginary parts of the flight time δ vs y_1. The blue and red points correspond to higher-order (*i.e.*, δ_+) and first-order (*i.e.*, δ_1) estimates of the flight time defined in Eqs. (6.21). Note that the norm is fixed at $||\mathbf{y}_-|| = 0.0842268$.

Figure 6.4 presents a similar investigation of $G(\delta, y_1)$ and δ_+ discussed in Fig. 6.3. In this case, the value of y_2 is kept fixed at 0.02299 obtained numerically from $\mathbf{y}_-$ while y_1 is varied between $-0.1 \leq y_1 \leq 0.1$. Note that the norm of $\mathbf{y}_-$ changes since y_1 varies independently. Figure 6.4(a) shows a surface plot of $G(\delta, y_1)$ against δ and y_1 ranging between $-1.0 \leq \delta \leq 0.3$ and $-0.1 \leq y_1 \leq 0.1$. The blue and red points correspond to δ_+ and δ_- defined in Eqs. (6.21). The higher-order results indicate that impacts do not occur for all values of y_1. Trajectories in the vicinity of $\mathbf{x}_i$ with component y_1 impact $\Sigma_{i,j}$ only $G(\delta, y_1) = 0$. Such points exist in the intersection of $G(\delta, y_1)$ with the $G(\delta_+, y_1) = 0$ plane (sky-blue plane in Fig. 6.4(a)). The locus of points on the plane is given by the positive root δ_+ from Eq. (6.21). Figure 6.4(b) presents the real and imaginary values of first-order (shown in red) and higher-order (shown in blue) flight times as y_1 is varied. The higher-order corrections imply that trajectories with component y_1, for which the imaginary part of δ_+ vanishes (points

lying on the green plane), show an impact with $\Sigma_{i,j}$ after time $t_i + \delta_+$. The widely accepted first-order flight time results predict that impacts occur for all values of y_1, contradicting the proposed higher-order results. Therefore not all trajectories in the local neighborhood of an impacting orbit will reach $\Sigma_{i,j}$. Impact occurrence depends on the magnitude of perturbation at the instant of an impact.

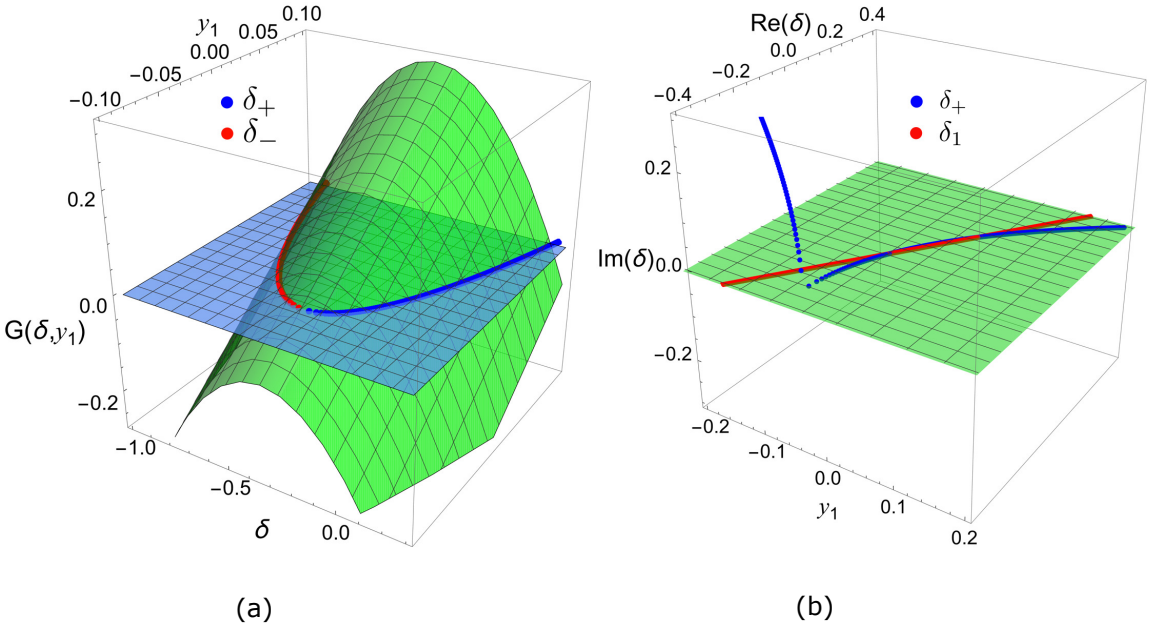

Figure 6.4: (a) Surface plot of $G(\delta, y_1)$ vs δ and y_1 for $f = 0.57$N at $\mathbf{x}_i = \{1.5, -0.349336\}$. The sky-blue plane corresponds to solutions satisfying $G(\delta, y_1) = 0$. The locus of the curve where $G(\delta, y_1)$ intersects the sky blue plane are shown as blue and red points and correspond to the positive and negative roots satisfying $G(\delta, y_1) = 0$; given by Eqs. (6.21). (b) Scatter plot of real and imaginary parts of the flight time δ vs y_1. The blue and red points correspond to higher-order (*i.e.*, δ_+) and first-order (*i.e.*, δ_1) estimates of the flight time defined in Eqs. (6.21). The second component of $\mathbf{y}_-$ is fixed at $y_2 = 0.02299$.

A comparison between the first-order estimates with the actual behavior of orbits is presented next to validate the predictions of the higher-order flight time results. Figure 6.5 are phase-portrait diagrams showing the evolution of two nearby orbits post transient effects for four different values of f. The blue and red orbits in Fig. 6.5(a) corresponds to a P1 limit cycle $\mathbf{x}$ for $f = 0.7825$N and slightly perturbed orbit $\mathbf{x} + \mathbf{y}$ with initial perturbation $\mathbf{y} = 0.35/\sqrt{2}\{1, 1\}$. The black orbit represents the true evolution of the system if it was initiated from $\mathbf{x} + \mathbf{y}$. The true behavior implies that $\mathbf{x}+\mathbf{y}$ is being integrated using Eqs. (6.1) in comparison to the evolution of $\mathbf{y}$ governed by the Jacobian of system using Eqs. (6.2). Figure 6.5(b) presents a more zoomed phase-portrait of both the trajectories undergoing impact with $\Sigma_{i,j}$. The first-order results predict that the perturbed orbit (red trajectory) will impact $\Sigma_{i,j}$ after 0.283s from the instant the primary orbit (blue trajectory) undergoes an impact. Hence, the first-order theory predicts a state transition of the perturbed

state defined by the saltation matrix (see Eq. (6.18)). The discontinuous jump in Fig. 6.5(a) and (b) of the perturbed trajectory is the first-order TDM. However, the higher-order expression defined by Eq. (6.21) estimates an imaginary flight time of $\delta_+ = 0.718e^{-0.48I} \in \mathbb{C}$. This implies that no real root exists which satisfies $H(\mathbf{x}_i + \mathbf{y}_-) = 0$, and therefore, no impact should occur. This is verified by the true perturbed trajectory simulated by the black curve, which misses the discontinuity barrier $\Sigma_{i,j}$. Similarly, Figs. 6.5(c), (e), and (g) are the phase portraits of two nearby limit cycles corresponding to $f = 0.564$, 0.566, and 0.57 while Figs. 6.5(d), (f), and (h) are the zoomed-in phase portraits near $\mathbf{x}_i$. Similarly, for all these cases, the first-order corrections are given by Eqs. (6.10) and (6.18) which predict finite flight time estimates (δ_1 in Eq. (6.21)) and TDM. The higher-order corrections given by Eq. (6.21) predict imaginary values implying no impacts should occur. This is verified numerically as the true evolution along the perturbed path (black trajectories in Figs. 6.5(d), (f) and (h)) do not show any impact with $\Sigma_{i,j}$. Note that the results of Figs. 6.3 and 6.4 predicted that impacts do not always occur for the case of $f = 0.57$N. This is verified numerically in Figs. 6.5(g) and (h). A comparison of δ_1 and δ_+ in Eqs. (6.21) indicates that the higher-order corrections consider crucial system parameters like stiffness, damping, the mass of the oscillator, and external force parameters like f and ω, which the first-order expression ignores. Therefore, the higher-order flight time estimate and TDM is a much better approximation of trajectories in the local neighborhood of an impacting orbit.

Incorrect impact estimates of trajectories near an impacting orbit at $\mathbf{x}_i$ can have severe consequences. This effect is more pronounced when the primary orbit interacts with the discontinuity boundary several times or for higher-period limit cycles. To illustrate the consequences, consider the four different impacting orbits presented earlier in Figs. 6.5. In Fig. 6.6(a), the time series of a P1 orbit $\mathbf{x}$ (blue curve) and a slightly perturbed orbit $\mathbf{x} + \mathbf{y}$ (red curve) has been shown over one time period for $f = 0.7825$. The first-order approximation predicts that $\mathbf{x} + \mathbf{y}$ will impact $\Sigma_{i,j}$ after a finite time, while the second-order predicts no impact. This is verified by the true path shown as a black curve. Moreover, the black curve, after one time period, always remains in S_i and is further away from the primary orbit than the predicted orbit, ultimately leading to an incorrect stability estimate. This is also evident in Fig. 6.5(a). Similarly, the time series of two nearby orbits over two time periods, corresponding to a P2 limit cycle, has been shown in Figs. 6.6(b), (c), and (d), respectively. These correspond to different cases discussed previously in Figs. 6.5 for $f = 0.564$N, 0.566N and 0.57N. In Fig. 6.6(b), the first-order results predict that $\mathbf{x} + \mathbf{y}$ will undergo an impact, the higher-order predicts that an impact will not occur, and the perturbed orbit will always remain in S_i, as verified by the true behavior shown as black curve. In Fig. 6.6(c), the true perturbed orbit (black curve) does not impact $\Sigma_{i,j}$ at the first instant but later returns and crosses $\Sigma_{i,j}$

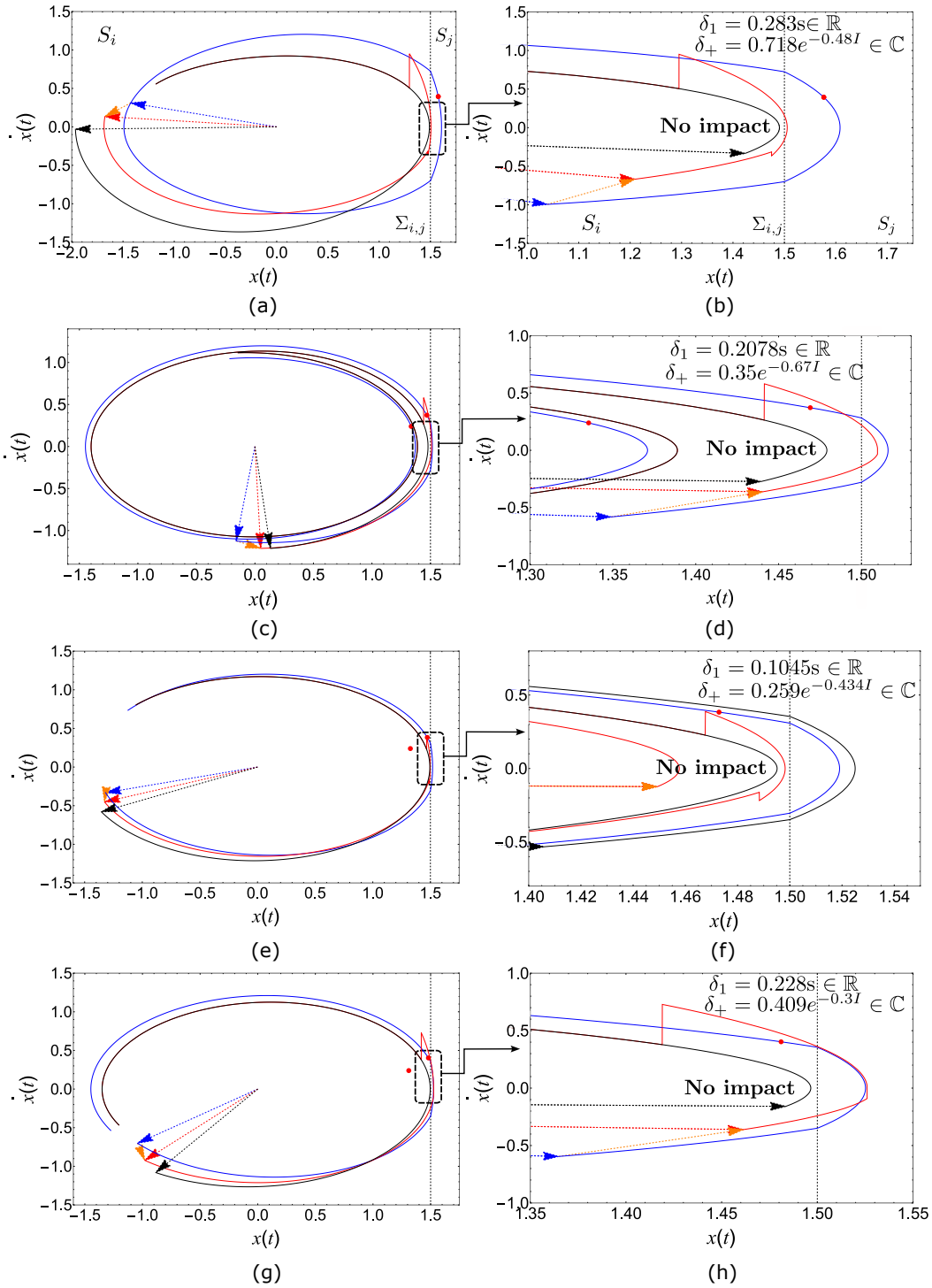

Figure 6.5: Phase portrait showing the evolution of a periodic orbit $\mathbf{x}$ (blue curve) and a secondary orbit $\mathbf{x}+\mathbf{y}$ (red curve) slightly perturbed from $\mathbf{x}$ corresponding to (a) P1 orbit for $f = 0.7825$N, and P2 orbits for (c) $f = 0.564$N, (e) $f = 0.566$N and (g) $f = 0.57$N. The first-order TDM of $\mathbf{x}+\mathbf{y}$ near the discontinuity barrier $\Sigma_{i,j}$ when $\mathbf{x}$ undergoes impact is shown for (b) $f = 0.7825$N, (d) $f = 0.564$N, (f) $f = 0.566$N and (h) $f = 0.57$N. The first-order flight time $\delta_1 \in \mathbb{R}$ predicts a real value after which impacts should occur. The higher-order flight time $\delta_+ \in \mathbb{C}$ results in an imaginary solution implying no impact. The black-dashed curve shows the exact perturbed solution verifying that impacts do not occur as predicted by the higher-order scheme.

when the primary orbit does not. The first-order TDM fails to predict this, as the predicted orbit impacts only the first time and remains in S_i over two periods. Similarly, in Fig. 6.6, the true perturbed orbit (black curve) does not impact $\Sigma_{i,j}$, as predicted using the higher-order δ_+, but later returns and crosses $\Sigma_{i,j}$. However, the first-order perturbed path (red curve) undergoes an impact at the first instant, then diverges away from the primary orbit (blue curve) and crosses $\Sigma_{i,j}$. At this instant, since the primary orbit does not impact $\Sigma_{i,j}$, the first-order TDM cannot be applied to the $\mathbf{x}+\mathbf{y}$. Hence, the first-order flight time and TDM cannot correctly estimate the behavior of orbits in the local neighborhood of an impacting orbit. The higher-order δ_+ can correctly predict impact occurrences that resemble the true behavior of perturbed orbits.

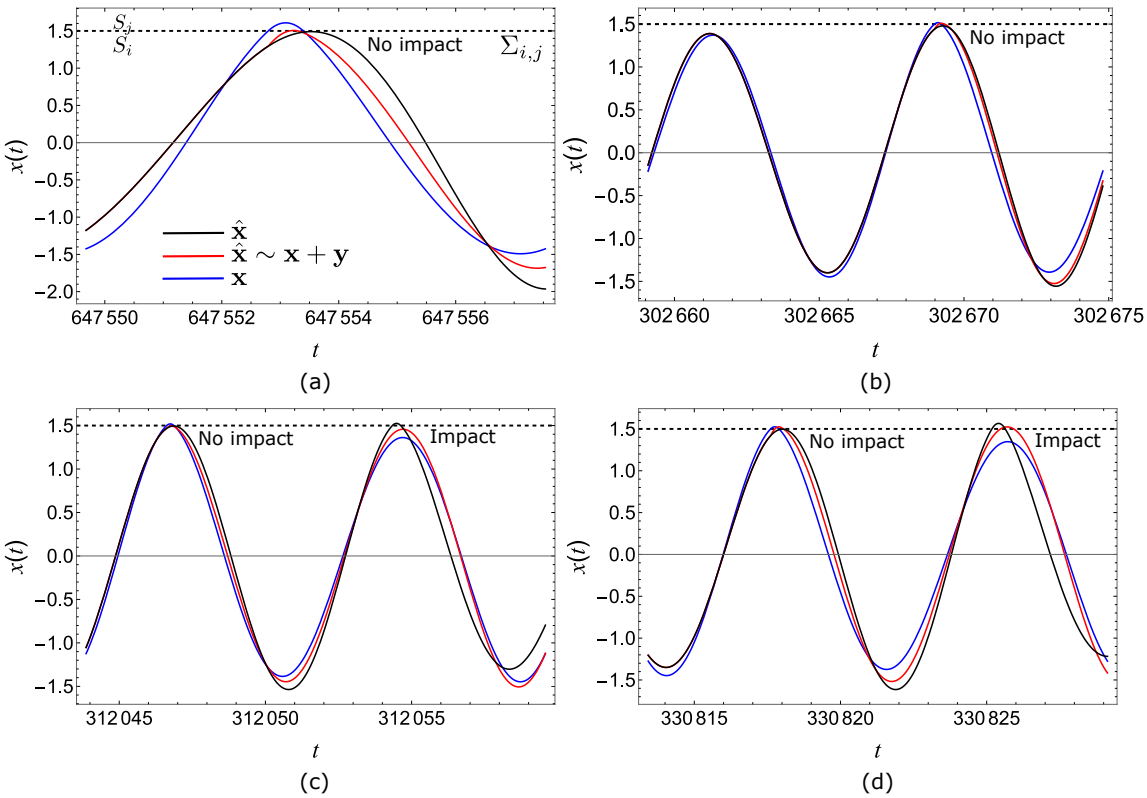

Figure 6.6: Displacement $x(t)$ post transients of a (a)P1 orbit for $f = 0.7825$N, and P2 orbits for (b)$f = 0.564$N, (c)$f = 0.566$N and (d)$f = 0.57$N. Two nearby trajectories $\mathbf{x}$ and $\mathbf{x}+\mathbf{y}$ separated by perturbation $\mathbf{y}$ are shown as blue and red orbits. The black curve represents the true orbit $\hat{\mathbf{x}} = \mathbf{x}+\mathbf{y}$ as it would evolve using Eq. (6.1). The solution of the perturbed orbit (black curve) shows no impact as predicted by an imaginary value of the higher-order flight time δ_+; this leads to disparate results when integrated over the respected time period. The first-order Saltation matrix cannot capture this.

The higher-order flight time estimate δ_+ implies that perturbations undergo impact with the discontinuity barrier only within a certain local neighborhood of the primary impacting orbit. Therefore, in Fig. 6.7, the imaginary part of δ_+ is shown as

the first component of perturbation y_1 is varied. In Fig. 6.7(a), the imaginary part of δ_+ is shown as y_1 is varied by fixing the norm $||\mathbf{y}_-||$ during impact at $t_i = 330818$s. The higher-order results indicate that impacts should occur when perturbation are not too large *i.e.*, when y_1 is bounded within a certain limit. This range can be calculated analytically by solving the condition $B^2 - 4AC$ in Eq. (6.11). For the system Eq. (6.19), this condition can be determined by solving,

$$(2m(v + y_2))^2 - 8m(f\cos\omega t - k_1\sigma - \xi_1 v)y_1 \geq 0, \tag{6.22}$$

where the impact state is $\mathbf{x}_i = \{\sigma, v\} = \{1.5, -0.349336\}$ at $t_i = 330818$s, perturbed state is $\mathbf{y}_- = \{y_1, y_2\}$ for $f = 0.57$N. For the case of Fig. 6.7(a), the bounded ranges, for which impacts should occur, are calculated as $-0.04086 \geq y_1 \geq 0.08422$. Similarly, in Fig. 6.7(b), the imaginary part of δ_+ is shown versus y_1 by keeping y_2 fixed at $y_2 = 0.02299$. The higher-order corrections results in an imaginary value of δ_+ implying no impacts when $y_1 \leq -0.05726$ as calculated analytically using Eq. (6.22). The chosen values of $\mathbf{x}_i$, t_i and $\mathbf{y}_-$ correspond to the cases shown in Figs. 6.3, 6.4, 6.5(g)-(h) and 6.6(d) where no impacts take place when compared to the true solution of the perturbed trajectory. Hence the higher-order corrections can correctly predict impact occurrence and provided the critical range within which the perturbations should be bounded for impacts to occur; the first-order saltation matrix fails to do so and incorrectly predicts that impacts occur for all values of y_1.

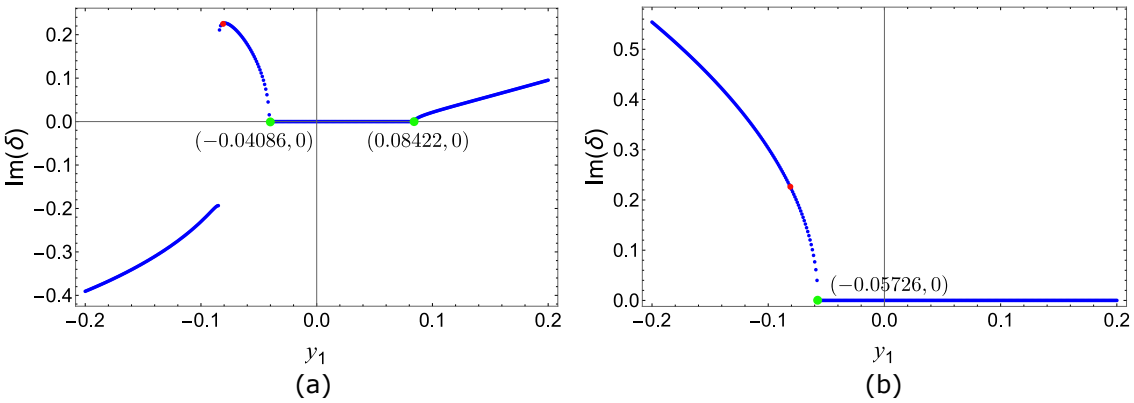

Figure 6.7: Imaginary part of higher-order flight time estimate δ_+ vs. first component of perturbation y_1. Figure shows (a) $\text{Im}(\delta_+)$ vs. y_1 by fixing $||\mathbf{y}_-|| = 0.0842268$ and (b) $\text{Im}(\delta_+)$ vs. y_1 by fixing $y_2 = 0.02299$. The higher-order δ_+ predicts that impacts only take place in (a) when $-0.0408646 \leq y_1 \leq 0.0842249$ (green points) and (b) when $y_1 = -0.05726$ (green point) by solving the impact condition $B^2 - 4AC \geq 0$ from Eq. (6.11); see Eq. (6.22). The first-order δ_1 incorrectly predicts impacts for all values of y_1. The red point corresponds to value of δ_+ where no impact occurs for $\mathbf{y}_- = \{-0.081026, 0.02299\}$ as verified in Figs. 6.5(h) and 6.6(d).

Figure 6.8(a) and (b) compares the percent error in flight time δ predicted by the first-order approximation δ_1 and higher-order δ_+ (see Eqs. (6.21)) as the initial

perturbation is varied for two P2 orbits $f = 0.564$N and $f = 0.57$N. In Fig. 6.8(a), a primary P2 orbit with $f = 0.564$N, initiated from t_0, undergoes an impact with the discontinuity barrier at some instant t_i. A closely perturbed orbit with norm $||\mathbf{y}(t_0)||$ undergoes impact at $t_i+\delta$. The prediction of the fight time for the perturbed orbit to reach the discontinuity barrier is estimated using Eqs. (6.21). The percent error in δ is compared between the $\mathcal{O}(1)$ and $\mathcal{O}(2)$ approximations. The results have been calculated using the exact values an orbit initiated from the perturbed state would take to reach the discontinuity barrier. The blue and yellow impact and no impact regions in Fig. 6.8(a) and (b) correspond to the values of $||\mathbf{y}(t_0)||$ when impacts occur and when the perturbed path misses the barrier. In the impact zone, both the first-order δ_1 and higher-order δ_+ flight times are real, but the higher-order estimates are superior with improvements up to 45%. In the no-impact region, the first-order δ_1 is real and incorrectly predicts an impact while δ_+ is imaginary. This implies that no roots exist, and hence the higher-order corrections can correctly predict impact occurrences while the first-order fails to do so. Similarly, Fig. 6.8(b) shows the percent error in δ between first-order δ_1 and higher-order δ_+ flight time estimates as the initial separation $||\mathbf{y}(t_0)||$ is varied for $f = 0.57$N. The higher-order corrections show a reduction in error up to 40% in the impact zone while correctly predicting no impacts as $\delta_+ \in \mathbb{C}$ in the no-impact zone.

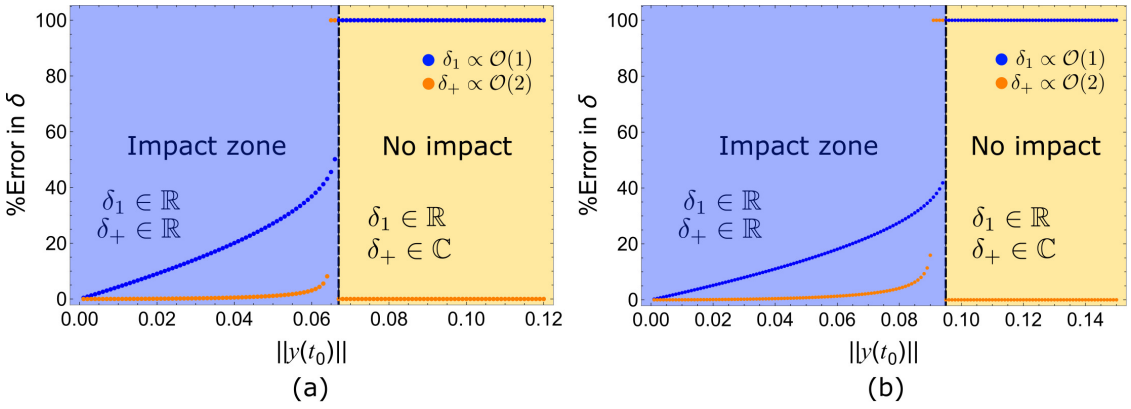

Figure 6.8: Comparison of percent error of flight time between first-order δ_1 and proposed higher-order δ_+ estimates versus initial separation $||\mathbf{y}(t_0)||$ between two nearby orbits. The blue and yellow regions (separated by a black dashed line) are the values of $||\mathbf{y}(t_0)||$ for which impact occurs or not when compared with the exact solution. Higher-order estimates are superior in predicting when impacts occur in the impact zone, whereas first-order results incorrectly predict impact in the no-impact zone. In the no-impact zone, the higher-order δ_+ correctly predicts that no real solution exists for which impacts occur.

The higher-order TDM defined in Eq. (6.16) is a derived quantity requiring the flight time estimate to map orbits in the local neighborhood at the instant of impact with the barrier. To illustrate the TDM, the phase portraits of two closely initiated P2 orbits for $f = 0.705$N is shown in Fig. 6.9(a). The phase portrait shows

the evolution of a primary P2 orbit (shown as a blue curve) and a perturbed orbit (shown as a red curve) initiated from $\mathbf{y}(t_0) = -0.2/\sqrt{2}\{1,1\}$. The exact numerical simulation of the perturbed orbit is shown as a black dashed curve. Fig. 6.9(b) shows the TDM of the perturbed orbit near $\Sigma_{i,j}$ when crossing from S_i to S_j and returning back to S_i from S_j. In Fig. 6.9(c) the perturbed orbit reaches $\mathbf{x}_0$ at impact instant t_i and gets mapped to $\mathbf{x}_2$ defined by the higher-order TDM as,

$$\mathbf{y}_+ = \begin{pmatrix} y_1 - \frac{\delta_+^2}{2m}(k_2\sigma + \xi_2 v) \\ \\ y_2 + \frac{\delta_+}{m}((\sigma + y_1)k_2 + (v + y_2)\xi_2) + \frac{\delta_+^2}{2m^2}(mk_2 v + k_2(\xi_1 + \xi_2)\sigma \\ +\xi_2(\xi_2 v - k_1\sigma) + \xi_2 f\cos\omega t_i) \end{pmatrix}_{2\times 1} \tag{6.23}$$

for the system Eq. (6.19) when the orbit crosses $\Sigma_{i,j}$ from S_i to S_j. The flight time δ_+ is defined in Eq. (6.21). In Fig. 6.9(d), the mapped state $\mathbf{x}_2$ correctly reaches $\mathbf{x}_1 \in \Sigma_{i,j}$ as predicted theoretically. This is verified since the exact numerical result, shown as black dashed lines, also reaches $\mathbf{x}_1$, lying on the discontinuity boundary at the instant $t_i + \delta_+$. Similarly in Fig. 6.9(e), while crossing $\Sigma_{i,j}$ from S_j to S_i, the perturbed state reaches $\mathbf{x}_0$ and gets mapped to $\mathbf{x}_2$, defined by the higher-order TDM as,

$$\mathbf{y}_+ = \begin{pmatrix} y_1 + \frac{\delta_+^2}{2m}(k_2\sigma + \xi_2 v) \\ \\ y_2 - \frac{\delta_+}{2m}(k_2(\sigma + y_1) + \xi_2(v + y_2)) + \frac{\delta_+^2}{2m^2}(-mk_2 v + k_2(\xi_2 - \xi_1)\sigma \\ +\xi_2(k_1\sigma + \xi_2 v) - \xi_2 f\cos\omega t_i) \end{pmatrix}_{2\times 1} \tag{6.24}$$

In Fig. 6.9(f), the mapped state $\mathbf{x}_2$ reaches $\mathbf{x}_1 \in \Sigma_{i,j}$ at the instant $t_i + \delta_+$. The results also agree with the numerically obtained perturbed path, shown as a black dashed line, since both the trajectories reach $\mathbf{x}_1$ on $\Sigma_{i,j}$. Therefore, the proposed higher-order TDM can accurately predict the behavior of trajectories in the local neighborhood of an impacting orbit.

Figure 6.10 compares the evolution of nearby orbits, $\mathbf{x}$ and $\mathbf{x} + \mathbf{y}$ initiated from $\mathbf{y}(t_0) = -0.2/\sqrt{2}\{1,1\}$ after they have been mapped with the first-order and the higher-order TDM for $f = 0.705$N. In Fig. 6.10(a), the perturbed state (shown as a red curve) $\mathbf{x}_0$ gets mapped to $\mathbf{x}_2$ using the first-order TDM (*i.e.*, saltation matrix) given by

$$\mathbf{y}_+ = \begin{pmatrix} y_1 \\ \\ \frac{-1}{mv}(k_2\sigma + \xi_2 v)y_1 + y_2 \end{pmatrix}_{2\times 1} \tag{6.25}$$

for the system Eqs. (6.19). Note that the orbits are evolving from S_i to S_j. The perturbed state reaches $\mathbf{x}_1$ after the first-order flight time $t_i + \delta_1$. However, it is

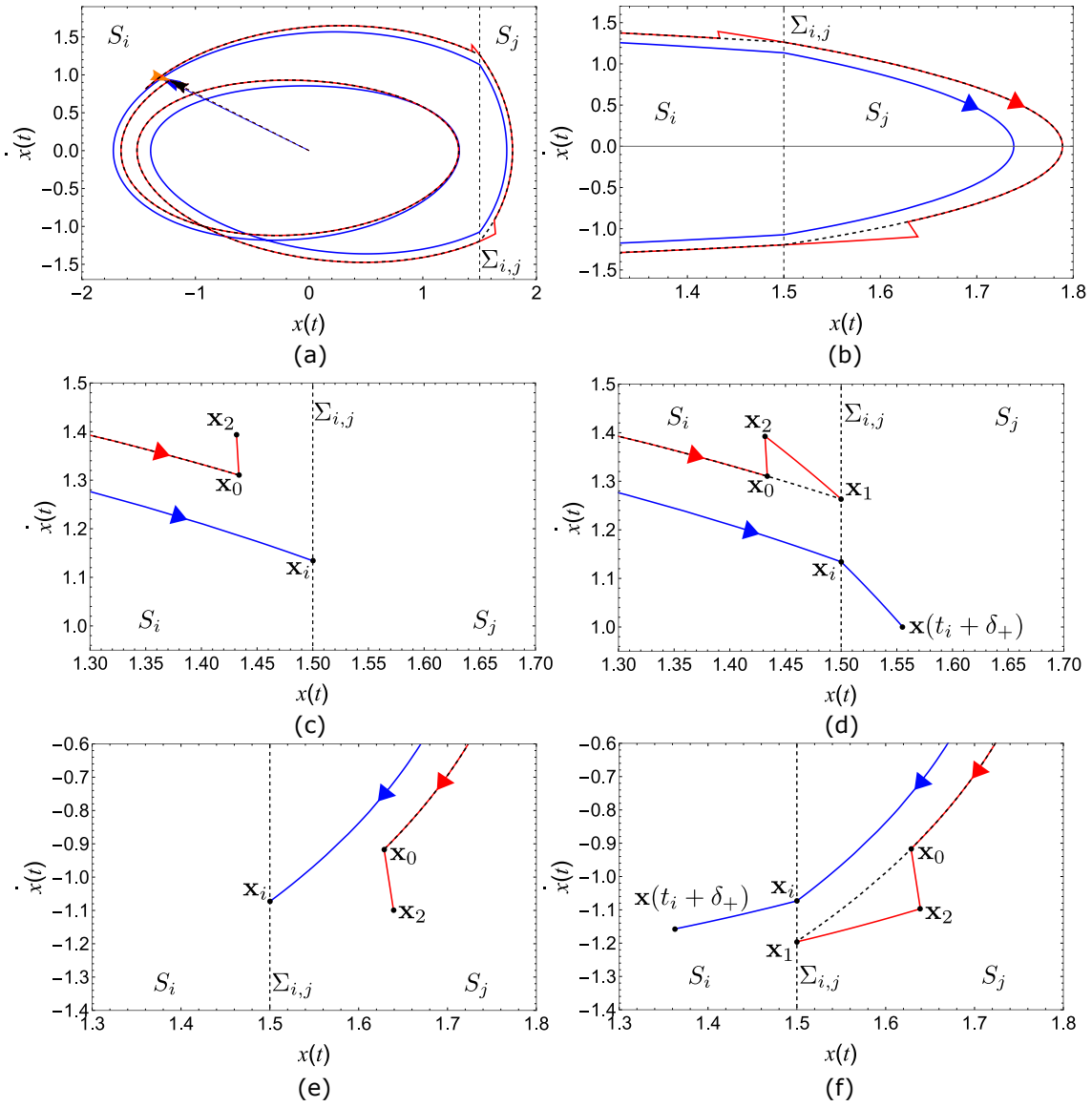

Figure 6.9: (a) Phase-portrait of a P2 orbit (blue curve) for $f = 0.705$N and a slightly perturbed orbit (red curve) undergoing TDMs at impact instances. (b) Two nearby orbits of (a) executing higher-order TDM in the vicinity of the discontinuity barrier. Higher-order TDM of perturbed orbit from $\mathbf{x}_0$ to $\mathbf{x}_2$ when primary orbit reaches $\Sigma_{i,j}$ at $t = t_i$ while orbits cross $\Sigma_{i,j}$ from (c) S_i to S_j and (e) S_j to S_i. Evolution of orbits post higher-order TDM to reach $\mathbf{x}_1$ on $\Sigma_{i,j}$ after predicted flight time $t = t_i + \delta_+$ while orbits cross $\Sigma_{i,j}$ from (d) S_i to S_j and (f) S_j to S_i. The black dashed orbit is the true solution that coincides with the predicted paths.

evident that $\mathbf{x}_1$ does not lie on the discontinuity boundary $\Sigma_{i,j}$. Additionally, the mapped trajectory does not coincide with the numerically obtained (shown as a black dashed line) perturbed trajectory and is, therefore, inaccurate. However, in Fig. 6.10(b), the state $\mathbf{x}_0$ gets mapped to $\mathbf{x}_2$ using the higher-order TDM and reaches $\mathbf{x}_1$ after $t_i + \delta_+$ which lies on $\Sigma_{i,j}$. Moreover, when mapped using higher-order corrections, the orbit coincides with the numerically obtained perturbed orbit. When crossing $\Sigma_{i,j}$ from S_j to S_i, the state $\mathbf{x}_0$ in Fig. (6.10)(c) gets mapped to $\mathbf{x}_2$

given by the first-order TDM

$$\mathbf{y}_+ = \begin{pmatrix} y_1 \\ \\ \frac{1}{mv}(k_2\sigma + \xi_2 v)y_1 + y_2 \end{pmatrix}_{2\times 1} \tag{6.26}$$

and eventually reaches $\mathbf{x}_1$. However, the state $\mathbf{x}_1$ over estimates $\Sigma_{i,j}$ as it does not accurately lie on the discontinuity boundary. The higher-order TDM correctly maps $\mathbf{x}_0$ to $\mathbf{x}_2$, which eventually reaches $\mathbf{x}_1$ after a flight time of $t_i + \delta_+$ as shown in Fig. 6.10(d). The higher-order mapped state $\mathbf{x}_2$ reaches the discontinuity mapping in Fig. 6.10(d) at the correct time when compared with the numerically obtained perturbed trajectory shown as a black dashed line. Therefore, the higher-order TDM can accurately predict the behavior of orbits local to an impacting orbit compared to the widely accepted first-order approaches.

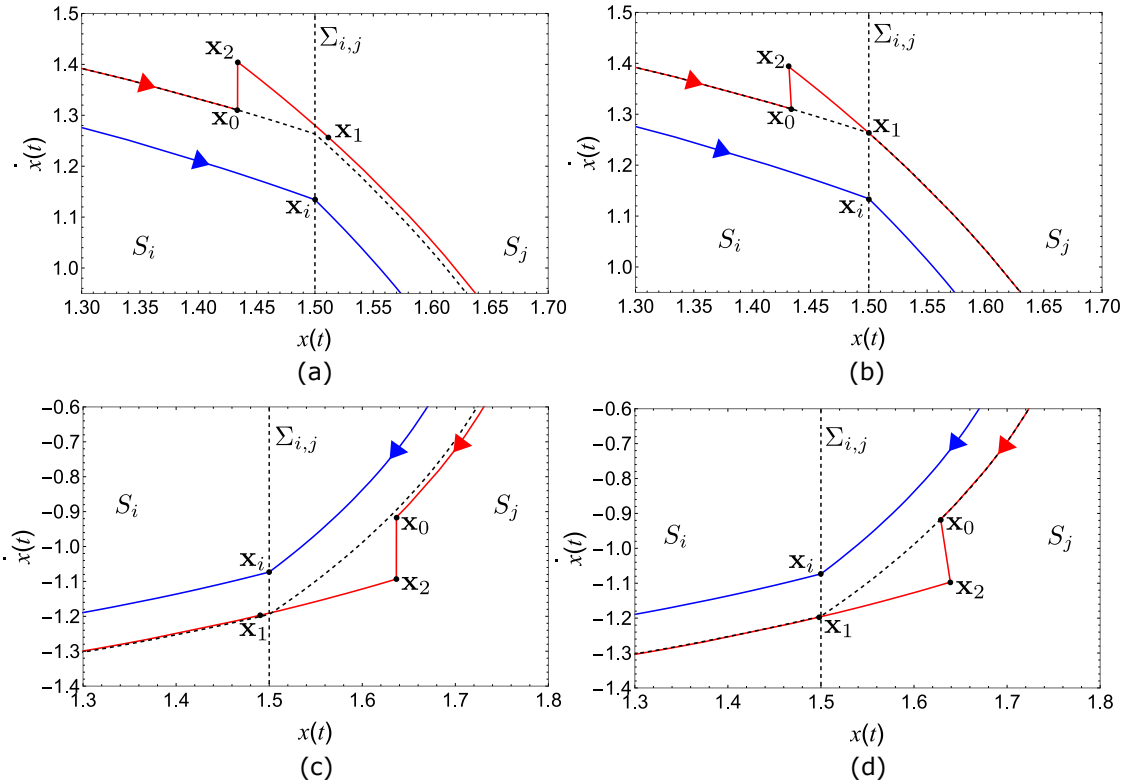

Figure 6.10: Comparison of (a) first-order (when crossing $\Sigma_{i,j}$ from S_i to S_j), (b) higher-order (when crossing $\Sigma_{i,j}$ from S_i to S_j) (c) first-order (when crossing $\Sigma_{i,j}$ from S_j to S_i) and (d)higher-order (when crossing $\Sigma_{i,j}$ from S_j to S_i) TDM from $\mathbf{x}_0$ to $\mathbf{x}_2$ of a perturbed orbit $\mathbf{x} + \mathbf{y}$ in the local neighborhood of $\mathbf{x}$ impacting $\Sigma_{i,j}$ at $\mathbf{x}_i$. Orbits mapped using higher-order TDM accurately reaches $\mathbf{x}_1$ on $\Sigma_{i,j}$ as verified numerically by the exact solution shown as black dashed orbit.

The following section discusses methods to perform stability analysis incorporating the higher-order flight time estimates and $\mathcal{O}(2)$ TDM derived in Sec. 6.2. Methods to calculate Floquet multipliers and Lyapunov exponents are discussed

next which are validated by the bifurcation diagrams for the system defined by Eqs. (6.19).

6.4 Stability analysis

This section investigates the behaviour of orbits for the soft impact oscillator as the external force f is varied. Fig. 6.11 is a bifurcation diagram of the displacement x_0 of mass m for the system Eqs. (6.19) as f is varied. The displacement x_0 is measured stroboscopically every $T = 2\pi/\omega$ s after $400T$ cycles to eliminate transients as shown in Fig. 6.11(a). The red and blue curves in Fig. 6.11(a) are the forward and backward bifurcations obtained by increasing and decreasing f between $0.50 \leq f \leq 0.92$N. At every instance, x_0 is stored for a given f after $400T$ s which becomes the initial condition for the next parameter values f. Note that for the next parameter, the integration resumes from $400T$ to $800T$ and so on since the respective system (see Eqs. (6.19)) is non-autonomous or has explicit time dependence. When increasing f in Fig. 6.11, a P1 orbit first bifurcates to a P2 orbit at $f = 0.5535$N. The resultant stable P2 orbits are observed till $f = 0.861$N when suddenly the P2 orbit disappears, and a P1 orbit is born, which persists till $f = 0.92$N. While decreasing f (blue curve in Fig. 6.11(a)), the P1 orbits remain stable till $f = 0.7815$N and disappear, giving birth to P2 orbits which coincides with the forward bifurcation curve shown as a red curve. Therefore, a phenomenon of hysteresis is observed where both P1 and P2 orbits remain stable and can be observed when initiated on the respective basin of attractions. Additionally, a stable P3 orbit (shown as a black curve) exists in the vicinity of P1 orbits between $0.53085 \leq f \leq 0.5377$. Fig. 6.11(b) is a bifurcation diagram showing the stable P3 orbits observed when f is increased gradually from 0.50N. Next, a stability analysis is carried out to investigate the appearance and disappearance of P1, P2, and P3 orbits observed in Figs. 6.11 using the higher-order TDM derived in Sec. 6.2.

6.4.1 Floquet multipliers

Floquet theory dictates that the stability of an orbit can be determined using eigenvalue analysis of its global state transition matrix (STM) or the monodromy matrix. However, Floquet theory is applicable to systems where perturbations are governed by periodic Jacobian matrices of vector fields which are smooth functions of their arguments. For piecewise-smooth systems, the monodromy matrix cannot be directly evaluated either using matrix exponentials or the integration of fundamental solution matrices (FSMs). The presence of discontinuities in phase space for PWS systems should be accompanied by STMs (known as saltation matrices) at an instant of impact. First-order approaches implement a saltation matrix defined in

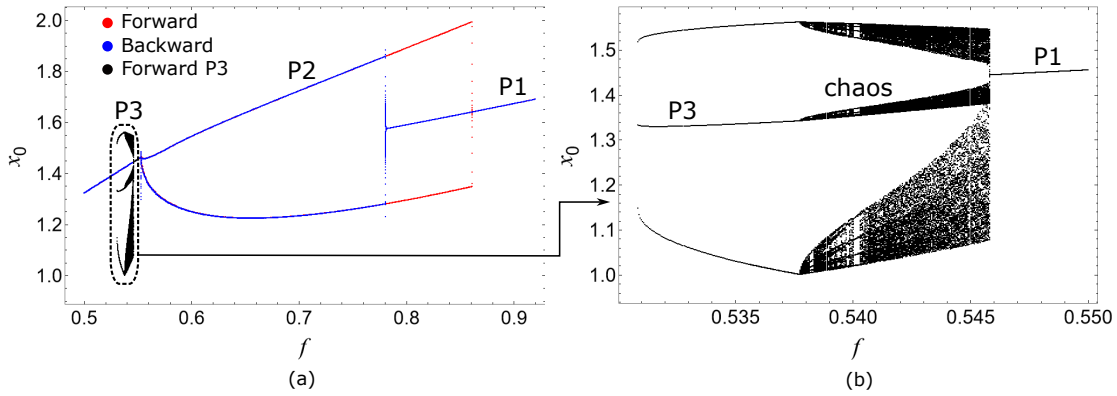

Figure 6.11: Bifurcation diagram of stroboscopic displacement x_0 vs forcing amplitude f where (a) red and blue curves denote the displacement when f is increasing and decreasing between $0.50 \leq f \leq 0.92$N. The black curve denotes a P3 orbit coexisting with a P1 orbit when f is increased. (b) Displacement, x_0 vs f, shows P3 orbits coexisting with P1 orbits when f increases.

Eq. (6.18) at an instant of an impact. However, calculations of STMs at impact occurrences incorporating higher-order corrections are not straightforward. This is because it is not possible to obtain a closed-form analytical matrix transformation that relates perturbations before and after an impact, see Eq. (6.17). The higher-order TDM results in vector mapping of perturbations before and after impacts; a closed-form linear transformation between them cannot be calculated. Hence, a numerical method is presented next to obtain a higher-order saltation matrix for Filippov systems to resolve this.

Consider an arbitrary PWS system of size n, represented by the state $\mathbf{x} \in \mathbb{R}^n$. The dynamics of $\mathbf{x}$ and perturbations $\mathbf{y}$ in its local neighborhood are defined by Eqs. (6.1) and (6.2). Next, an orthogonal set of perturbations lying on a hyper-sphere of radius r_0 is initiated. These vectors can be defined in the form of a matrix $\mathbf{Y}$ such that the column entries are the perturbations $\mathbf{y}_i$ where $i = 1, 2 \ldots n$, *i.e.*,

$$\mathbf{Y}_{n\times n}(t) = r_o[\mathbf{y}_1, \mathbf{y}_2, \ldots \mathbf{y}_i, \mathbf{y}_{i+1}, \ldots, \mathbf{y}_n] \tag{6.27}$$

It is straightforward to infer that the dynamics of the matrix-valued function $\mathbf{Y}(t)$ is also determined by the Jacobian of the vector field defined for the respective subspace S_i. Next, let $\mathbf{Y}_{-,impact}$ and $\mathbf{Y}_{+,impact}$ denote $\mathbf{Y}(t)$ before and after perturbations are

mapped using the higher-order TDM of Eq. (6.16). Therefore,

$$\mathbf{Y}_{+,impact} = \begin{bmatrix} y^{(1)}_{+,1} & \cdots & y^{(1)}_{+,n} \\ \vdots & \ddots & \vdots \\ y^{(n)}_{+,1} & \cdots & y^{(n)}_{+,n} \end{bmatrix}_{n\times n}, \text{and} \tag{6.28a}$$

$$\mathbf{Y}_{-,impact} = \begin{bmatrix} y^{(1)}_{-,1} & \cdots & y^{(1)}_{-,n} \\ \vdots & \ddots & \vdots \\ y^{(n)}_{-,1} & \cdots & y^{(n)}_{-,n} \end{bmatrix}_{n\times n}, \tag{6.28b}$$

where $y^{j}_{-,i}$ and $y^{j}_{+,i}$ correspond to the j^{th} component of the i^{th} perturbation vector $\mathbf{y}_i$ before and after impact. Now, a matrix transformation $\mathbf{S_2}$ can be obtained between two square matrices such that,

$$\mathbf{Y}_{+,impact} = \mathbf{S}_2 \cdot \mathbf{Y}_{-,impact}. \tag{6.29}$$

Alternately,

$$\mathbf{S}_2 = \mathbf{Y}_{+,impact} \cdot \mathbf{Y}^{-1}_{-,impact}, \tag{6.30}$$

where $\mathbf{S}_2$ is the higher-order STM or saltation matrix obtained numerically at the instant of an impact. This numerically obtained saltation matrix comprises higher-order corrections with the superior and more accurate flight-time estimate δ_+. The next step is to calculate the monodromy matrix using STMs at impacts (*i.e.*, higher-order saltation matrix) defined by Eq. (6.30) and FSMs of the orbit between impacts. The monodromy matrix comprises products of STMs multiplied in the order of their occurrences. To illustrate this, consider the phase portrait of a P2 orbit in Fig. 6.12 for $f = 0.80$N. The orbit is initiated from $\mathbf{x}(t_0)$ and impacts $\Sigma_{i,j}$ twice at $\mathbf{x}^1_i(t^1_i)$ and $\mathbf{x}^2_i(t^2_i)$, finally returning to $\mathbf{x}$ after $t = t_0 + 2T$s. Let $\mathbf{\Phi}_1(t)$, $\mathbf{\Phi}_2(t)$ and $\mathbf{\Phi}_3(t)$ denote the FSMs (*i.e.*, $\mathbf{\Phi}_1(0) = \mathbf{\Phi}_2(0) = \mathbf{\Phi}_3(0) = \mathbb{I}_{n\times n}$) for the flow between $\mathbf{x}(t_0)$ to $\mathbf{x}^1_i$ in the region S_i, $\mathbf{x}^1_i$ to $\mathbf{x}^2_i$ in S_j and $\mathbf{x}^2_i$ to $\mathbf{x}(t_0 + 2T)$ in S_i.

Therefore, the monodromy matrix for the P2 orbit can be defined as,

$$\mathbf{\Phi} = \mathbf{\Phi}_3 \cdot \mathbf{S}^2_2 \cdot \mathbf{\Phi}_2 \cdot \mathbf{S}^1_2 \cdot \mathbf{\Phi}_1, \tag{6.31}$$

where $\mathbf{S}^1_2$ and $\mathbf{S}^2_2$ are the higher-order numerically obtained saltation matrices defined in Eq. (6.30). Therefore, for any periodic orbit with period Pk, the monodromy matrix can be defined as,

$$\mathbf{\Phi}(kT) = \mathbf{\Phi}_{k+1} \cdot \prod_{i=1}^{k} \mathbf{S}^i_2 \cdot \mathbf{\Phi}_i, \tag{6.32}$$

where $\mathbf{\Phi}_i$ are the STMs between impacts and $\mathbf{S}^i_2$ are the saltation matrices at i^{th} im-

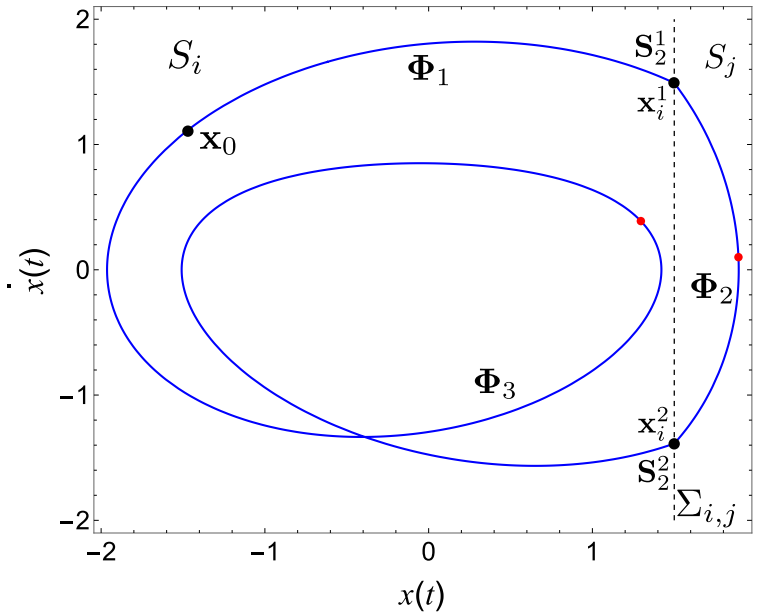

Figure 6.12: Phase portrait of a P2 orbit for $f = 0.80$N. The orbit impacts $\Sigma_{i,j}$ at $\mathbf{x}_i^1$ and $\mathbf{x}_i^2$ when the respective saltation matrices are calculated. The monodromy matrix is constructed using STMs ($\mathbf{\Phi}_1$, $\mathbf{\Phi}_2$ and $\mathbf{\Phi}_3$) and saltation matrices ($\mathbf{S}_2^1$ and $\mathbf{S}_2^2$). The red points correspond to the states stored stroboscopically when t mod $T = 0$.

pact with $\Sigma_{i,j}$. To evaluate the monodromy matrix defined in Eq. (6.32), two FSMs $\mathbf{Y}_1$ and $\mathbf{Y}_2$ are integrated to obtain the respective STMs and saltation matrices separately such that,

$$\begin{aligned} \mathbf{Y}_1(0) &= r_0 \mathbb{I}_{n\times n}, \quad \text{for saltation matrices } \mathbf{S}_2^i \\ \mathbf{Y}_2(0) &= \mathbb{I}_{n\times n}, \quad \text{for STMs } \mathbf{\Phi}_i. \end{aligned} \tag{6.33}$$

The numerical procedure to calculate higher-order saltation matrices, monodromy matrix and consequently its Floquet multipliers using Eqs. (6.30), (6.32) and (6.33) is given in Appendix F. The eigenvalues or Floquet multipliers of the numerically obtained monodromy matrix can determine the stability of any periodic orbit. All eigenvalues are inside the unit circle in the Argand plane for stable orbits with a norm less than unity. If any Floquet multiplier is greater than unity, then the respective orbit is unstable since a norm greater than unity infers exponential divergence of perturbations in the local neighborhood of the orbit.

The TDM and hence the saltation matrix are not defined for impact occurrences when the higher-order flight time predicts an imaginary value. This is because the perturbed orbit never impacts the barrier, as demonstrated in Fig. 6.5. For instances when δ_+ is real, the higher-order TDM can be evaluated from Eqs. (6.23) and (6.24). For $f = 0.85$, the first-order and higher-order saltation matrix, for a perturbed orbit initiated with a norm of 10^{-5} on the first impact with $\Sigma_{i,j}$, calculated analytically

(from Eq. (6.18)) and numerically (from Eq. (6.30)), is given by,

$$\mathbf{S}_1 = \begin{pmatrix} 1 & 0 \\ -1.80927 & 1 \end{pmatrix} \quad \text{and} \quad \mathbf{S}_2 = \begin{pmatrix} 1.00001 & -1.9 \times 10^{-7} \\ -1.80928 & 0.999988 \end{pmatrix} \tag{6.34}$$

for the system Eq. (6.19). Therefore, the higher-order saltation matrix is similar to the first-order results but with the additional benefit of being able to predict an impact that the first-order fails to capture accurately.

Next, Figs. 6.13(a) and (b) compares the norm of the Floquet multipliers with the forward and backward bifurcation results obtained using the higher-order TDM when the parameter f increases and decreases between $0.5 \leq f \leq 0.92$. Both the Floquet multipliers in Fig. 6.13(a) have the same norm when both change discontinuously at $f = 0.5535$N to values less than unity. A new stable P2 orbit is born in the corresponding bifurcation diagram at this instant. Upon further increasing f until $f = 0.861$N, both the norms change suddenly to new values, which are still less than unity. At this instant, the existing P2 orbit disappears, and a new stable P1 orbit is observed as validated by the corresponding bifurcation diagram of Fig. 6.13(a). This observation becomes more intuitive when the Floquet multipliers are evaluated while decreasing f, as shown in Fig. 6.13(b). Once again, both the Floquet multipliers have norms less than unity, indicating that the existing P1 orbit is stable. The norms have the same values until $f = 0.8925$N, and upon further decreasing f, one of the Floquet multipliers (shown as a green curve) becomes greater than unity at $f = 0.7805$N. At this instant, the existing P1 orbit becomes unstable and disappears. When f is further decreased, the norms become equal and discontinuously jump to a value less than the unity implying that a new stable P2 orbit is born and should persist until the norms change again. These results are also validated by the corresponding bifurcation diagrams of Fig. 6.13(b). There is an overlap in the values of the Floquet multipliers when f is either increased or decreased. This is shown in Fig. 6.14(a), where all the Floquet multipliers have been shown with different colors indicating the ranges of f for which P1 and P2 orbits should exist. The results obtained also match with the respective forward (shown as a red curve) and backward (shown as a blue curve) bifurcation diagrams shown in Fig. 6.14(a). Fig. 6.14(b) compares the norm of the Floquet multipliers with the bifurcation results comprising P3 orbits in the vicinity of P2 orbits near $f = 0.53085$N, presented earlier in Fig. 6.11(b). The yellow region in Fig. 6.14(b) corresponds to values of f for which aperiodic solutions were obtained, and therefore the Floquet theory is not applicable. However, in the parameter space for which P3 orbits were observed, the norm $||\rho_1||$ approaches and becomes greater than unity at $f = 0.53085$N. This implies that the P3 orbit should become unstable and disappear, as verified by the respective bifurcation diagram, see Fig. 6.14(b).

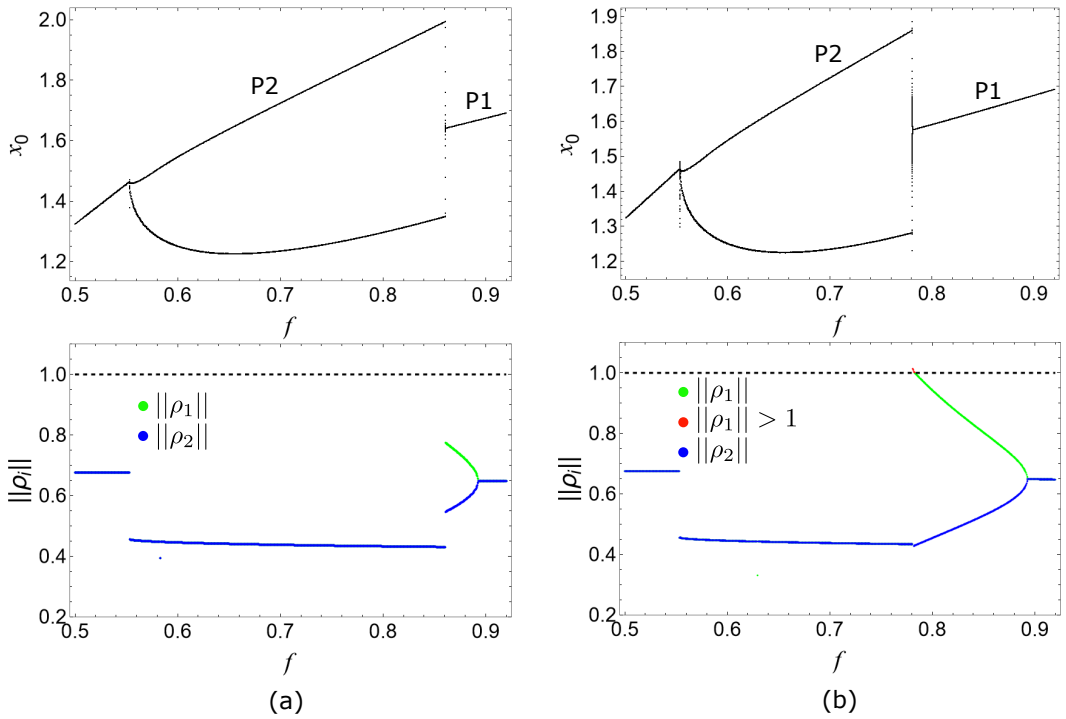

Figure 6.13: Comparison of bifurcation diagram of stroboscopic displacement x_0 vs forcing amplitude f against norm of Floquet multipliers ρ_1 and ρ_2 while (a) f is increasing (forward bifurcation) and (b) f is decreasing (backward bifurcation) between $0.50 \leq f \leq 0.92$N. The black dashed lines correspond to Floquet multipliers with unit norm above which the orbits are unstable. The norm of ρ_1 for the stable P1 orbits increase and become greater than unity at $f = 0.7825$N. At this instant, the P1 orbit becomes unstable and disappears; the system jumps to a nearby P2 orbit as validated by the backward bifurcation diagram.

Investigation of the Floquet multipliers gives a better insight into how the P1 orbits become unstable in the backward bifurcation diagram of Fig. 6.13(b). Figure 6.15 is an Argand diagram showing the Floquet multipliers ρ_1 and ρ_2 when f ranges between $0.7820 \leq f \leq 0.92$N. Initially, the norms are within the unit circle at $f = 0.92$N. As f is decreased, the norms of the eigenvalues increase, and at $f = 0.7830$N, becomes $\rho_1 = -0.999796$. Upon slightly decreasing f, the P1 orbit becomes unstable at $f = 0.7825$N and loses stability via a period-doubling bifurcation. This is also validated by the bifurcation results in Figs. 6.13(b) and 6.14(a).

However, stability analysis using Floquet theory is only applicable to periodic solutions. Hence, the next section presents methods to evaluate the largest Lyapunov exponent and its spectrum applicable to an aperiodic solution using the higher-order flight time δ_+ and TDM of Eq. (6.16).

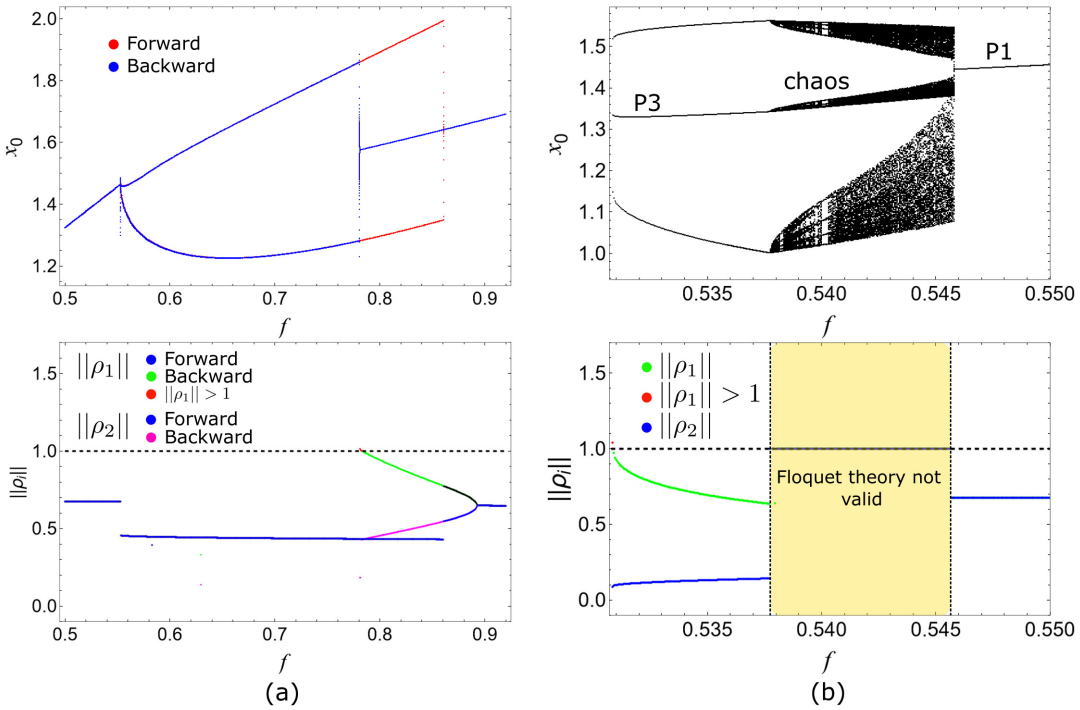

Figure 6.14: Comparison of bifurcation diagram of stroboscopic displacement x_0 vs forcing amplitude f against the norm of Floquet multipliers ρ_1 and ρ_2 while (a) f is increasing and decreasing between $0.50 \leq f \leq 0.92$N and (b) f is increasing when P3 orbits coexisting with P1 orbits. The black dashed lines correspond to Floquet multipliers with unit norm above which the orbits are unstable. The norms become greater than unity implying that existing solutions have become unstable. The yellow region in (b) correspond to aperiodic orbits; the periodicity of the Jacobian matrix for the system is not well-defined here and hence Floquet theory is not applicable.

6.4.2 Lyapunov exponents

Lyapunov exponents are measures of the rate of exponential divergence of trajectories initiated from the local neighborhood of a primary orbit. Broadly, a positive and negative exponent infers that trajectories will either diverge away or shrink towards each other. In general, an accurate estimate of the exponents is obtained by averaging the rate at which perturbations grow within a small interval of time while the system is integrated over a longer time. For smooth systems, the dynamics of perturbations are defined by the Jacobian matrix of the primary system, see Eqs. 6.1 and 6.2. However, for PWS systems, the perturbations do not evolve smoothly at the instant of impacts with the discontinuity boundary. This problem can be easily tackled by ensuring the mapping of perturbations using the higher-order TDM defined by Eqs. (6.23) and (6.24), at impact occurrences given by Eq. (6.21). For a dynamical system of size n, linear algebra dictates that perturbations can be written as a superposition of the fundamental set of solutions that constitute the eigenvectors of the Jacobian matrix. Therefore, perturbations at any given time will have n

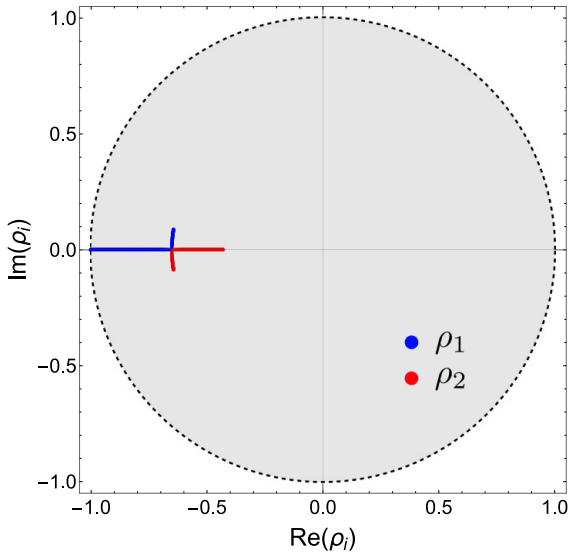

Figure 6.15: Floquet multipliers ρ_1 and ρ_2 in the complex plane for f ranging between $0.7820 \leq f \leq 0.92$N. The black dashed circle represents the stable region of orbits with Floquet multipliers having a norm less than unity. The norm ρ_1 of the P1 orbits from Figs. 6.12(b) or 6.13(a) exit the unit circle when $\rho_1 = -0.999796$ at $f = 0.7830$N; implying that the P1 orbit should become unstable via a period-doubling bifurcation.

rates of exponential divergences. Such exponents, or simply the Lyapunov spectrum, are given by,

$$\lambda_i = \frac{1}{\tau N} \sum_{j=1}^{N} \log \frac{r_i}{r_0}, \tag{6.35}$$

where r_i is the norm of perturbation, with initial norm r_0, at every time interval τ measured stroboscopically for N times. To evaluate the spectrum λ_is, perturbations, initially lying on a hypersphere of radius r_0 to ensure orthogonality, are integrated over a period of time τ. After the time elapse of τ, the norms of the perturbations are stored. This is achieved using a QR decomposition carried out by the Gram-Schmidt process. This method yields the growth rates r_i of all n perturbations along the directions of the eigenvectors of the Jacobian matrix. Once the growth rates are stored, the vectors are reinitialized with a norm of r_0, and the process repeats, ensuring that the direction of the perturbation with the most dominant eigenvalue is not altered. The QR decomposition ensures this. Note that for chaotic systems, perturbations can rapidly grow away from each other and become larger than the radius of convergence of the vector field. Since the dynamics of perturbations rely on the local linearizations around the vector field, the initial radius of the hyper-sphere is kept small at $r_0 = 10^{-6}$. Further, to estimate the Lyapunov exponents accurately, λ_is has been measured using Eq. (6.35) after averaging over 1500 estimates. This procedure to evaluate the Lyapunov spectrum, by incorporating the higher-order TDM, has been outlined in Appendix G for Filippov systems of arbitrary size.

Figure 6.16(a) and (b) compares the results of the corresponding forward and backward bifurcation diagrams of displacement x_0 measured stroboscopically with the estimated Lyapunov spectrum calculated using the higher-order TDM at impact occurrences. Both the Lyapunov exponents remain negative in the forward bifurcation diagram of Fig. 6.16(a) even after a sudden jump in values at $f = 0.861$N. At this instant, the existing P2 orbit disappears, and a new P1 orbit is observed numerically, as verified by the corresponding bifurcation diagram. The Lyapunov spectrum for the case of backward bifurcation gives a better insight, as shown in Fig. 6.16(b). Initially, the LE spectrum is negative corresponding to the observed P1 orbit. Upon decreasing f, the largest Lyapunov exponent λ_1 increases and becomes positive at $f = 0.7825$N. The existing P1 orbit becomes unstable at this instant, disappearing from the bifurcation diagram, and a new P2 orbit is obtained. Therefore, the Lyapunov exponents calculated using the higher-order TDM can accurately predict when orbits become unstable corresponding well with the respective bifurcation diagrams.

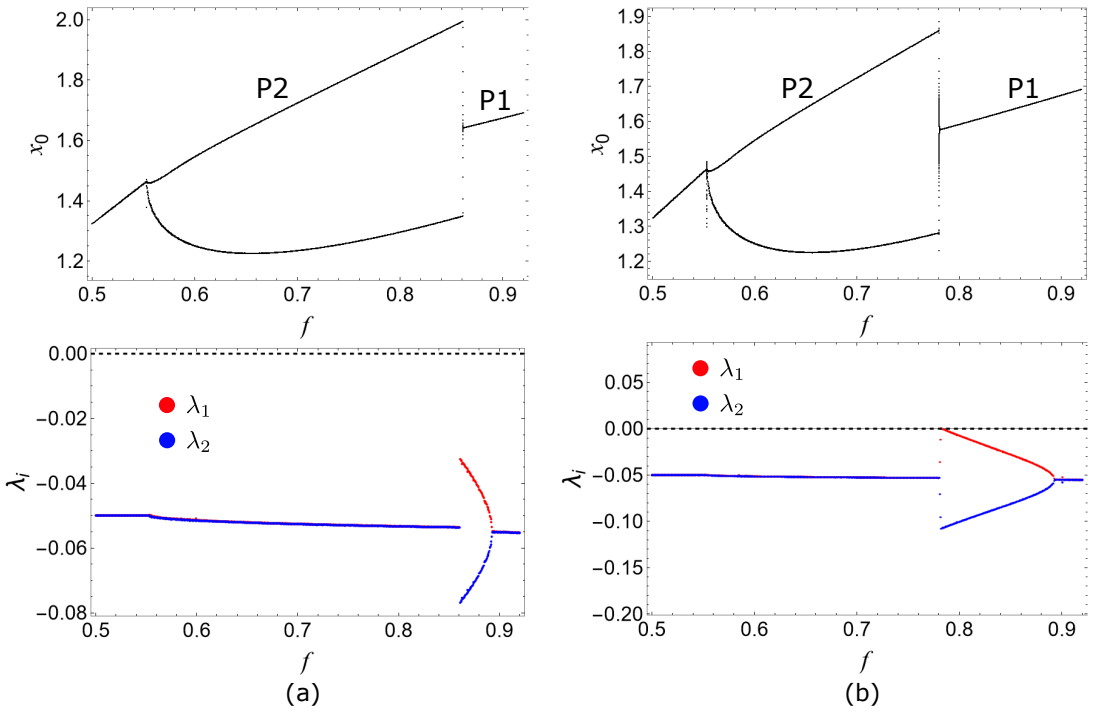

Figure 6.16: Comparison of bifurcation diagram of stroboscopic displacement x_0 vs. forcing amplitude f against Lyapunov exponents λ_1 and λ_2 while (a) f is increasing and (b) decreasing between $0.50 \leq f \leq 0.92$N. P1 orbits become unstable and disappear when the largest Lyapunov exponent λ_1 becomes 0. The black dashed line represents $\lambda_i = 0$.

Numerical investigations of the respective Filippov system considered in Eq. (6.19) reveal occurrences of discontinuity-induced bifurcations. The next section presents an experimental validation of occurrences of such DIBs (existence of P1,

P2 and P3 orbits under parametric variation for the soft-impact oscillator case) observed for Filippov systems.

6.5 Equivalent electronic circuit of an impact oscillator having a pre-compressed barrier

This section attempts to experimentally validate the occurrence of discontinuity-induced bifurcations obtained numerically in Fig. 6.11 for the soft-impact oscillator of Eq. (6.19). An equivalent electronic analog of the mechanical oscillator is constructed by using an electric circuit comprising capacitors, resistors and an inductor (*i.e*, an LCR circuit). The mass, stiffness and damping of the mechanical oscillator of Eq. (6.19) is modeled by an inductor (inductance L), capacitors (capacitance C_1 and C_2) and resistors (resistance R_1 and R_2). The LCR circuit is shown in Fig. 6.17 and the governing dynamics is given by,

$$L\ddot{q} = \begin{cases} A\cos\omega t - \frac{1}{C_1}q - R_1\dot{q}, & q < q_0 \\ A\cos\omega t - \left(\frac{1}{C_1} + \frac{1}{C_2}\right)q - (R_1 + R_2)\dot{q}, & q \geq q_0 \end{cases} \tag{6.36}$$

where the input voltage $V_{in} = A\cos\omega t$ is supplied by an alternating current (AC) source with amplitude A and frequency ω. A reference voltage $V_0 = q_0/C_1$ is maintained which is the electrical counterpart of the soft barrier located at $d = L_2 - L_1$ in Fig. 6.2. When the voltage across the capacitor C_1 (*i.e.*, V_{C_1}) is less than V_0, the dynamics is governed by C_1 and R_1. When $V_{C_1} \geq V_0$ a physical switch, controlled using a comparator, is activated which changes the direction in which the current flows. Under this condition, the dynamics is governed by C_1, C_2, R_1 and R_2; see Eq. (6.36). Next, Eqs. (6.19) and (6.36) is expressed in a dimensionless form for a direct one to one comparison between the mechanical and electrical system. Defining dimensionless time $\tau = \omega_{d_1}t$, displacement $x_d = x/d$, damping $2\xi_{d_1} = \xi_1/(m\omega_{d_1})$ and $2\xi_{d_2} = \xi_2/(m\omega_{d_1})$, force $f_0 = f/(md\omega_{d_1}^2)$, Eq. (6.19) becomes,

$$x_d'' = \begin{cases} f_0\cos\omega_0\tau - x_d - 2\xi_{d_1}x_d', & x_d < 1 \\ f_0\cos\omega_0\tau - \big(1+\beta\big)x_d - 2(\xi_{d_1} + \xi_{d_2})x_d', & x_d \geq 1 \end{cases} \tag{6.37}$$

where $\omega_{d_1}^2 = k_1/m$ and $\beta = k_2/k_1$. Similarly, defining dimensionless time $\tau = \omega_1 t$, charge $q_d = q/q_0$, resistors $2R_{d_1} = R_1/(L\omega_1)$ and $2R_{d_2} = R_2/(L\omega_1)$, voltage $A_0 = A/(q_0 L\omega_1)$, Eq. (6.36) becomes,

$$q_d'' = \begin{cases} A_0\cos\omega_0\tau - q_d - 2R_{d_1}q_d', & q_d < 1 \\ A_0\cos\omega_0\tau - \big(1+\gamma\big)q_d - 2(R_{d_1} + R_{d_2})q_d', & q_d \geq 1 \end{cases} \tag{6.38}$$

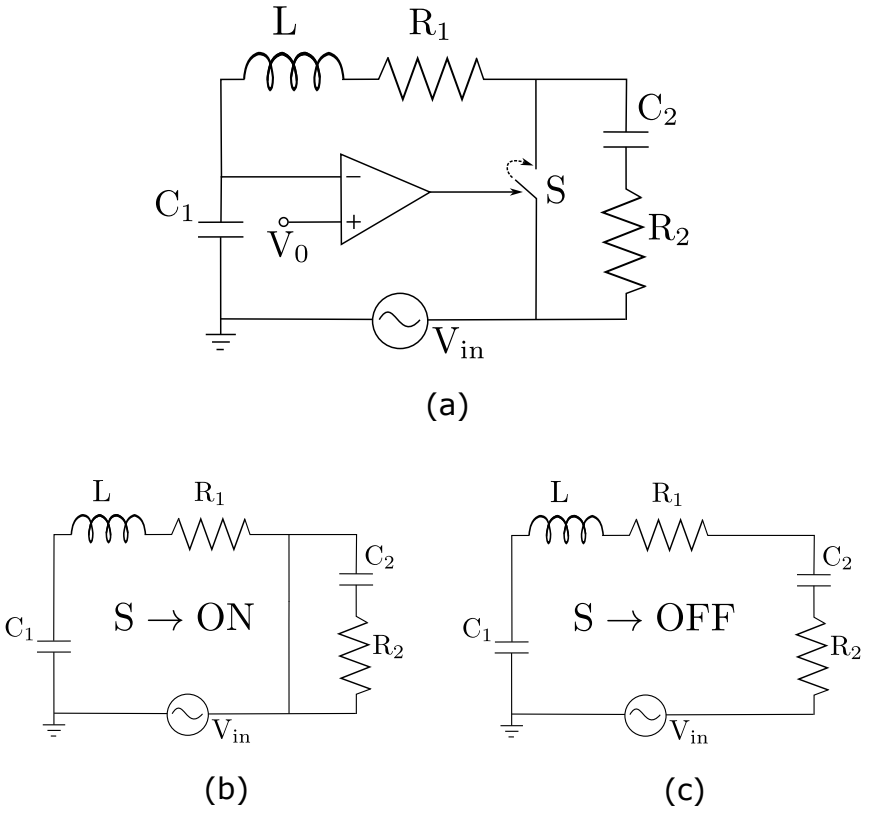

Figure 6.17: (a) An LCR circuit modeling a Filippov system with a pre-compressed barrier where the dynamics is controlled by a switch S. (b) Switch ON state for which current flows through C_1-L-R_1 loop. (c) Switch OFF state for which current flows through C_1-L-R_1-C_2-R_2 loop.

where $\omega_1^2 = 1/(LC_1)$ and $\gamma = C_1/C_2$. Essentially Eqs. (6.37) and (6.38) are identical dimensionless equations. Next, the experimental results are discussed below by choosing $C_1 = 1.0095$nF, $C_2 = 201.01$pF for which $\beta = \gamma \approx 5$, $R_1 = 998\Omega$, $R_2 = 1001\Omega$ for which $\xi_{d_1} = R_{d_1} = 0.05$, $L = 101$mH for which $\omega/(2\pi) = 12.732$KHz (ensuring $\omega = 0.8$ for the mechanical system Eq. (6.19)) and $V_0 = 1.0$V. The circuit diagram of the experiment and its implementation on a breadboard is shown in Figs. 6.18 and 6.19.

Fig. 6.20 shows the time series of voltage V_{C_1} measured across C_1. In Fig. 6.20(a), V_{C_1} is less than the reference voltage $V_0 = 1.0$V when $V_{in} = 345$mV due to which the comparator output is high. At this instant, the orbit has not yet impacted the discontinuity boundary V_0. When $V_{C_1} \geq 1.0$V as shown in Fig. 6.20(b), the comparator operates in the Off state which changes the direction in which current flows as defined in Eq. 6.36. This results in a period one or P1 orbit. As V_{in} is increased to 347mV, a period three or P3 orbits is observed as shown in Fig. 6.20(c). Similarly, a period two or P2 orbit is observed when $V_{in} = 394$mV as shown in Fig. 6.20(d). The phase portraits corresponding to a P1 for $V_{in} = 347$mV, P3 for $V_{in} = 360$mV, P2 for $V_{in} = 394$mV and P1 for $V_{in} = 800$mV orbit, obtained by measuring voltages V_{R_1}, V_{C_1} across R_1 and C_1, are shown in Figs. 6.21(a), (b),

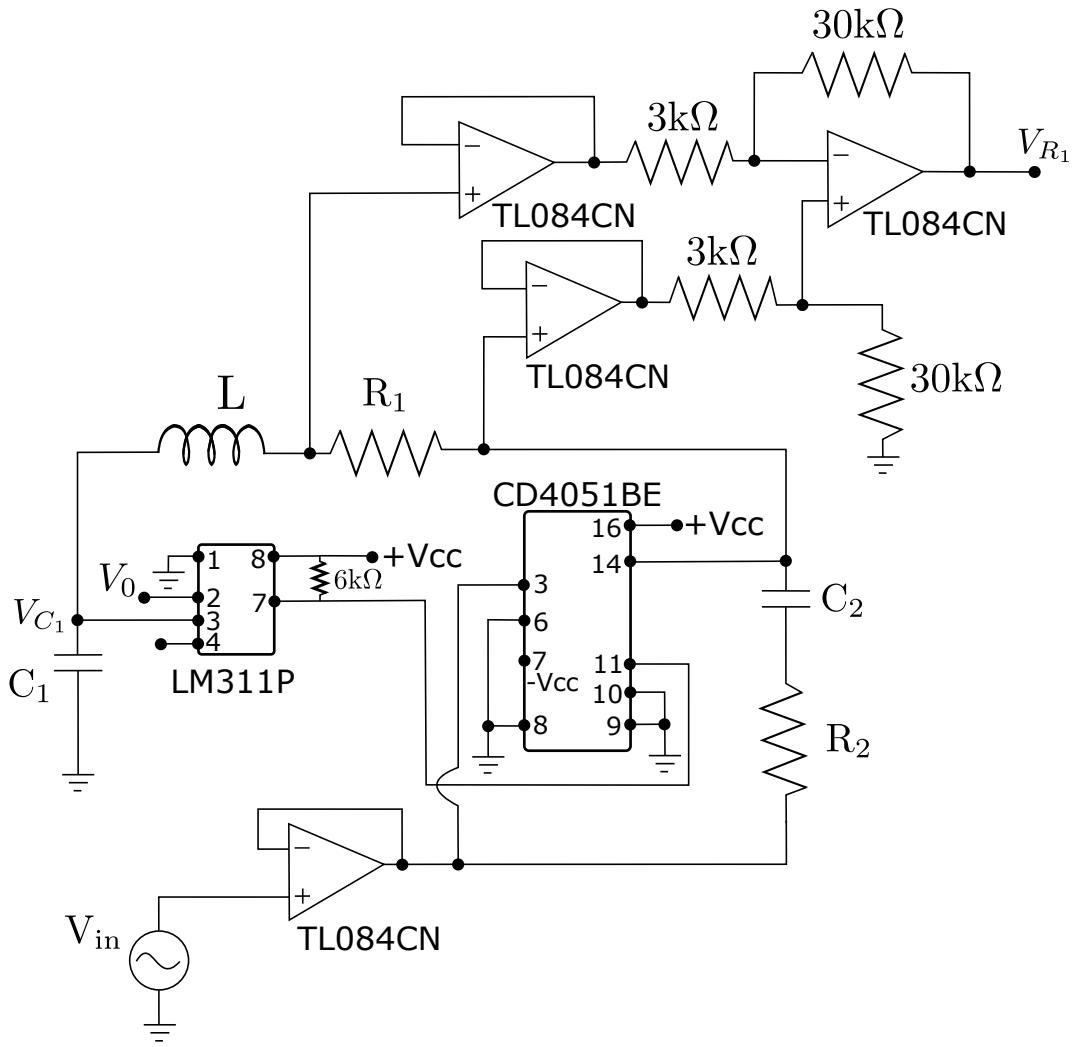

Figure 6.18: Electronic implementation of the circuit diagram shown in Fig. 6.16. The IC LM311P is a comparator measuring V_{C_1} against reference voltage V_0. The IC CD4051BE is a 8 channel multiplexer/de-multiplexer. The current, being proportional to voltage across resistors, is measured by recording potential difference V_{R_1} between R_1.

(c) and (d). The phase portraits obtained experimentally validate the occurrence of discontinuity-induced bifurcations, also obtained numerically for the representative case of an impact oscillator undergoing impacts with a pre-compressed barrier.

A bifurcation diagram obtained experimentally is shown in Fig. 6.22(a). The results (time-series) have been recorded for a total of 42 different values by varying the input voltage V_{in} between $0.345\text{V} \leq V_{in} \leq 0.550\text{V}$. Results validate the occurrence of P1, P3, and P2 orbits as a result of discontinuity-induced bifurcations for Filippov systems. Fig. 6.22(b) is the bifurcation diagram obtained numerically showing results while updating (shown as blue) and not updating (*i.e.*, integration start from $\{0, 0\}$ shown as red) initial conditions for the same experimental values of V_{in}. A comparison between Figs. 6.22(a) and (b) reveals that the parameter values at which bifurcations occur are not the same. Note that the nature or shape

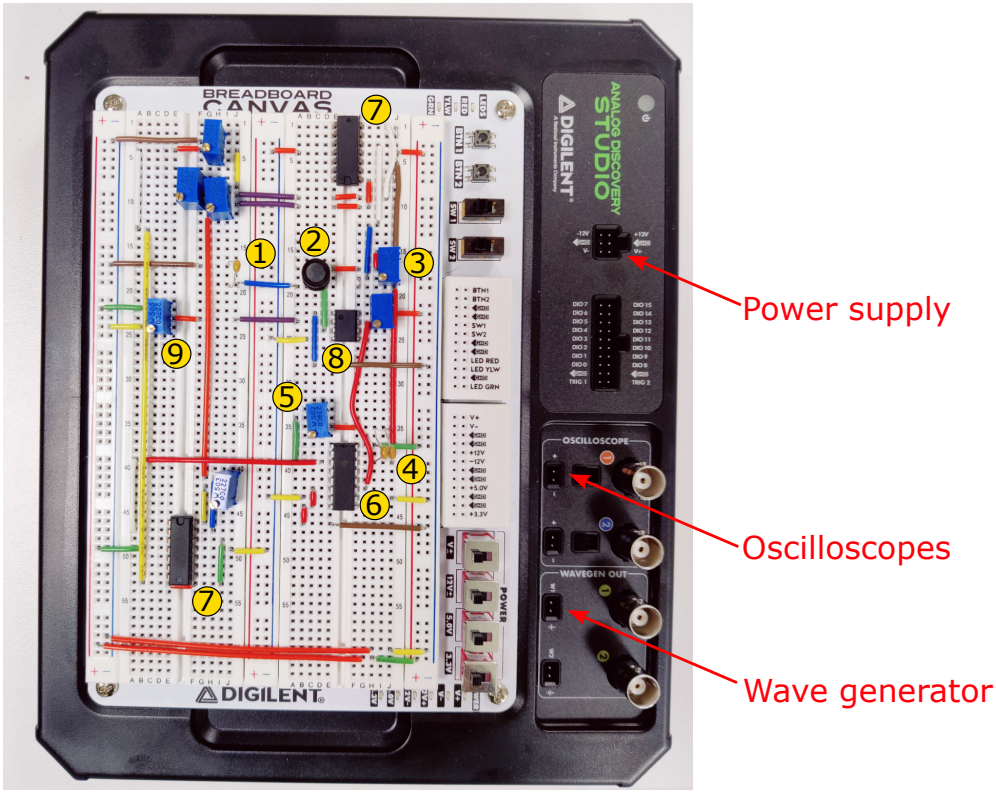

Figure 6.19: Circuit implementation on breadboard. The numbered parts are as follows. 1) $C_1 = 1.009$nF, 2) $L = 100.3$mH ($R_L = 214\Omega$), 3) $R_1 = 784\Omega$, 4) $C_2 = 201.01$pF, 5) $R_2 = 1001\Omega$, 6) 8 channel multiplexer/de-multiplexer CD4051BE, 7) Op Amp TL084CN, 8) Comparator LM311P and 9) $V_0 = 1.0$V.

of the bifurcation curve need not be identical for both the figures as the voltages in Fig. 6.22(b) are measured numerically in a stroboscopic manner while experimentally recorded values are from the digital oscilloscope. However, the parameter values where bifurcations occur do not match. There can be several reasons why the results do not match. One reason can possibly be that the capacitor C_2 does not discharge immediately between two consecutive ON states. This results in some residual charge left in C_2 at the instant when the next cycle begins. A possible way to resolve this is by considering higher capacitance values of C_2 or by reducing R_2 to ensure that the discharge rate is close to being instantaneous. Additionally, for some values of V_{in}, the orbits switch between P1 and P2 states, resulting in a noisy time series. This can be due to thermal fluctuations, loosely connected breadboard probes, or inaccurate wave generation from the digital oscilloscope. These existing questions will be taken up for future investigations. However, the experimental results reveal the existence of P1, P3, and P2 orbits which qualitatively validates the occurrence of DIBs for Filippov systems, as predicted analytically and numerically. The higher-order TDM derived above can determine when orbits become unstable, resulting in DIBs.

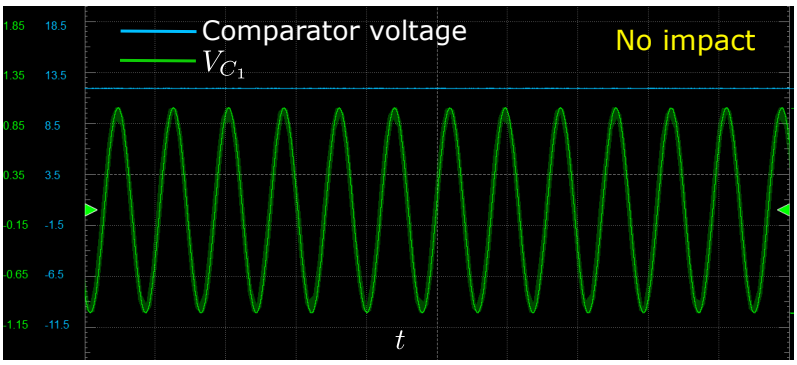

(a)

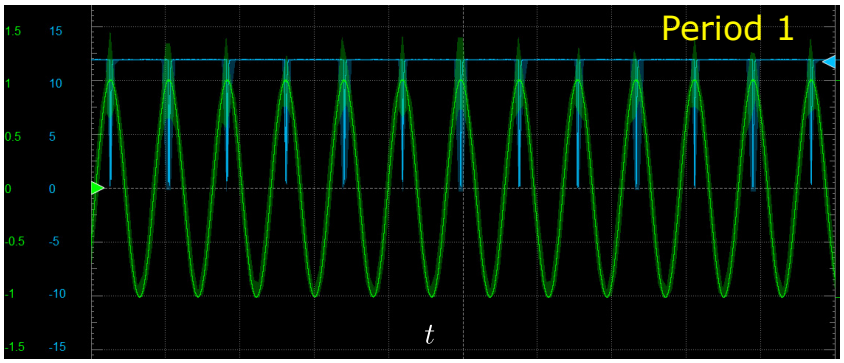

(b)

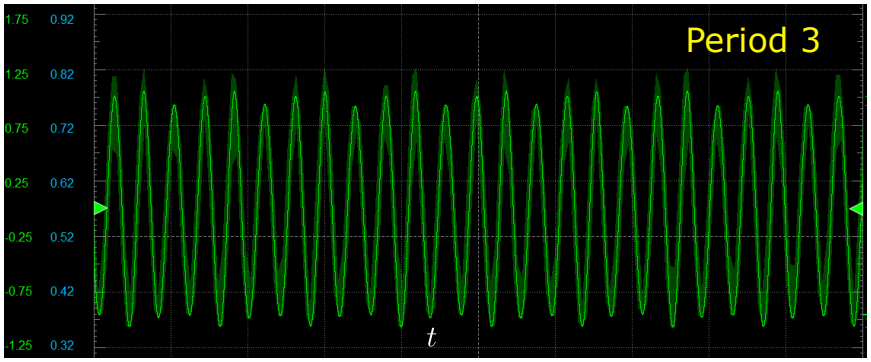

(c)

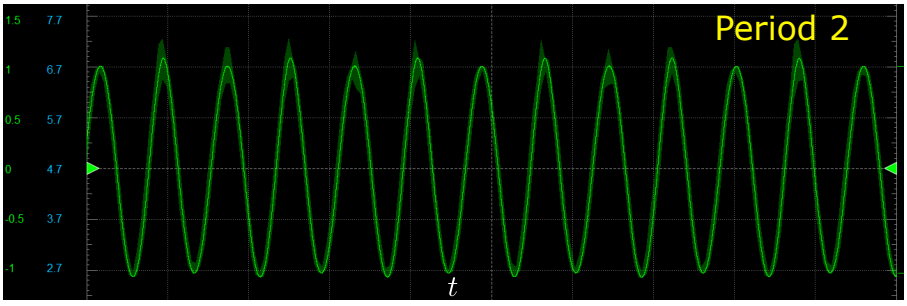

(d)

Figure 6.20: Time series showing V_{C_1} vs. t (green curve) and comparator voltage across CD4051BE vs. t (blue curve) captured in digital oscilloscope corresponding to (a) no impact when $V_{in} = 345$mV and (b) P1 orbit when $V_{in} = 347$mV, the switch is set to ON state when $V_{C_1} \geq 1.0$V. Time series showing V_{C_1} vs. t corresponding to a (c) P3 orbit when $V_{in} = 360$mV and (d) P2 orbit when $V_{in} = 394$mV.

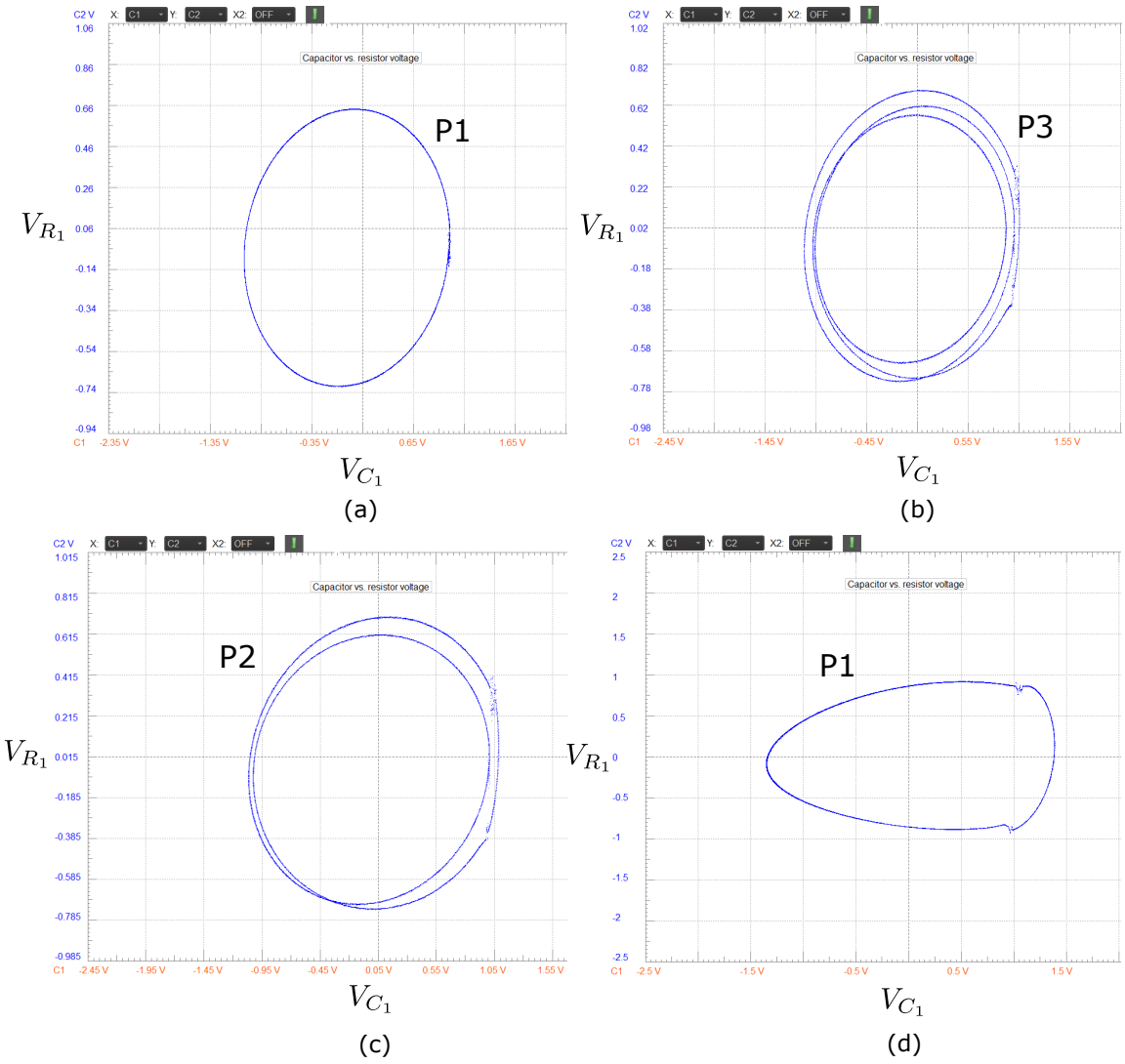

Figure 6.21: Phase portrait captured in digital oscilloscope showing V_{R_1} vs. V_{C_1} corresponding to a (a) P1 orbit when $V_{in} = 347$mV, (b) P3 orbit when $V_{in} = 360$mV, (c) P2 orbit when $V_{in} = 394$mV and (d) P1 orbit when $V_{in} = 800$mV.

6.6 Conclusions

A closed-form expression of a higher-order transverse discontinuity mapping (TDM) for piecewise-smooth Filippov systems has been derived. The proposed higher-order corrections can successfully predict impact occurrences that the widely accepted first-order approaches fail to determine. Additionally, since a closed-form expression of the state transition matrix at impact occurrences (*i.e.*, saltation matrix) comprising higher-order corrections cannot be directly expressed, a numerical procedure to calculate the higher-order saltation matrix has been discussed. The numerically calculated saltation matrices are validated via stability analysis by evaluating Floquet multipliers and Lyapunov exponents. The results obtained agree with the corresponding forward and backward bifurcation diagrams.

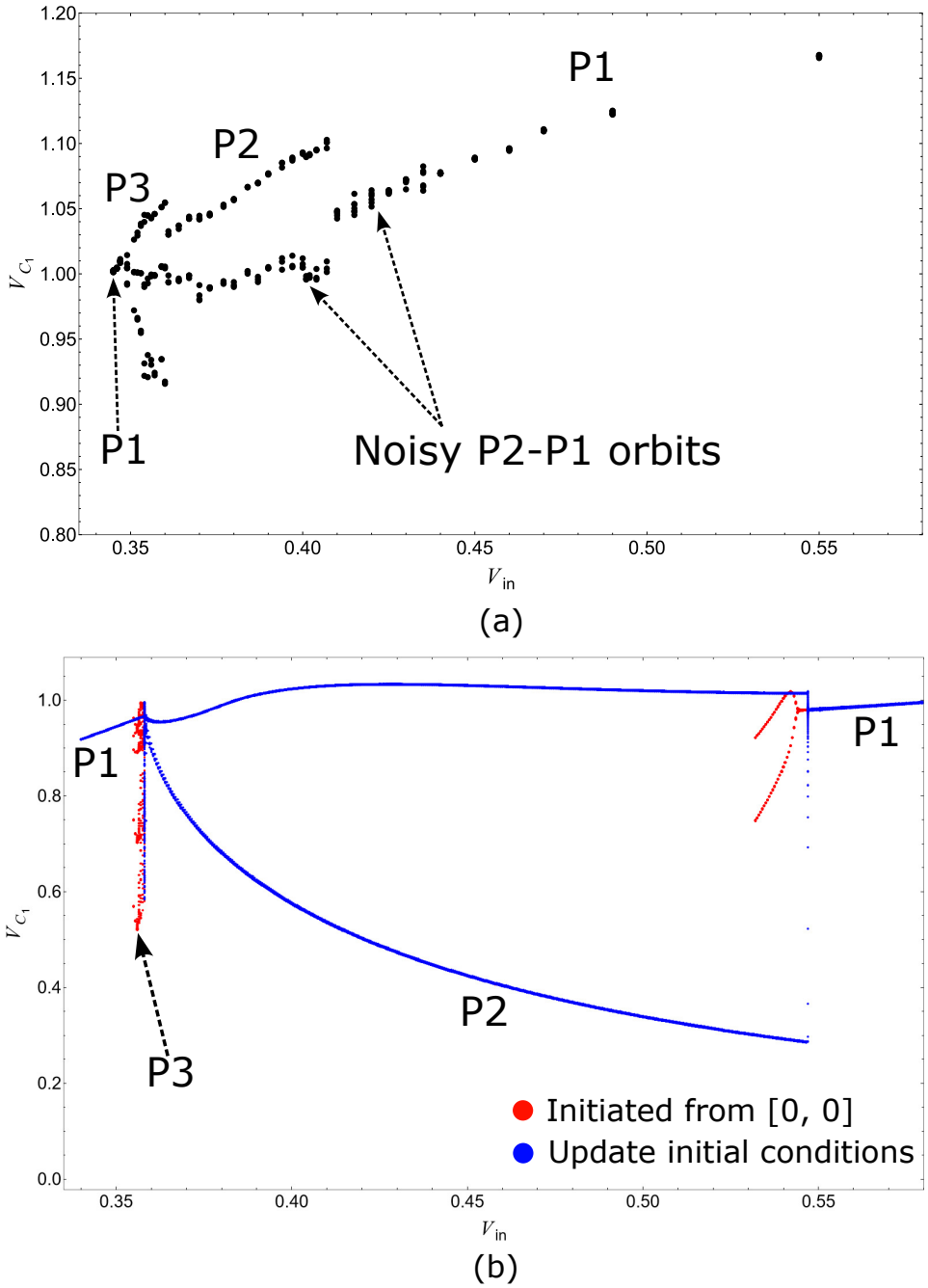

Figure 6.22: Bifurcation diagram obtained (a) Experimentally by implementing electronic circuit shown in Figs. 6.17 and 6.18, and (b) Numerically for two cases by starting with zero initial conditions (shown as red) and updating initial conditions (shown as blue) while varying V_{in} between $0.345\text{V} \leq V_{in} \leq 0.550\text{V}$.

The derived higher-order flight time estimates when perturbed trajectories in the local neighborhood of an impacting orbit will reach the discontinuity boundary. The proposed higher-order corrections provide a superior estimate of impact occurrences that the first-order saltating terms cannot capture correctly and, therefore, incorrectly predicts impacts that do not occur when compared to the exact solution. This is mainly due to the quadratic nature of the higher-order flight time estimate, which can provide imaginary roots, indicating that perturbations miss the disconti-

nuity barrier. Additionally, the higher-order flight time expression can theoretically provide a range within which perturbations should be bounded for impacts to occur. In the contrary, the widely implemented first-order flight time results in a fraction which incorrectly predicts impacts for all values of perturbations. This is primarily because the first-order terms do not consider crucial system parameters that define how the orbits evolve; the higher-order corrections resolve this problem. Moreover, the proposed method accurately predicts the behavior of aperiodic trajectories and orbits with a large time period in the vicinity of a discontinuity barrier.

A numerical method is proposed to calculate the saltation matrix with higher-order corrections. This method implements matrix inversions to accommodate the higher-order terms, resulting in a higher-order state transition matrix. This method can also be adapted to include corrections of order $\mathcal{O}(3)$ or higher. Monodromy matrices are evaluated next using the higher-order saltation matrices. An eigenvalue analysis of the monodromy matrix is carried out for a representative system of an impact oscillator undergoing impacts with a pre-compressed deformable barrier. The numerically evaluated Floquet multipliers can predict parameter values at which orbits become unstable. These predictions also match with the respective forward and backward bifurcation diagrams, explaining when orbits become unstable during hysteresis. A numerical procedure comprising higher-order corrections to the TDM is presented to calculate the Lyapunov spectrum and the largest Lyapunov exponent. Unlike the requirement of an analytical form of transcendental maps, the proposed method does not require prior knowledge of the solution during an impact. The calculated Lyapunov spectrum for a wide range of parameter values agrees well with the respective bifurcation diagrams and can correctly predict when orbits become unstable during hysteresis.

Next, the occurrence of discontinuity-induced bifurcation, as obtained numerically, is validated experimentally. An electronic implementation comprising two LCR circuits with switching mechanism has been carried out. The governing dynamics of the electronic circuit is equivalent to a soft-impact oscillator impacting a pre-compressed barrier investigated numerically. The phase-portraits, time-series and corresponding bifurcation diagram obtained experimentally validates the occurrence of period one, two and three orbits respectively under parametric variation. This observation also agrees with the analytical and numerical results obtained using the proposed higher-order transverse discontinuity mapping.

Therefore, the results discussed in this chapter can accurately determine when orbits become unstable resulting in discontinuity-induced bifurcations for Filippov systems, especially when the widely accepted linearized saltation matrix fail to do so.

Chapter 7

Conclusions

7.1 Contributions

Discontinuity mappings and normal forms have been fundamental in systematically investigating why topological changes occur to a family of curves under parametric variation for piecewise-smooth (PWS) dynamical systems. Existing literature in this area has primarily focused on linearized approximations of discontinuity mappings, specifically for periodic orbits transversally interacting with the discontinuity barrier. Chapters 1 and 2 introduce various discontinuity mappings and their normal forms that several authors research to understand and explain how discontinuity-induced bifurcations occur. This thesis attempts to highlight the limitations of widely accepted linearized approaches and how such approximations can lead to incorrect predictions regarding the behavior of perturbations in the local neighborhood of an orbit interacting with the discontinuity barrier. The thesis proposes a higher-order transverse discontinuity mapping (TDM) for hybrid and Filippov systems, which rectifies the problems encountered when implementing first-order approximations to the discontinuity mapping. Methods to construct higher-order saltation and monodromy matrices, and consequently Floquet multipliers and Lyapunov exponents for stability analysis, have been discussed for PWS systems with degrees of smoothness zero and higher. This chapter discusses the main results and shortcomings of the thesis, followed by recommendations for future work.

Chapter 3 derives the higher-order transverse discontinuity mapping for hybrid systems governed by PWS ODEs and discrete maps at the instances of impacts with a discontinuity barrier transversally. The flight time to impact between nearby trajectories was derived considering higher-order correction terms. Unlike the first-order flight time, which is usually a real-valued fraction, implying that impacts occur for all perturbations, the higher-order flight time is a quadratic function. This quadratic form of the flight time considers all the crucial parameters of the respective system under investigation; the first-order results do not depend on any

system parameter. An imaginary root of the derived quadratic flight time implies that impacts do not occur for all values of perturbations. A comparison between the well-known first-order results with the higher-order terms to predict impact occurrences for a representative case of an impact oscillator with a rigid barrier reveals that, for large enough perturbations, impacts do not occur. On the contrary, the first-order saltation matrix incorrectly predicts impact occurrences for all perturbations. The results are validated against the exact solutions of the numerically obtained perturbed trajectory. Therefore, the higher-order correction terms are superior in accurately predicting impact occurrences, especially when the first-order saltation matrix fails to do so. Incorrect predictions of impact occurrence also have a consequence while performing stability analysis of nearby orbits having exponential orbital divergence. Since impacts determine the order in which state transition matrices (saltation matrices) are multiplied to obtain the correct monodromy matrix, the consequent eigenvalue analysis can lead to different predictions regarding the stability of an orbit. The ability of the derived higher-order TDM to predict when impacts occur resolves the problem of possible incorrect monodromy matrices while using the first-order saltation matrix.

Next, methods to numerically obtain higher-order saltation and monodromy matrices, and consequently Floquet multipliers, have been discussed. A closed-form expression for the higher-order saltation matrix is not possible due to the nature of the higher-order TDM being in the form of a vector. A matrix inversion method has been proposed to achieve this. Further, methods have been discussed to estimate the largest Lyapunov exponent and the remaining Lyapunov spectrum incorporating the higher-order correction terms. The numerically obtained results correspond well with the respective bifurcation diagrams of two representative cases of an impact oscillator and a pair-impact oscillator with two barriers. The methods outlined in this chapter apply to any arbitrary hybrid system undergoing impacts with multiple barriers. The proposed numerical procedure to estimate Floquet multipliers and Lyapunov spectrum can also incorporate higher-order TDMs of order $\mathcal{O}(3)$ and higher.

Chapter 4 systematically investigates the bifurcation behavior of a fluid-structure interaction system under the influence of vortex-induced vibrations (VIV) and undergoing impacts with a rigid wall. Several investigations on the VIV characteristics of FSI systems exist in the literature, but incorporating vibro-impacts with rigid barriers is not well explored. Therefore, unlike traditional methods like direct numerical simulations of VIVs in cylindrical bluff bodies, this chapter aims to implement a low-order, non-smooth phenomenological FSI model. Hence, the primary cylindrical bluff body and the lift forces, at near wake dynamics, acting on the structure are represented by a harmonic oscillator and a Van der Pol equation. Additionally, a non-deformable barrier obstructs the cylinder motion, giving rise to

instantaneous impacts defined by a restitutive law. Discontinuity-induced bifurcations like period-adding cascades separated by chaotic orbits were obtained when bifurcation parameters like fluid velocity and barrier distance were varied. The existence of multiple solutions corresponding to period one or P1 and two or P2 orbits was found separated by their basins of attractions. Period four or P4 orbits sandwiched between two P2 orbits were observed when the coefficient of restitution between impacts was varied. A cascade of higher periodic orbits was obtained at near grazing conditions by varying the coupling strength between the structure and wake oscillator. Numerical methods to evaluate Floquet multipliers and Lyapunov exponents using first-order saltation matrices were developed to investigate the stability of orbits. It was observed that the norm of one of the Floquet multipliers approached unity as the orbit became unstable. At the same instants, the largest Lyapunov exponent, measured independently, became positive. Jumps in Floquet multipliers indicated when an existing stable orbit would disappear and give birth to a new stable orbit.

Chapter 5 highlights the advantages of the higher-order TDM derived in Chapter 3 over the widely accepted saltation matrices for a 4-dimensional hybrid PWS system defined using several parameters. To illustrate the accuracy of a higher-order approach, a hybrid system representing the simplest case of fluid-structure interaction (FSI) undergoing impacts with a rigid barrier has been chosen. Occurrences of discontinuity-induced bifurcations for this FSI system were numerically explored in detail in Chapter 4. In Chapter 5, the behavior of perturbations in the local neighborhood of a stable solution impacting the barrier has been investigated using a higher-order TDM derived previously in Chapter 3. The higher-order flight time provided better estimates of impact occurrences with reductions in percent error up to 40% compared to the first-order results. The inclusion of higher-order terms in the flight time estimate results in a quadratic function. Thus, when perturbations become large, the flight time estimate returns an imaginary value, implying that orbits in the local neighborhood should not impact the discontinuity barrier. This contradicts the widely accepted linearized flight time, which incorrectly predicts that impact occurs for all perturbations. The range of perturbations beyond which impacts do not occur depends on the parameters which define the dynamical system. For non-smooth dynamical systems with several variables, like the 4-D FSI system considered here, the errors become large when using first-order saltation matrices. The widely accepted linearized flight time estimate is independent of the parameters that define the system, resulting in poor impact estimates. In such cases, the higher-order TDM considers all parameters, accurately predicting impact occurrences. The higher-order quadratic function for flight estimate can also provide the range within which perturbations should be bounded for impacts to occur. The first-order linearized theory cannot capture this. Next, the matrix inversion method discussed

in Chapter 3 has been implemented to evaluate higher-order saltation matrices at the instances of impacts for this 4-D non-smooth FSI system. In the limit of small perturbations, the numerically obtained higher-order saltation matrix becomes similar to the first-order saltation matrix, validating that the method should work for hybrid systems with several degrees of freedom.

Chapter 6 derives closed-form expressions of higher-order transverse discontinuity mappings derived for Filippov systems crossing a discontinuity barrier transversally. As illustrated in Chapter 3 for hybrid systems, the higher-order transverse discontinuity mapping can correctly predict impact occurrences, which the widely accepted first-order saltation matrix fails to capture for Filippov systems where trajectories can cross the discontinuity barrier transversally. The derived higher-order flight time determines when trajectories in the local neighborhood of a transversally crossing orbit reach the discontinuity barrier. The derived flight time with higher-order correction terms results in a quadratic function, which can become imaginary when nearby orbits diverge away *i.e.* when perturbations become too large. This implies that perturbations should miss the discontinuity barrier even when the primary orbit has crossed the discontinuity barrier. This is in contradiction to the predictions made when using first-order linearizations. The first-order flight time estimate provides a real value, implying that impacts occur for all perturbations and do not depend on the parameters defining the respective Filippov system. A comparison with the exact solution of the perturbed orbits concludes that the higher-order transverse discontinuity mapping correctly predicts no impacts. In contrast, the widely accepted saltation matrix incorrectly predicts impacts. Additionally, the higher-order correction terms result in a quadratic function. Solving the critical range of perturbations for which the roots are not imaginary is straightforward. This implies that impacts can only occur for perturbations with a norm within this range. For perturbations with a norm larger than the critical range, no impacts should occur, and therefore, the first-order predictions become incorrect. These findings are then backed up numerically by investigating the behavior of orbits for a soft-impact oscillator undergoing impacts with a pre-compressed deformable barrier. A comparison with the exact solution indicates that perturbations with a norm greater than the critical value, derived from the higher-order quadratic flight time form, do not undergo impacts with the discontinuity barrier. The first-order flight time incorrectly predicts an impact.

Next, a numerical procedure to estimate the saltation matrix with higher-order corrections has been discussed since it is impossible to express a closed-form expression of the saltation matrix comprising $\mathcal{O}(2)$ terms. The derived higher-order TDM for the Filippov systems results in a vector equation. This vector equation is incompatible with the variational equation since the dynamics of perturbations are governed by a Jacobian matrix. Therefore, a numerical method comprising matrix

inversions is proposed to evaluate saltation, monodromy matrices, and the Floquet multipliers. A numerical investigation of the respective soft-impact oscillator, impacting a pre-compressed barrier, reveals the presence of discontinuity-induced bifurcations like period one (P1), two (P2), and three (P3) orbits. The calculated Floquet multipliers using the higher-order transverse discontinuity mapping can correctly predict when bifurcations occur compared to the corresponding forward and backward bifurcation diagrams. Results indicate that orbits become unstable via a period-doubling bifurcation for parameter ranges when the phenomenon of hysteresis is observed. Additionally, methods to evaluate the largest Lyapunov exponent and Lyapunov spectrum while implementing the higher-order transverse discontinuity mapping have been discussed in Chapter 6. This method does not require prior knowledge regarding the solution during an impact and is easily adaptable to include corrections of order $\mathcal{O}(3)$ or higher.

Chapter 6 concludes with an attempt to validate the occurrence of discontinuity-induced bifurcations for Filippov systems experimentally. An electrical circuit comprising two separate LCR circuits with a switching mechanism also behaves like a Filippov system, equivalent to a mechanical impact oscillator undergoing impacts with a pre-compressed wall. The results obtained from the experiment validate the occurrence of period one, two, and three orbits, respectively, under parametric change of the input voltage. The qualitative change in the topology observed experimentally resembles the predictions of the analytical and numerical results, confirming that discontinuity-induced bifurcations can occur for Filippov systems when orbits become unstable.

7.2 Critical assessment

The thesis compares the accuracy of the proposed higher-order transverse discontinuity mappings with the widely accepted linearized approaches to predict the behavior of perturbed trajectories for piecewise-smooth dynamical systems. Although the theory attempts to resolve issues arising from first-order transverse discontinuity mapping, some areas of the proposed methodology can be refined to better contribute to the existing literature.

The derived higher-order transverse discontinuity mapping can accurately predict impact occurrences that the first-order fails to capture. Yet, in numerical instances, when perturbations become small (in the order of 10^{-5}), the higher-order results become identical to the first-order saltation matrix. Under such circumstances, the higher-order correction terms do not improve the first-order saltation matrix for hybrid and Filippov systems. Next, the higher-order saltation matrix derived in Chapter 6 has been implemented on a Filippov system where sliding does not occur. A wide range of discontinuity-induced bifurcations appear for Filippov systems [30]

where the vector fields are either attractive or repulsive on both sides of the discontinuity boundary. The higher-order discontinuity mappings derived for Filippov systems need to be evaluated for sliding cases to ensure that the methodology caters to a wide range of non-smooth dynamical systems. The proposed discontinuity mapping must also be validated by implementing the methodology on a piecewise-continuous system for which the Jacobian matrices of the corresponding vector fields vary on either side of the discontinuity barrier.

The phenomenological model considered in Chapters 4 and 5, which represents a hybrid fluid-structure interaction system, does not consider the effects of the geometry of the barrier on the fluid medium. Adding a barrier near a fluid-structure interaction system undergoing vortex-induced vibrations should also affect the fluid-flow velocity. The present model considered in this thesis does not account for such effects and needs to be explored. Experimental validation is also required to verify the occurrence of period-adding cascades in the structure's motion as predicted numerically. Additionally, the hybrid fluid-structure interaction model in the thesis considers a simplistic impact model with a rigid barrier when immersed in water. For a fluid medium with density and viscosity greater than water, the impact model must be replaced by a more sophisticated model that can capture the true physics observed experimentally.

7.3 Recommendations for future work

The higher-order transverse discontinuity mapping derived in this thesis applies to hybrid and Filippov systems with transversal interaction with the discontinuity boundary. Higher-order corrections terms to the zero-time discontinuity mapping and Poincaré-section discontinuity mapping for grazing incidence are still open for investigation and will be considered in the future. Many numerical [7, 94] and experimental [53] investigations reveal large amplitude chaos over a small range of parameter values. This phenomenon is known in the literature as narrow-band chaos. Simpson et al. [108] showed that the Nordmark map cannot capture the narrow-band chaos observed during the grazing of orbits with the discontinuity barrier. Simpson et al. [108] constructed a Poincare map to investigate the square-root character of it for both soft and hard impact oscillators. This Poincare map comprises function compositions of smooth and non-smooth maps, and the discontinuous non-smooth part is evaluated by constructing a Poincare-section discontinuity mapping. Simpson compared the Poincare and the Nordmark map, showing that the Nordmark map does not comprise a narrow-band chaos near the grazing parameter value. Instead, the Nordmark map showed a stable period three orbit when the existing period one orbit grazed the discontinuity barrier. The stable period three orbit appears because the basin of attraction of the primary period one solution shrinks to zero - this

situation is identical to dangerous border-collision bifurcation found in piecewise-smooth maps. Simpson highlighted the failure of the Nordmark map since it rapidly deviates from the Poincare map away from the grazing value. The Poincare map is a global phenomenon, while the Nordmark map is derived based on local linearizations around the grazing parameter value. Since very little is known about the size of the local neighborhood to which the Nordmark map approximates the Poincare map, it is essential to consider higher-order correction terms for the Nordmark map in the future. This approach can better match the Nordmark map with the global Poincare map to better resemble the true dynamics of the attractor for a relatively larger local neighborhood.

Next, the higher-order transverse discontinuity mapping in Chapter 6 was tested for a representative case of a Filippov system where no sliding occurs. The impact oscillator impacting a pre-compressed wall allows trajectories to cross the switching manifold since the vector fields on the barrier are not attractive or repulsive. Therefore, a Filippov system with sliding can be considered in the future. An example of such a representative Filippov system is an elastically connected harmonic oscillator placed on a conveyor belt [68].

Numerous possibilities for experimental validation of discontinuity-induced bifurcations exist. For example, the LCR circuit investigated experimentally in Chapter 6 requires further investigation to validate the presence of coexisting attractors as predicted by the numerical results. With the present chosen resistance and capacitance values, the capacitors comprise residual charges that the numerical model does not consider. By tweaking the capacitance and resistance values and ensuring a faster exponential discharge, the experiment should behave similarly to the numerical model of a Filippov system. Next, the LCR circuit attempts to model a Filippov system undergoing soft impacts with a deformable barrier. A similar electronic equivalent circuit representing a hybrid system experiencing hard impacts with a rigid wall has yet to be investigated. Several attempts have been made to model mechanical impact oscillators using leaf spring setups mounted on an electrodynamic shaker. However, the experimental design is tedious since mechanical impacts can excite higher oscillatory modes, interfering with the results. Therefore, an equivalent electronic circuit can significantly reduce the complications in such experiments where mechanical bodies impact one another. Such an electronic circuit can also validate the occurrence of period-adding cascades of solution observed numerically when modeling a fluid-structure interaction system undergoing impacts with a rigid wall.

Appendix A

Lyapunov exponents for hybrid systems

The steps to evaluate the largest Lyapunov exponent and the Lyapunov spectrum are described below by implementing higher-order transverse discontinuity mapping for piecewise-smooth hybrid dynamical systems.

Algorithm 1 Lyapunov exponent for PWS hybrid systems using higher-order TDM

1. Initialize: $\mathbf{x}(0)$ ensuring $H(\mathbf{x} \geq 0)$ and ω or α ▷ Bifurcation parameter
2. Initialize: $\mathbf{y}_i(0)$ for $i \leq n$ using QRD
3. Rescale: $\mathbf{y}_i(0) \leftarrow r_0 \times \mathbf{y}_i(0)$ and set n_{max} ▷ Maximum allowable impacts

while count $\leq n_{max}$ **do**
  Integrate: $\dot{\mathbf{x}} = \mathbf{F}(\mathbf{x})$
  if $H(\mathbf{x}) = 0$ **then** ▷ Occurrence of impact
    Evaluate: δ, $\mathbf{R}(\mathbf{x})$ and $\mathbf{y}_+$
    Apply reset maps: $\mathbf{x} \leftarrow \mathbf{R}(\mathbf{x})$ and $\mathbf{y}_i \leftarrow \mathbf{y}_{i,+}$ ▷ Implement TDM
  end if
  if $\left(t\%\frac{2\pi}{\omega}\right) = 0$ **then**
    if count $\geq n_{max}/2$ **then**
      Store: $r_i \leftarrow \frac{1}{r_0}\|\mathbf{y}_i\|$ ▷ store the growth rate
    end if
    Reinitialize: $\mathbf{y}_i \leftarrow r_0 \times$ QRD of $\mathbf{y}_i$
  end if
end while

4: Evaluate: $\log_e r_i$ ▷ Store all $log_e r_i$
5: $\mathrm{LE}_i \leftarrow \frac{\omega}{2\pi} \times$ Partial sum of $\log_e r_i$
6: $\lambda_i \leftarrow \langle \mathrm{LE}_i \rangle$ ▷ Mean of all LEs

Appendix B

Higher-order saltation matrix for hybrid systems

The steps to evaluate higher-order saltation, monodromy matrices, and subsequent Floquet multipliers by incorporating higher-order transverse discontinuity mapping for piecewise-smooth hybrid dynamical systems are described below.

Algorithm 2 Floquet multipliers from monodromy matrix ϕ

1. Initialize: $\mathbf{x}(0)$ ensuring $H(\mathbf{x}) \geq 0$ and ω or α ▷ Bifurcation parameter
2. Initialize: $\mathbf{\Phi} = \mathbb{I}_{n\times n}$, T= 100, count $= 0$, n_{max} ▷ Maximum allowable impacts

while count $\leq n_{max}$ **do**
  Integrate: $\dot{\mathbf{x}} = \mathbf{F}(\mathbf{x})$
  if $H(\mathbf{x}) = 0$ **then** ▷ Occurrence of impact
    Reset Map: $\mathbf{x} \leftarrow \mathbf{R}(\mathbf{x})$
  end if
  if $\dot{x} = 0$ && count $\geq (0.9 * n_{max})$ **then**
    $T = \{t \in \mathbb{R}^1 : x(t + \tilde{n}T) = x(t), \tilde{n} \in \mathbb{I}\}$ ▷ Store x, t for evaluation of time period T
  end if
  if count $= n_{max}$ **then** ▷ Remove transients and as store initial condition
    Store: $\mathbf{x}_{init} \leftarrow \mathbf{x}(t)$ and $t_{init} \leftarrow t$
  end if
end while

Initialize: $\mathbf{x} \leftarrow \mathbf{x}_{init}$ at t_{init} ▷ Begin at steady state
Initialize: $r_0 \ll 1$, $\mathbf{Y}_1(0) = r_0\mathbb{I}_{n\times n}$, $\mathbf{Y}_2(0) = \mathbb{I}_{n\times n}$ ▷ Evaluation of $\mathbf{S}_2$ and $\mathbf{\Phi}_i$
while $t_{init} \leq t \leq (t_{init} + T)$ **do** ▷ Integrate over period T
  Integrate: $\dot{\mathbf{x}} = \mathbf{F}(\mathbf{x})$, $\dot{\mathbf{Y}}_1 = (\nabla\mathbf{F})^T \cdot \mathbf{Y}_1$ and $\dot{\mathbf{Y}}_2 = (\nabla\mathbf{F})^T \cdot \mathbf{Y}_2$
  if $H(\mathbf{x}) = 0$ **then** ▷ Occurrence of impact
    $\mathbf{\Phi}_i \leftarrow \mathbf{Y}_2$ and $\mathbf{\Phi} \leftarrow \mathbf{\Phi}_i \cdot \mathbf{\Phi}$
    Evaluate δ and $\mathbf{y}_+$ from $\mathbf{x}_4$ for all $\mathbf{y}_i$ ▷ TDM
    Evaluate $\mathbf{Y}_{+,impact}$ from $\mathbf{y}_+$ and $\mathbf{Y}_{-,\text{ impact}} \leftarrow \mathbf{Y}_1$
    Evaluate $\mathbf{S}_2 \leftarrow \mathbf{Y}_{+,impact} \cdot \mathbf{Y}^{-1}_{-,impact}$ and set $\mathbf{\Phi} \leftarrow \mathbf{S}_2 \cdot \mathbf{\Phi}$ ▷ saltation matrix
    Reset Map: $\mathbf{x} \leftarrow \mathbf{R}(\mathbf{x})$
    Reinitialize: $\mathbf{Y}_1 \leftarrow r_0\mathbb{I}_{n\times n}$ and $\mathbf{Y}_2 \leftarrow \mathbb{I}_{n\times n}$
  end if
end while

3. $\mathbf{\Phi} \leftarrow \mathbf{Y}_2 \cdot \mathbf{\Phi}$ ▷ Evaluate monodromy matrix
4. Evaluate eigenvalues of $\mathbf{\Phi}$ to get Floquet multipliers

Appendix C

Floquet multiplier for non-smooth FSI system

The steps to evaluate first-order saltation, monodromy matrices, and subsequent Floquet multipliers by incorporating first-order transverse discontinuity mapping for piecewise-smooth hybrid FSI system are described below.

Algorithm 3 Floquet multipliers from monodromy matrix ϕ

1. Initialize: $\mathbf{x}(0)$, ensure $H(\mathbf{x}) > 0$
2. Initialize U_r ▷ Bifurcation parameter
3. Initialize: $\mathbf{\Phi} = \mathbb{I}_{n\times n}$, count $= 0$
4. Initialize: n_{max} ▷ Maximum allowable impacts

while count $\leq n_{max}$ **do**
  Integrate: $\dot{\mathbf{x}} = \mathbf{F}(\mathbf{x})$
  if $H(\mathbf{x}) = 0$ **then** ▷ Occurrence of impact
    Reset Map: $\mathbf{x} \leftarrow \mathbf{R}(\mathbf{x})$
  end if
  if $\dot{x} = 0$ && count $\geq (0.9 * n_{max})$ **then**
    Store $\mathbf{x}$, t for evaluation of time period T
    $T = \{t \in \mathbb{R}^1 : \mathbf{x}(t + \tilde{n}T) = \mathbf{x}(t), \tilde{n} \in \mathbb{I}\}$
  end if
  if count $= n_{max}$ **then** ▷ Remove transients and store for initial condition
    Store: $\mathbf{x}_{init} \leftarrow \mathbf{x}(t)$ and $t_{init} \leftarrow t$
  end if
end while

Initialize: $\mathbf{x} \leftarrow \mathbf{x}_{init}$ at t_{init} ▷ Begin at steady state
Initialize: $\mathbf{Y}(0) = \mathbb{I}_{n\times n}$ ▷ Evaluation of $\mathbf{\Phi}_i$
while $t_{init} \leq t \leq (t_{init} + T)$ **do** ▷ Integrate over period T
  Integrate: $\dot{\mathbf{x}} = \mathbf{F}(\mathbf{x})$
  Integrate: $\dot{\mathbf{Y}} = (\nabla\mathbf{F}(\mathbf{x}))^T \cdot \mathbf{Y}$
  if $H(\mathbf{x}) = 0$ **then** ▷ Occurrence of impact
    $\mathbf{\Phi}_i \leftarrow \mathbf{Y}$
    $\mathbf{\Phi} \leftarrow \mathbf{\Phi}_i \cdot \mathbf{\Phi}$
    Evaluate $\mathbf{S}_i$ from Eq. (4.12) ▷ saltation matrix
    $\mathbf{\Phi} \leftarrow \mathbf{S}_i \cdot \mathbf{\Phi}$
    Reset Map: $\mathbf{x} \leftarrow \mathbf{R}(\mathbf{x})$
    Reinitialize: $\mathbf{Y} \leftarrow \mathbb{I}_{n\times n}$
  end if
end while

5. $\mathbf{\Phi} \leftarrow \mathbf{Y} \cdot \mathbf{\Phi}$ ▷ Evaluate monodromy matrix
6. Evaluate eigenvalues of $\mathbf{\Phi}$ to get Floquet multipliers

Appendix D

Lyapunov exponents for non-smooth FSI system

The steps to evaluate the largest Lyapunov exponent and the Lyapunov spectrum, by implementing first-order transverse discontinuity mapping for the piecewise-smooth hybrid FSI system, is described below.

Algorithm 4 Lyapunov exponent for hybrid systems using $\mathcal{O}(1)$ TDM

1. Initialize: $\mathbf{x}(0)$, ensure $H(\mathbf{x} \geq 0)$
2. Initialize: U_r ▷ Bifurcation parameter
3. Initialize: $\mathbf{y}_i(0)$ for $i \leq n$ using QRD
4. Rescale: $\mathbf{y}_i(0) \leftarrow r_0 * \mathbf{y}_i(0)$
5. Initialize: n_{max} ▷ Maximum allowable impacts

while count $\leq n_{max}$ **do**
  Integrate: $\dot{\mathbf{x}} = \mathbf{F}(\mathbf{x})$
  if $H(\mathbf{x}) = 0$ **then** ▷ Occurrence of impact
    Evaluate: $\mathbf{R}(\mathbf{x})$ and $\mathbf{y}_+$
    Reset Map: $\mathbf{x} \leftarrow \mathbf{R}(\mathbf{x})$
    Reinitialize: $\mathbf{y}_i \leftarrow \mathbf{y}_{i,+} = \mathbf{S}_i \cdot \mathbf{y}_{i,-}$ ▷ TDM using saltation matrix
  end if
  if $\left(t \% t_0\right) = 0$ **then**

    if count $\geq n_{max}/2$ **then**
      Store: $r_i \leftarrow \frac{1}{r_0}\|\mathbf{y}_i\|$
    end if
    Reinitialize: $\mathbf{y}_i \leftarrow r_0 *$ QRD of $\mathbf{y}_i$
  end if
end while

6: Evaluate: $\ln \frac{r_i}{r_0}$ ▷ Store all $\ln \frac{r_i}{r_0}$
7: $\mathrm{LE}_i \leftarrow \frac{1}{N*T} \sum_{n=1}^{N} \ln \frac{r_n}{r_0}$ ▷ i^{th} LEs measured N times
8: $\lambda_i \leftarrow \langle \mathrm{LE}_i \rangle$ ▷ Mean of all LEs

Appendix E

Higher-order transverse discontinuity mapping for non-smooth FSI system

For the representative system in Chapter 5 modeling non-smooth fluid-structure interaction when subjected to impacts with a rigid barrier, the higher-order TDM maps perturbations in the local neighborhood of an impacting orbit from $\mathbf{x}_0$ to $\mathbf{x}_4$. Since, $\mathbf{x}_0 = \mathbf{x}_i + \mathbf{y}_-$ and $\mathbf{x}_4 = \mathbf{R}(\mathbf{x}_i) + \mathbf{y}_+$ in Fig. 5.3, the TDM defined in Chapter 3 (see Eq. (3.12)) maps perturbations from $\mathbf{y}_-$ to $\mathbf{y}_+$ and is given by,

$$\mathbf{y}_+ = \mathbf{A} + \mathbf{B} + \mathbf{C} + \mathbf{D} + \mathbf{E} + \mathbf{F} + \mathbf{G} + \mathbf{H}, \tag{E.1}$$

where,

$$\mathbf{A} = \begin{pmatrix} y_1 \\ -ry_2 \\ y_3 \\ y_4 \end{pmatrix},$$

$$\mathbf{B} = \delta_+ \begin{pmatrix} \dot{y} \\ -r(\delta^2 y - \alpha\dot{y} + Mx) \\ \dot{x} \\ -x - \epsilon(x^2-1)\dot{x} + A(\delta^2 y - \alpha\dot{y} + Mx) \end{pmatrix},$$

$$\mathbf{C} = \delta_+ \begin{pmatrix} r\dot{y} \\ -(-\delta^2 y + \alpha r\dot{y} + Mx) \\ -\dot{x} \\ x + \epsilon(x^2-1)\dot{x} - A(-\delta^2 y + \alpha r\dot{y} + Mx) \end{pmatrix},$$

$$\mathbf{D} = \delta_+ \begin{pmatrix} y_2 \\ -r(-\delta^2 y_1 - \alpha y_2 + M y_3) \\ y_4 \\ -A\delta^2 y_1 - A\alpha y_2 + (AM - 1 - 2\epsilon x\dot{x}) y_3 - \epsilon(x^2-1) y_4 \end{pmatrix},$$

$$\mathbf{E} = \frac{1}{2}\delta_+^2 \begin{pmatrix} -\delta^2 y - \alpha\dot{y} + Mx \\ -r(-\delta^2\dot{y} - \alpha(-\delta^2 y - \alpha\dot{y} + Mx) + M\dot{x}) \\ -x - \epsilon(x^2-1)\dot{x} + A(-\delta^2 y - \alpha\dot{y} + Mx) \\ -A\dot{y}\delta^2 - \alpha A(-\delta^2 y - \alpha\dot{y} + Mx) + \dot{x}(AM - 1 - 2\epsilon x\dot{x}) \dots \\ -\epsilon(x^2-1)(-x - \epsilon(x^2-1)\dot{x} + A(-\delta^2 y - \alpha\dot{y} + Mx)) \end{pmatrix},$$

$$\mathbf{F} = \delta_+ \begin{pmatrix} -r^2 y_2 \\ \delta^2 y_1 + \alpha r^2 y_2 - M y_3 \\ -y_4 \\ A\delta^2 y_1 + A\alpha r^2 y_2 - (AM - 1 - 2\epsilon x\dot{x}) + \epsilon(x^2-1) y_4 \end{pmatrix},$$

$$\mathbf{G} = \delta_+^2 \begin{pmatrix} -r^2(-\delta^2 y - \alpha\dot{y} + Mx) \\ \delta^2\dot{y} + \alpha r^2(-\delta^2 y - \alpha\dot{y} + Mx) + M\dot{x} \\ x + \epsilon(x^2-1)\dot{x} - A(-\delta^2 y - \alpha\dot{y} + Mx) \\ \delta^2 A\dot{y} + r^2 A\alpha(-\delta^2 y - \alpha\dot{y} + Mx) - (AM - 1 - 2\epsilon x\dot{x})\dot{x} \dots \\ +\epsilon(x^2-1)(-x - \epsilon(x^2-1)\dot{x} + A(-\delta^2 y - \alpha\dot{y} + Mx)) \end{pmatrix},$$

$$\mathbf{H} = \frac{1}{2}\delta_+^2 \begin{pmatrix} -r(-\delta^2 y + r\alpha\dot{y} + Mx) \\ r\delta^2\dot{y} + r\alpha(-\delta^2 y + r\alpha\dot{y} + Mx) + M\dot{x} \\ -x - \epsilon(x^2-1)\dot{x} + A(-\delta^2 y + r\alpha\dot{y} + Mx) \\ rA\delta^2\dot{y} + rA\alpha(-\delta^2 y + r\alpha\dot{y} + Mx) + (AM - 1 - 2\epsilon x\dot{x})\dot{x} \dots \\ -\epsilon(x^2-1)(-x - \epsilon(x^2-1)\dot{x} + A(-\delta^2 y + r\alpha\dot{y} + Mx)) \end{pmatrix},$$

$\alpha = (2\xi\delta + \gamma/\mu)$ and y_i are the components of the perturbed state $\mathbf{y}_-$.

Appendix F

Higher-order saltation matrix for Filippov systems

The steps to evaluate higher-order saltation matrices, monodromy matrices and the subsequent Floquet multipliers, by incorporating higher-order transverse discontinuity mapping for piecewise-smooth Filippov systems, are described below.

Algorithm 5 Floquet multipliers from monodromy matrix ϕ

1. Initialize: $\mathbf{x}(0)$ and f ▷ Bifurcation parameter
2. Initialize: $\mathbf{\Phi} = \mathbb{I}_{n\times n}$, $T = 2\pi/\omega$ ▷ Set time period T of external force

while t $\leq 300T$ **do**
  Integrate: $\dot{\mathbf{x}} = \mathbf{F}(\mathbf{x})$
  if $\dot{x} = 0$ && $t \geq (0.9 * 300 * T)$ **then**
    $T_p = \{t \in \mathbb{R}^1 : x(t + \tilde{n}T_p) = x(t), \tilde{n} \in \mathbb{I}\}$ ▷ Store x, t for evaluation of time period T_p
  end if
  if $t == 300T$ **then** ▷ Remove transients
    Store: $\mathbf{x}_{init} \leftarrow \mathbf{x}(t)$ and $t_{init} \leftarrow t$
  end if
end while
Initialize: $\mathbf{x} \leftarrow \mathbf{x}_{init}$ at t_{init} ▷ Begin at steady state
if $H(\mathbf{x}_{init}) < 0$ **then**
  Initialize: region $\leftarrow -1$ ▷ state $\mathbf{x}_{init} \in S_i$
else $H(\mathbf{x}_{init} > 0)$
  Initialize: region $\leftarrow +1$ ▷ state $\mathbf{x}_{init} \in S_j$
end if
Initialize: $r_0 \ll 1$, $\mathbf{Y}_1(0) = r_0\mathbb{I}_{n\times n}$, $\mathbf{Y}_2(0) = \mathbb{I}_{n\times n}$ ▷ Evaluation of $\mathbf{S}_2$ and $\mathbf{\Phi}_i$
while $t_{init} \leq t \leq (t_{init} + T_p)$ **do** ▷ Integrate over period T
  Integrate: $\dot{\mathbf{x}} = \mathbf{F}(\mathbf{x})$, $\dot{\mathbf{Y}}_1 = (\nabla\mathbf{F}(\mathbf{x}))^T \cdot \mathbf{Y}_1$ and $\dot{\mathbf{Y}}_2 = (\nabla\mathbf{F}(\mathbf{x}))^T \cdot \mathbf{Y}_2$
  if $H(\mathbf{x}) = 0$ **then** ▷ Occurrence of impact with $\Sigma_{i,j}$
    $\mathbf{\Phi}_i \leftarrow \mathbf{Y}_2$ and $\mathbf{\Phi} \leftarrow \mathbf{\Phi}_i \cdot \mathbf{\Phi}$
    Evaluate δ_+ and $\mathbf{y}_+$ using $\mathbf{x}_4$ for all $\mathbf{y}_i$ ▷ Implement higher-order TDM according to region -1 or $+1$
    Initialize: region $\leftarrow -1*$region ▷ state $\mathbf{x}$ crosses from $S_i \leftarrow S_j$ or $S_j \leftarrow S_i$
    Evaluate $\mathbf{Y}_{+,impact}$ from $\mathbf{y}_+$ and $\mathbf{Y}_{-,\text{ impact}} \leftarrow \mathbf{Y}_1$
    Evaluate $\mathbf{S}_2 \leftarrow \mathbf{Y}_{+,impact} \cdot \mathbf{Y}^{-1}_{-,impact}$ and set $\mathbf{\Phi} \leftarrow \mathbf{S}_2 \cdot \mathbf{\Phi}$ ▷ Higher order saltation matrix
    Reinitialize: $\mathbf{Y}_1 \leftarrow r_0\mathbb{I}_{n\times n}$ and $\mathbf{Y}_2 \leftarrow \mathbb{I}_{n\times n}$
  end if
end while
3. $\mathbf{\Phi} \leftarrow \mathbf{Y}_2 \cdot \mathbf{\Phi}$ ▷ Evaluate monodromy matrix
4. Evaluate eigenvalues of $\mathbf{\Phi}$ to get Floquet multipliers

Appendix G

Lyapunov exponents for Filippov systems

The steps to evaluate the largest Lyapunov exponent and the Lyapunov spectrum, by implementing higher-order transverse discontinuity mapping for piecewise-smooth Filippov systems, are described below.

Algorithm 6 Lyapunov exponent for Filippov systems using TDM

1. Initialize: $\mathbf{x}(0)$ and f ▷ Bifurcation parameter
2. Initialize: $\mathbf{y}_i(0)$ for $i \leq n$ using QRD
3. Rescale: $\mathbf{y}_i(0) \leftarrow r_0 \times \mathbf{y}_i(0)$ and set $T = 2\pi/\omega$ ▷ Initialize time period

if $H(\mathbf{x}(0)) < 0$ **then**
  Initialize: region $\leftarrow -1$ ▷ state $\mathbf{x}(0) \in S_i$
else $H(\mathbf{x}(0) > 0)$
  Initialize: region $\leftarrow +1$ ▷ state $\mathbf{x}(0) \in S_j$
end if
while t $\leq 1500 * T$ **do**
  Integrate: $\dot{\mathbf{x}} = \mathbf{F}(\mathbf{x})$
  if $H(\mathbf{x}) = 0$ **then** ▷ Occurrence of impact with $\Sigma_{i,j}$
    Evaluate: δ_+ and $\mathbf{y}_+$ ▷ Implement higher-order TDM according to region -1 or $+1$
    $\mathbf{y}_i \leftarrow \mathbf{y}_{i,+}$ ▷ Implement higher-order TDM
  end if
  if $\big(t \mod T\big) = 0$ **then**
    if t $\geq 1000T$ **then**
      Store: $r_i \leftarrow \dfrac{1}{r_0}\|\mathbf{y}_i\|$ ▷ store the growth rate
    end if
    Reinitialize: $\mathbf{y}_i \leftarrow r_0 \times$ QRD of $\mathbf{y}_i$
  end if
end while
4: Evaluate: $\log_e \frac{r_i}{r_0}$ ▷ Store all $log_e \frac{r_i}{r_0}$
5: $\mathrm{LE}_i \leftarrow \frac{1}{N*T} \sum_{n=1}^{N} \log_e \frac{r_n}{r_0}$
6: $\lambda_i \leftarrow \langle \mathrm{LE}_i \rangle$ ▷ Mean of all LEs

Bibliography

[1] V. Acary. Higher order schemes for nonsmooth mechanical systems. In *12th Seminar" NUMDIFF" on Numerical Solution of Differential and Differential-Algebraic Equations*, 2009.

[2] J. Awrejcewicz and C.-H. Lamarque. *Bifurcation and chaos in nonsmooth mechanical systems*, volume 45. World Scientific, 2003.

[3] S. Balasubramanian and R. Skop. A nonlinear oscillator model for vortex shedding from cylinders and cones in uniform and shear flows. *Journal of Fluids and Structures*, 10(3):197–214, 1996.

[4] M. Balcerzak, A. Dabrowski, B. Blazejczyk-Okolewska, and A. Stefanski. Determining lyapunov exponents of non-smooth systems: Perturbation vectors approach. *Mechanical Systems and Signal Processing*, 141:106734, 2020.

[5] S. Banerjee and K. Chakrabarty. Nonlinear modeling and bifurcations in the boost converter. *IEEE Transactions on Power Electronics*, 13(2):252–260, 1998.

[6] S. Banerjee and C. Grebogi. Border collision bifurcations in two-dimensional piecewise smooth maps. *Physical Review E*, 59(4):4052, 1999.

[7] S. Banerjee, J. Ing, E. Pavlovskaia, M. Wiercigroch, and R. K. Reddy. Invisible grazings and dangerous bifurcations in impacting systems: the problem of narrow-band chaos. *Physical Review E*, 79(3):037201, 2009.

[8] S. Banerjee, P. Ranjan, and C. Grebogi. Bifurcations in two-dimensional piecewise smooth maps-theory and applications in switching circuits. *IEEE Transactions on Circuits and Systems I: Fundamental Theory and Applications*, 47(5):633–643, 2000.

[9] S. Banerjee, J. A. Yorke, and C. Grebogi. Robust chaos. *Physical Review Letters*, 80(14):3049, 1998.

[10] I. Belykh, R. Kuske, M. Porfiri, and D. J. Simpson. Beyond the bristol book: Advances and perspectives in non-smooth dynamics and applications. *Chaos: An Interdisciplinary Journal of Nonlinear Science*, 33(1), 2023.

[11] G. Benettin, L. Galgani, A. Giorgilli, and J.-M. Strelcyn. Lyapunov characteristic exponents for smooth dynamical systems and for hamiltonian systems; a method for computing all of them. part 1: Theory. *Meccanica*, 15(1):9–20, 1980.

[12] G. Benettin, L. Galgani, and J.-M. Strelcyn. Kolmogorov entropy and numerical experiments. *Physical Review A*, 14(6):2338, 1976.

[13] G. Bennetin, L. Galgani, A. Giorgilli, and J.-M. Strelcyn. Lyapunov characteristic exponents for smooth dynamical systems and for hamiltonian systems: A method for computing all of them. part 2: Numerical application. *Meccanica*, 15(1):21–30, 1980.

[14] M. Bernardo, C. Budd, A. R. Champneys, and P. Kowalczyk. *Piecewise-smooth dynamical systems: theory and applications*, volume 163. Springer Science & Business Media, 2008.

[15] R. E. D. Bishop and A. Hassan. The lift and drag forces on a circular cylinder oscillating in a flowing fluid. *Proceedings of the Royal Society of London. Series A. Mathematical and Physical Sciences*, 277(1368):51–75, 1964.

[16] R. D. Blevins. Flow-induced vibration. *New York*, 1977.

[17] C. Budd and F. Dux. Chattering and related behaviour in impact oscillators. *Philosophical Transactions of the Royal Society of London. Series A: Physical and Engineering Sciences*, 347(1683):365–389, 1994.

[18] C. Budd, F. Dux, and A. Cliffe. The effect of frequency and clearance variations on single-degree-of-freedom impact oscillators. *Journal of sound and vibration*, 184(3):475–502, 1995.

[19] K. Chakrabarty, G. Poddar, and S. Banerjee. Bifurcation behavior of the buck converter. *IEEE transactions on power electronics*, 11(3):439–447, 1996.

[20] R. Chawla and V. Pakrashi. Dynamic responses of a damaged double euler–bernoulli beam traversed by a 'phantom'vehicle. *Structural Control and Health Monitoring*, 29(5):e2933, 2022.

[21] R. Chawla, A. Rounak, and V. Pakrashi. Stability analysis of hybrid systems with higher order transverse discontinuity mapping. *arXiv preprint arXiv:2203.13222*, 2022.

[22] W. Chin, E. Ott, H. E. Nusse, and C. Grebogi. Grazing bifurcations in impact oscillators. *Physical Review E*, 50(6):4427, 1994.

[23] W. Chin, E. Ott, H. E. Nusse, and C. Grebogi. Universal behavior of impact oscillators near grazing incidence. *Physics Letters A*, 201(2-3):197–204, 1995.

[24] M. J. Coleman, A. Chatterjee, and A. Ruina. Motions of a rimless spoked wheel: a simple three-dimensional system with impacts. *Dynamics and stability of systems*, 12(3):139–159, 1997.

[25] A. Dabrowski. Estimation of the largest lyapunov exponent from the perturbation vector and its derivative dot product. *Nonlinear Dynamics*, 67(1):283–291, 2012.

[26] H. Dankowicz and A. B. Nordmark. On the origin and bifurcations of stick-slip oscillations. *Physica D: Nonlinear Phenomena*, 136(3-4):280–302, 2000.

[27] S. L. De Souza and I. L. Caldas. Calculation of lyapunov exponents in systems with impacts. *Chaos, Solitons & Fractals*, 19(3):569–579, 2004.

[28] M. Di Bernardo, C. Budd, and A. Champneys. Normal form maps for grazing bifurcations in n-dimensional piecewise-smooth dynamical systems. *Physica D: Nonlinear Phenomena*, 160(3-4):222–254, 2001.

[29] M. Di Bernardo, C. J. Budd, and A. R. Champneys. Grazing and border-collision in piecewise-smooth systems: A unified analytical framework. *Physical Review Letters*, 86(12):2553, 2001.

[30] M. Di Bernardo and S. Hogan. Discontinuity-induced bifurcations of piecewise smooth dynamical systems. *Philosophical Transactions of the Royal Society A: Mathematical, Physical and Engineering Sciences*, 368(1930):4915–4935, 2010.

[31] M. Di Bernardo, P. Kowalczyk, and A. Nordmark. Bifurcations of dynamical systems with sliding: derivation of normal-form mappings. *Physica D: Nonlinear Phenomena*, 170(3-4):175–205, 2002.

[32] M. L. Facchinetti, E. De Langre, and F. Biolley. Coupling of structure and wake oscillators in vortex-induced vibrations. *Journal of Fluids and structures*, 19(2):123–140, 2004.

[33] G. Floquet. On linear differential equations with periodic coefficients. In *Annales scientifiques de l'École Normale Supérieure*, volume 12, pages 47–88, 1883.

[34] S. Foale and S. Bishop. Dynamical complexities of forced impacting systems. *Philosophical Transactions of the Royal Society of London. Series A: Physical and Engineering Sciences*, 338(1651):547–556, 1992.

[35] S. Foale and S. Bishop. Bifurcations in impact oscillations. *Nonlinear dynamics*, 6:285–299, 1994.

[36] M. H. Fredriksson and A. B. Nordmark. Bifurcations caused by grazing incidence in many degrees of freedom impact oscillators. *Proceedings of the Royal Society of London. Series A: Mathematical, Physical and Engineering Sciences*, 453(1961):1261–1276, 1997.

[37] M. H. Fredriksson and A. B. Nordmark. On normal form calculations in impact oscillators. *Proceedings of the Royal Society of London. Series A: Mathematical, Physical and Engineering Sciences*, 456(1994):315–329, 2000.

[38] R. D. Gabbai and H. Benaroya. An overview of modeling and experiments of vortex-induced vibration of circular cylinders. *Journal of sound and vibration*, 282(3-5):575–616, 2005.

[39] A. Ganguli and S. Banerjee. Dangerous bifurcation at border collision: When does it occur? *Physical Review E*, 71(5):057202, 2005.

[40] O. Gendelman. Analytic treatment of a system with a vibro-impact nonlinear energy sink. *Journal of Sound and Vibration*, 331(21):4599–4608, 2012.

[41] D. Giaouris, S. Banerjee, B. Zahawi, and V. Pickert. Stability analysis of the continuous-conduction-mode buck converter via filippov's method. *IEEE Transactions on Circuits and Systems I: Regular Papers*, 55(4):1084–1096, 2008.

[42] R. Govardhan and C. Williamson. Modes of vortex formation and frequency response of a freely vibrating cylinder. *Journal of Fluid Mechanics*, 420:85–130, 2000.

[43] R. Govardhan and C. Williamson. Critical mass in vortex-induced vibration of a cylinder. *European Journal of Mechanics-B/Fluids*, 23(1):17–27, 2004.

[44] H. Goyder and C. Teh. A study of the impact dynamics of loosely supported heat exchanger tubes. 1989.

[45] P. Grassberger and I. Procaccia. Measuring the strangeness of strange attractors. *Physica D: nonlinear phenomena*, 9(1-2):189–208, 1983.

[46] D. J. Griffiths. Introduction to electrodynamics, 2005.

[47] J. Guckenheimer and P. Holmes. Global bifurcations. *Nonlinear oscillations, dynamical systems, and bifurcations of vector fields*, pages 289–352, 1983.

[48] R. Han, A. Luo, and W. Deng. Chaotic motion of a horizontal impact pair. *Journal of Sound and Vibration*, 181(2):231–250, 1995.

[49] R. T. Hartlen and I. G. Currie. Lift-oscillator model of vortex-induced vibration. *Journal of the Engineering Mechanics Division*, 96(5):577–591, 1970.

[50] M. A. Hassouneh, E. H. Abed, and H. E. Nusse. Robust dangerous border-collision bifurcations in piecewise smooth systems. *Physical review letters*, 92(7):070201, 2004.

[51] F. Hendriks. Bounce and chaotic motion in impact print hammers. *IBM Journal of Research and Development*, 27(3):273–280, 1983.

[52] P. Holmes, R. J. Full, D. Koditschek, and J. Guckenheimer. The dynamics of legged locomotion: Models, analyses, and challenges. *SIAM review*, 48(2):207–304, 2006.

[53] J. Ing, E. Pavlovskaia, M. Wiercigroch, and S. Banerjee. Experimental study of impact oscillator with one-sided elastic constraint. *Philosophical Transactions of the Royal Society A: Mathematical, Physical and Engineering Sciences*, 366(1866):679–705, 2008.

[54] H. Jiang, A. S. Chong, Y. Ueda, and M. Wiercigroch. Grazing-induced bifurcations in impact oscillators with elastic and rigid constraints. *International Journal of Mechanical Sciences*, 127:204–214, 2017.

[55] L. Jin, Q.-S. Lu, and E. Twizell. A method for calculating the spectrum of lyapunov exponents by local maps in non-smooth impact-vibrating systems. *Journal of sound and Vibration*, 298(4-5):1019–1033, 2006.

[56] A. Kahraman and R. Singh. Non-linear dynamics of a spur gear pair. *Journal of sound and vibration*, 142(1):49–75, 1990.

[57] K. Karagiannis and F. Pfeiffer. Theoretical and experimental investigations of gear-rattling. *Nonlinear dynamics*, 2:367–387, 1991.

[58] A. Khalak and C. H. Williamson. Motions, forces and mode transitions in vortex-induced vibrations at low mass-damping. *Journal of fluids and Structures*, 13(7-8):813–851, 1999.

[59] N. J. Kong, J. J. Payne, G. Council, and A. M. Johnson. The salted kalman filter: Kalman filtering on hybrid dynamical systems. *Automatica*, 131:109752, 2021.

[60] N. J. Kong, J. J. Payne, J. Zhu, and A. M. Johnson. Saltation matrices: The essential tool for linearizing hybrid dynamical systems. *arXiv preprint arXiv:2306.06862*, 2023.

[61] P. Kowalczyk and M. di Bernardo. On a novel class of bifurcations in hybrid dynamical systems: The case of relay feedback systems. In *Hybrid Systems: Computation and Control: 4th International Workshop, HSCC 2001 Rome, Italy, March 28–30, 2001 Proceedings 4*, pages 361–374. Springer, 2001.

[62] S. Krenk and S. R. Nielsen. Energy balanced double oscillator model for vortex-induced vibrations. *Journal of Engineering Mechanics*, 125(3):263–271, 1999.

[63] A. M. Krivtsov and M. Wiercigroch. Dry friction model of percussive drilling. *Meccanica*, 34:425–434, 1999.

[64] S. Kundu, S. Banerjee, J. Ing, E. Pavlovskaia, and M. Wiercigroch. Singularities in soft-impacting systems. *Physica D: Nonlinear Phenomena*, 241(5):553–565, 2012.

[65] H. Lamba and C. Budd. Scaling of lyapunov exponents at nonsmooth bifurcations. *Physical Review E*, 50(1):84, 1994.

[66] R. Landl. A mathematical model for vortex-excited vibrations of bluff bodies. *Journal of Sound and Vibration*, 42(2):219–234, 1975.

[67] R. Leine. Non-smooth stability analysis of the parametrically excited impact oscillator. *International Journal of Non-Linear Mechanics*, 47(9):1020–1032, 2012.

[68] R. I. Leine. Bifurcations in discontinuous mechanical systems of filippov-type. 2002.

[69] H. Li and A. Li. Potential of a vibro-impact nonlinear energy sink for energy harvesting. *Mechanical Systems and Signal Processing*, 159:107827, 2021.

[70] T. Li, C.-H. Lamarque, S. Seguy, and A. Berlioz. Chaotic characteristic of a linear oscillator coupled with vibro-impact nonlinear energy sink. *Nonlinear Dynamics*, 91(4):2319–2330, 2018.

[71] T. Li, S. Seguy, and A. Berlioz. On the dynamics around targeted energy transfer for vibro-impact nonlinear energy sink. *Nonlinear Dynamics*, 87:1453–1466, 2017.

[72] A. C. Luo. *Discontinuous dynamical systems*. Springer.

[73] A. C. Luo. *Discrete and switching dynamical systems*. L& H Scientific Publishing, 2011.

[74] A. C. Luo. *Regularity and complexity in dynamical systems*. Springer, 2012.

[75] A. C. Luo and Y. Guo. *Vibro-impact dynamics*. John Wiley & Sons, 2012.

[76] Y. Ma, M. Agarwal, and S. Banerjee. Border collision bifurcations in a soft impact system. *Physics Letters A*, 354(4):281–287, 2006.

[77] Y. Ma, J. Ing, S. Banerjee, M. Wiercigroch, and E. Pavlovskaia. The nature of the normal form map for soft impacting systems. *International Journal of Non-Linear Mechanics*, 43(6):504–513, 2008.

[78] J. Mallet-Paret and J. A. Yorke. Snakes: oriented families of periodic orbits, their sources, sinks, and continuation. *Journal of Differential Equations*, 43(3):419–450, 1982.

[79] K. Mandal, C. Chakraborty, A. Abusorrah, M. Al-Hindawi, Y. Al-Turki, and S. Banerjee. An automated algorithm for stability analysis of hybrid dynamical systems. *The European Physical Journal Special Topics*, 222:757–768, 2013.

[80] P. C. Müller. Calculation of lyapunov exponents for dynamic systems with discontinuities. *Chaos, Solitons & Fractals*, 5(9):1671–1681, 1995.

[81] N. Mureithi, H. Kanki, and T. Nakamura. Bifurcation and perturbation analysis of some vortex shedding models. In *Proceedings of the Seventh International Conference on Flow-Induced Vibrations, Luzern, Switzerland. Balkema, Rotterdam*, pages 61–68, 2000.

[82] A. H. Nayfeh and B. Balachandran. *Applied nonlinear dynamics: analytical, computational, and experimental methods*. John Wiley & Sons, 2008.

[83] D. J. Newman and G. E. Karniadakis. A direct numerical simulation study of flow past a freely vibrating cable. *Journal of Fluid Mechanics*, 344:95–136, 1997.

[84] A. Nordmark. Effects due to low velocity impact in mechanical oscillators. *International Journal of Bifurcation and Chaos*, 2(03):597–605, 1992.

[85] A. B. Nordmark. Non-periodic motion caused by grazing incidence in an impact oscillator. *Journal of Sound and Vibration*, 145(2):279–297, 1991.

[86] A. B. Nordmark. Universal limit mapping in grazing bifurcations. *Physical review E*, 55(1):266, 1997.

[87] H. E. Nusse, E. Ott, and J. A. Yorke. Border-collision bifurcations: An explanation for observed bifurcation phenomena. *Physical Review E*, 49(2):1073, 1994.

[88] H. E. Nusse and J. A. Yorke. Border-collision bifurcations including "period two to period three" for piecewise smooth systems. *Physica D: Nonlinear Phenomena*, 57(1-2):39–57, 1992.

[89] M. Oestreich, N. Hinrichs, and K. Popp. Bifurcation and stability analysis for a non-smooth friction oscillator. *Archive of Applied Mechanics*, 66(5):301–314, 1996.

[90] M. Oestreich, N. Hinrichs, K. Popp, and C. Budd. Analytical and experimental investigation of an impact oscillator. In *International Design Engineering Technical Conferences and Computers and Information in Engineering Conference*, volume 80425, page V01CT15A008. American Society of Mechanical Engineers, 1997.

[91] R. Ogink and A. Metrikine. A wake oscillator with frequency dependent coupling for the modeling of vortex-induced vibration. *Journal of sound and vibration*, 329(26):5452–5473, 2010.

[92] V. I. Oseledec. A multiplicative ergodic theorem. liapunov characteristic number for dynamical systems. *Trans. Moscow Math. Soc.*, 19:197–231, 1968.

[93] M. P. Païdoussis and G. X. Li. Cross-flow-induced chaotic vibrations of heat-exchanger tubes impacting on loose supports. *Journal of Sound and Vibration*, 152(2):305–326, 1992.

[94] E. Pavlovskaia, J. Ing, M. Wiercigroch, and S. Banerjee. Complex dynamics of bilinear oscillator close to grazing. *International Journal of Bifurcation and Chaos*, 20(11):3801–3817, 2010.

[95] E. Pavlovskaia, M. Wiercigroch, and C. Grebogi. Two-dimensional map for impact oscillator with drift. *Physical Review E*, 70(3):036201, 2004.

[96] Y. B. Pesin. Characteristic lyapunov exponents and smooth ergodic theory. *Russian Mathematical Surveys*, 32(4):55, 1977.

[97] P. T. Piiroinen, L. N. Virgin, and A. R. Champneys. Chaos and period-adding; experimental and numerical verification of the grazing bifurcation. *Journal of Nonlinear Science*, 14(4):383–404, 2004.

[98] P. Plaschko. Global chaos in flow-induced oscillations of cylinders. *Journal of Fluids and Structures*, 14(6):883–893, 2000.

[99] K. Popp, M. Oestreich, and N. Hinrichs. Numerical and experimental investigation of nonsmooth mechanical systems. In *IUTAM Symposium on New Applications of Nonlinear and Chaotic Dynamics in Mechanics*, pages 293–302. Springer, 1999.

[100] Y. Qu and A. V. Metrikine. A single van der pol wake oscillator model for coupled cross-flow and in-line vortex-induced vibrations. *Ocean Engineering*, 196:106732, 2020.

[101] M. T. Rosenstein, J. J. Collins, and C. J. De Luca. A practical method for calculating largest lyapunov exponents from small data sets. *Physica D: Nonlinear Phenomena*, 65(1-2):117–134, 1993.

[102] A. Rounak and S. Gupta. Bifurcations in a pre-stressed, harmonically excited, vibro-impact oscillator at subharmonic resonances. *International Journal of Bifurcation and Chaos*, 30(08):2050111, 2020.

[103] T. Sarpkaya. A critical review of the intrinsic nature of vortex-induced vibrations. *Journal of fluids and structures*, 19(4):389–447, 2004.

[104] S. Shaw and P. Holmes. A periodically forced impact oscillator with large dissipation. 1983.

[105] S. W. Shaw. The dynamics of a harmonically excited system having rigid amplitude constraints, part 1: Subharmonic motions and local bifurcations. 1985.

[106] S. W. Shaw and P. Holmes. A periodically forced piecewise linear oscillator. *Journal of sound and vibration*, 90(1):129–155, 1983.

[107] S. W. Shaw and P. J. Holmes. A periodically forced piecewise linear oscillator. *Journal of sound and vibration*, 90(1):129–155, 1983.

[108] D. J. Simpson, V. Avrutin, and S. Banerjee. Nordmark map and the problem of large-amplitude chaos in impact oscillators. *Physical Review E*, 102(2):022211, 2020.

[109] D. J. Simpson, S. J. Hogan, and R. Kuske. Stochastic regular grazing bifurcations. *SIAM Journal on Applied Dynamical Systems*, 12(2):533–559, 2013.

[110] D. J. Simpson and R. Kuske. Mixed-mode oscillations in a stochastic, piecewise-linear system. *Physica D: Nonlinear Phenomena*, 240(14-15):1189–1198, 2011.

[111] D. J. W. Simpson and R. Kuske. The influence of localized randomness on regular grazing bifurcations with applications to impacting dynamics. *Journal of vibration and control*, 24(2):407–426, 2018.

[112] R. A. Skop and S. Balasubramanian. A new twist on an old model for vortex-excited vibrations. *Journal of Fluids and Structures*, 11(4):395–412, 1997.

[113] E. J. Staunton and P. T. Piiroinen. Noise and multistability in the square root map. *Physica D: Nonlinear Phenomena*, 380:31–44, 2018.

[114] E. J. Staunton and P. T. Piiroinen. Noise-induced multistability in the square root map. *Nonlinear Dynamics*, 95:769–782, 2019.

[115] E. J. Staunton and P. T. Piiroinen. Discontinuity mappings for stochastic nonsmooth systems. *Physica D: Nonlinear Phenomena*, 406:132405, 2020.

[116] E. J. Staunton and P. T. Piiroinen. Estimating the dynamics of systems with noisy boundaries. *Nonlinear Analysis: Hybrid Systems*, 36:100863, 2020.

[117] A. Stefanski. Estimation of the largest lyapunov exponent in systems with impacts. *Chaos, Solitons & Fractals*, 11(15):2443–2451, 2000.

[118] A. Stefanski, A. Dabrowski, and T. Kapitaniak. Evaluation of the largest lyapunov exponent in dynamical systems with time delay. *Chaos, Solitons & Fractals*, 23(5):1651–1659, 2005.

[119] A. Stefański and T. Kapitaniak. Estimation of the dominant lyapunov exponent of non-smooth systems on the basis of maps synchronization. *Chaos, Solitons & Fractals*, 15(2):233–244, 2003.

[120] D. E. Stewart. Rigid-body dynamics with friction and impact. *SIAM review*, 42(1):3–39, 2000.

[121] S. H. Strogatz. *Nonlinear dynamics and chaos with student solutions manual: With applications to physics, biology, chemistry, and engineering*. CRC press, 2018.

[122] N. Suda and S. Banerjee. Why does narrow band chaos in impact oscillators disappear over a range of frequencies? *Nonlinear Dynamics*, 86:2017–2022, 2016.

[123] Y. Termonia. Kolmogorov entropy from a time series. *Physical Review A*, 29(3):1612, 1984.

[124] P. Tung and S. Shaw. A method for the improvement of impact printer performance. 1988.

[125] A. F. Vakakis, O. V. Gendelman, L. A. Bergman, D. M. McFarland, G. Kerschen, and Y. S. Lee. *Nonlinear targeted energy transfer in mechanical and structural systems*, volume 156. Springer Science & Business Media, 2008.

[126] A. F. Vakakis, O. V. Gendelman, L. A. Bergman, A. Mojahed, and M. Gzal. Nonlinear targeted energy transfer: state of the art and new perspectives. *Nonlinear Dynamics*, 108(2):711–741, 2022.

[127] A. J. Van Der Schaft and J. M. Schumacher. *An introduction to hybrid dynamical systems*, volume 251. Springer London, 2000.

[128] G. Whiston. Global dynamics of a vibro-impacting linear oscillator. *Journal of Sound and Vibration*, 118(3):395–424, 1987.

[129] G. Whiston. The vibro-impact response of a harmonically excited and preloaded one-dimensional linear oscillator. *Journal of Sound and Vibration*, 115(2):303–319, 1987.

[130] M. Wiercigroch and E. Budak. Sources of nonlinearities, chatter generation and suppression in metal cutting. *Philosophical Transactions of the Royal Society of London. Series A: Mathematical, Physical and Engineering Sciences*, 359(1781):663–693, 2001.

[131] M. Wiercigroch, R. Neilson, and M. Player. Material removal rate prediction for ultrasonic drilling of hard materials using an impact oscillator approach. *Physics Letters A*, 259(2):91–96, 1999.

[132] S. Wiggins. *Global bifurcations and chaos: analytical methods*, volume 73. Springer Science & Business Media, 2013.

[133] S. Wiggins and M. Golubitsky. *Introduction to applied nonlinear dynamical systems and chaos*, volume 2. Springer, 2003.

[134] C. Williamson and R. Govardhan. A brief review of recent results in vortex-induced vibrations. *Journal of Wind engineering and industrial Aerodynamics*, 96(6-7):713–735, 2008.

[135] C. H. Williamson and R. Govardhan. Vortex-induced vibrations. *Annual Review of Fluid Mechanics*, 36:413–455, 2004.

[136] A. Wolf, J. B. Swift, H. L. Swinney, and J. A. Vastano. Determining lyapunov exponents from a time series. *Physica D: nonlinear phenomena*, 16(3):285–317, 1985.

[137] S. Yin, G. Wen, H. Xu, and X. Wu. Higher order zero time discontinuity mapping for analysis of degenerate grazing bifurcations of impacting oscillators. *Journal of Sound and Vibration*, 437:209–222, 2018.

[138] G. Yuan, S. Banerjee, E. Ott, and J. A. Yorke. Border-collision bifurcations in the buck converter. *IEEE Transactions on Circuits and Systems I: Fundamental Theory and Applications*, 45(7):707–716, 1998.